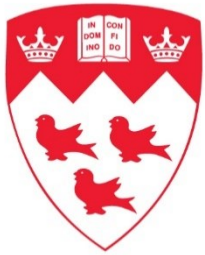


Seismic Evaluation of Existing Steel Moment-Resisting Frame Structures with Unreinforced Masonry Infill Walls Built Between the 1960s and 1990s in Areas of Moderate Seismic Activity

By

Mohammad Sohayeb Akiel



McGill

Department of Civil Engineering

McGill University

Montreal, Quebec, Canada

March 2024

A thesis submitted to McGill University in partial fulfillment of the requirements for the degree of Doctor of Philosophy

© Mohammad S. Akiel, 2024

ABSTRACT

The seismic performance of existing steel moment-resisting frame structures (MRF) constructed before the 1990s in regions of moderate seismic activity in North America has attracted the attention of the research community due to advancements in current knowledge, standards and provisions. These structures often feature infilled unreinforced masonry walls, whose contribution to the lateral loading resistance system was frequently overlooked. Research has shown that infill walls interact with surrounding frames under seismic forces, significantly altering the dynamic characteristics of buildings. Additionally, column base connections are crucial in steel structures, facilitating force transmission to foundations. Exposed column base connections showed popularity in low- to mid-rise steel MRF structures, yet guidelines for their design were lacking until recent years, despite evidence that they are neither fully pinned nor fixed. This study aims to characterize the seismic response of existing low- to mid-rise steel MRF structures, focusing on realistic behaviour, including exposed column base connections with L-shaped anchor rods and considering the presence and impact of unreinforced masonry infill walls on frame stiffness and strength. The research combines experimental and numerical explorations of exposed column base connections at a component level, followed by comprehensive numerical seismic analysis of the entire frame, integrating all components. Experimental tests include two- and four-anchor rod column base connections subjected to reversed cyclic lateral deformations with constant axial loading, considering anchor rod corrosion. The corrosion effect was more pronounced in two-anchor rod specimens, with four-anchor rod specimens showing a 57% increase in yielding and ultimate moment capacities on average. A parametric study investigated the influence of anchor rod diameter, transverse spacing, base plate thickness and dimensions, column section size, axial loading level and steel grade on cyclic performance. Finite element models demonstrated high

agreement with tested four-anchor rod connections, with further improvement expected for two-anchor rod connections with additional data on grout material. The influence of various parameters on moment-rotation relationships, ductility and energy dissipation capacity of connections is presented. Nonlinear analysis included four models: bare steel frame, frame accounting for column base connections, frame accounting for unreinforced masonry infill walls and frame incorporating both base connections and infill walls. Base connection modeling significantly affected drift and base shear capacities, while infill walls dominated dynamic properties of simulations.

RÉSUMÉ

La performance sismique des structures existantes en acier à ossature partielle résistante aux moments (MRF) construites avant les années 1990 dans les régions d'activité sismique modérée en Amérique du Nord a attiré l'attention de la communauté scientifique en raison des avancées dans les connaissances actuelles, les normes et les dispositions. Ces structures comportent souvent des murs de maçonnerie non armés remplis, dont la contribution au système de résistance aux charges latérales était souvent négligée. La recherche a montré que les murs de remplissage interagissent avec les cadres environnants sous l'effet des forces sismiques, modifiant significativement les caractéristiques dynamiques des bâtiments. De plus, les connexions à la base des colonnes sont cruciales dans les structures en acier, facilitant la transmission des forces aux fondations. Les connexions à la base des colonnes exposées ont été populaires dans les structures MRF en acier de faible à moyenne hauteur, mais des directives pour leur conception faisaient défaut jusqu'à ces dernières années, malgré des preuves montrant qu'elles ne sont ni entièrement articulées ni fixes. Cette étude vise à caractériser la réponse sismique des structures existantes à ossature partielle MRF en acier de faible à moyenne hauteur, en se concentrant sur un comportement réaliste, y compris les connexions à la base des colonnes exposées avec des tiges d'ancrage en forme de L, et en tenant compte de la présence et de l'impact des murs de remplissage en maçonnerie non armée sur la rigidité et la résistance des cadres. La recherche combine des explorations expérimentales et numériques des connexions à la base des colonnes exposées au niveau des composants, suivies d'une analyse sismique numérique complète de l'ensemble du cadre, intégrant tous les composants. Les tests expérimentaux comprennent des connexions à la base des colonnes à deux et quatre tiges d'ancrage soumises à des déformations latérales cycliques inversées avec une charge axiale constante, en tenant compte de la corrosion des tiges d'ancrage.

L'effet de la corrosion était plus prononcé dans les spécimens à deux tiges d'ancrage, les spécimens à quatre tiges d'ancrage montrant une augmentation de 57 % des capacités de moment de cession et ultime en moyenne. Une étude paramétrique a examiné l'influence du diamètre des tiges d'ancrage, de l'espacement transversal, de l'épaisseur et des dimensions de la plaque de base, de la taille de la section de colonne, du niveau de charge axiale et de la qualité de l'acier sur les performances cycliques. Les modèles par éléments finis ont démontré un accord élevé avec les connexions à quatre tiges d'ancrage testées, avec une amélioration supplémentaire attendue pour les connexions à deux tiges d'ancrage avec des données supplémentaires sur le matériau de coulis. L'influence de divers paramètres sur les relations moment-rotation, la ductilité et la capacité de dissipation d'énergie des connexions est présentée. L'analyse non linéaire comprenait quatre modèles : cadre en acier nu, cadre prenant en compte les connexions à la base des colonnes, cadre prenant en compte les murs de remplissage en maçonnerie non armée, et cadre incorporant à la fois les connexions à la base et les murs de remplissage. La modélisation des connexions de base affectait significativement les capacités de déformation et de cisaillement de la base, tandis que les murs de remplissage dominaient les propriétés dynamiques des simulations.

ACKNOWLEDGMENTS

I would like to express my sincere gratitude to all those who have supported me throughout my journey towards completing this PhD thesis. First and foremost, I am deeply grateful to my supervisor, Professor Colin Rogers, for his invaluable guidance, encouragement and unwavering support throughout this research endeavor. I extend my appreciation to Professor Dimitrios Lignos, for his insightful feedback and valuable contributions in the column base connections testing and simulation.

I am indebted to the Department of Civil Engineering at McGill University for providing me with the opportunity to pursue my doctoral studies and for facilitating an enriching academic environment. Special thanks are due to the staff at the Jamieson Structures Laboratory, McGill University, for their assistance and expertise in conducting the lab testing essential to this research. In particular, I am grateful to Dr. William Cook and Mr. John Bartczak for their invaluable assistance with the experimental work.

Financial support from the Natural Sciences and Engineering Research Council of Canada (NSERC), the Fonds de recherche du Québec – Nature et technologies (FRQ-NT) and the Centre d'études interuniversitaire des structures sous charges extrêmes (CEISCE) is gratefully acknowledged. I am honored to have been awarded the McGill Engineering Doctoral Award, the Grad Excellence Award in Engineering, the John Bonall Porter Fellowship, the Lorne Trottier Engineering Fellowship and the John Adjeleian Fellowship from the Faculty of Engineering at McGill University. I am also thankful to Groupe Acier CAMNOR for their collaboration in the fabrication and supply of the steel components and anchor rods essential to this research.

I am deeply appreciative of the support and encouragement from my friends and colleagues, with special thanks to Muhammad Musanna, Mohamed Afifi, Ahmed Dalaq, Mohamed Shokr, Bashar Hariri and many others whose support has been invaluable.

Lastly, I dedicate this thesis to my beloved family. To my parents, whose love and support have been my guiding light. To my siblings, for their unwavering encouragement. To my wife and soul, Basmah, for her endless patience and unwavering support. And to my children, Fatema, Mohammad, Abdul Rahman, Sarah, Anas and Maria, whose presence has been the source of my strength and motivation to overcome challenges and persevere in my PhD journey.

Contribution to Original Knowledge

An assessment of existing steel moment-resisting frame (MRF) structures built between before 1990s in regions of moderate seismic activity is presented in this thesis. The evolution of standards and provisions in North America, coupled with advancements in testing and simulation techniques, underscores the necessity of characterizing the seismic performance of these structures. Given their diverse applications in hospitals, schools, government buildings and other vital infrastructure, ensuring their seismic adequacy is paramount for the preservation of safety, economy and heritage.

The research outcomes served in advancing the knowledge in the following areas:

1. Experimental evaluation of column base connections' detailing that was overlooked in the literature, while being shown popularity in existing steel structures' structural plans.
2. Investigating the effects of anchor rods' corrosion on the cyclic performance of column base connections.
3. Developing and validating finite element models capable of simulating the cyclic response of steel column base connections and employing them in a parametric study investigating the influence of various components and parameters of the column base connections on their cyclic response.
4. Developing numerical models and employing them in conducting nonlinear response history analyses on a steel MRF hospital case study designed according to the Canadian standards circa 1965, while exploring different simulation assumptions to highlight the importance of accounting for the column base connections and unreinforced masonry infill walls.

Contribution of Authors

This thesis is presented in a traditional monograph style in accordance with the requirements of McGill University. It comprises six chapters, including an introduction, literature review, experimental program on column base connections, cyclic simulation of column base connections, seismic evaluation of existing steel moment resisting frame structures and summary and conclusions chapter.

The contributions of the author and his advisory committee are as follows:

- The principal author, Mohammad S. Akiel, conducted the literature review, reviewed structural plans of existing structures, developed the testing matrix, conducted the tests, developed finite element models, devised the parametric study matrix and models, designed the case study, developed numerical models for the case study, ran simulations for both Chapters 4 and 5, analyzed experimental and numerical results and wrote the thesis.
- The research supervisor, Colin Rogers, provided thorough supervision of the research, operated the testing apparatus, reviewed and edited the thesis.
- The advisory member, Dimitrios Lignos, reviewed the testing matrix of the column base connections, evaluated the column base connection finite element model and provided material combined hardening parameters.

Table of Contents

ABSTRACT	I
RÉSUMÉ.....	III
ACKNOWLEDGMENTS.....	V
Contribution to Original Knowledge.....	VII
Contribution of Authors	VIII
Table of Contents	IX
List of Tables.....	XIII
List of Figures	XV
Chapter 1: Introduction	1
1.1 Research motivation	1
1.2 Objectives and methodology	3
1.3 Thesis outline	4
Chapter 2: Literature Review	7
2.1 Introduction	7
2.2 Development of seismic provisions	7
2.3 Development of steel MRFs.....	10
2.3.1 Studies on the steel MRF	11
2.3.2 Column base connections	23
2.4 Unreinforced masonry infill walls.....	33

2.5 Summary and research gaps	42
Chapter 3: Experimental Program	44
3.1 Introduction	44
3.2 Test program.....	45
3.2.1 Test specimens.....	46
3.2.1.1 Accounting for AR corrosion	47
3.2.1.2 Two-AR specimens	48
3.2.1.3 Four-AR specimens	48
3.3 Fabrication of specimens.....	48
3.4 Test setup and instrumentation.....	49
3.5 Material properties	50
3.5.1 Steel elements	50
3.5.2 Concrete and grout.....	51
3.6 Experimental results	51
3.6.1 Mode of failure	51
3.6.2 Moment-rotation relationship	54
3.6.3 Ductility and energy dissipation capacity.....	56
3.7 Conclusions	57
Chapter 4: Cyclic Simulation of Steel Column Base Connections	77
4.1 Introduction	77

4.2 Modelling approach.....	78
4.2.1 Finite element type, solver and meshing	78
4.2.2 Boundary conditions and contacts	79
4.2.3 Material models	80
4.3 Model validation.....	83
4.4 Parametric evaluation of existing column base connections	85
4.4.1 Simulation matrix	85
4.4.2 Parametric simulation results.....	86
4.4.2.1 Mode of failure	87
4.4.2.2 Moment - rotation relationship	89
4.4.2.3 Ductility and energy dissipation capacity.....	94
4.5 Summary and conclusions.....	97
 Chapter 5: Seismic Evaluation of 1960s Steel Moment Resisting Frame Structure	 130
5.1 Introduction	130
5.2 Design of a four-storey steel structure	130
5.2.1 Prototype building	131
5.2.2 Steel design.....	133
5.3 Nonlinear building model.....	136
5.3.1 Modeling of steel beams.....	138
5.3.2 Modeling of steel columns	139

5.3.3 Modeling of panel zone	140
5.3.4 Modeling of column base connections	141
5.3.5 Modeling of the masonry infill.....	142
5.4 Seismic performance assessment	144
5.4.1 Gravity and eigenvalue analysis	145
5.4.2 Nonlinear static (pushover) analysis.....	146
5.4.3 Nonlinear response history analysis	147
5.4.3.1 Ground motion selection and scaling	147
5.4.3.2 NRHA global results	149
5.4.3.3 NRHA local results.....	151
5.5 Summary and conclusions.....	152
Chapter 6: Research Summary and Conclusions	172
6.1 Summary	172
6.2 Conclusions	173
6.2.1 Experimental testing on column base connections.....	173
6.2.2 Development of FE models and parametric study.....	174
6.2.3 Design of a prototype building and seismic assessment.	175
6.3 Limitations and recommendations for future studies	176
Bibliography.....	179
Appendix	188

List of Tables

Table 3.1: Column base plate test matrix.....	59
Table 3.2: Instrumentation plan	59
Table 3.3: Measured material properties	59
Table 3.4: Concrete mix details	60
Table 3.5: Summary of test results	60
Table 4.1: Mesh details	100
Table 4.2: Elastic-plastic steel material definition and properties	100
Table 4.3: Combined hardening steel material definition and properties	100
Table 4.4: CDP flow parameters.....	100
Table 4.5: Parametric simulation matrix.....	101
Table 4.6: Simulation matrix materials.....	102
Table 4.7: Summary of connections' mode of failure	102
Table 4.8: Summary of connections' moment-rotation relationships.....	103
Table 4.9: Comparison of connections' moment-rotation relationships results	104
Table 4.10: Ductility of the simulated connections along with their failure modes	105
Table 5.1: Gravity loading details.....	155
Table 5.2: Wind load calculation	155
Table 5.3: Minimum earthquake design load parameter, K , estimation	156
Table 5.4: Seismic weight, W , evaluation.....	156
Table 5.5: Beams design loads and preliminary moments	156
Table 5.6: Preliminary column sections.....	156
Table 5.7: Column analysis results	157

Table 5.8: Final column sections	157
Table 5.9: Column base connection assumptions in OpenSees model	158
Table 5.10: Details of infill walls' material and assumptions in OpenSees model	159
Table 5.11: Eigenvalue analysis results, periods in sec	159
Table 5.12: 2% per 50 years acceleration using NBC 2020 Seismic Hazard Tool	159

List of Figures

Figure 3.1: 3D view of the test specimen	61
Figure 3.2: AISC symmetric cyclic lateral loading protocol, modified.....	61
Figure 3.3: Two-AR specimens' shop-drawings, dimensions in mm.....	62
Figure 3.4: Four-AR specimens' shop-drawings, dimensions in mm	62
Figure 3.5: Top-plate shop-drawing, dimensions in mm.....	62
Figure 3.6: RC foundation and floor anchors layout, dimensions in mm.....	63
Figure 3.7: L-Shaped AR detailing, dimensions in mm	64
Figure 3.8: BPL layout: (a) Two-AR and (b) Four-AR, dimensions in mm	64
Figure 3.9: Formwork and steel cages prior to casting: (a) 2-AR and (b) 4-AR	65
Figure 3.10: RC Foundation blocks post concrete casting	65
Figure 3.11: Testing setup, (a) Test in progress and (b) Schematic of the testing frame	66
Figure 3.12: Schematic and location of the steel coupon for mechanical properties evaluation	67
Figure 3.13: 4-AR-U connection at peak drift ratios	68
Figure 3.14: Post-testing 4-AR-U specimen's components.....	69
Figure 3.15: Post-testing 4-AR-C specimen's components.....	69
Figure 3.16: 2-AR-C connection at peak drift ratios	70
Figure 3.17: Post-testing 2-AR-C specimen's components.....	71
Figure 3.18: Post-testing 2-AR-U specimen's components.....	71
Figure 3.19: Moment-rotation relation friction subtraction.....	72
Figure 3.20: Definition of yielding point and initial stiffness, k_y , on the $M-\theta$ envelop	72
Figure 3.21: Moment-rotation relation for 4-AR-U specimen.....	73
Figure 3.22: Moment-rotation relation for 4-AR-C specimen.....	73
Figure 3.23: Moment-rotation relation for 2-AR-U specimen.....	74

Figure 3.24: Moment-rotation relation for 2-AR-C specimen.....	74
Figure 3.25: Ductility factors of the tested specimens.....	75
Figure 3.26: Cumulative energy dissipation capacity of the tested specimens.....	75
Figure 3.27: Dissipated energy per cycle.....	76
Figure 4.1: 3D FE model overview.....	106
Figure 4.2: Boundary conditions.....	107
Figure 4.3: CDP model compressive relationship	108
Figure 4.4: CDP model tensile relationship.....	108
Figure 4.5: Specimen 4-AR-U and its deformed shape	109
Figure 4.6: 4-AR-U base connection deformation, (a) Test and (b) FE model	109
Figure 4.7: Moment-displacement relation for FE-model validation, 4-AR-U specimen	110
Figure 4.8: Specimen 2-AR-C and its deformed shape	110
Figure 4.9: 2-AR-C base connection deformation, (a) Test and (b) FE model	111
Figure 4.10: Moment-displacement relation for FE-model validation, 2-AR-C specimen	111
Figure 4.11: Specimen No.4 FE model (Gomez, 2010) and its deformed shape	112
Figure 4.12: Moment-rotation relation for FE-model validation, specimen No.4 (Gomez, 2010)	112
Figure 4.13: Specimen 8F FE model (Picard and Beaulieu, 1985) and its deformed shape	113
Figure 4.14: Moment-rotation relation for FE-model validation, specimen 8F (Picard and Beaulieu, 1985)	113
Figure 4.15: Deformed shape of the connections at the first peak of the last cycle of simulation.....	115
Figure 4.16: Effect of transverse spacing on the deformability of the base plate, (a) S19 and (b) S21	116
Figure 4.17: Moment-rotation relationship S1-W250-19x350x500-19.....	117
Figure 4.18: Moment-rotation relationship S2-W250-19x350x500-25.....	117
Figure 4.19: Moment-rotation relationship S3-W250-19x400x550-25.....	118

Figure 4.20: Moment-rotation relationship S4-W310-19x400x550-25.....	118
Figure 4.21: Moment-rotation relationship S5-W310-25x400x550-25.....	119
Figure 4.22: Moment-rotation relationship S6-W310-25x450x600-25.....	119
Figure 4.23: Moment-rotation relationship S7-W310-25x450x600-32.....	120
Figure 4.24: Moment-rotation relationship S8-W360-25x450x600-32.....	120
Figure 4.25: Moment-rotation relationship S9-W360-32x450x600-32.....	121
Figure 4.26: Moment-rotation relationship S10-W360-32x450x600-38.....	121
Figure 4.27: Moment-rotation relationship S11-S1-W250-19x350x500-19-30%.....	122
Figure 4.28: Moment-rotation relationship S12-S2-W250-19x350x500-25-30%.....	122
Figure 4.29: Moment-rotation relationship S13-S4-W310-19x400x550-25-30%.....	123
Figure 4.30: Moment-rotation relationship S14-S5-W310-25x400x550-25-30%.....	123
Figure 4.31: Moment-rotation relationship S15-S4-W310-19x400x550-25-10%.....	124
Figure 4.32: Moment-rotation relationship S16-S5-W310-25x400x550-25-10%.....	124
Figure 4.33: Moment-rotation relationship S17-S2-W250-19x350x500-25-300 MPa	125
Figure 4.34: Moment-rotation relationship S18-S4-W310-19x400x550-25-300 MPa	125
Figure 4.35: Moment-rotation relationship S19-S4-W310-19x400x550-25-(-25 mm AR)	126
Figure 4.36: Moment-rotation relationship S20-S5-W310-25x400x550-25-(-25 mm AR)	126
Figure 4.37: Moment-rotation relationship S21-S4-W310-19x400x550-25-(+25 mm AR)	127
Figure 4.38: Moment-rotation relationship S22-S5-W310-25x400x550-25-(+25 mm AR)	127
Figure 4.39: Cumulative energy dissipation capacity of connections S1 to S5.....	128
Figure 4.40: Cumulative energy dissipation capacity of connections S6 to S10.....	128
Figure 4.41: Cumulative energy dissipation capacity of connections S11 to S16.....	129
Figure 4.42: Cumulative energy dissipation capacity of connections S17 to S22.....	129
Figure 5.1: Building layout, dimensions in m.....	160
Figure 5.2: Building elevation, dimensions in m.....	160

Figure 5.3: MRF wind loads.	161
Figure 5.4: MRF earthquake loads.....	161
Figure 5.5: Representation of OpenSees model.....	162
Figure 5.6: Idealized moment-rotation relation's backbone curve	163
Figure 5.7: Schematic of the panel zone parallelogram model.....	163
Figure 5.8: Column base connections' response in ABAQUS vs OpenSees	164
Figure 5.9: Pushover base shear vs roof drift ratios.....	165
Figure 5.10: Target spectrum and period ranges	165
Figure 5.11: Target spectrum and suite 1 individual records.....	166
Figure 5.12: Target spectrum and suite 2 individual records.....	166
Figure 5.13: NRHA peak SDR	167
Figure 5.14: NRHA peak normalized storey shear	168
Figure 5.15: NRHA residual SDR	169
Figure 5.16: Elements probability of yielding across the 22 ground motions – BSF model.....	170
Figure 5.17: Elements probability of yielding across the 22 ground motions – SFX model.....	170
Figure 5.18: Elements probability of yielding across the 22 ground motions – SFM model.....	171
Figure 5.19: Elements probability of yielding across the 22 ground motions – SFR model.....	171

Chapter 1: Introduction

1.1 Research motivation

The evolution of seismic standards and provisions in North America, such as the National Building Code of Canada (NBC) (NRC, 2020), serves as a testament to the ongoing commitment to enhancing structural resilience in the face of seismic hazards. Significant seismic events, including the 1964 Alaskan, 1971 San Fernando, 1985 Mexico City, 1989 Loma Prieta, 1994 Northridge, 2001 Nisqually and 2010 Haiti earthquakes, have played pivotal roles in shaping seismic design methodologies and regulatory frameworks. Engineers and researchers have continuously endeavoured to refine seismic design methods, introducing innovative techniques and principles aimed at improving the performance of structures under seismic loading conditions. However, despite these advancements, persistent gaps remain in our understanding of the seismic response of existing steel MRF structures.

The significance of investigating the seismic performance of existing steel MRF structures extends beyond academic interest to practical implications for public safety and infrastructure resilience. Numerous steel MRF structures were constructed in North America during the 1960s to 1990s, lacking proper seismic design and giving rise to significant concerns (Kyriakopoulos, 2012). As a result, these structures often exhibit relatively poor performance under earthquake loads compared to newly constructed steel MRF structures, due to their insufficient lateral resistance and limited energy dissipation capacity (Leon and Kim, 2004). Among these structures are critical infrastructure such as hospitals, schools and government facilities, which are particularly susceptible to earthquake-induced damage. The identification and thorough analysis

of vulnerable structures are imperative in assessing and mitigating their seismic risk, thereby averting potential human and economic catastrophes.

Moreover, one of the key components of steel MRF structures that received limited attention in the literature is the column base connections. These connections, which facilitate the transmission of forces from the structure to the underlying foundations, play a critical role in ensuring structural integrity during seismic events. Furthermore, seismic events such as the Northridge and Kobe earthquakes have highlighted the vulnerability of exposed column base connections to damage (Tremblay et al., 1995), emphasizing the need for a more comprehensive understanding of their behaviour under seismic loading conditions.

In addition to column base connections, the interaction between unreinforced masonry infill walls and steel frames presents another significant challenge in assessing the seismic performance of existing steel MRF structures. Unreinforced masonry infill walls, which are often utilized as interior partitions or exterior facade in buildings, are generally regarded as nonstructural elements (Asgarian and McClure, 2014). While their weight contributes to the overall mass of the structure, their contribution to lateral stiffness is often ignored leading to higher seismic forces that were not considered in the design stage. Furthermore, research studies have demonstrated that infill walls tend to interact with their surrounding frames under seismic forces, significantly modifying the dynamic characteristics of buildings (Memari et al., 1999; El-Dakhakhni et al., 2004; Liu and Manesh, 2013). While numerous studies have examined masonry infilled frames, these investigations have primarily focused on reinforced concrete structures, highlighting the need for a thorough investigation of their influence when assessing existing steel MRFs.

1.2 Objectives and methodology

The global objective of this research is to assess the seismic performance of existing steel MRF structures built in 1960s with unreinforced masonry infill walls in regions of moderate seismic activity in North America. This objective was achieved through the following:

1. **Experimental testing on column base connections:** This involved conducting experimental testing specifically focusing on configurations not previously documented in literature but commonly found in structural plans from structures built in the 1960s and 1970s.
2. **Assessment of anchor rods corrosion:** Evaluation of the influence of anchor rods corrosion, a common occurrence in column base connections from that era, on the cyclic response of column base connections.
3. **Development and validation of FE models:** Developing and validating Finite Element (FE) models to conduct a parametric study. This aimed to assess the influence of various factors such as anchor rods' diameter and transverse spacing, base plate thickness and dimensions, column section size, level of axial loading and steel grade on the cyclic performance of column base connections.
4. **Design of a prototype hospital building:** Designing a four-storey hospital building adhering to the 1965 NBC (NRC, 1967) to serve as a representative prototype building for the seismic assessment of existing steel MRF structures from the 1960s.
5. **Numerical modeling and seismic analysis:** Development of numerical models and subsequent execution of nonlinear static and response history analyses. These analyses were conducted to investigate the seismic performance of the prototype hospital

building under various scenarios: as a bare steel frame, with column base connections, with unreinforced masonry infill walls and as a complete model incorporating both column base connections and unreinforced masonry infill walls.

1.3 Thesis outline

A thorough review of past studies pertinent to the topic is presented in Chapter 2, organized into three main sections. Firstly, the evolution of seismic provisions and standards is examined, spanning from the 1965 NBC (NRC, 1967) to the 2020 NBC (NRC, 2020), showcasing significant developments since the 1960s. Secondly, past studies on steel MRFs from the 1960s onward are summarized, focusing on beam-to-column and column base connections. This section highlights advancements in beam-to-column connections, their performance in recent earthquakes and the growing emphasis on further research into column base connections. The third section emphasizes the importance of considering infill walls in seismic evaluations of steel MRFs, addressing relevant research and identifying gaps in the literature. Lastly, a comprehensive summary of the reviewed literature emphasizes the significance of the research topic.

The experimental program on the column base connections is presented in Chapter 3. Description of the test specimens, including how corrosion of anchor rods was incorporated into the testing program, is firstly presented. Following that is an overview of the fabrication of the test specimens, test setup, instrumentation and mechanical properties of the materials used. Discussion of the experimental results, including the mode of failure, moment-rotation relationship, ductility and energy dissipation capacity of the tested column base connections, is provided, followed by a thorough summary and conclusions from the testing phase of this research.

Chapter 4 of the thesis delves into the parametric study on column base connections. It commences with a description of the modeling approach, followed by the validation of the model. Validation was attained by integrating the results of the testing program outlined in Chapter 3, along with simulating two additional specimens from different testing programs found in the literature. Subsequently, a simulation matrix is developed to encompass various parameters affecting the performance of column base connections. The findings of the parametric study are then presented and meticulously discussed. Finally, conclusions drawn from the parametric study are summarized.

The seismic evaluation of a prototype building representing existing steel MRF structures built in the 1960s is presented in Chapter 5 of the thesis. Initially, the design of a four-storey hospital building following the 1965 NBC (NRC, 1967) provisions is outlined. Subsequently, a two-dimensional steel MRF model is developed using the Open System for Earthquake Engineering Simulation platform (McKenna, 1997). A thorough explanation of the modeling approach adopted for steel beams, columns, panel zones and column base connections as well as the modeling of unreinforced masonry infill walls is provided. Gravity load and eigenvalue analysis results are then presented, followed by nonlinear static and response history analyses of four representations of the prototype building, including the bare steel frame, steel frame with column base connections, steel frame with unreinforced masonry infill walls and a full frame incorporating base connections and infill walls.

The summary of the entire research endeavour is provided in Chapter 6. In addition to the summary of the research findings, recommendations based on the conclusions drawn from the

study are also presented in Chapter 6. Furthermore, suggestions for future research directions, guiding subsequent investigations in the field, are offered in Chapter 6 of this thesis.

Chapter 2: Literature Review

2.1 Introduction

The principal objective of this research is to characterize the seismic performance of existing steel moment-resisting frame (MRF) structures that were constructed prior to the 1990s in regions of infrequent seismic activity in North America. These structures have garnered the attention of the research community due to developments in the current state of knowledge, as well as related standards and provisions. A comprehensive literature review concerning various aspects relevant to the topic is presented in this chapter. Specifically, it delves into the evolution of seismic provisions and requirements and the historical development of steel MRF structures. The column base connections and unreinforced masonry infill walls, as parts of this lateral load resisting system, were reviewed as well. The review encompassed both experimental and numerical studies, effectively identifying existing research gaps.

2.2 Development of seismic provisions

The evolution of seismic provisions in North America since the 1960s signifies an extraordinary journey characterized by collaboration, scientific inquiry and regulatory transformation. Throughout this period, a series of vital seismic events hit the region, such as the 1964 Alaskan, 1971 San Fernando, 1985 Mexico City, 1989 Loma Prieta, 1994 Northridge, 2001 Nisqually and 2010 Haiti earthquakes. These seismic events, among others, assumed key roles in molding the development of seismic standards, provisions and building codes across North America, fostering an enduring commitment to advancing safer and more resilient construction practices.

Engineers and researchers in Canada and the United States (US) took on the challenging task of addressing seismic forces on structures. This effort led to the creation of the first seismic provisions. These innovations refined seismic design methods, introducing techniques like response spectrum analysis and seismic zone categorization. These breakthroughs allowed engineers to customize designs for different levels of seismic risk, improving accuracy and safety. The establishment of vital institutions such as the National Building Code of Canada (NBC), Canadian Standards Association (CSA), International Building Code (IBC), American Institute of Steel Construction (AISC) and Federal Emergency Management Agency (FEMA), among others, provided critical platforms for the development and distribution of seismic provisions. Over time, these provisions underwent a transformative evolution, expanding from a singular focus on life safety to encompass performance-based design principles. This holistic approach considered not only structural integrity but also the functionality of buildings during seismic events, featuring a comprehensive commitment to safeguarding lives and preserving the built environment. As the 21st century unfolded, seismic provisions matured into comprehensive codes, guided by insights gleaned from significant seismic occurrences like the 1994 Northridge earthquake and the 2001 Nisqually earthquake. This ongoing journey reflects an unwavering dedication to fortifying the resilience of structures, illustrating how North America continues to forge ahead, armed with the knowledge and experience gained from seismic challenges.

To exemplify the progression of these standards and provisions, the NBC serves as an illustrative example. The NBC underwent substantial enhancements during this period. A thorough exploration of the NBC's evolution is elaborately documented in Mitchell et al. (2010) and Humar (2015). Herein, a concise overview of these modifications is presented. Initially, the minimum lateral load V , where $V = C \times W$, depended solely on soil bearing capacity, where W signifies the

structure's weight and C denotes the soil factor. Subsequently, zone maps and the number of storeys introduced additional factors to the equation. By 1965, the minimum lateral force incorporated parameters such as an importance factor, foundation characteristics, torsional effects, structural location and a construction factor adaptable to the employed structural system. The 1970 edition of NBC (NRC, 1970) saw further advancements. Zone maps underwent revision, and the fundamental period of structures was integrated into the assessment of design lateral loads. This version introduced a lateral force at the top of a building to account for higher mode impacts and to mitigate overturning moments. The seismic response factor emerged, along with provisions for dynamic analysis, marking significant progress by the 1980 NBC (NRC, 1980). In 1985 NBC (NRC, 1985), the code introduced fresh zoning maps grounded in a 10% exceedance probability over 50 years, yielding larger design earthquakes. The 1990 NBC (NRC, 1990) retained these maps but replaced the 1965-1985 construction factor with a force modification factor to signify the onset of yielding in structures. The 1995 NBC (NRC, 1995) contributed further, offering diverse ductility factors (R) for distinct seismic force-resistant structures. Innovations encompassed refined formulas for structural periods and novel expressions for torsional eccentricity, along with the introduction of a site-specific response spectral acceleration approach. These revised parameters possessed a 2% exceedance probability over 50 years, distinguishing this 2005 NBC (NRC, 2005). Throughout this dynamic progression, the NBC has incessantly evolved, incorporating seismic insights and advancements to create a more resilient and robust built environment. The period between 2010 and 2015 saw a wealth of new ground motion data leading to significant updates. These changes encompassed hazard values and site effect factors, including the replacement of foundation factors F_a and F_v with distinct factors for specific time periods. Additionally, site effect factors were introduced for peak ground acceleration and velocity.

A streamlined approach for designing structures in low-seismic areas has been introduced. New regulations cover previously unaddressed design aspects, including flexible diaphragms, inclined columns, energy dissipation, base isolation, glazing systems and steel pallet storage racks and elevators. Moreover, enhanced knowledge of materials and their structural behaviour resulted in updates to modification factors (R_d and R_o). Finally, the NBC 2020 (NRC, 2020) brought extensive updates to seismic hazard information through new data, Ground Motion Models and site amplification methods. Notable changes included the direct seismic hazard calculation for varied site types, a shift from site coefficients to $F(T)$, revised site determination with over 3m of softer material above rock, log-log interpolation for spectral acceleration values, additional requirements for post-disaster and high importance buildings, adjusted higher mode factors and base overturning reduction factors, as well as the inclusion of vertical effects in non-linear dynamic analysis for type 9 irregularity.

Considering the comprehensive updates highlighted in the preceding discussion concerning the development of building codes and standards, it becomes imperative to conduct a thorough assessment of existing steel MRF structures. The dynamic evolution of seismic provisions, including refined ground motion data, modified factors and innovative methodologies, necessitates an evaluation of the performance and resilience of these structures. Ensuring their ongoing adequacy in light of the latest provisions is paramount for upholding safety and structural integrity.

2.3 Development of steel MRFs

Steel MRFs have gained greater popularity over steel braced frames as a preferred lateral load-resisting system due to their enhanced structural performance and design flexibility. Steel MRFs offer inherent ductility and energy dissipation capabilities, when designed in accordance

with the latest standards and provisions, crucial for withstanding seismic and wind-induced forces. Unlike steel braced frames, which may undergo concentrated deformation in the braces, steel MRFs distribute lateral loads and deformations more uniformly throughout the structure. This results in reduced localized damage and better overall structural resilience. Additionally, steel MRFs allow for larger open spaces and architectural freedom, as they eliminate the need for diagonal bracing, which can interfere with interior layouts. Numerous steel MRF structures were constructed in North America during the 1960s to 1990s, lacking proper seismic design and giving rise to significant concerns (Kyriakopoulos, 2012). As a result, these structures often exhibit relatively poor performance under earthquake loads, when compared to newly constructed steel MRF structures, due to their insufficient lateral resistance and limited energy dissipation capacity (Leon and Kim, 2004). Among these structures are critical infrastructure buildings such as hospitals, schools and government facilities. Buildings that were designed prior to the 1990s are notably susceptible to earthquake-induced damage. These structures fail, when compared to the current standards and provisions, to meet fundamental capacity design requirements, such as maintaining a strong-column to weak-beam ratio, satisfying panel zone strength prerequisites, implementing prequalified beam-to-column connection details and adhering to column splicing specifications. The identification and thorough analysis of these vulnerable structures hold utmost importance in assessing and mitigating their seismic risk. Such measures are imperative in averting potential human and economic catastrophes stemming from earthquakes.

2.3.1 Studies on the steel MRF

Extensive exploration within the literature has been dedicated to investigating steel MRFs, particularly focusing on the beam-to-column connections within them. These connections are

commonly classified into three types: pinned, semi-rigid and rigid. The key factor that determines a connection's classification is its moment-rotation relationship, where the rotation indicates the relative angular variation between the beam and column centerlines at the joint. Nader and Astaneh (1989) established a criterion for a rigid connection: it is characterized by its ability to generate a moment at the beam end that is equal to or exceeds 90% of the fixed-end moments, while simultaneously maintaining an end rotation within or below 10% of the rotation in a pin-supported beam. In contrast, a pinned connection is defined by its capacity to produce a moment at the beam end that is less than 20% of the fixed-end moment, accompanied by an end rotation that reaches or exceeds 80% of the end rotation in a pin-supported beam. Meanwhile, a semi-rigid connection falls between a pinned and a rigid connection, displaying a stiffness greater than that of a pinned connection yet less rigid than a fully rigid one. From the 1960s onward, structural engineers have dedicated substantial efforts to enhancing the details of beam-to-column connections. Various research initiatives have been directed toward refining these connections, with the dual objectives of simplifying their construction details and enhancing their ductile capabilities. An instrumental contribution in this regard came from the cyclic testing on steel connections by Popov and Pinkney (1969), which substantiated that a bolted web-welded flange arrangement, designed for ease of construction, could effectively offer the necessary ductility. The affirmation of this connection's ductile attributes marked a significant milestone, paving the way for the development of a pre-qualified ductile moment resisting connection adhering to strength-based design principles. The introduction of this connection to practitioners resulted in its widespread adoption and utilization. However, as time progressed and testing methodologies advanced, further assessments and analyses of these connections uncovered specific areas of deficiency, primarily demonstrating as brittle failures near the bottom welds following a few cycles of inelastic deformations. These

shortcomings were subsequently substantiated through inspections carried out on damaged steel buildings in the aftermath of the 1994 Northridge earthquake. Following the formation of committees and subsequent investigations that unveiled their recommendations, along with upgrades to the ground motions database and improvements in testing facilities and techniques, the post-Northridge era has witnessed significant advancements in the development of beam-to-column connections. Notably, innovations such as the implementation of the reduced-beam-section and capacity performance design have led to a profound enhancement in the ductility and energy dissipation capacity of these connections. To provide an overview of the primary studies that have delved into beam-to-column connections in steel MRFs since the 1960s, a summary is presented herein.

Clough and Benuska (1967) conducted an analytical analysis of seismic response in tall steel MRF buildings designed as per the Uniform Building Code (UBC,1961). They found that the response to a moderate earthquake resulted in greater forces and moments than code predictions, but buildings designed to remain elastic under code lateral forces can withstand strong earthquakes due to safety factors. Their study focused on a 20-storey open-frame building subjected to the El Centro earthquake, revealing that during severe earthquakes, member deformations concentrate in girders, with exception of the columns in the top few storeys, with girder ductility factors ranging from 4 to 6. They concluded that the building height and the period of vibration have limited impact on ductile deformations.

Arnold et. al. (1968) tested a one-bay single-storey steel MRF comprising 4.5 m bay width and 2.65 m height. The frame was designed to represent multi-storey steel MRF structure. The focus was to develop a practical design procedure that considers the inelastic behaviour of these

frames. The investigation aimed to establish rational approximations for secondary effects, especially axial loads and strain hardening. The behaviour of high-strength steel columns combined with structural carbon steel beams was also examined. The research concluded that high-strength members can be confidently used in such frames and their behaviour can be predicted using conventional methods.

Anderson and Gupta (1972) investigated the dynamic behaviour of multi-storey buildings subjected to intense ground shaking. Their study was motivated by the need to better understand and manage inelastic responses during severe earthquakes due to the changes in construction practices, where exterior walls were becoming predominantly window areas and interior walls were being replaced by lightweight partitions, yet the design spectrum of the high-rise building was developed based on the performance of old buildings in the previous earthquakes. To achieve this, a comprehensive design procedure was proposed, combining a carefully selected design spectrum with ultimate strength concepts. The authors stressed that relying solely on historical performance data of older structures during earthquakes might not accurately inform the seismic design of newer high-rise buildings. To counter this, they advocated for the use of a prescribed response spectrum tailored to the anticipated seismic activity of the structure's operational life. They suggested that under this spectrum, the frame should be designed to experience minimal damage during the design-level earthquake while remaining functional during stronger seismic events. The study outlined a step-by-step approach to design unbraced frames with this innovative philosophy. Their findings emphasized the significant impact of strong motion duration on the ductility requirements of the frames, challenging the conventional emphasis solely on peak ground accelerations. Furthermore, they highlighted that the proposed seismic design method, though requiring more effort in determining seismic forces, could ultimately simplify the process of

member selection, especially with the availability of advanced computer codes for spectral analyses.

Carpenter and Lu (1973) conducted two series of tests to investigate the behaviour of full-sized single-bay ASTM A36 (ASTM, 1970) steel frames subjected to both constant gravity loads on the beams and columns and reversed cyclic lateral displacements. The tests simulated parts of an eight-storey ductile steel frame subjected to earthquake-like loading. The first series focused on a single-storey and a three-storey frame, designed and detailed according to the seismic design practices of the era. Inelastic behaviour was confined to the beams, and panel zones were stiffened following the 1970 AISC (AISC, 1970) specification requirements. The second series explored the effects of local beam buckling, minor axis bending of columns and the behaviour of beam-to-column connections in different configurations. The results showed that the frames exhibited substantial load-carrying capacity and ductility when subjected to reverse lateral displacement cycles. Maximum lateral loads from the tests exceeded predicted analytical loads for monotonic static loading by 17% to 40%. Stable hysteresis behaviour was observed, and the study examined factors such as strain hardening, local buckling, inelastic moments in columns and the influence of gravity loads. The performance of beam-to-column connections and panel zone stiffening details were also evaluated, revealing that connections effectively transmitted increased and repeatedly applied moments despite being designed based on plastic beam moments.

Popov and Bertero (1973) conducted an experimental study on the seismic design considerations for conventional buildings in earthquake-prone regions. The primary goal of their experiments was to assess the cyclic behaviour of large connections used in high-rise building construction. Two connection types, one all-welded and the other featuring bolted web-welded

flanges, were examined due to their economic significance. The study concluded that both types of connections exceeded predicted strengths due to strain-hardening effects. The strength of the connection without web attachment even surpassed the calculated plastic moment capacity during shear transmission, highlighting the efficiency of flanges in shear transfer. Although high-strength bolts were employed, they exhibited slippage under severe cyclic loads, emphasizing the importance of clean faying surfaces. The study observed stable and consistent load-deflection hysteresis loops for repeated loadings, providing insight into normalized curvature capacities for analysis and design. The study proposed a skew-symmetric bilinear moment-curvature skeleton curve for cyclic loading, anticipating its applicability in seismic analysis.

Krawinlder and Mohasseb (1987) conducted a study to explore the influence of beam-to-column connection's strength and deformation on frame performance. The study focused on two distinct frame configurations. A seven-storey and a ten-storey frame structure were used in this study. Both structures were designed in accordance with the 1982 UBC (UBC, 1982), considering all requirements for ductile moment frames located in Seismic Zone 4. The frames were made of ASTM A36 (ASTM, 1985) structural steel. The beam-to-column connection was conceptualized as a pair of scissor-like components linked by a hinge and a rotational spring, facilitating relative rotation. The study encompassed nonlinear static analysis and inelastic dynamic analysis. The research findings underscored the substantial impact that shear deformations within the beam-to-column connection can exert on both structural strength and stiffness. Furthermore, the study revealed that these deformations also influence the distribution of inelastic distortions within a frame structure when subjected to seismic excitations.

Tsai and Popov (1990) conducted three large-scale tests on beam end-plate moment connections to column flanges under severe cyclic loading conditions. These connections were commonly utilized in the construction of low-rise steel frames when on-site welding is impractical. The tests aimed to evaluate the behaviour of these connections under cyclic loading, with a particular focus on achieving ductile behaviour. The results revealed that the conventional design of end-plate connections led to unequal force distribution among the bolts and premature fracture of an interior bolt in a four-tension bolt type specimen. To improve this, reinforcement of the end plate with rib stiffeners along the web and the use of stronger bolts were introduced, demonstrating enhanced performance under large cyclic loads. Additionally, a specimen with larger bolts and a slightly thicker end plate displayed superior behaviour. The study emphasized that due to beam strain hardening, larger bolts are required compared to conventional designs.

Redwood et al. (1990) conducted an analytical study of earthquake-resistant design principles for steel MRFs within the Canadian code regulations. They employed an illustrative instance of an eight-storey frame to showcase the implications of these regulations. These guidelines operate under the principle of capacity design. They concluded that the ductile properties of the joint are sensitive to the choice of doubler plate thickness, and since the joint will frequently be critical, over design of the doubler plate may lead to more stringent detailing requirements for the beams and columns. Since critical columns should be avoided, if possible, it is important that such over design be minimized.

Engelhardt and Husain (1993) conducted a series of cyclic tests on large-scale bolted web-welded flange connections. The primary objective was to investigate the need for supplemental welds, particularly in cases where the web contributes significantly to the beam's flexural strength.

Such supplemental web welds were being mandated by model seismic codes in the US. The study aimed to assess the performance of these connections under severe seismic conditions. The test results exhibited considerable variability in the performance of the eight specimens. Plastic rotations developed by the beams before connection failure were found to be inadequate for severe seismic applications. All tested connections ultimately failed due to fracture near or at the beam-flange groove welds. The inconsistent behaviour of the beam flange groove welds appeared to be the predominant factor influencing the overall response of the specimens. The authors recommend a careful review of design, detailing practices, welding and quality control issues related to the welded flange-bolted web moment connection detail in order to address the observed variability and ensure its adequacy for seismic-resistant structures.

Roeder and Foutch (1996) performed an investigation on the previous experimental programs on the beam-to-column connections of the steel MRF following the 1994 Northridge earthquake. The researchers carefully inspected 120 experiments, delving deeply into the details of 91 specific specimens. Throughout this process, they engaged in comprehensive comparisons across various influential factors and conducted rigorous statistical analyses. Among the notable revelations, the study uncovered the intricate interplay of different variables that impacted the flexural ductility of these steel frames. Shear yielding within panel zones emerged as a significant contributor to reduced ductility, as did increased beam depth. The relative thickness of beam flanges, the orientation of columns and the ratio of beam span to depth collectively wield influence over the flexural ductility. Furthermore, the study highlighted the consequences of welding practices, welding characteristics and the material properties of the steel used. The authors drew attention to the critical observation that connections featuring panel-zone yielding offered commendable ductility, yet this advantageous trait is offset by an increased vulnerability of connected beams to

early failure. Moreover, the researchers shed light on the behaviour of connections under different types of column bending, revealing that minor-axis bending connections exhibit less ductility compared to their major-axis counterparts. Interestingly, connections experiencing shear yielding in the panel zone emerged as the least ductile, indicating the complex nature of their response under seismic forces.

Popov et al. (1998) investigated pre-Northridge and post-Northridge earthquake welded beam-to-column connections within typical steel MRFs. Employing three-dimensional elastic-plastic finite elements, they analyzed stress concentration at the juncture of welded beam and column flanges, explaining fracture locations—attributed to triaxial actions—and no apparent yielding. The influence of backing bars was examined using fracture mechanics, highlighting the unfused backing bar surface as an artificial crack that initiates rupture during beam bending, particularly at the bottom flange. The researchers' analytical cyclic load-deflection curves correlated favourably with experimental tests, while presented remedies involving reduced beam section (RBS) and reinforcing plates exhibited enhanced ductility and avoidance of brittle fractures. Pre-Northridge specimen tests revealed rapid fracture-type failures, with cracks originating at the bottom beam flange-column juncture and propagating through the column flange. The study emphasized the significance of backing bar removal, transforming vertical unfused interfaces into open fine cracks.

Biddah and Heidebrecht (1998) undertook a comprehensive investigation to assess the seismic performance of steel MRF buildings under varying seismic hazard levels and design philosophies. The study focused on low and medium-rise structures. The investigation comprised three distinct design approaches: Strong-column weak-beam, weak-column strong-beam and strong-column

weak-panel zone, each adapted for high, intermediate and low seismic hazard levels. The analytical model considered connection flexibility and panel zone shear deformation. Through dynamic simulations utilizing an ensemble of scaled strong motion records, the study evaluated critical response parameters such as lateral deflections, inter-storey drifts, ductility and damage indices. Furthermore, the research delves into the performance expectations of different frame designs, shedding light on the complex interplay between seismic hazard levels and design approach, ultimately influencing the overall level of protection and performance of the MRF buildings. They concluded that the type of structural element chosen for inelastic deformation plays a crucial role in controlling the performance of the steel MRF.

Yousuf and Bagchi (2009) aimed to comprehensively investigate the Canadian seismic design provisions, 2005 NBC (NRC, 2005) and S160-01 (CSA, 2001), particularly focusing on the transition from prescriptive to performance-based design philosophy. The research involved meticulous design and subsequent evaluation of four distinct ductile steel MRF buildings, each varying in height from 5 to 20 storeys, situated in the seismic context of Vancouver City. The seismic performance of these designed structures was rigorously examined through the utilization of synthesized ground motion records. The results of the study demonstrated the successful achievement of the primary collapse prevention objective as prescribed by the NBC 2005, yet unveiled intriguing variations in performance parameters that were notably influenced by factors such as the presence of infill walls and the inherent characteristics of selected ground motion records. Moreover, the research underscored the intricate interplay between ground motion records, scaling methodologies and structural modeling in the nuanced evaluation of seismic performance. This underlined the necessity for meticulous design detailing, particularly in scenarios involving infilled frames.

Kyriakopoulos and Christopoulos (2013) conducted an experimental study to investigate the seismic performance of a representative 1960s Type 2 construction steel MRF hospital structure, initially designed solely for lateral wind loads. The structure exhibited characteristics of a soft first storey and substantial sensitivity to $P-\Delta$ effects. The tested connections exhibited inherent ductility, enduring inter-storey drifts up to 2.0% despite lacking a designated ductile cyclic response. Employing advanced strength degradation modeling, the structure's seismic behaviour was assessed through nonlinear time-history analysis using ground motions from Montreal and Vancouver. However, the study revealed that the structure's performance falls short of satisfactory levels under the considered design hazard conditions. In response, the study proposed retrofit strategies, employing a performance-based approach coupled with supplemental damping for two orthogonal frames. This approach circumvents the need for localized enhancements to connection ductility.

Gómez et. al. (2015) investigated the seismic performance of typical six-storey steel MRF buildings in Vancouver and Montreal, designed according to three different provisions of the Canadian standards from different decades (1960s, 1980s and 2010). Numerical models were developed using the Open System for Earthquake Engineering Simulation (OpenSees) platform (McKenna, 2000) to assess the seismic behaviour of these structures, considering degradation in strength and stiffness through calibrated representations of beam-column connection behaviours based on experimental data. The study employed pushover and nonlinear time history analyses to evaluate the buildings' responses. The results of the pushover analyses revealed that both the 1960s and 2010 steel MRFs in both cities exhibited a strong-column weak-beam failure mode, while the 1980s steel MRFs displayed a soft-storey mechanism. Fragility curves were generated based on nonlinear time history analyses, providing valuable insights for regional seismic impact

assessment studies. They concluded that the 2010 MRFs displayed the highest seismic performance due to stricter design criteria.

Stenecker et. al. (2018) conducted numerical study on the seismic performance of beam-to-column connections in steel MRF structures, aiming to address issues identified after the 1994 Northridge Earthquake. Their research comprehensively examined seven beam-to-column connections, encompassing the original pre-Northridge, reduced beam section, welded unreinforced flange, welded unstiffened end plate and welded stiffened end plate connections as well as two innovative low-damage connections like: the sliding hinge joint and self-centering sliding hinge joint connections. The study employed analytical tools within OpenSees to model each connection, utilizing available component test data for calibration. The collapse behaviour of a representative frame was examined. Although the welded unstiffened end plate connection exhibited the weakest collapse performance, the difference among the four prequalified connections was within a 5% range. Substituting the self-centering sliding hinge joint connection for the sliding hinge joint connection led to a 5% rise in the median collapse capacity.

In conclusion, while numerous studies have been conducted on beam-to-column connections, investigating their impact on the seismic response of steel MRFs, newer studies often contradict previous research conclusions, identifying concerns and offering new recommendations. Furthermore, the count of existing buildings assessed within the framework of the latest state of knowledge and regulations is negligible when compared to the abundance of existing steel buildings in service. This emphasizes the necessity for a more extensive evaluation of existing steel MRF structures, utilizing the most up-to-date engineering tools and knowledge available.

2.3.2 Column base connections

Column base connections play a fundamental role in steel structures, facilitating the transmission of forces from the structure to the underlying foundations. These connections come in three types: exposed, shallow embedded and deep embedded. Exposed column base connections have gained popularity in low- to mid-rise steel MRF structures due to their cost-effectiveness and straightforward construction. Picard and Beaulieu (1985) conducted tests on standard exposed column base plate connections and discovered unexpected base fixity, which contrasted with the then-common assumption of zero "pinned" fixity in design. Seismic events like the Northridge and Kobe earthquakes have underscored the vulnerability of existing exposed column base plate connections to damage. Tremblay et al. (1995) documented significant damage to these connections following these earthquakes, despite assumptions about their seismic resilience. Grauvilardell et al. (2005) conducted an extensive review of late-century work on column base connections, emphasizing the importance of this subject and the necessity for further investigations to enhance comprehension of these structural components and their response to seismic events. Most literature studies have concentrated on newly constructed column base plate connections, and there has been relatively limited exploration of these connections in existing steel MRF structures, particularly within the context of new standards and provisions. It's imperative to examine how these connections perform under various conditions to ensure their resilience to seismic loading as well as their influence on the seismic performance of the steel MRF. Furthermore, engineers engaged in assessing and retrofitting existing steel structures need to conduct nonlinear response history analyses. For this purpose, experimental data on column base plate connections are indispensable. Such data is used to calibrate numerical models utilized in the

evaluation process. The following is a summary of the primary studies that have investigated exposed column base connections in steel MRFs since the 1960s.

Picard and Beaulieu (1985) conducted an experimental study investigating the behaviour of steel column base connections. They tested connections comprising two and four threaded anchor rods with double nuts. The study involved testing 15 specimens to establish moment-rotation curves, enabling the calculation of fixity factors for the base connections while considering axial compression loads. Their findings revealed that the presence of a compression force within the column notably enhanced the flexural rigidity of the base connection. Moreover, the rotational restraint provided by the column base was deemed substantial enough to be taken into account during design considerations. The researchers also concluded that the method employed for determining the ultimate moment capacity of the base connection displayed a conservative nature. The investigated type of column base connection, despite traditionally being treated as a hinge in analyses, exhibited a capacity to transmit end moments to the concrete footing.

Picard and Beaulieu (1987) continued their research in investigating the behaviour of steel column base connections. The primary objective in this paper was to ascertain the rigidity ratio at the column base (G_L). Conventionally considered hinge-like in nature, the connection is advised to be assessed with $G_L = 10$ to determine the effective length factor of the column. The study revealed that for minor-axis buckling, a conservative rigidity ratio value was $G_{Ly} = 0.50$, while for major-axis buckling, $G_{Lx} = 1.50$, assuming no relative displacement of column ends. Consequently, the effective length of the column is reduced. Notably, the column strength experienced approximately a 30% increase for practical slenderness ratios. The investigation built upon prior papers addressing similar column base connections and their behaviour. Emphasizing the benefits

of considering actual rigidity, the study demonstrated reduced lateral displacement in frames due to partial rotational restraint. Furthermore, the analysis method for predicting ultimate moment capacity was deemed conservative based on the test outcomes.

Fahmy (2000) addressed the seismic vulnerabilities of steel MRF buildings exposed by the 1994 Northridge and 1995 Kobe earthquakes. The study aimed to investigate the seismic behaviour of full-scale column base connections, comprising threaded rods with double nuts, designed according to US practices. Both experimental and analytical investigations were conducted to examine the connections' performance. Analytical efforts explored factors like normal force, plate thickness and component stiffness impact, along with semi-rigidity's effect on steel MRFs, mechanical characteristics in terms of stress and strain and parameters for experimental studies. Experimental work aimed to understand cyclic loading response, energy dissipation, strength, stiffness, detailing influence on potential brittle failure modes, anchor rod pattern's effect and the genuine degree of semi-rigidity. Variables included size/thickness of the base plate, anchor rod size/locations, axial load magnitude, geometrical/mechanical properties of the column and concrete foundation properties. Analytically, the column base connection was modeled as a column on a spring foundation. The results demonstrated that the axial force level significantly impacted the connection strength, ductility and failure mode. The response of the column base connections aligned with semi-rigid behaviour, with an initial rotational stiffness of $2.0 E I_c / L_c$, where E is young's modulus of the column, I_c is the moment of inertia of the column and L_c is the length of the column. Concrete stress distribution differed from the classical design assumption, with stress concentrating at the flange edges. Anchor rod number/distribution influenced stress magnitude/distribution.

Grauvilardell et al. (2005) conducted a comprehensive review of studies performed on steel column base connections in the last century. Their study was motivated by the limited unified seismic design provisions for these connections in the US, despite the significant role these connections play in the seismic performance of steel MRFs, as well as the poor performance of these connections in recent earthquakes, such as extensive anchor rod elongation, unexpected early anchor rod failure, shear key failure and brittle base plate fractures. The authors identified one particularly relevant topic that had not received adequate attention: the combined action of moments and pull-out axial forces, especially in scenarios where gravity loads on the sides of the frames are low and lateral forces are significant. Additionally, the authors highlighted that previous studies had been unable to accurately estimate the initial elastic stiffness of actual partially restrained column base connections. This stiffness not only affects sidesway stiffness but also impacts the strength of the critical first storey. Furthermore, the study noted that the formation of plastic hinges in base connections, while undergoing inelastic deformation, had not been adequately addressed. These issues, along with others outlined in the report, though later investigated by the research community, underscore the uncertainty in the seismic response of column base connections built before the 1990s.

Gomez (2010) presented findings from two phases of large-scale test programs. The first phase of the research focused on shear transfer within exposed column base connections. The tests explored three common shear transfer mechanisms: surface friction, anchor rod bearing and shear key bearing, aiming to simulate real-world field conditions rather than isolated components. The specimens were created following the AISC Design Guide One (AISC, 2006) to replicate US construction practices. Whereas the second phase tests investigated the behaviour of exposed column base connections under combined flexural moments and axial compression. The

experiments encompassed various parameters such as base plate thickness, axial load levels, anchor rod grade, number of anchor rods and the loading protocol (monotonic or cyclic). The main purpose of these experiments was to expand the available database of column base connections and use the collected data, along with ancillary material information, to assess the strength predictions provided by common design guidelines. Additionally, Finite element (FE) simulations of the test specimens were discussed in conjunction with the physical testing. The research underscored the inadequacies of current design provisions and proposed improvements based on experimental data. Notably, the tests revealed potential weaknesses in existing strength design provisions and conservative approaches to flexural loading.

Kanvinde et al. (2012) discussed the importance of considering the rotational flexibility of column base connections in structural simulations of steel MRF structures. The study aimed to present a method for characterizing the rotational flexibility of such connections and validating it against experimental data. The authors pointed out that while structural response is sensitive to base flexibility, current design practice often assumes bases to be either fixed or pinned, which might lead to inaccurate results. The rotational flexibility of base connections can significantly affect structural behaviour, including inter-storey drifts, column moments and overall structural reliability. However, methods to properly characterize base flexibility have not been readily available. A new approach to characterize the rotational flexibility of exposed column base connections was introduced. The method leveraged existing design procedures for base connections, making it relatively easy to calculate the rotational stiffness once the design has been completed. The approach was validated by comparing its predictions with results from nine experiments that explore various parameters such as base-plate size and thickness, axial load level, anchor rod strength and concrete strength. The research concluded that the proposed method

provided a relatively accurate prediction of the rotational stiffness of exposed column base connections. On average, the predicted stiffness is 89% of the test stiffness, indicating reasonable accuracy. However, the method is particularly accurate for cases where the moment-to-axial-load ratio is large, but it tends to overestimate the stiffness of connections with high axial loads relative to the applied moment.

Rodas et al. (2016) developed a hysteretic model to simulate the cyclic moment-rotation response of exposed column base connections commonly used in steel MRFs. The research aimed to enable the use of these connections as dissipative elements in seismic design. The authors highlighted that connections have been traditionally designed to remain elastic, assuming plastic hinges will form in other elements of the structure. The developed hysteretic model was able to capture the behaviour of the column base connections under cyclic loading, including pinching, yielding, strength and stiffness degradation and recentering effects induced by axial compression. The developed model incorporated a trilinear backbone curve and hysteretic rules for various response modes. It involved 16 parameters, categorized into core and ancillary parameters. Core parameters are those that can be determined through physics-based analysis, while ancillary parameters require empirical calibration. The model was validated against experimental data to assess its ability to simulate the key aspects of hysteretic response exhibited by exposed column base connections.

Lim et al. (2017a) conducted an experimental study that investigated the cyclic performance of exposed column base connections in small size steel structures. The authors conducted tests on nine specimens with variations in base plate thickness, anchor rods embedment length and the presence of hook and rib plates. They examined flexural strength, deformation capacity, energy

dissipation and stiffness. Key findings of the study are as follows: The flexural performance of exposed column base connections was significantly affected by the location and number of anchor rods. Connections with more anchor rods located outside the column cross-section tend to exhibit improved structural performance in terms of moment capacity and deformation behaviour. The presence of rib plates did not notably impact the moment capacity of the connections, whereas the number and location of anchor rods played a more substantial role. The stiffness of the tested connections was compared to current standards, revealing that connections had stiffness values around 15% of the lower limit value for fixed-end connections. However, their stiffness remained notably higher than the upper limit value for pinned-end connections.

Lim et al. (2017b) studied the seismic performance of exposed column base connections experiencing minor-axis loading. Six specimens were subjected to reversed cyclic loading to assess the connections' behaviour. The parameters under investigation included the thickness of base plates, the presence of rib plates and the characteristics of anchor rods. The study highlighted the significant impact of base plate thickness and anchor rods bond performance on the structural response of these connections. Of particular importance was the recognition that even when base plates met the minimum requirements outlined in prevailing design codes, their yielding before the plastic moment capacity of the steel column could lead to diminished structural performance. The findings emphasized the necessity of robust design considerations for these weak-axis connections, particularly in situations where the base plate may yield prematurely. Furthermore, the study provided insights into the mechanics of connections that utilized rib plates, indicating that adequate base plate thickness and extended rib plates were essential to maintain seismic performance.

Kavoura et al. (2017) conducted an experimental study to evaluate the performance of pinned column base connections commonly used in low-rise steel building. With a focus on understanding elastic stiffness, deformation capacity and energy absorption characteristics. The test program included 11 full-scale column stubs subjected to horizontal cyclic displacements and constant axial loads. They aimed to investigate the behaviour of these connections under various parameters, including base plate dimensions and anchor rod characteristics. Different failure modes were categorized, including plastic hinge formation in the column, plastic hinge formation in the base plate and balanced mechanisms. The findings highlighted the substantial influence of anchor rod diameter, base-plate thickness and flange dimensions on the connections' rotational stiffness and moment capacity.

Kavoura et al. (2018) aimed to address the discrepancy between common design assumptions and the actual behaviour of pinned column base connections in low-rise steel buildings. While such connections are typically treated as having zero rotational stiffness and moment capacity in design codes, past research indicated otherwise. The research focused on assessing the applicability of existing design codes, specifically the 2016 American Steel Construction Manual (AISC, 2016), the 2010 Eurocode 3 (CEN, 2010) and the Canadian Handbook of Steel Construction (CISC, 2017), in estimating the rotational stiffness and moment capacity of these connections. The study recognized that accurate modeling of column base connections is essential for economical and effective design, as ignoring rotational stiffness may lead to overestimation of lateral displacement and result in more costly designs. The research evaluated experimental data from the literature against predictions provided by the codes. Key findings included: The codes generally provided conservative estimates of moment capacity but lacked accurate predictions of rotational stiffness. The authors emphasized the potential need for revising existing codes to

incorporate rotational stiffness and moment capacity considerations for these connections in future design practices.

Hassan et al. (2021) presented a new method to characterize the internal stress distribution and anchor rod forces in exposed column base connections subjected to biaxial bending and axial compression. The proposed method was developed through a series of FE simulations. The method extended the AISC Design Guide One (AISC, 2006) approach, which is designed for column base connection loaded in uniaxial direction, to the biaxial loading scenario. The authors concluded that their approach accurately predicted the anchor rods' forces across various configurations and loadings and that their proposed method extends the current guide approach by providing a mechanics-based procedure to design biaxially loaded exposed column base connections.

Kabir (2021) developed data-driven Machine Learning (ML) techniques for failure mode identification of column base connections subjected to combined axial load and biaxial bending in steel MRF structures. The author started by developing a FE model in the ABAQUS platform, validated his model against experiments from the literature, and then conducted parametric FE simulations to feed his ML model. The ML model effectively identified failure modes. The rigidity of exposed column base connections under biaxial bending was found to be in the semi-rigid region, and existing methods overestimate connection stiffness.

Sing and Wood (2022) developed numerical modeling techniques to effectively capture the nonlinear cyclic behaviour inherent in exposed column base connections. They investigated two distinct modeling approaches: one for detailed 3D connection analysis and another for nonlinear time-history analysis of structures, specifically in 2D. The veracity of these methodologies was verified through comparison with experimental data, particularly referencing the research

conducted by Gomez et al. (2010). The 3D model was developed in ABAQUS software, while the 2D model was implemented in OpenSees. The 3D models exhibited a commendable ability to represent the intricate cyclic response, forecasting ultimate strength with a deviation of under 5%. The 2D model demonstrated a significant enhancement in computational efficiency, concluding the analysis in approximately one minute per simulation, a substantial 70 times faster than their 3D counterparts. This heightened efficiency positions them favourably for practical integration into nonlinear time-history analyses. However, it is crucial to note that this computational efficiency came at the cost of result precision, as the 2D model was unable to accurately simulate the decline in load capacity.

Hassan et al. (2022) presented a comprehensive study involving full-scale experiments and FE analyses on exposed column base connections with ductile anchor rods. The connections employed anchor rods with smooth shanks, allowing designated stretch lengths for inelastic deformations. The shank was isolated from the footing using polyethylene tape. Four full-scale experiments investigated axial force, rod diameter and rod material grade effects. Line element-based and continuum finite-element simulations extend the understanding of the observed response to untested configurations. The research showed a promising approach to develop high-ductility connections for seismic design, specifically the exposed column base detail with yielding anchors within the foundation body. The study highlighted the importance of concentrating yielding in anchor rods to maximize rotation capacity. However, the study acknowledged limitations, such as its focus on connection response alone, not considering frame interactions, and the need for caution when applying results to untested configurations.

To sum up, despite the considerable number of studies conducted to investigate the response of exposed column base connections, several gaps have been identified. The majority of these studies focused on enhancing the column base connections according to current practices and design guides. To the author's knowledge, there appears to be a lack of studies re-evaluating the behaviour of connections in old buildings, especially those originally designed to support structural loads during column erection. Upon reviewing plans for buildings constructed before the 1990s, the author observed that many column base connections relied solely on two anchor rods within the column flanges. However, this particular anchor rod configuration has received minimal attention in the literature, despite its original intended use during erection, and it no longer complies with current codes and standards. Moreover, only a limited number of studies have tested column base connections comprising L-shaped anchor rods, despite their popularity in existing structures. Lastly, even in newer studies, which aimed to investigate the seismic performance of exposed column base connections, there is a failure to adequately explore their influence on the seismic response of steel structures while considering their actual partial rigidity, as opposed to relying on the assumption of them being either pinned or fixed.

2.4 Unreinforced masonry infill walls

The extensive utilization of masonry infill walls is readily evident by observing buildings, whether they are existing structures or newly constructed ones, around us in almost every location. This widespread adoption has captured the attention of the research community since the last century. While numerous studies have delved into masonry infilled frames, these investigations have predominantly revolved around reinforced concrete structures (Fiorato et. al., 1971, Klingner and Bertero, 1976, Bertero and Brokken, 1983, Zarnic and Tomazevic, 1985, Schmidt 1989 and

Mehrabi et. al., 1996). This has resulted in a lack of dependable modeling techniques for masonry infills when assessing existing steel MRFs in accordance with contemporary seismic codes. The significance of investigating unreinforced masonry infill walls stems from their dual role. On one hand, these walls are often utilized as interior or exterior partitions in buildings, though they are generally regarded as nonstructural elements (Asgarian and McClure, 2014). This status frequently leads to their neglect in structural analysis and design. On the other hand, their weight is factored into the assessment of the structure's mass, a critical consideration when estimating the natural period that holds a pivotal role in determining seismic forces. Additionally, research studies have concluded that infill walls tend to interact with their surrounding frames under seismic forces (Memari et al., 1999, El-Dakhakhni et al., 2004 and Liu and Manesh, 2013), leading to a significant modification in the dynamic characteristics of buildings. While this interaction can enhance the structural performance by effectively reinforcing the building's frame, it also unintentionally results in an increase in the initial stiffness of the structure. Consequently, this heightened stiffness can attract additional seismically induced lateral inertia forces for which the structure might not have been originally designed. Furthermore, studies have demonstrated that infilled frames can manifest various potential failure mechanisms, including corner crushing, sliding shear, diagonal compression, diagonal cracking and frame failure (El-Dakhakhni et al, 2003). The specific failure mode that emerges depends on factors such as the strength and stiffness of the bounding frames relative to those of the infills, as well as the geometric configuration of the framing system. The majority of current analytical models concentrate on either one specific mechanism or another, lacking universal applicability across all types of infilled structures. Consequently, both the design of engineered infilled frames and the assessment of existing ones continue to pose challenges. While classical diagonal strut models have undergone more comprehensive evaluations using new

experimental data, diverse limit analysis approaches have emerged to accommodate the various load-resisting mechanisms within infilled frames (Di Sarno and Wu, 2021). Additionally, intricate finite element models have been formulated to meticulously analyze the nonlinear behaviour of infilled frames (Wu et al., 2022). The subsequent section provides an overview of several noteworthy studies in this field.

Memari et al. (1999) conducted an experimental assessment on a six-storey steel structure to investigate its dynamic behaviour, encompassing natural frequencies, damping ratios and mode shapes. Ambient vibration tests were conducted in two stages: first, involving only the steel frames and slabs, and later, after introducing infill walls. The experimental findings were then compared with numerical simulations. The primary focus of the study was to compare the use of autoclaved cellular concrete (ACC) block infills with traditional masonry infills. The study determined that ACC infills increased the stiffness of the steel frame, but this enhancement was approximately 50% of that achieved by traditional masonry infills. In terms of seismic response, traditional masonry infills notably influenced the performance of the steel frame, whereas ACC infills could be disregarded. Lastly, when compared against experimental results, the fundamental period equations provided by standards yielded conservative outcomes.

El-Dakhkhni et al. (2003) explored the influence of masonry infill panels on the behaviour of steel structures. Specifically, the study examined the significant impact of these infills on the strength, stiffness and ductility of the structures. The authors categorized the various failure modes of masonry-infilled frames into five distinct types: corner crushing, sliding shear, diagonal compression, diagonal cracking and frame failure. Of these modes, corner crushing and sliding shear were deemed particularly important due to their frequent presence in such composite

systems, with corner crushing being the most prevalent. The study emphasized the significance of comprehending these modes to understand the behaviour of infilled frames and subsequently design for their effects. They developed an analytical model, with a particular focus on the corner crushing mode. This model employed a multi-strut approach, wherein the masonry panel was replaced with diagonal and off-diagonal struts to replicate the interaction between the panel and the frame. The model consisted of two primary components: one addressing the geometrical representation of the elements, and another concentrating on material models for both steel and masonry. The researchers concluded that the model effectively captured the confinement effect exerted by the frame on the masonry infill, enabling the panel to bear more load and exhibit a ductile response before reaching ultimate failure.

El-Dakhakhni et al. (2004) aimed to develop a retrofitting solution for unreinforced masonry infilled steel frame structures. This initiative was triggered by the rapid degradation in stiffness, strength and energy dissipation of these structures due to brittle failure. The researchers emphasized that the presence of these walls significantly alters the stiffness of these composite systems, subsequently impacting seismic demands and the natural period of the structures. Ignoring the valuable strength contributions of infill walls, especially in regions with low to moderate seismic activity, can result in designs that are not economically efficient. In response to these challenges, an experimental study was conducted to explore the potential of retrofitting unreinforced masonry infilled steel frame structures using glass fiber-reinforced polymer (GFRP). The primary aim was to enhance the seismic performance of unreinforced masonry infill walls subjected to cyclic loading. The research encompassed the testing of six full-scale single-storey single-bay steel frames with various infill configurations. This included bare frames without GFRP, as well as retrofitted frames featuring different infill arrangements. Some retrofitted frames

incorporated GFRP on solid walls or walls with symmetrical door openings on one or both faces. The outcomes of the investigation illuminated the transformative impact of GFRP on unreinforced masonry walls. The retrofitting approach preserved structural integrity, averting brittle collapse, while localized damaged GFRP maintained stability after failure. In contrast to unreinforced masonry walls, masonry-GFRP composite walls exhibited gradual, stronger and more energy-efficient failure modes. This observation indicated potential benefits in analysis, including higher response modification factors. Additionally, GFRP laminates provided a cost-effective external reinforcement for masonry walls, aiding adherence to evolving seismic codes.

Liu and Manesh (2013) undertook an experimental study to investigate the behaviour and capacity of masonry infills enclosed by steel frames. The testing program comprised five specimens along with one bare frame specimen, all subjected to in-plane lateral loads applied at the top beam level of the frame. Furthermore, eight specimens were tested under combined in-plane axial and lateral loading. These specimens exhibited various grouting conditions, including non-grouted, partially grouted and fully grouted infills. In cases of lateral loading only, the load was progressively increased until specimen failure. For combined loading scenarios, axial load was first incrementally applied and held, followed by lateral loading until failure. The point of failure was determined by a significant lateral deflection accompanied by an irreversible decrease in load. Throughout the tests, observations were made regarding cracking load, crack patterns, failure modes and ultimate loads. Conclusions drawn from the study indicate that corner crushing predominantly emerged as the failure mode under lateral loading. However, specimens with partially grouted infills or openings experienced significant diagonal cracking before encountering corner crushing. Under combined loading, primary splitting cracks led to failure by dividing the infill into two parts, circumventing corner crushing. The study demonstrated that enhanced

grouting notably increased stiffness and ultimate load. Nevertheless, the presence of openings resulted in decreased values for both aspects, though not linearly proportional to the opening area. Comparison with design values revealed that the CSA S304 (CSA, 2004) standard tended to overestimate stiffness by approximately 3.2 times and underestimate strength by 2.5 times. This tendency could potentially yield conservative designs for infills but unsafe outcomes for other lateral load-resisting components.

Farazman et. al. (2013) delved into the role of unreinforced masonry infill panels in enhancing the resilience of composite steel framed buildings when faced with abrupt column loss. Their study aimed to characterize the contribution of infill panels through a simplified approach that isolated their impact from the surrounding frame. The modeling approach included using diagonal truss elements to represent infill panels, while line elements represented frame components. Multiple struts were employed to account for bending and shear forces, considering both the inelastic behaviour of the frame and infill. A reduction factor was applied to strut area for openings in panels, accounting for their effect. The study determined that corner crushing is the prevailing failure mode, with infill panels enhancing structural robustness. The adopted robustness assessment method transformed nonlinear static response into pseudostatic capacity, quantifying robustness by comparing pseudostatic capacity to applied gravity load. The presence of infill panels significantly boosted structural robustness, highlighting their importance in design and assessment practice for multistorey buildings, assuming quality control during construction. Further research into different panel constructions and scenarios was recommended to fully harness their potential contribution to structural robustness.

Asgarian and McClure (2014) undertook a study to assess the impact of infill walls on the structural behaviour of a pediatric research hospital in Montreal, Canada. They aimed to find reliable methods to incorporate the influence of unreinforced masonry infill walls into analysis and design and to evaluate the effects of seismic retrofitting and infill walls on the building's seismic response. They employed both experimental and numerical approaches, conducting ambient vibration measurements on the hospital's separate blocks to determine dominant dynamic properties. Numerical models, including infill walls represented through two-dimensional panels or equivalent diagonal compression struts, were developed for the buildings. Results indicated that the continuum model best described the effect of infill walls. Incorporating masonry infill walls significantly impacted the buildings' dynamic properties, reducing fundamental periods by around 66% and 27% for blocks No. 8 and 7 of their case study, respectively. Neglecting this effect in seismic design could lead to underestimated earthquake loads. The study highlighted the importance of accounting for infill walls in seismic design to ensure accurate predictions of structural response.

Di Sarno et al. (2021) conducted a comprehensive study to assess the behaviour of steel MRF structures with masonry infill walls through experimental and numerical analyses. The investigation was prompted by the aftermath of the 2016 Central Italy earthquakes, which revealed significant failures in existing steel MRF buildings, including yielding at beam-column connections, soft-storey mechanisms and damage to non-structural elements such as masonry infill walls. The selected case study was a two-storey steel MRF with insufficient seismic detailing, representative of non-seismically designed frames. The study considered two configurations: the prototype and the scaled mock-up. The presence of masonry infills intensified the severity of soft-storey mechanisms, leading to reduced displacement capacities of about 40%. Various damage

modes were observed in the infill walls, ranging from local damage to global modes, e.g., diagonal tension, sliding shear and diagonal compression. Interlocking between bolts and brick top layers played a role in preventing corner crush damage by forming local struts. Steel column flanges offered some constraint against out-of-plane deformation, delaying diagonal compression damage. The cyclic response of the infilled frame exhibited pinching effects due to crack opening and closing. Uniformly distributed infill walls could trigger soft-storey mechanisms, especially when load carrying capacity is compromised. Experimental results indicated that the mock-up's fundamental period elongated after corner cracks but stabilized during subsequent pseudo-dynamic tests, suggesting limited stiffness degradation during the earthquake sequence.

Di Sarno and Wu (2021) investigated the fragility of non-seismically designed steel MRFs with masonry infills. The study comprised two parts: the first assessed the fragility of the undamaged steel frame using standard procedures, while the second introduced an enhanced aftershock assessment framework employing state-dependent aftershock fragility curves to evaluate the resilience of damaged steel MRFs. The influence of masonry infills was considered in both parts of the analysis. The case study involved a three-storey steel MRF building located in Central Italy, designed without seismic considerations. Numerical models were developed using OpenSees (McKenna et al., 2000), encompassing force-based beam and column elements with fiber sections. The authors employed the Giuffr -Menegotto-Pinto constitutive law for structural steel (Menegotto and Pinto, 1973) and the Gupta-Krawinkler model for column panel zones (Gupta, 1999). Masonry infill walls were represented using the single-strut model, considering their properties and the confining frame. The study found that mild post-mainshock damage allowed the steel frame to maintain its full resistance against aftershocks, suggesting that post-earthquake assessment can be based on the frame's original state. Conversely, moderate post-

mainshock damage had a more significant impact on performance, necessitating reduced capacity consideration in post-earthquake assessment.

Wu et al. (2022) endeavoured to establish a framework for defining force-displacement relationships within single-strut models for masonry infill walls attached to steel MRFs. Given the limited availability of experimental seismic response data for steel MRFs with masonry infills, the study employed finite element micro-models generated using ABAQUS to construct a comprehensive database. Through regression analysis, a generalized quadrilinear model for masonry struts was developed and subsequently validated using additional micro-models. The study's novelty lies in its utilization of a genetic algorithm to calibrate masonry single-strut models, ultimately leading to the formulation of a generalized nonlinear force-displacement model for masonry struts seamlessly integrated into prevailing steel MRFs. The methodology was effectively demonstrated through a case study involving a large-scale two-storey steel MRF specimen. The study highlighted the significant impact of wall aspect ratio, defined as the ratio of the length to the height of the infill wall, on behaviour, identifying it as a pivotal parameter shaping the seismic response of infilled steel MRFs. However, the single-strut models demonstrated limitations in simulating localized column responses due to their simplified configuration, even as they excelled in capturing the overall structural response.

In summary, it is vital to incorporate the stiffness and strength of unreinforced masonry infill walls into the analysis and design of steel MRF structures. It has been demonstrated that unreinforced masonry infill walls interact with the infilled frames, underscoring the necessity of characterizing the behaviour of existing steel MRFs while considering this infill-wall interaction. This consideration holds significant importance in upholding public safety and ensuring the

continued functionality of these structures when subjected to seismic activity. However, due to the manifold complexities posed by various failure modes, the behaviour of this composite structural system, while under investigation by researchers, still entails numerous intricacies that warrant further analysis.

2.5 Summary and research gaps

A comprehensive literature review concerning various aspects related to the seismic performance of steel MRF structures was undertaken. The evolution of seismic standards and provisions was explored, revealing significant uncertainties in assessing the ability of old steel MRF structures to withstand seismic events under the latest standards. The core objective of the present research is to characterize the seismic response of pre-1990s existing steel MRF structures. The review particularly focused on the crucial components: beam-to-column connections, column base connections and unreinforced masonry infill walls. Recent studies on beam-to-column connections often contradict prior research, indicating knowledge gaps. Evaluating existing structures based on contemporary understanding falls short; thus, a thorough assessment with advanced tools is essential. Gaps also persist in examining exposed column base connections, primarily concentrating on modern practices and overlooking older buildings and specific anchor rod configurations. Additionally, integrating unreinforced masonry infill walls' stiffness and strength is vital for steel MRF analysis and design, especially during capacity design, necessitating a thorough characterization of their interaction with frames for public safety during seismic events. The complexity of this behaviour mandates further investigation.

The author's literature review unveiled the absence of studies encompassing all three aforementioned steel MRF components. To bridge this knowledge gap, the study aims to

characterize the seismic response of existing low- to mid-rise steel MRF structures built in the 1960s. It specifically focuses on realistic behaviour, including exposed column base connections with L-shape anchor rods, and accounts for the presence of unreinforced masonry infill walls, and their impact on frame stiffness and strength. The research plan encompasses both experimental and numerical explorations of exposed column base connections at a component level, followed by a comprehensive numerical seismic analysis of the entire frame, integrating all components.

Chapter 3: Experimental Program

3.1 Introduction

Many research studies, in the literature, focused on investigating the behaviour of the column base connections for newly constructed steel structures Kanvinde et al. (2012), Rodas et al. (2016), Lim et al. (2017), Kavoura et al. (2018) and Hassan et al. (2022). The behaviour of the column base connections in existing steel structures, built between 1960s and 1990s, has received less attention by researchers. These structures include hospitals, schools and government buildings, among others. Experimental data on column base connections are necessary to calibrate numerical models that are used in the evaluation of existing steel structures and to ensure their seismic adequacy. To this purpose, a testing program was conducted to assess the cyclic performance of the standard column base connections that form part of existing steel moment-resisting frames (MRFs). The results of the experimental program will be used to develop and calibrate finite element models, which will be used to further the understanding of these connections under seismic loading and the frames which they support.

This detailed overview of the test program is presented herein for four column base connection specimens that represent two of the standard design practices in the existing steel MRF structures in the areas of low- to mid-seismic activities in Eastern North America. The specimens were fabricated and delivered to the Jamieson Structures Laboratory at McGill University, where they were instrumented, connected to reinforced concrete (RC) foundations, and tested in reversed cyclic loading protocol in the presence of the axial loading.

3.2 Test program

The test program comprised a total of four W310 × 79 steel column base connections. Figure 3.1 shows a test specimen and its isometric view. To determine the properties of the test specimens, such as the shape and length of the anchor rods, spacings between the anchor rods and edges of the base plates, as well as the thicknesses of the base plate and grout layer, various sources were reviewed. These sources included a literature review, a design standard from Dominion Bridge, a leading engineering firm before the 1990s, and plans of existing steel structures collected from more than three consulting firms. The Specimens were divided into two groups, as illustrated in Table 3.1, based on the number of anchor rods (ARs), Two-ARs and four-ARs. The connections were constructed and subjected to a constant axial load that corresponded to 20% P_y , where P_y is the cross-section yield force (i.e. $P_y = A_g F_y$), A_g is the cross-sectional area and F_y is the column nominal yield strength. Following the application of axial loading, it was observed that the maximum variation in axial loading, despite the vertical actuator was operating in load control, occurred in the four anchor rod connections, remaining within $\pm 5\%$. Specimens were also subjected to simultaneous varying lateral deformations, incorporating the standard symmetric cyclic lateral loading protocol by Clark et al. (1997). The symmetric loading protocol was slightly modified by reducing the number of cycles to lessen the overall testing time, as shown in Figure 3.2. Each group included two nominally identical columns and base plates (BPLs). Given that the test program is targeting the existing steel column base connections between the 1960s and 1990s, corrosion of the anchor rods is anticipated; hence, each group incorporated a connection that accounted for the anchor rods' corrosion in addition to the nominal anchor rods connection.

3.2.1 Test specimens

The fabrication drawings for the two- and the four-AR specimens are shown in Figure 3.3 and Figure 3.4, respectively. Figure 3.5 shows the shop drawing of specimens' top plate. The columns had a clear length of 1360 mm and were welded using an all-around fillet weld of 8 mm thickness to the 25.4 mm thick base plates. It is worth mentioning that an all-around weld was not part of the common design practice in the existing column base connections; however, studying the influence of the weld on the connection was considered to be out of the scope of research. The columns were also welded to 50.8 mm thick top-end plates that were used to connect the specimens to the loading actuators. A non-shrink cementitious grout (SikaGrout[®] 212) layer of 25.4mm was cast between the column base plate and the underlying RC foundation. L-shape anchor rods were used in the testing program, because of their absence in the literature and their popularity in the reviewed old structure plans. No leveling nuts were used under the base plate. The leveling of the column was established by the testing setup (i.e., using vertical and horizontal actuators).

The column bases were supported by RC foundations. The RC foundation blocks were connected to the strong floor of the structure lab using 50.8mm high strength steel threaded rods and plates. The nuts of the high strength threaded rods were tightened with a hydraulic wrench to produce a total of 1000 kN vertical force on the RC foundations to prevent any movement during the testing, Figure 3.6 shows the RC foundation arrangement. The design process of the RC foundation was carried out using the strut and tie method. The strut and tie method is a structural analysis and design approach used for deep and complex RC members that are subjected to high loads or irregular shapes. The method involves breaking down the member into a simplified truss-like structure comprising struts, ties and nodes. The struts represent compression elements, while the

ties represent tension elements. The nodes are the points where the struts and ties intersect. The method involves selecting an appropriate truss configuration based on the loading and geometry of the foundation. Then, the forces acting on the truss members are calculated and distributed among the members to ensure that they are in equilibrium. The truss members are then sized and reinforced as required to ensure that they can resist the applied forces.

3.2.1.1 Accounting for AR corrosion

The approach adopted to account for the material loss due to corrosion was established by Andrade et al. (1993). Thus, to calculate the volume of rust produced at the anode, they established an empirical relationship between current density i_{corr} (defined as the mean annual corrosion current per unit anodic surface area of steel in $\mu\text{A}/\text{cm}^2$) and the volume of steel consumed at the anode. Thus, the reduced diameter $D_{rb}(t)$ of a steel bar with initial diameter of D_b (mm) and subjected to corrosion for a time period (in years) Δ_t is

$$D_{rb} = D_b - 0.023 i_{corr} \Delta_t \quad \text{Eq. 3-1}$$

The time period, Δ_t , was assumed to be 43 years, which corresponds to the time period from 1975 (average between 1960 and 1990) to 2018 (the testing year). Whereas D_b was 25.4mm and an i_{corr} value of 1.2 as recommended by Celarec et al. (2011). Figure 3.7 shows a typical anchor rod and the location of the reduced section in the anchor rods that were used in specimens which accounted for the corrosion. It should be noted that the reduced section was also subjected to random pitting to have a more realistic surface replicate of the corrosion.

3.2.1.2 Two-AR specimens

The two-AR specimens comprise base plates measuring 350 mm in length and 300 mm in width. The two anchor rods were positioned 150 mm apart on the neutral axis (NA) of the base plate in the direction of the lateral loading, in line with conventional practices of such standard connections. The two specimens are identical in everything except for the use of the modified anchor rods in the specimen that accounted for the corrosion. Figure 3.8.a shows the anchor rods layout of the two-AR specimens.

3.2.1.3 Four-AR specimens

Similarly, the four-AR specimens comprise two identical specimens with one specimen that accounted for the steel corrosion; however, the specimens were welded to base plates that have a length and width of 500 mm and 350 mm, respectively. The four anchor rods were positioned to have spacings of 400 mm and 250 mm in the loading and the transverse directions, respectively. The spacings were selected to achieve 50 mm clear edge spaces as was found in the common practices for these types of connections. Figure 3.8.b shows the arrangement of the four-AR specimens.

3.3 Fabrication of specimens

The steel columns were delivered by the supplier welded to the end-plates. They were instrumented then connected to the RC foundation by means of the anchor rods. The L-shape anchor rods were delivered to the testing facility, where milling and pitting were performed on the specimens that incorporated the corrosion effects as illustrated in Figure 3.7. A ready-mix concrete was used to construct the RC foundation blocks. Figure 3.9.a and Figure 3.9.b show the formworks

and steel cages prior to the casting of the concrete, for the two-AR and four-AR specimens, respectively, whereas Figure 3.10 shows the RC blocks post the concrete casting.

3.4 Test setup and instrumentation

The test setup is illustrated in Figure 3.11.a and Figure 3.11.b. The setup comprised vertical and horizontal actuators. The vertical actuator had an 11.4 MN compressive load capacity and an 8 MN tensile capacity with a displacement range of ± 150 mm. Whereas the horizontal actuator had a ± 1 MN and ± 250 mm load and displacement capacities, respectively. Both actuators were connected, through axially rigid links, to a high precision structural pin at the column's top end. The vertical actuator was operated in load-control mode, such that the axial loading was maintained throughout testing, while the horizontal actuator was used to apply the lateral deformations, and it was operating in displacement-control mode. In-line bracing was utilized to provide an in-plane lateral stability to the vertical actuator. Two guiding beams were employed to provide lateral stability at the column's top end. For further details on the testing frame, pin assembly, deformed shape of the test setup, as well as evaluations of base moment and rotation, please refer to Suzuki, Y. (2019).

The instrumentation plan comprised load cells, displacement sensors, strain gauges, inclinometers, string potentiometers, linear variable differential transformers (LVDTs) and a 3D Krypton K600 optical wireless measuring system, which was used as a backup recording system. Table 3.2 summarizes the instrumentation plan.

3.5 Material properties

Mechanical properties of the utilized materials were evaluated at the Jamieson Structures Laboratory. Base plate, anchor rods and the column's web and flange coupons were tested prior to testing the main column base connections. The concrete cylinders and beams, which were cast along with the RC foundation blocks, were tested while the main testing was in progress. Grout mixture used to be prepared and cast between the base plate and the RC block one-to-two days before testing of the connection, to allow for the setting and hardening time.

3.5.1 Steel elements

Three coupons were cut from the web and flange of the specimens' parent column that was used in the testing. The details and location of the web and flange coupons are shown in Figure 3.12. The average of the column's depth, d , was found to be 305.5 mm. The average thicknesses of the column's webs, t_w , and the flanges, t_f , were found to be 8.9 mm and 14.2 mm, respectively, whereas the flange width, b_f , was 252.2 mm. Similarly, three coupons were extracted from the base plate for evaluation of the mechanical properties. The average of the thickness of the base plates was 25.4 mm. The anchor rods were provided along with three 600 mm smooth and undamaged rods samples. The anchor rods' diameter was measured, and the average value of the diameter for all the anchor rods, including the anchor rods which were used in the connections, was 25.4 mm. The average values of the deduced mechanical properties from the uniaxial tensile testing are summarized in Table 3.3. It is worth noting that the steel elements were tested using the available steel grades in the market. The author could not find a supplier offering materials similar to those used between the 1960s and 1990s. However, this limitation was addressed in the numerical parametric study outlined in Chapter 4 of this thesis.

3.5.2 Concrete and grout

The ready-mix concrete materials and proportions are summarized in Table 3.4. The mechanical properties of the concrete material including compression and split-cylinder were evaluated using cylinders measuring 100 mm in diameter and 200 mm in length in accordance with the CSA Standard A23.3-9C (CSA, 2014a) and CSA Standard A23.3-13C (CSA, 2014b), respectively. The modulus of fracture of the concrete mix was evaluated using the four-point bending tests, which were carried out with rectangular beams measuring 100mm in depth, 100mm in width and 300mm in length in accordance with the CSA Standard A23.3-8C (CSA, 2014c). The mechanical properties of the concrete mix are 36.7, 4.04 and 3.15 MPa, respectively. The non-shrink cementitious grout (SikaGrout® 212) layer used between the base plate and the RC foundation had on average a compressive strength of 56.9 MPa. The grout compressive strength was evaluated using $50 \times 50 \times 50$ mm cubes.

3.6 Experimental results

The primary objective of the experimental stage of this research was to evaluate two standard exposed column base connections that showed popularity in the existing steel MRF before 1990s, yet they were not documented in the literature. The results of the experimental program will, then, be used to develop Finite Element models that will provide better insight on the cyclic performance of the existing steel MRF column bases.

3.6.1 Mode of failure

Literature review concluded that the failure of the exposed column base connections can be either by the failure of the base plate, anchor rods, concrete footing, or the steel column. Failure in

the base plate could be due to the yielding of the compressive or tensile side of base plate. The anchor rods' yielding and plastic elongation is the mode of failure that is associated with the damage in the anchor rods. Fracture of the anchor rods is another mode of failure that could be experienced when the damage is concentrated in the anchor rods. Exposed column base connections that comprise strong base plate and anchor rods (i.e., high strength and large thickness) may experience the pull-out of the anchor rods mode of failure, bearing failure of the concrete foundation and/or the yielding of steel column.

The four-AR specimens (4-AR-U and 4-AR-C) experienced an almost identical mode of failure. The failure of the four-AR specimens was initiated by the yielding of the anchor rods, and the reversed cyclic demands led to plastic deformations in the anchor rods. While the anchor rods did not experience a complete fracture and remain functional until the end of the test, the anchor rods' threads were damaged. The nuts slipped at the location where the threads were damaged, and a sudden loss of the load carrying capacity occurred. A permanent deformation was, also, observed in the base plate at the end of the test due to the flexural demands. The grout exhibited some cracks that developed in the area surrounding the anchor rods and underneath the edges of the base plate. No concrete crushing was observed in the footing, despite the development of cracks in the concrete footing. Most of these cracks developed at the instant when the footings were connected to the strong floor using the 50.8 mm threaded rods, steel plate and the hydraulic jack. Signs of yielding were observed at the bottom of the columns; however, the columns did not form a plastic hinge due to the rocking behaviour, which these types of exposed column base connections exhibit.

The unreduced anchor rods specimen (4-AR-U) started to show a gap between the grout and the base plate in the 1st cycle of the 0.75% drift. The plastic deformation in the anchor rods

increased as the test progressed, hence the gaps between the washers and the nuts were getting wider. Figure 3.13.a through Figure 3.13.j show the connection at the peak levels of the lateral demand and in the last cycle for the drift ratio levels that have more than one cycle. The grout layer started to show a gap with the concrete at 1% drift level, and the flanges of the column started to yield on the compression side. The gap between the base plate and the grout layer passed the NA of the base plate at 1.5% drift ratio. The base plate began to deform plasticly at drift ratio of 2%. The anchor rods' threads experienced excessive damage and reduction in the cross section, which led to the slip of the nuts along the damaged threads and drops in the load carrying capacity. The drops occurred on one side of the loading, at the south anchor rods. Figure 3.14.a through Figure 3.14.g show the different components of the 4-AR-U specimen after the test was concluded.

The “corroded” anchor rod specimen (4-AR-C) comprised four anchor rods, which were subjected to milling and random pitting. The 4-AR-C specimen exhibited an almost identical mode of failure compared to the 4-AR-U specimen. The 4-AR-C specimen, however, experienced damage in the anchor rods on both sides of the loading (i.e., North and South). Figure 3.15.a through Figure 3.15.f show the different components of the 4-AR-C specimen after the test was concluded.

Similarly, the two-AR specimens exhibited an identical mode failure. The anchor rods in the two-AR specimens experienced plastic deformations; however, the plastic elongation was less pronounced in the two-AR specimens compared to the four-AR specimens, for the fact that the anchor rods in the two-AR specimens lay on the neutral axis of the loading, hence the anchor rods, in the two-AR specimens, experienced smaller tensile demands. Figure 3.16.a through Figure 3.16.i show the 2-AR-C specimen at peak drift ratios. The plastic deformations in the base plates

of the two-AR specimens were not noticeable, this could be due to the short overhang length beyond the column's flanges. Post-testing photos are shown in Figure 3.17 and Figure 3.18 for the 2-AR-C and 2-AR-U specimens, respectively. The columns' web did not develop yielding waves in contrast to the flanges. Moreover, the anchor rods' threads did not show the damage that was experienced by the four-AR specimens.

3.6.2 Moment-rotation relationship

The test setup assembly developed friction in the structural pins and between the angles and the guiding beams. The reported moment-rotation relations have been postprocessed such that friction has been subtracted from the measurements as illustrated in Figure 3.19.

The yielding moment is defined using the moment-rotation envelop by drawing a line from the origin to pass a point corresponding to 75% of the peak moment on the moment-rotation envelop. Then, a horizontal line is drawn from the peak moment point. Next, a vertical line is drawn from the point, where the initial and horizontal lines intersect each other, to the moment-rotation envelop. Finally, the yielding point is the intersection of the vertical line and the moment-rotation envelop. Figure 3.20 shows a schematic of defining the yielding point, and Table 3.5 summarizes the main test results including the yielding moments and others.

The moment-rotation relations characterize the flag-shape hysteresis that is developed due to the plastic deformation in the anchor rods and the development of the gap, which was formed between the base plate and the grout layer. The pinching behaviour occurred when the base plate moved freely downwards in the unloading stage after it lost contact with the washers due to the plastic deformation of the anchor rods. Figure 3.21 and Figure 3.22 depict the moment-rotation

curves of the 4-AR-U and the 4-AR-C specimens, respectively. The four-AR specimens exhibited an almost symmetric hysteresis on the positive and negative sides of loading. In contrast, the two-AR specimens' hysteresis were affected by the history of the loading. The 2-AR-U specimen, for instance, loading started toward the positive direction, hence it has a moment value of 148 kN.m at +0.02 rad rotation, whereas the moment value is 138 kN.m at - 0.02 rad, as shown in Figure 3.23. The 2-AR-C specimen, however, was loaded in the negative direction then the positive direction, hence the hysteresis in the positive direction showed smaller area in the flag-shape compared to the negative direction as shown in Figure 3.24. It should be mentioned that specimen 2-AR-U was tested twice, for 30% and 20% of P_y , and the reported results here are these of the 2nd test, which is 20% P_y , and this explains the reason for the symmetry of the positive and negative hysteresis of the 2-AR-U specimen.

Although the number of anchor rods in action when resisting the lateral movement is the equal for all connections (i.e., two anchor rods), the four-AR specimens showed approximately 58% and 56% increase in the ultimate, M_m , and the yielding, M_y , moment values, respectively, compared to the two-AR specimens. This increase is justified by the location of the anchor rods and their distance from the neutral axis as well as the moment arm. The yielding rotation values of all specimens are lower in the positive direction regardless of the loading history. This could be ascribed by the increased stiffness in the positive direction which could be related to the horizontal actuator operation, e.g, pushing or pulling.

The section analysis of the tested column concluded that the elastic, S_x , and the plastic, Z_x , modulus, are $1.099 \times 10^6 \text{ mm}^3$ and $1.23 \times 10^6 \text{ mm}^3$, respectively. The plastic moment, $M_p = Z_x F_y$, which is the maximum moment the column section can attain, is 451.1 kN.m. The four-AR

specimens were able to reach approximately 52% of the M_p on average, whereas only 32% of the M_p , on average, was the maximum moment attained by the two-AR specimens.

3.6.3 Ductility and energy dissipation capacity

Ductility can be defined as the capacity of the structure, the connection in our case, to undergo inelastic deformations. One can determine the ductility by calculating the ratio of the deformation (e.g., rotation or displacement) at failure to the deformation at the onset of yielding. In some cases, failure may happen and a complete loss of the load carrying capacity occurs, whereas in some other cases the failure can be defined by the softening of the load carrying and loss of resilience. The ductility factors (DFs) of the tested specimens are shown in Figure 3.25, where DF is the ratio of the base rotation at peak moment, θ_m , to the rotation at yielding, θ_y . all specimens showed minimum DF of 3 and 4 for the negative and positive direction of loading, respectively. Specimens incorporated anchor rods that accounted for corrosion showed higher DFs compared to the “unreduced” anchor rods specimens, this could be due to the reduced section, hence earlier yielding in these specimens.

The energy dissipation capacity was obtained by calculating the enclosed area of first cycle per aimed rotation angle from the moment-rotation curve. Figure 3.26 depicts the cumulative energy dissipation capacity, which was determined by summing the energy dissipation capacity from zero to the aimed rotation angle, whereas the dissipated energy per cycle is plotted in Figure 3.27.

All specimens showed an almost equal energy dissipation capacity prior to the onset of yielding. At the onset of yielding, however, the effect of corrosion became more pronounced in

the two-AR specimens. This could be ascribed by the fact that the anchor rods were the main contributor to the plastic deformations in the two-ARs specimens, hence a higher energy dissipation was attained by the 2-AR-U specimen compared to the 2-AR-C. The difference between the cumulative dissipated energy of the 2-AR-U and 2-AR-C at 5% rotation angle, for instance, is 47%. In contrast, other components of the connection were involved in the plastic deformation of the four-AR specimens as explained in the mode of failure section; consequently, the 4-AR-U and 4-AR-C specimens show an almost the same energy dissipation capacity at the end of the test.

3.7 Conclusions

Full-scale reversed cyclic tests were conducted on four exposed column base connections. The connections represented standard column base connections in low- to mid-rise steel structures in areas of infrequent seismic activities in Eastern North America. The connections comprised two or four L-shape anchor rods. The effect of anchor rod corrosion was included and showed an influence on the cyclic performance of the tested connections. The mode of failure, moment rotation relationship, ductility and energy dissipation capacity were studied, and the following conclusions were drawn.

1. All specimens experienced plastic deformations in the anchor rods and pinching hysteresis. four-AR specimens experienced plastic deformations in their base plate and damage in the anchor rods' threads, which resulted in sudden drops of the load carrying capacity.

2. The four-AR specimens developed symmetric hysteresis; nonetheless, the two-AR specimens' hysteresis were asymmetric and were affected by the initial direction of loading.
3. The anchor rods' configuration (e.g., location) significantly affected the moment capacity. The four-AR specimens showed approximately 58% and 56% larger M_m and M_y , respectively, compared to the two-AR specimens.
4. Specimens comprising anchor rods that accounted for the corrosion effects (i.e., 2-AR-C and 4-AR-C) demonstrated smaller base rotation angles at yielding compared to their counterpart specimens; consequently, they showed higher ductility factors.
5. All specimens were able to dissipate energy through inelastic deformations. The anchor rods' corrosion effect on the energy dissipation capacity was more pronounced in the two-AR specimens. Whereas the four-AR specimens exhibited an almost same cumulative energy dissipation capacity at the end of the testing.

Table 3.1: Column base plate test matrix

Group	Specimen	BPL dimension ^c (mm)	In plane spacing (mm)	Out of plane spacing (mm)
2-AR	2-AR-U ^a	300 × 350	-	150
	2-AR-C ^b	300 × 350	-	150
4-AR	4-AR-U	350 × 500	400	250
	4-AR-C	350 × 500	400	250

^a Dimension is given as width × length

^b Un-corroded ARs

^c Corroded ARs

Table 3.2: Instrumentation plan

Instrument type	Number	Measurement type	Measurement range
Horizontal actuator sensors	2	Load	±1000 kN
		Displacement	±250 mm
Vertical actuator sensors	2	Load	11400kN Com. 8000kN Ten.
		Displacement	±150 mm
Strain gauges	20 or 26*	Strain	±50000 µε
String potentiometers	6	Displacement	±300 mm (4)
			±500 mm (2)
Inclinometers	4	Rotation	±25 degrees
LVDTs	8	Displacement	±50 mm
LED targets (Krypton)	26	3D Displacement	17m ³ volume

* Based on the number of the ARs

Table 3.3: Measured material properties

Material	$D-t$ (mm)	E (GPa)	F_y (MPa)	ϵ_y %	F_u (MPa)	ϵ_u %	ΔL %
AR	25.4	209	321	0.15	485	19.1	26.6
WEB	8.9	207	385	0.18	474	17.3	25.1
FLG	14.2	191	360	0.18	467	18.1	27.2
BPL	25.4	203	444	0.22	531	12.9	22.9

Table 3.4: Concrete mix details

Material	Type	Amount/ 1m ³
Cement	Portland, GUL	220 kg
Supplementary cementitious material	NewCem®, S	55 kg
Sand	Sand	932 kg
Aggregate	5-14mm	442 kg
Aggregate	10-20mm	541 kg
Water	Water	150 L
Air entrainer	MasterAir® AE 210	22 ml/100kg
Water reducer and retarder	MasterAir® R100	156 ml/100kg
Air	Air	5.50%

Table 3.5: Summary of test results

Specimen	Yielding						Peak			
	Positive (+)			Negative (-)			Positive (+)		Negative (-)	
	θ_y (%rad)	M_y (kN.m)	$k_y \times 10^3$ (kN.m/rad)	θ_y (%rad)	M_y (kN.m)	$k_y \times 10^3$ (kN.m/rad)	θ_m (%rad)	M_m (kN.m)	θ_m (%rad)	M_m (kN.m)
2-AR-U	0.54	119	22	0.62	123	20	2.48	152	1.84	150
2-AR-C	0.33	115	35	0.42	123	29	1.78	138	1.72	149
4-AR-U	0.63	188	30	0.91	193	21	2.82	233	3.30	242
4-AR-C	0.55	185	34	0.79	188	24	3.01	229	2.58	229

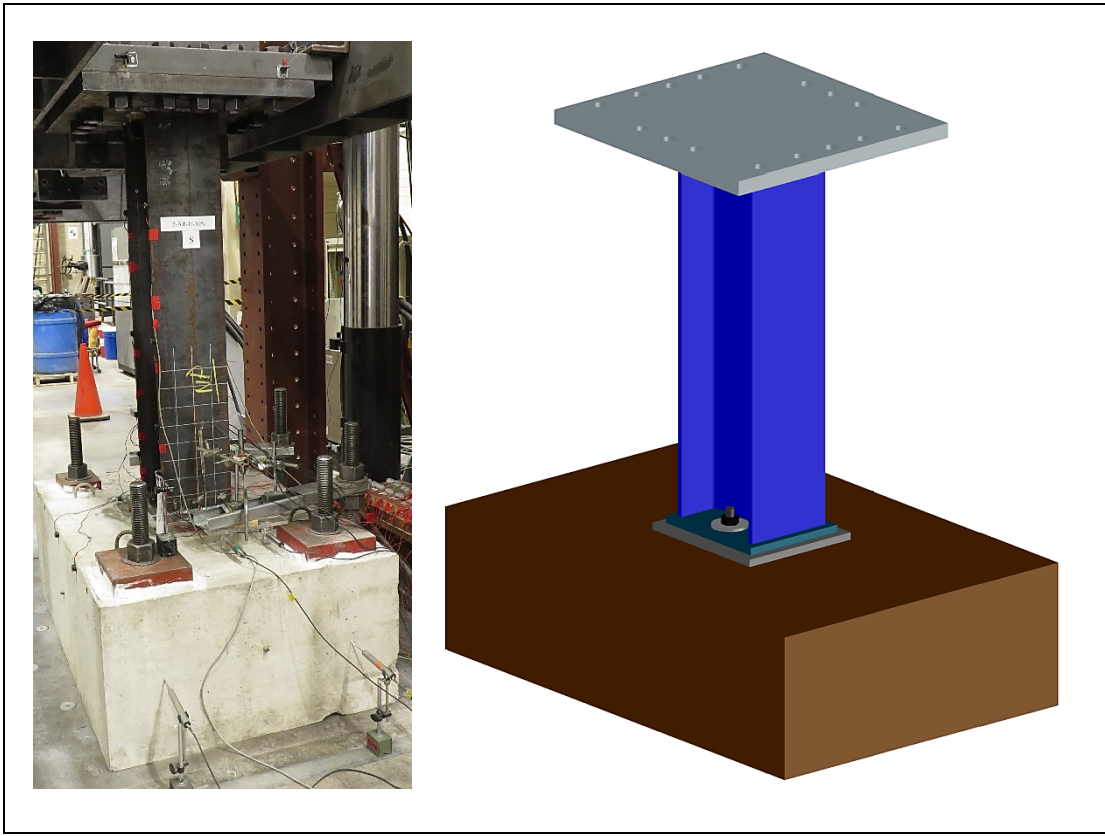


Figure 3.1: 3D view of the test specimen

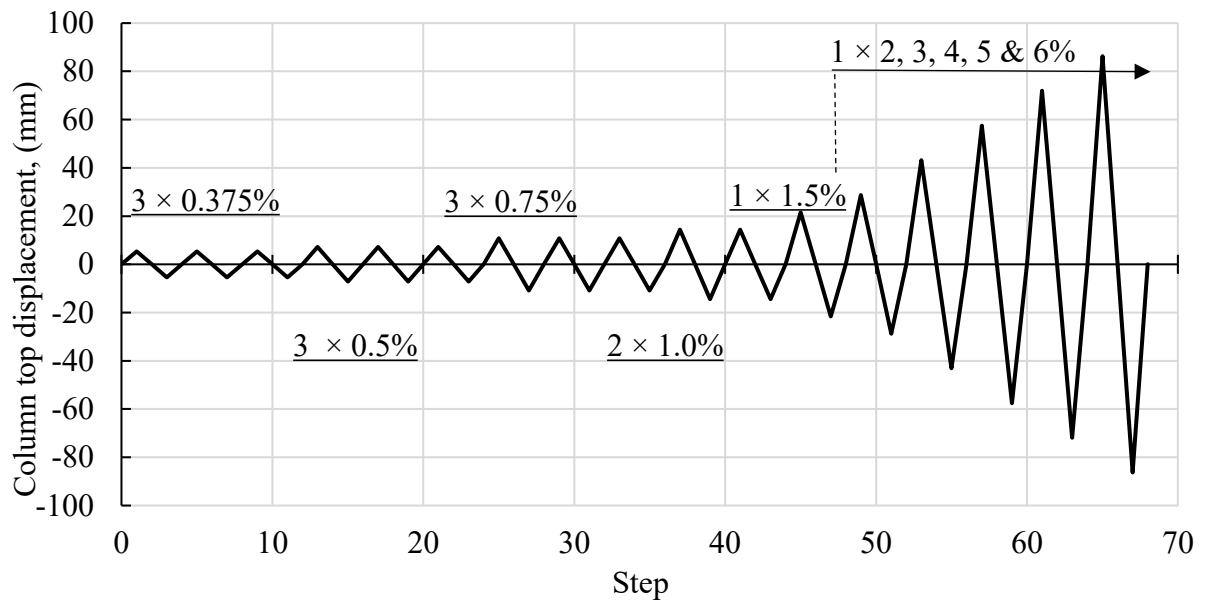


Figure 3.2: AISC symmetric cyclic lateral loading protocol, modified

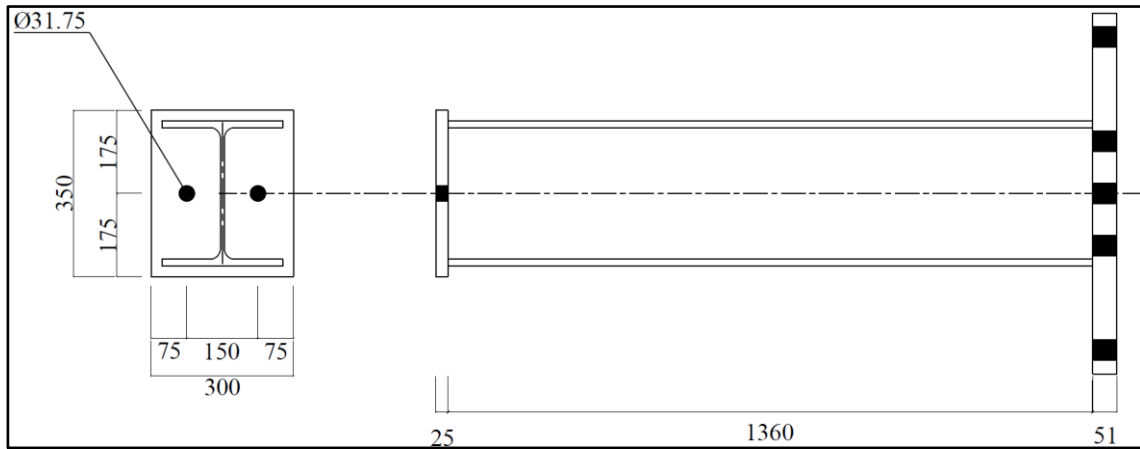


Figure 3.3: Two-AR specimens' shop-drawings, dimensions in mm

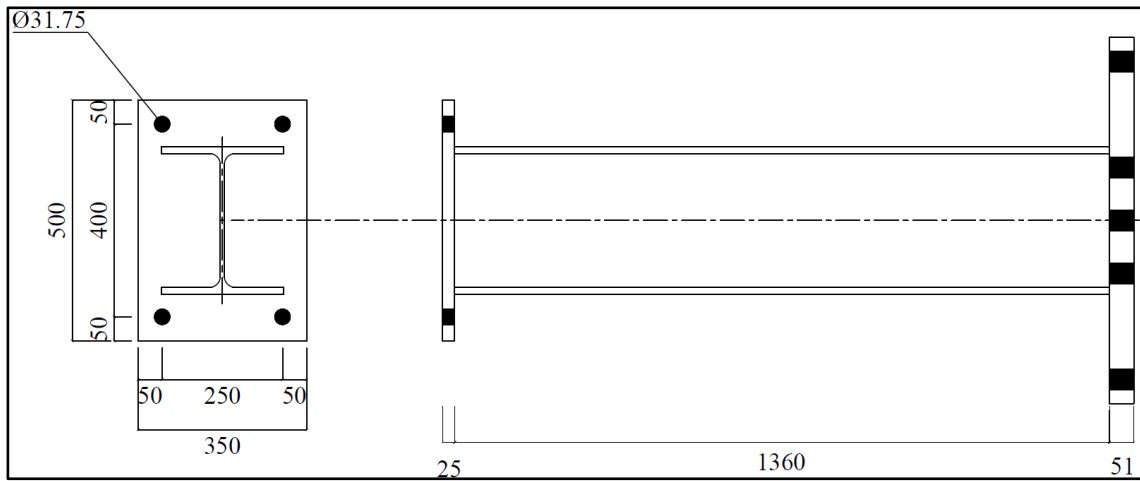


Figure 3.4: Four-AR specimens' shop-drawings, dimensions in mm

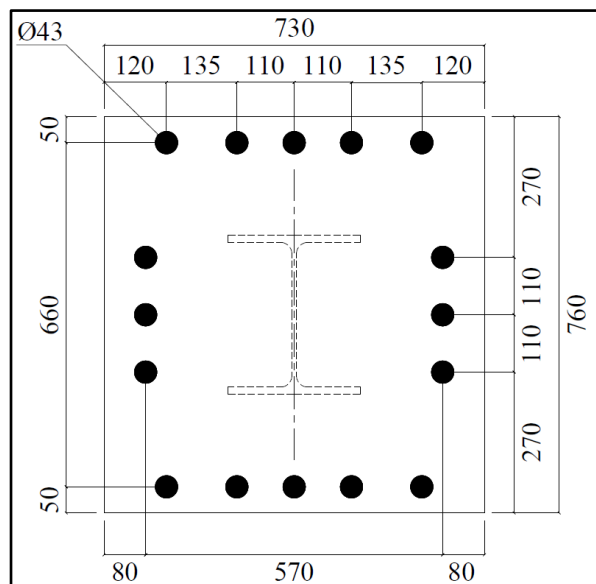


Figure 3.5: Top-plate shop-drawing, dimensions in mm

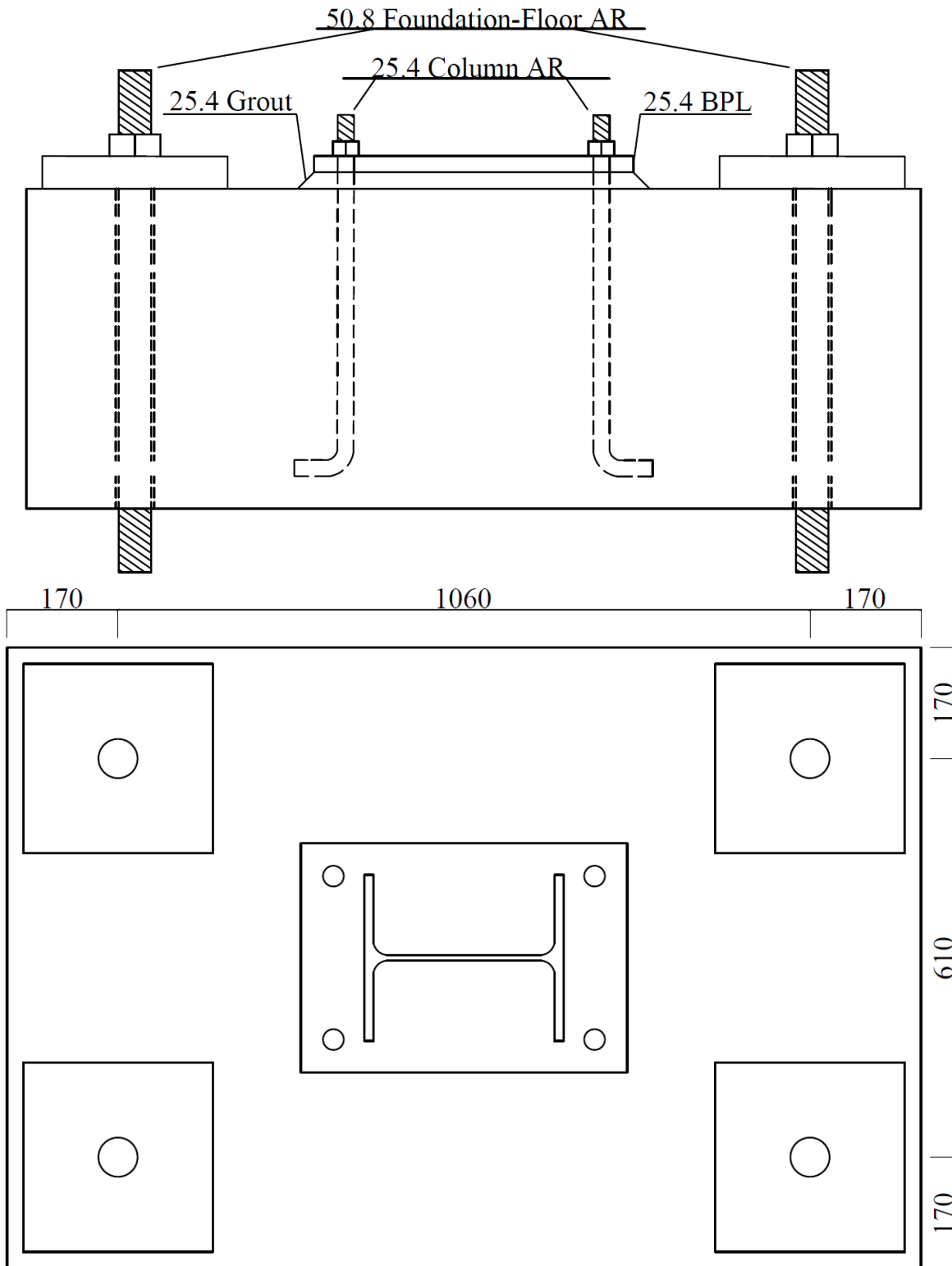


Figure 3.6: RC foundation and floor anchors layout, dimensions in mm

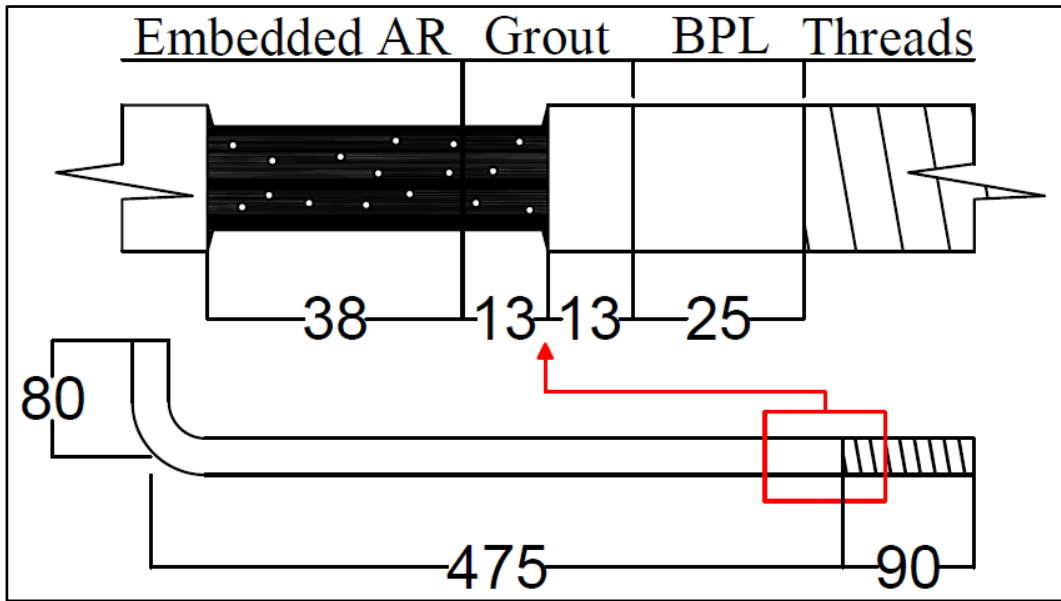


Figure 3.7: L-Shaped AR detailing, dimensions in mm

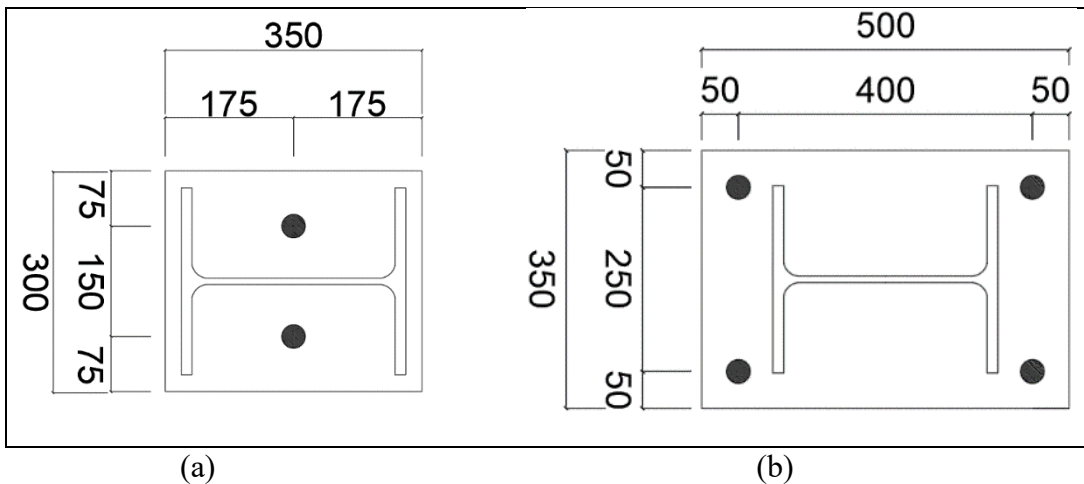


Figure 3.8: BPL layout: (a) Two-AR and (b) Four-AR, dimensions in mm



Figure 3.9: Formwork and steel cages prior to casting: (a) 2-AR and (b) 4-AR

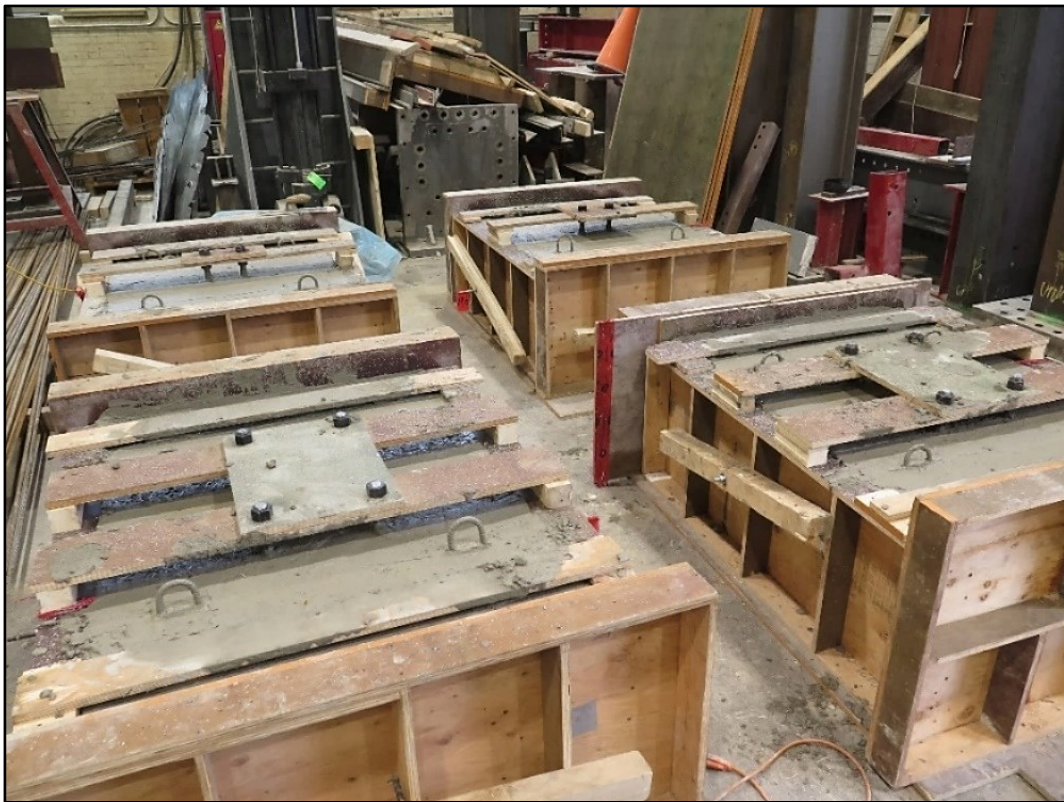
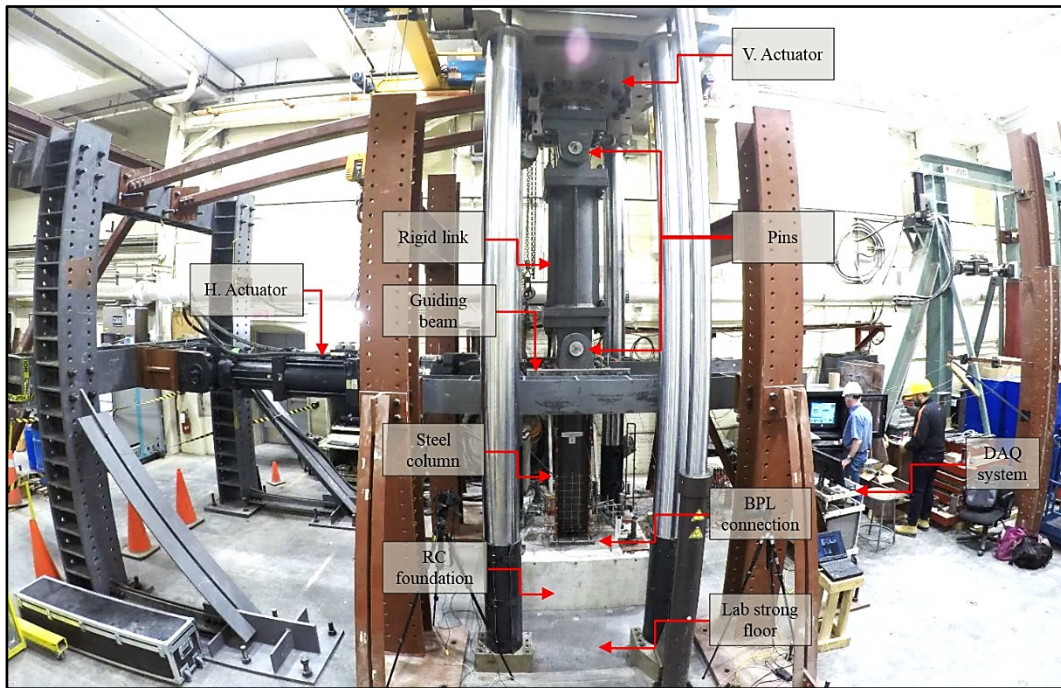
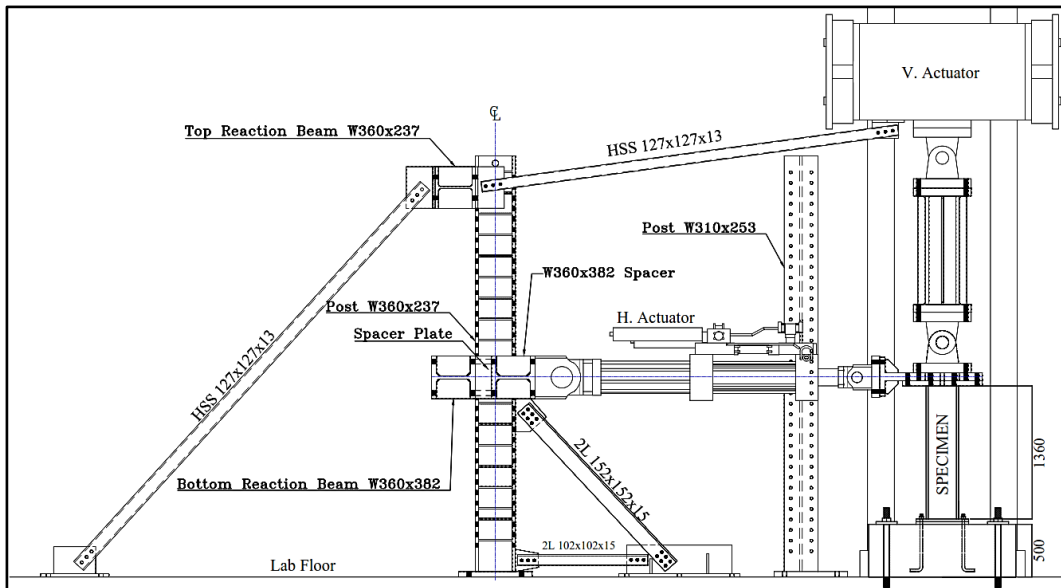


Figure 3.10: RC Foundation blocks post concrete casting



(a)



(b)

Figure 3.11: Testing setup, (a) Test in progress and (b) Schematic of the testing frame

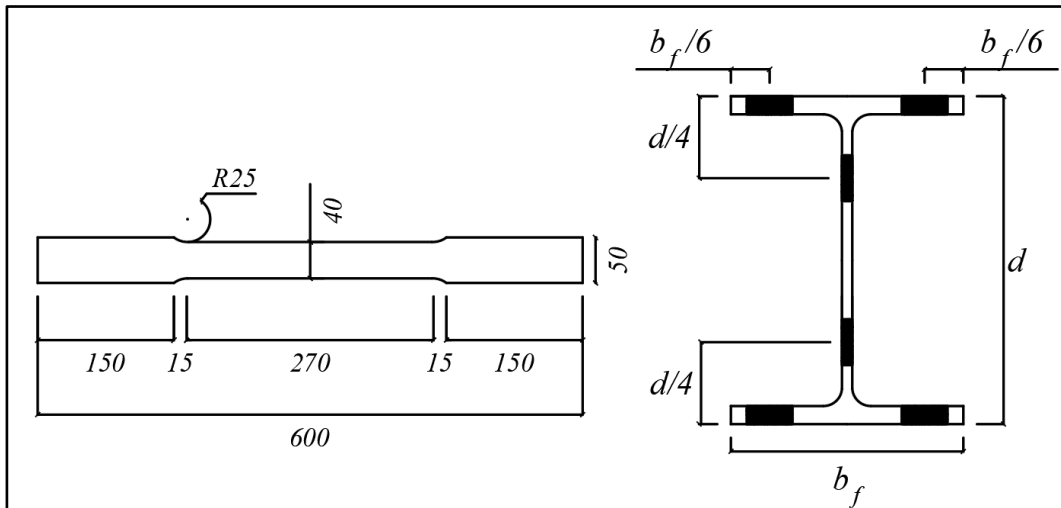


Figure 3.12: Schematic and location of the steel coupon for mechanical properties evaluation

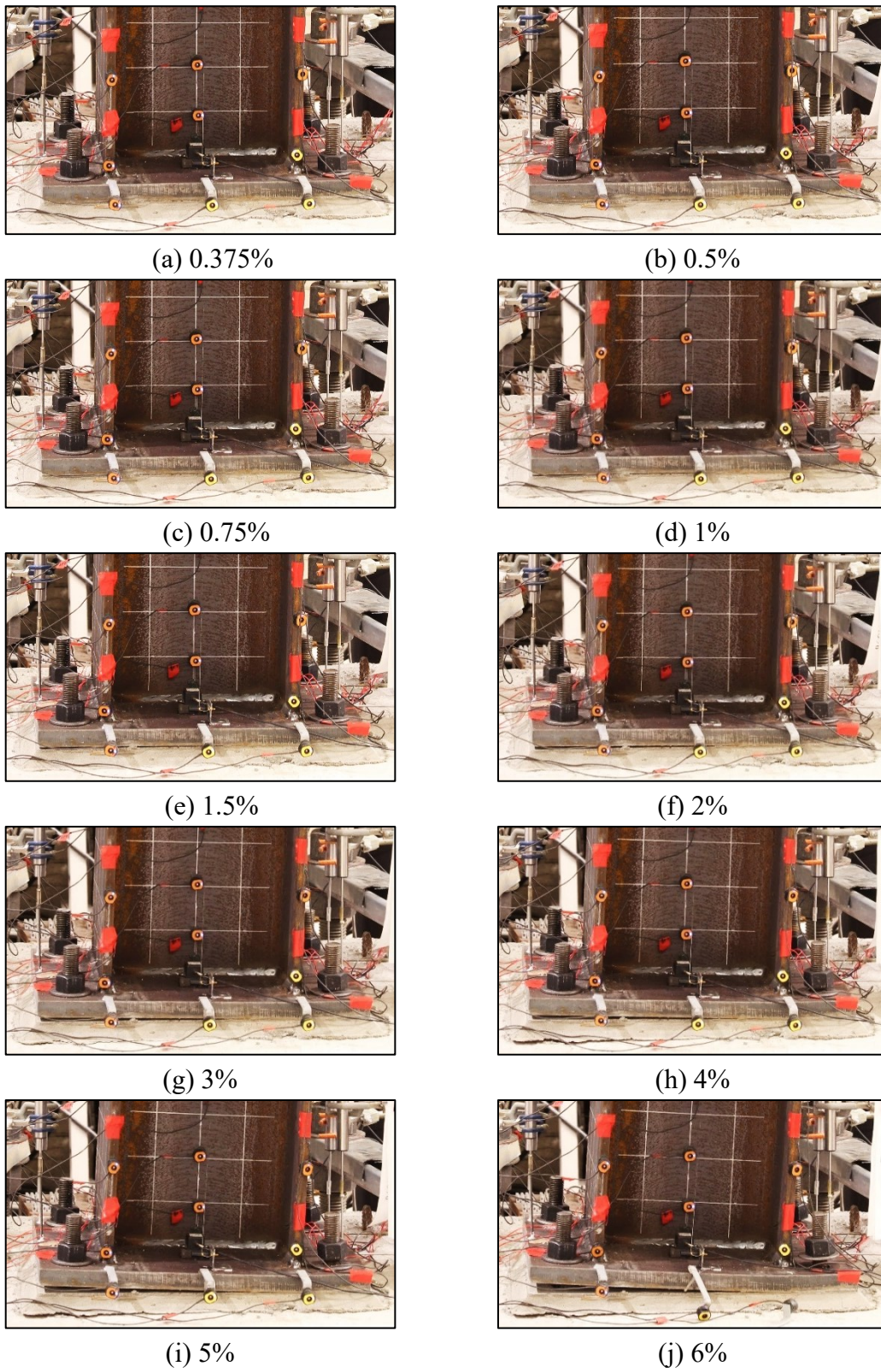


Figure 3.13: 4-AR-U connection at peak drift ratios

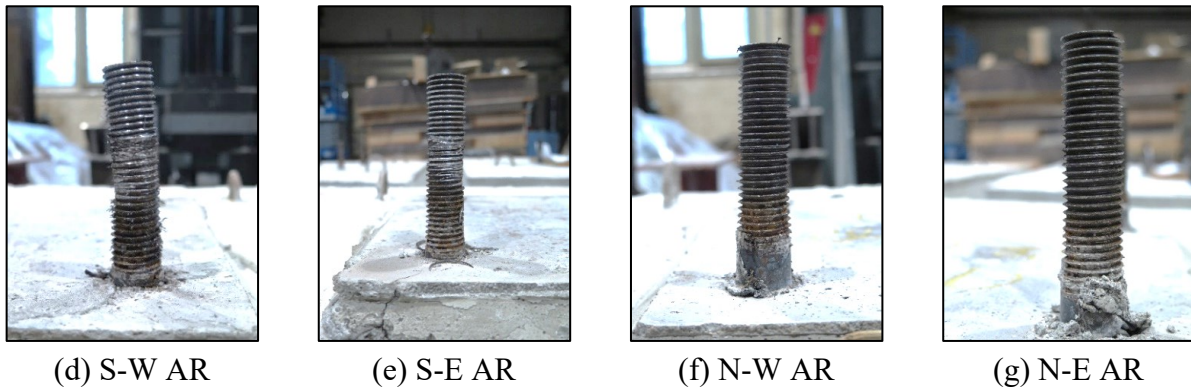
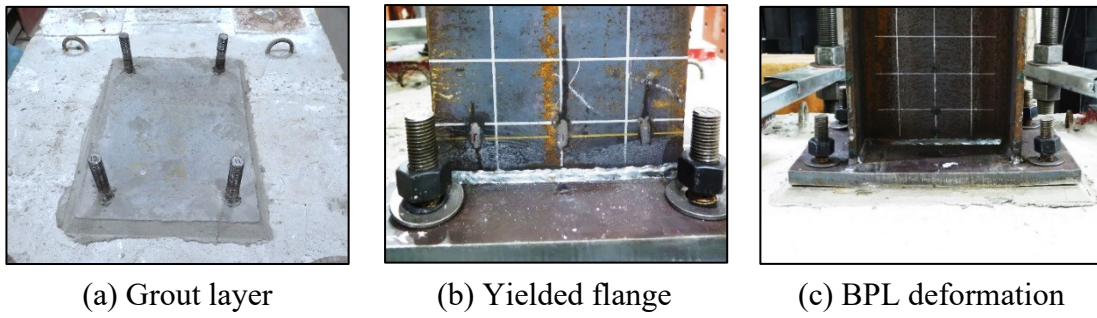


Figure 3.14: Post-testing 4-AR-U specimen's components

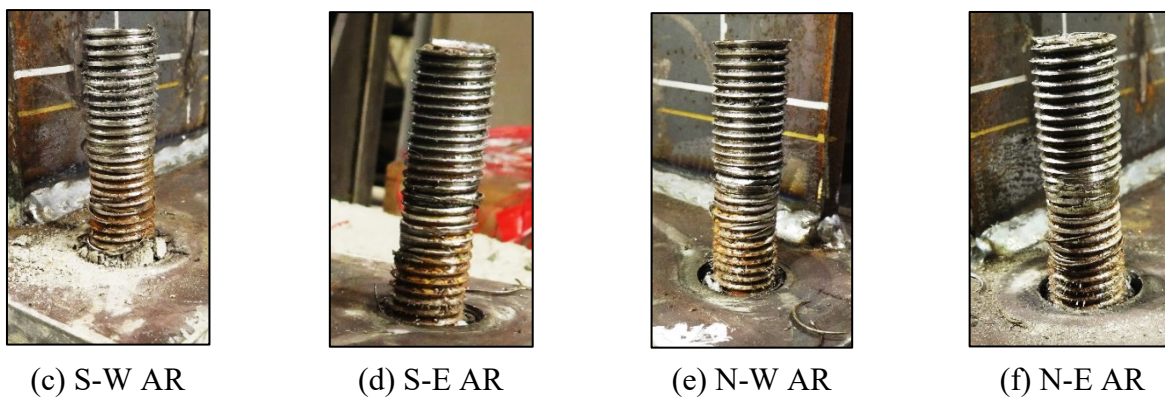
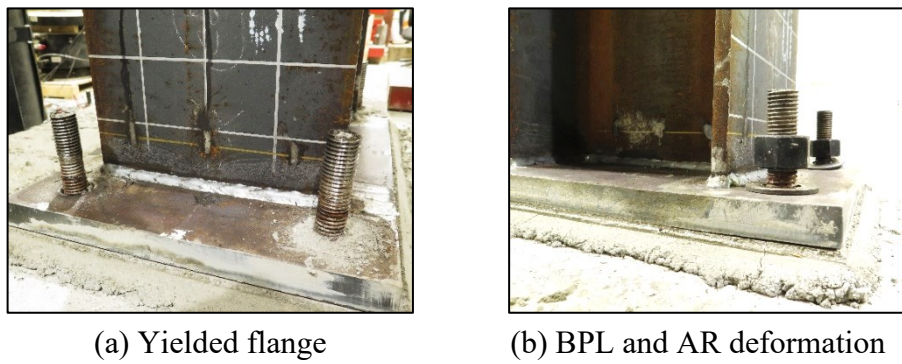


Figure 3.15: Post-testing 4-AR-C specimen's components

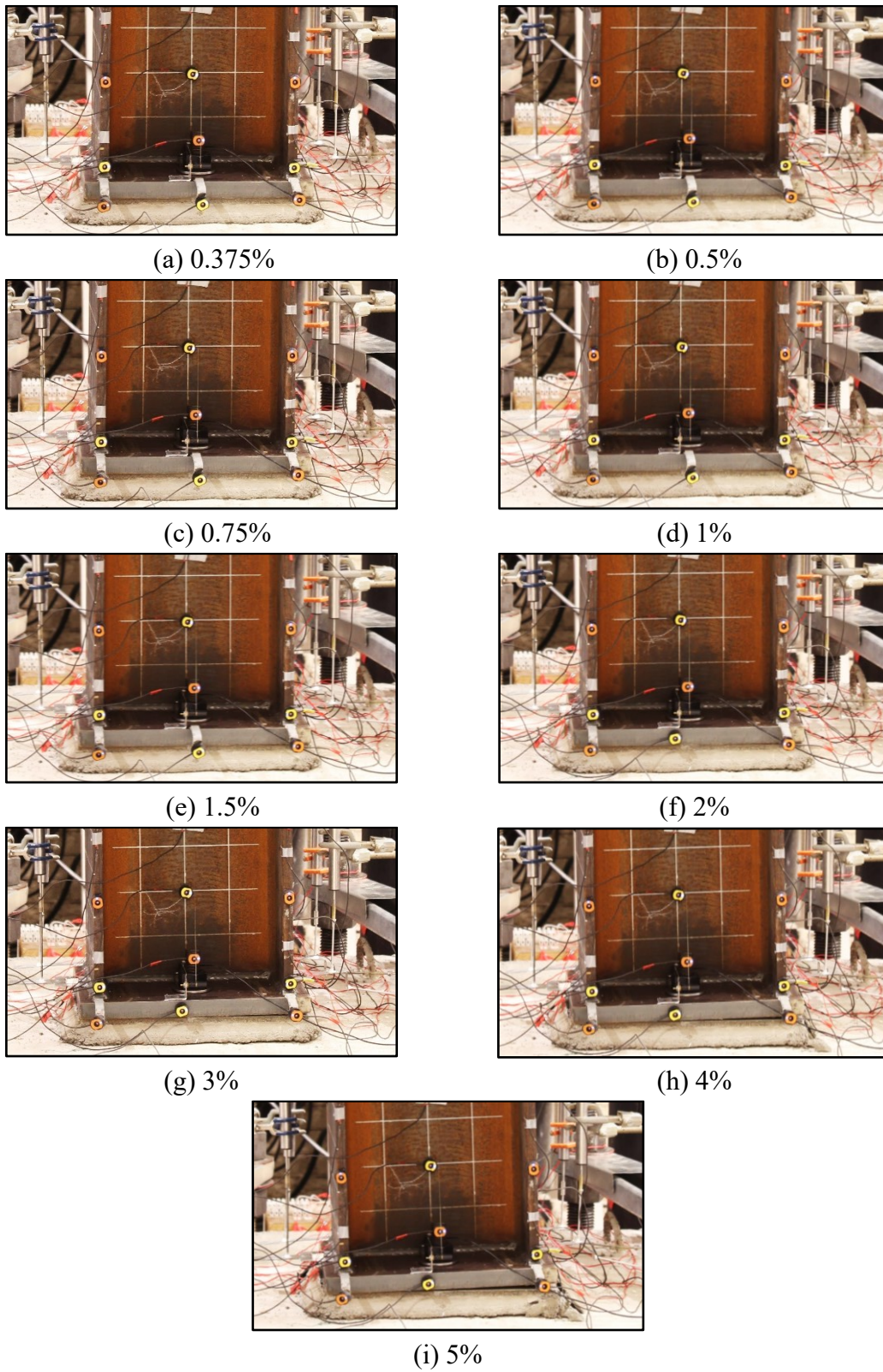


Figure 3.16: 2-AR-C connection at peak drift ratios

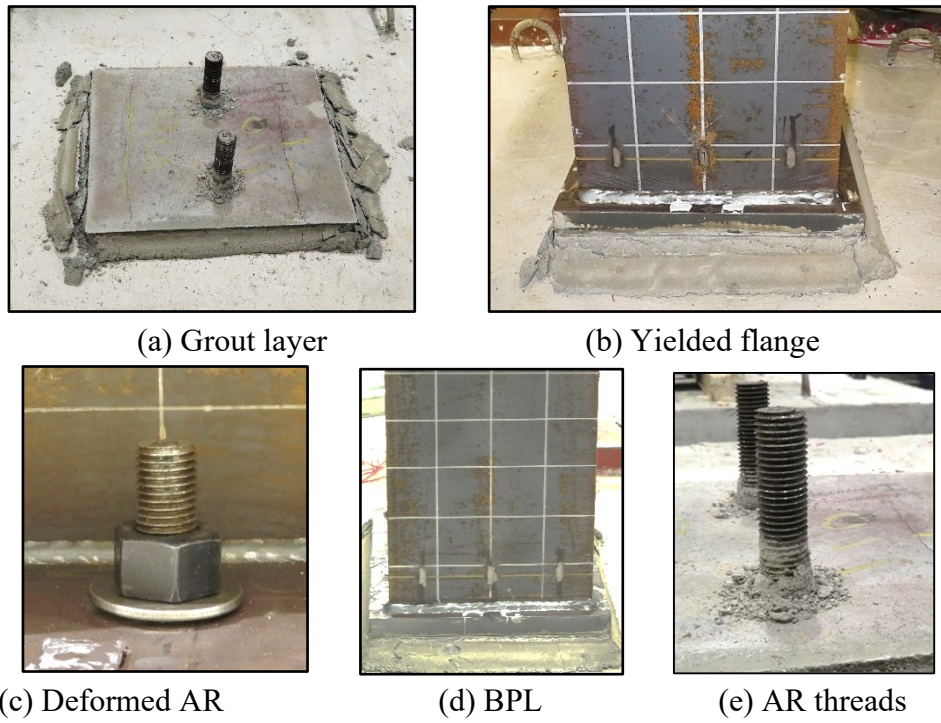


Figure 3.17: Post-testing 2-AR-C specimen's components

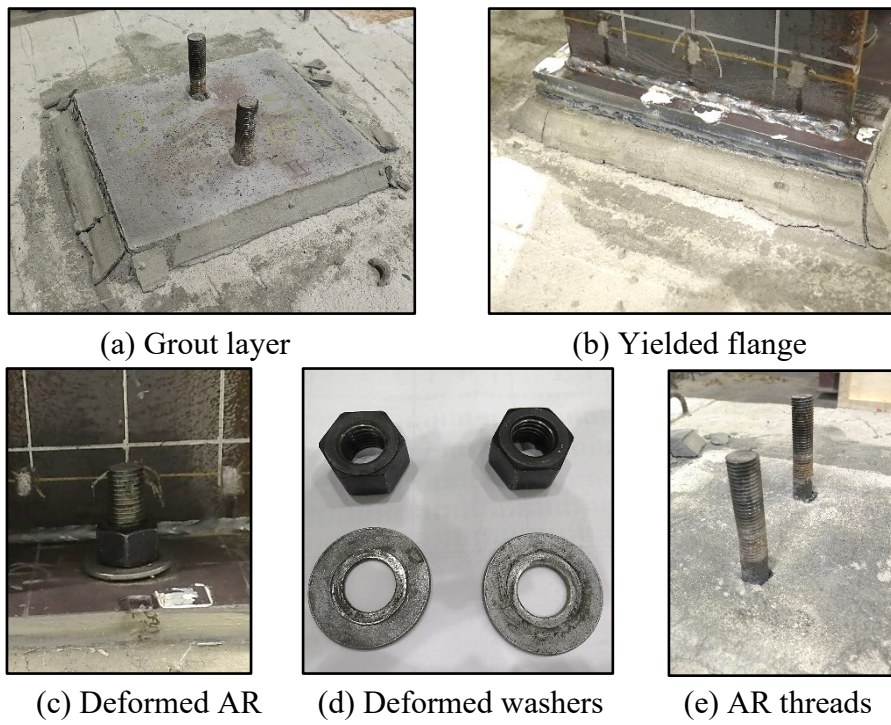


Figure 3.18: Post-testing 2-AR-U specimen's components

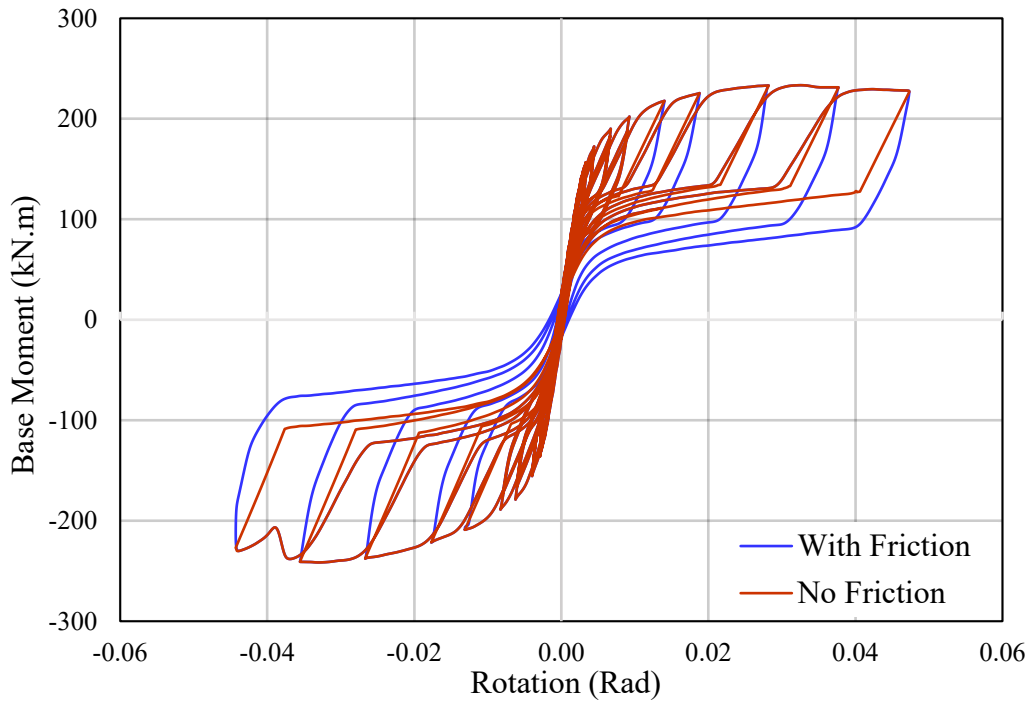


Figure 3.19: Moment-rotation relation friction subtraction

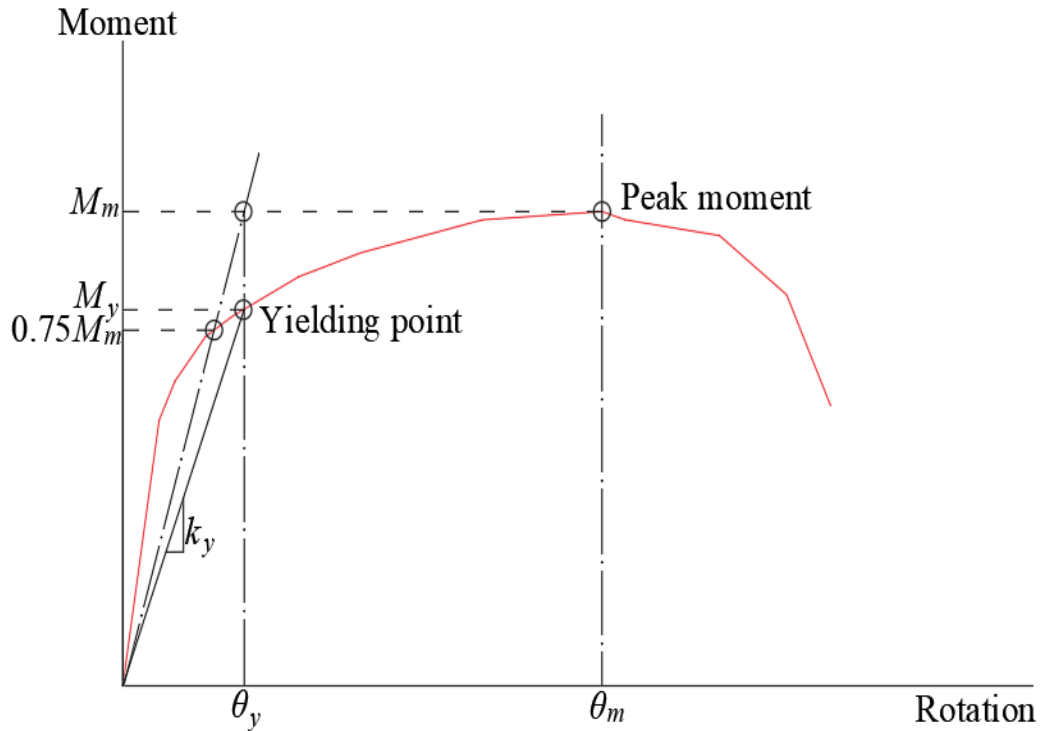


Figure 3.20: Definition of yielding point and initial stiffness, k_y , on the $M-\theta$ envelop

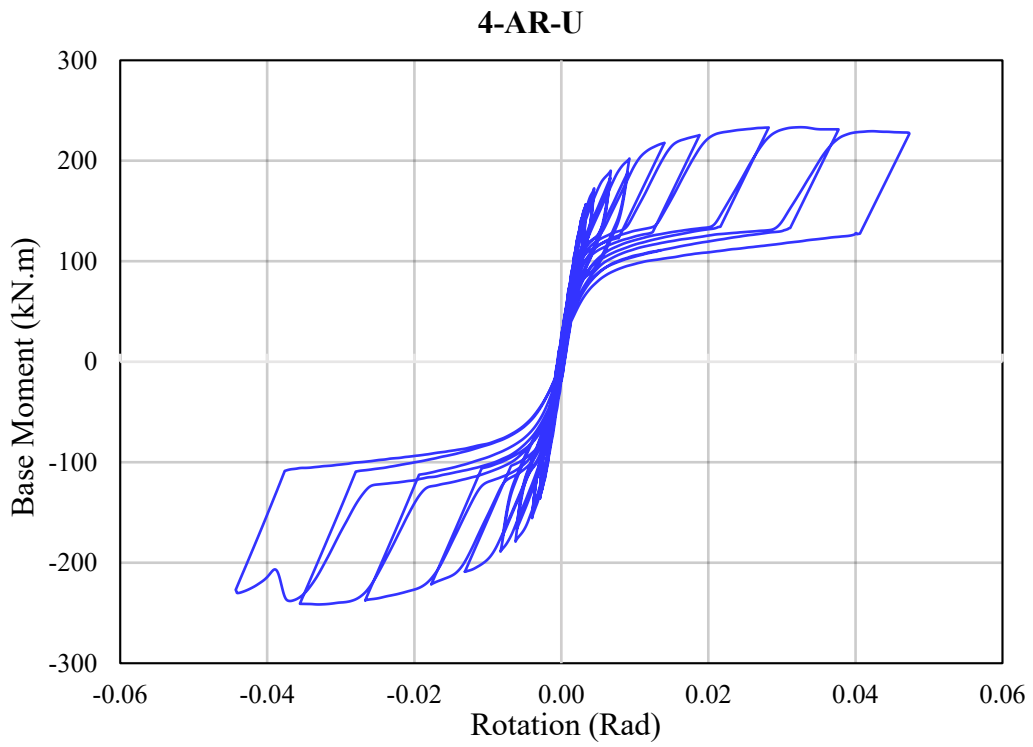


Figure 3.21: Moment-rotation relation for 4-AR-U specimen

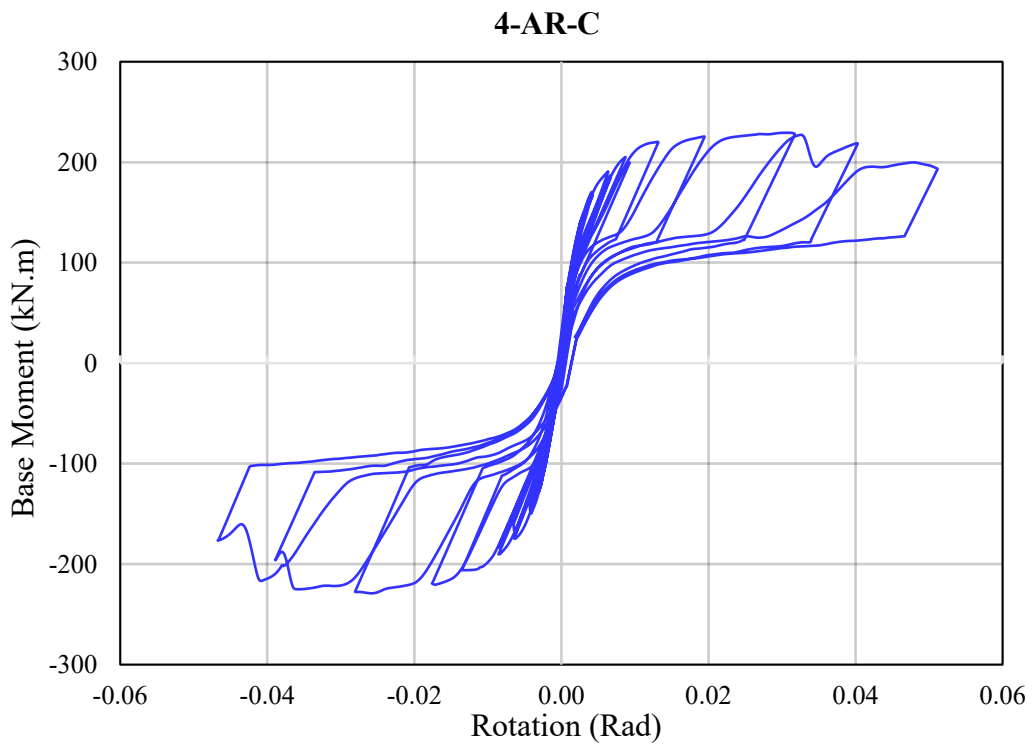


Figure 3.22: Moment-rotation relation for 4-AR-C specimen

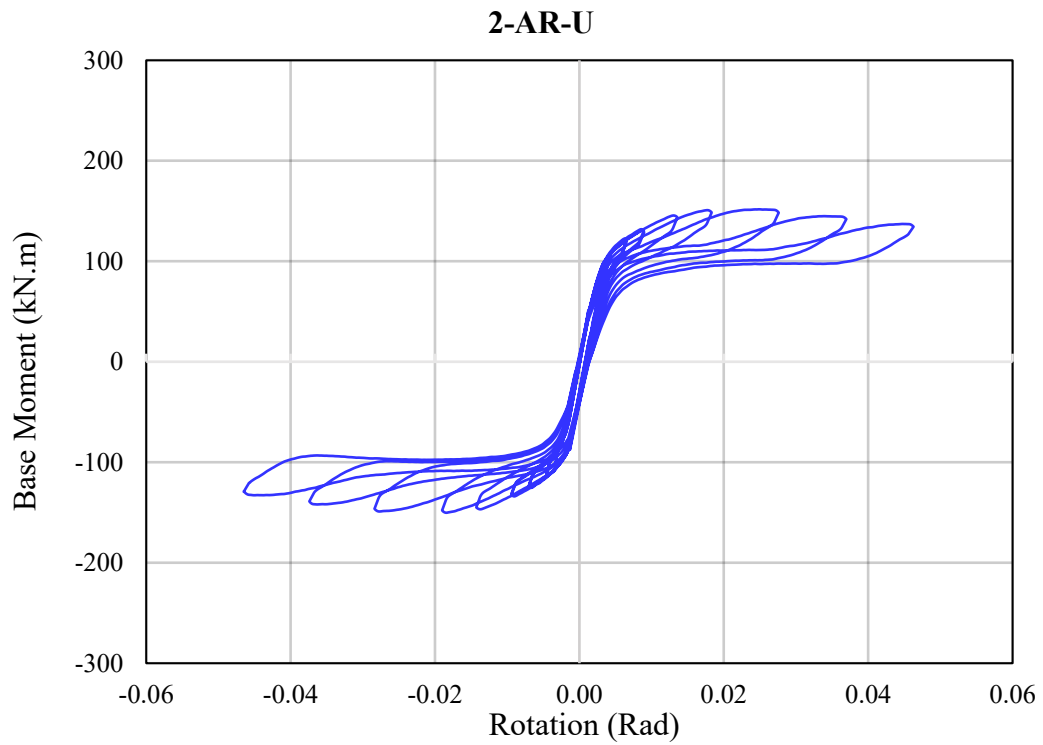


Figure 3.23: Moment-rotation relation for 2-AR-U specimen

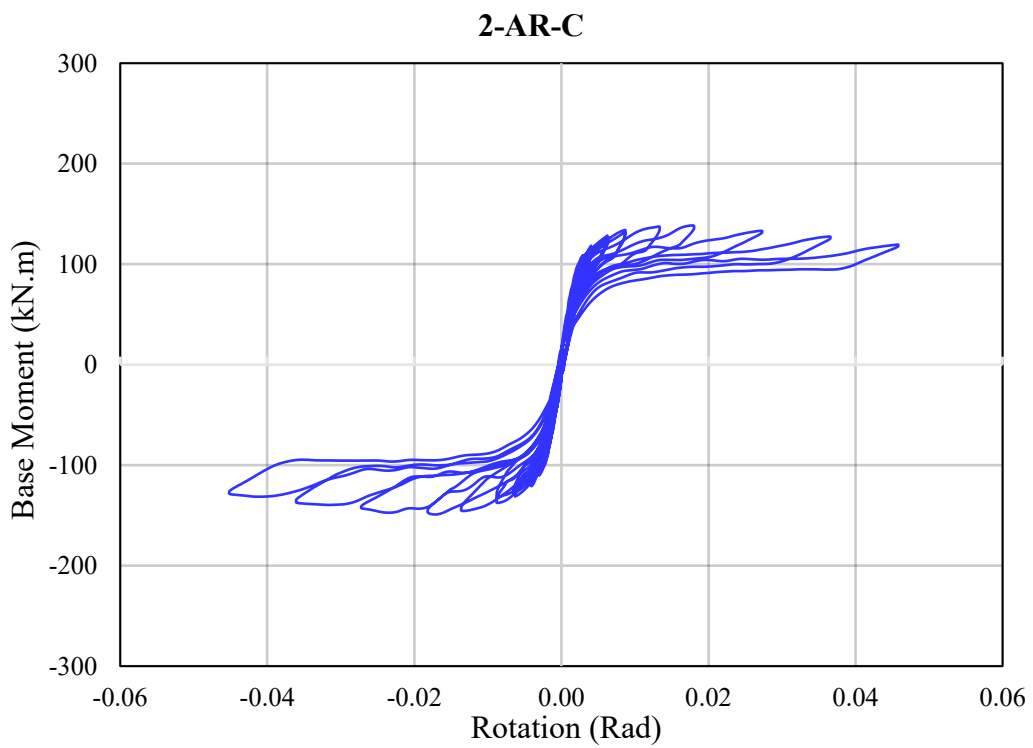


Figure 3.24: Moment-rotation relation for 2-AR-C specimen

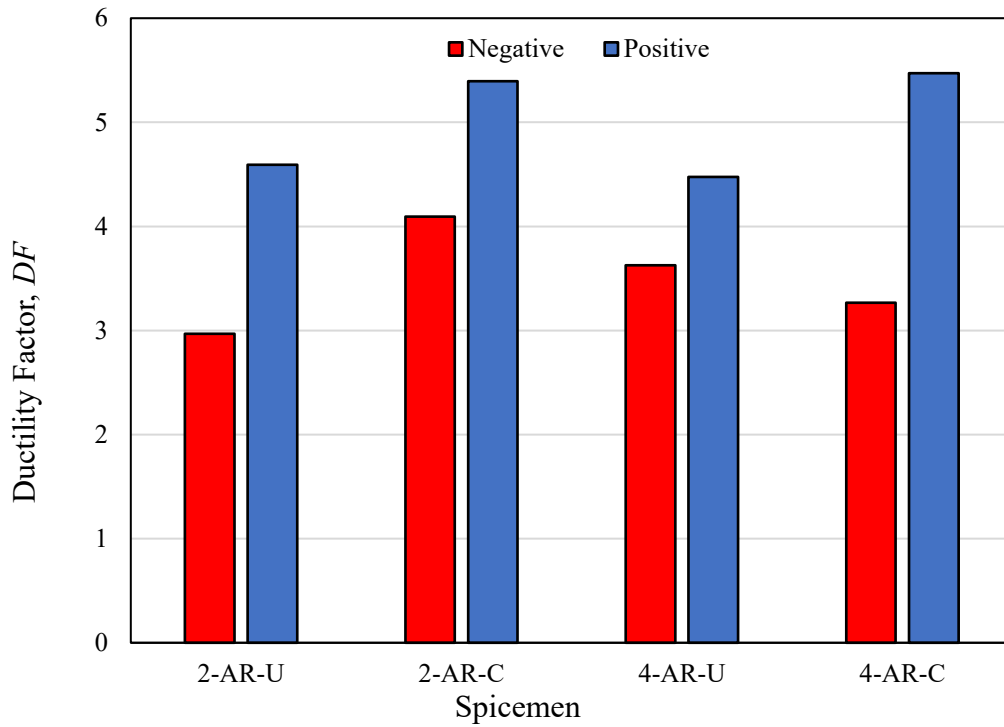


Figure 3.25: Ductility factors of the tested specimens

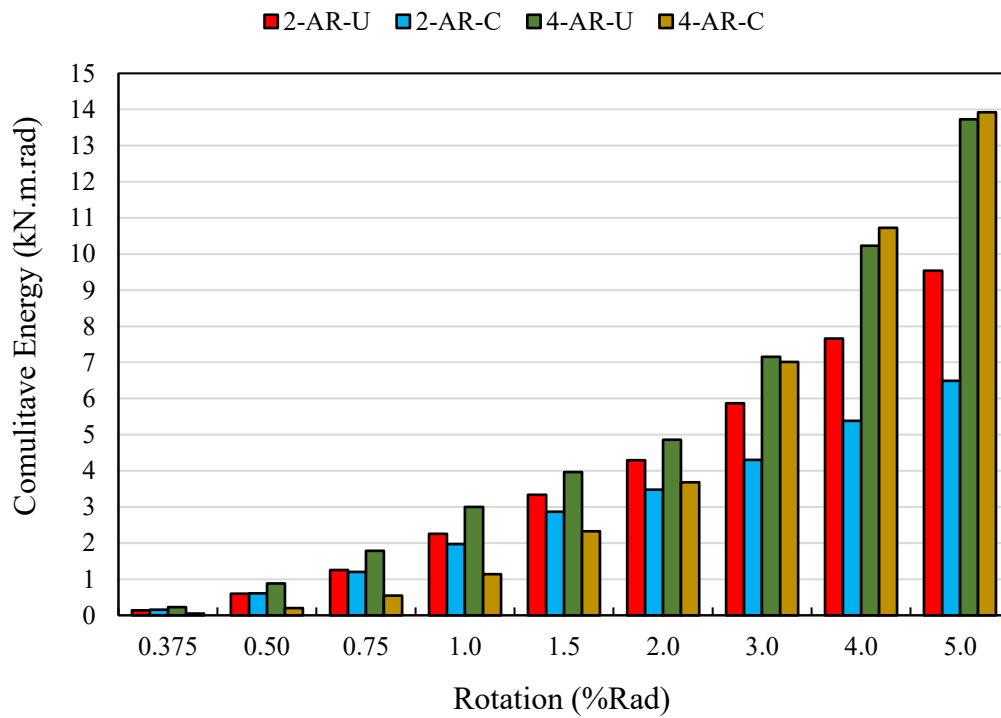


Figure 3.26: Cumulative energy dissipation capacity of the tested specimens

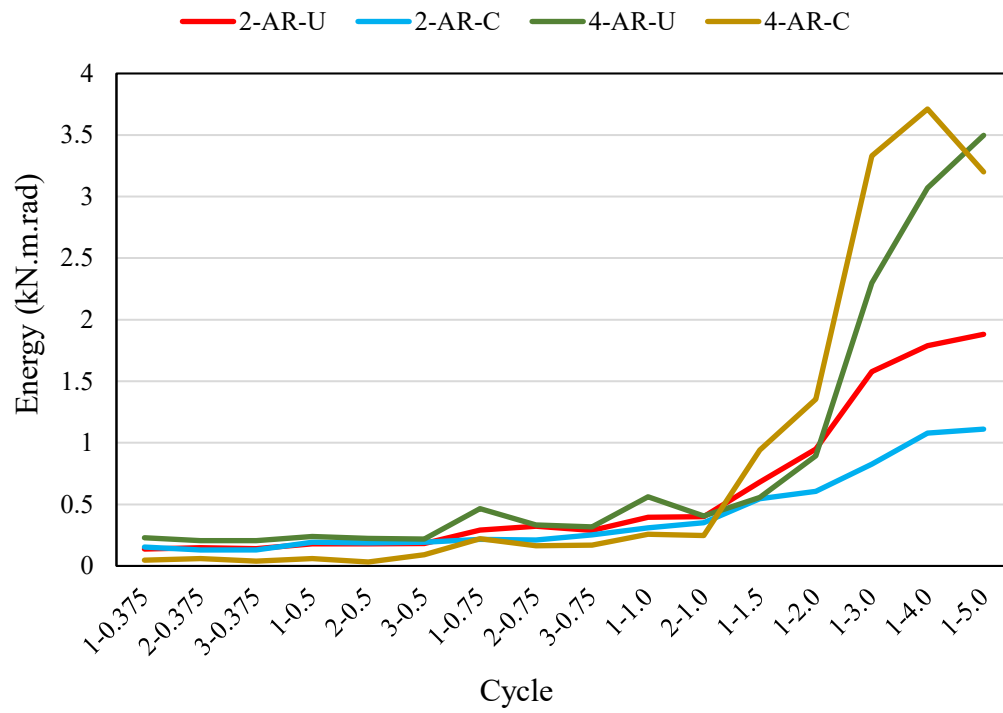


Figure 3.27: Dissipated energy per cycle

Chapter 4: Cyclic Simulation of Steel Column Base Connections

4.1 Introduction

The seismic assessment of existing structures requires conducting nonlinear response history analysis (NRHA). Strength and stiffness models, force-displacement (moment-rotation) relationships, are crucial for the NRHA. Developing these models and relationships requires a large amount of experimental data. Numerical simulation can be a powerful tool for understanding the behaviour of a structural system and predicting its performance. It can be a cost-effective and time-efficient alternative to experimental testing, especially when it is not possible or practical to perform physical experiments. Additionally, numerical simulation can provide valuable information that may not be captured by experimental testing. However, it is important to note that numerical simulation is only as accurate as the models and assumptions on which it is based, so it is important to validate the results against experimental data. The primary objective of this research is to evaluate the seismic response of the existing steel MRF. The column base connections, as part of the steel frame, have rarely been investigated, particularly in low to moderate seismic regions in North America. Detailed 3D finite element (FE) models were developed using the FE software ABAQUS CAE 2020 (Dassault Systèmes, 2020). The FE model will serve as an alternative to experimental testing and will allow the authors to conduct a parametric study to accommodate a range of parameters that will provide insight into the cyclic response of the exposed column base connections. The modeling approach, validation of the models, the parametric study and the limitations are presented in this chapter.

4.2 Modelling approach

The developed model, depicted in Figure 4.1, consists of a steel column, a base plate, a grout layer, a reinforced concrete (RC) foundation and anchor rods, as well as steel washers and nuts. The RC foundation includes steel reinforcement. The full model was initially developed and validated, and then, to take advantage of the symmetry, a half model was created and compared with the full model. The comparison confirmed that the half model accurately represents the full model, thus the half model was used for the parametric study. Axial loading was applied at the top of the column, followed by the lateral displacement protocol. Moment-displacement curves, rather than moment-rotation curves, were used for validation due to the difficulty in applying rotational deformations at the base of the connection. The “free body cut” feature in the ABAQUS CAE 2020 (Dassault Systèmes, 2020) platform was used at the base of the column to evaluate the base moment. The difference in vertical displacement of the nodes at the flanges' locations, shown in Figure 4.1, was used to determine the base rotation. The modeling approach was validated by comparing the results of the FE simulation to those of the experimental program. The model components were partitioned into more structural shapes to improve contact compatibility and computational efficiency. Two specimens from two different testing programs, Gomez (2010) and Picard and Beaulieu (1985), were also included for validation purposes.

4.2.1 Finite element type, solver and meshing

Linear brick elements with reduced integration and hourglass control (C3D8R) were used to model all components of the system, except for the steel reinforcement, which was modeled using plain truss elements. The nonlinear standard (implicit) static solver was used, and the simulation was divided into two steps. The first step was used to apply the axial loading to the top of the

column. The maximum increment was 10% (72 kN) of the total loading (720 kN). Lateral deformation was applied in the second step of the simulation, with a maximum displacement increment of 0.4 mm. It should be noted that these limits were determined after several attempts to balance the convergence and simulation time.

The mesh size varied based on the location and complexity of the different parts of the model. In general, all parts contained at least three elements in any direction. Mesh sensitivity analysis was conducted, hence finer mesh sizes for better stress transfer and compatibility were applied at the locations of contacts and interactions. Table 4.1 summarizes the global and minimum mesh sizes of each part in the model.

4.2.2 Boundary conditions and contacts

The simulated column had a length of 1360 mm, as shown in Figure 4.2. A fixed boundary condition was applied at the base of the RC foundation, restricting all six degrees of freedom. The top end of the column, where axial loading and lateral displacement were applied, had a partially fixed boundary condition. This boundary condition was applied at a reference point (*RP*) located at the center of the cross-section at the top end of the column, Figure 4.2. The edges of the column at the top end were tied to the *RP* using a rigid body constraint to prevent local stress concentrations. The top of the column had restraints on out-of-plane rotation (R_x) and displacement (U_z), as well as torsional rotation (R_y). Axial loading was applied to the top end surface of the column as a pressure representing a total of 20% P_y force, where P_y is the cross-section yield force (*i.e.*, $P_y = A_g F_y$), A_g is the cross-sectional area of the column and F_y is the yield strength of the column. Lateral loading was applied through in-plane displacement (U_x).

For simplicity, elements that experience insignificant movement along their interfaces were modeled as one part and then partitioned at the corresponding boundaries. For example, the column, base plate and washers were modeled as one part. Different sections, however, were assigned to the web, flange, base plate and washers. These sections define the materials assigned to these elements during the simulation. The steel base plate was modeled with two surface-to-surface contacts; a steel-on-steel surface contact was used between the base plate and the anchor rods at the holes, and a steel-on-grout surface contact was used between the base plate and the grout layer. The washers were bound to the top of the base plate to address the convergence issue that occurred when washers were free to slide between the nuts and the base plate. The grout layer was modeled with a surface-to-surface contact with the top surface of the concrete footing. All surface-to-surface contacts were modeled with "Hard" normal and "Penalty" tangential behaviours. Similarly, the anchor rod and nut were modeled as one part. The anchor rods were in surface-to-surface contact with the base plate, washers and grout layer. The nuts were in surface-to-surface contact with the washers. The embedded region constraint feature was employed between the RC footing and the segments from the anchor rods, which are within the RC body, and the steel reinforcement. The coefficients of friction were 0.6 for contacts involving concrete or grout with the steel (Rabbat and Russell 1985) and 0.2 for steel-on-steel contacts (Benenson et al., 2002).

4.2.3 Material models

Nonlinear material models were utilized to simulate various components of the model. Steel with a nonlinear combined (isotropic-kinematic) hardening materials were defined for the column, base plate and anchor rods. The concrete damaged plasticity (CDP) model was employed for the

RC foundation and grout. Elastic perfectly plastic material was defined for the steel reinforcement, washers and nuts as illustrated in Table 4.2. Initially, some plasticity was assumed in the nuts and washers material to account for the observed plastic deformation during the tests. While incorporating this plasticity showed slight improvement in the results compared to the experimental data, the author chose to disregard it due to the limited information available on the mechanical properties of the nuts and washers. Therefore, the models were kept with the assumption of elastic perfectly plastic behaviour for nuts and washers.

The column, base plate and anchor rods were simulated using a nonlinear combined isotropic-kinematic hardening material ABAQUS CAE 2020 (Dassault Systèmes, 2020) adopted the stress-strain constitutive model proposed by Chaboche (Chaboche et al., 1979) and Voce (Voce, 1948). The calibration of the model input parameters is discussed in Hartloper et al. (2021). The parameters, such as C (initial kinematic hardening modulus), γ (rate at which C decreases with cumulative plastic strain ϵ_{pl}), α (backstress), $\sigma_o|^\theta$ (equivalent yield stress at zero plastic strain, *i.e.*, F_y), Q_∞ (maximum change in the size of the yield surface) and b (rate at which the size of the yield surface changes as plastic deformation changes) are material type dependent and independent of the loading history. Table 4.3 summarized the material input for parts comprising the combined hardening model. It should be noted that the calibration of these parameters requires, in addition to the uniaxial monotonic coupon testing, constant and varying amplitude cyclic tests. Castro e Sousa et al. (2021) developed an approach that allows researchers to estimate the combined hardening parameters based on the available monotonic uniaxial stress-strain curve when cyclic tests were not conducted.

The RC foundation and grout layer were simulated using the CDP material model. The CDP features two different failure behaviours: the crushing of the concrete in compressive state and the cracking in tensile. The CDP uses the equivalent plastic strains to characterize the behaviour of the concrete during the simulation. The compressive relationship, Figure 4.3, passes through three stages: the material is linear and elastic until the point of initial yield, f_{co} , then a nonlinear hardening response takes place until the stress reaches the compressive strength of the concrete material, f_{cu} . Finally, softening of the stress-strain relationship is taking place when the concrete elements are loaded beyond their specified compressive strength. In contrast, when the concrete elements are under tension, the relationship between stress and strain is linear and elastic until the tensile failure stress, f_{to} , is reached. After the tensile failure, the material's response is characterized by a softening of the stress-strain relationship as shown in Figure 4.4. The typical compressive cylinder tests were used to construct the compressive material part of the model, and cylinder splitting tests were used to define tensile strength of the concrete. The plasticity flow parameters such as the dilation angle (ψ), eccentricity (e), the ration of the biaxial stress to the compressive yield stress (f_{bo}/f_{co}), the ratio of the second stress invariant on the tensile meridian to that on the compressive meridian at initial yield (K), and the viscosity parameter (μ) are set to default, as shown in Table 4.4. According to ABAQUS documentation manual (Dassault Systemes, 2020) the convergence of the model can be improved when μ is set to a value that is smaller than the characteristic time increment, which can be estimated using the mesh check feature in ABAQUS platform. It should be noted that due to the complexity of evaluating the mechanical properties of the grout material that are needed for the CDP model, the authors used same stress-strain data from the concrete material multiplied by the ratio of the compress strength of the grout to that of the concrete.

4.3 Model validation

The modeling approach was validated by comparing results from the simulation to results from the experimental tests on the column base connections discussed in Chapter 3. Two specimens were also utilized for validation purposes from previous experimental programs. In particular, specimen 8F and test No. 4 from Picard and Beaulieu (1985) and Gomez (2010) respectively, were modeled in ABAQUS platform following the same approach discussed in the previous sections. The validation was done by comparing the deduced moment-displacement curves for specimens 4-AR-U and 2-AR-C of the ongoing research, the force-displacement curve for test No. 4 from Gomez (2010) and the moment-rotation for specimen 8F from Picard and Beaulieu (1985). Models' overviews as well as the deformed shapes, at the peak of the last cycle, of the discussed specimens are also presented for the validation purposes.

Figure 4.5 depicts the 4-AR-U FE model and its deformed shape, clearly illustrating the extensive yielding of the anchor rods as concluded from the test. Additionally, Figure 4.6.a and Figure 4.6.b show the deformation of the base connection elements observed in the test and FE modeling, respectively. The FE model was able to predict the deformation of the connection in intricate detail. For instance, it not only captured the extensive yielding of the anchor rods but also accurately predicted their inclination towards the column due to the loading history, along with the gap between the grout and the concrete footing. Moreover, the FE moment-displacement response of the 4-anchor rods specimen exhibited good agreement with the moment-displacement observed in the test, as illustrated in Figure 4.7. The FE model achieved a maximum of 5% error in predicting the moment values. Similarly, Figure 4.8 shows the model and its deformed shape of the 2-anchor rods specimen. The model predicted the plastic deformation of the anchor rods. It was also able to

show minimal yielding in the other components of the connection (i.e., column and base plate) when compared to the 4-anchor rods' simulation in Figure 4.5. These findings align with the conclusions of the testing program discussed in Chapter 3 of this thesis. Furthermore, a close comparison of the connection's other components from the test in Figure 4.9.a, and from the simulation in Figure 4.9.b, demonstrates how well the model captured the damage to the grout layer. The FE moment-displacement response of the 2-anchor rods specimen is plotted against the test results in Figure 4.10. The model accurately predicted the moment-displacement response up to the point when the moment carrying capacity started to decrease in the initial loading direction from the higher cycles. This decrease could be attributed to the fact that the grout was the dominant source of damage in the model at these late stages of the simulation, as shown in Figure 4.9.b. Due to the complexity of accurately modeling the grout material and acquiring its material properties to define the CDP model, the author accepted the achieved level accuracy of the simulation for the 2-anchor rods specimens.

The validation of the model employed test No. 4 from Gomez (2010) and specimen 8F from Picard and Beaulieu (1985) to ensure the robustness of the modeling approach. The model for test No. 4 is shown in Figure 4.11, while the corresponding load-displacement curve is plotted in Figure 4.12. The deformed shape clearly depicts how the reduced section of the anchor rods, representing the threads, achieved the necking state in the simulation. This aligns with the reported damage to the anchor rods' threads in test No. 4 by Gomez (2010). Furthermore, the model accurately captured the pinched hysteretic response reported by Gomez (2010) and demonstrated acceptable agreement in terms of the load-displacement relationship, as illustrated in Figure 4.12. Similarly, Figure 4.13 shows the FE model and deformed shape of specimen 8F. The deformed shape reveals how the anchor rods reached the fracture state, as reported by the authors during the test of specimen 8F.

Additionally, Figure 4.14 demonstrates the agreement between the simulation's moment-rotation response and the corresponding test results.

4.4 Parametric evaluation of existing column base connections

The parametric study conducted on the column base connections, utilizing the FE modeling approach discussed in previous sections, explored various parameters such as column size, base plate dimension and thickness, anchor rods' diameter, level of axial loading and strength of the base plate material. Transverse spacing between anchor rods was also examined. All connections had a column length of 3600 mm, with consistent RC footing size, reinforcement and material across the board. A 25 mm thickness of grout layer was applied in all connections, adjusted in length and width according to the base plate dimensions, with an additional 25 mm beyond the edges of the base plates. The steel reinforcement, nuts, washers, concrete and grout materials used were the same as discussed in the modeling approach. The connections in the simulation matrix were subjected to the same loading conditions. The author specifically focused on the 4-anchor rods connections in the simulation matrix for two reasons. Firstly, more details were required to better simulate the 2-anchor rods connections, as discussed in the validation section. Secondly, the 4-anchor rods simulations can serve both existing and newly constructed column base connections, particularly considering that the 2-anchor rods configuration is no longer permitted in construction.

4.4.1 Simulation matrix

The simulation matrix is presented in Table 4.5, illustrating the various parameters considered in the study. The matrix included three column sizes: W250×49.1, W310×79 and W360×122. For the steel columns, a CSA G40.12 grade 300(CSA, 1970) material was utilized. The base plate

width ranged from 350 mm to 450 mm, while the length varied from 500 mm to 600 mm. These dimensions were selected to provide approximately 50 mm of clear edge length beyond the anchor rods. In the parametric study, the base plates had thicknesses ranging from 19 mm to 32 mm. A steel material of ASTM A36M grade 250 (ASTM, 1966) was used for the base plates. The anchor rods, also made of ASTM A36M grade 250 (ASTM, 1966) steel, varied in diameter from 19 mm to 38 mm. The level of axial load applied was typically 20% P_y , but variations of 10% P_y and 30% P_y were also examined to investigate their influence on the response. The aforementioned parameters, including the materials, dimensions, thicknesses and diameters, were all commonly found in the old plans that the author reviewed. However, for some plans specifying CSA G40.12 grade 300 (CSA, 1970) as the material for the column base plate, additional connections were added to include this material. The summary of the simulation matrix materials input can be found in Table 4.6.

4.4.2 Parametric simulation results

The performance of the column base connections is assessed through various aspects, including the mode of failure, moment-rotation relationship, ductility and energy dissipation capacity. These measures provide a comprehensive evaluation of the connections' response to cyclic loading. The mode of failure analysis reveals the critical failure mechanism observed in the column base connections. The moment-rotation relationship characterizes the connection's ability to resist bending moments and its stiffness during loading. Ductility and energy dissipation capacity analysis assess the connection's ability to undergo large deformations and absorb energy during loading. These properties are crucial for structures subjected to dynamic or seismic forces. In addition, the influence of the studied parameters is analyzed in the subsequent subsections. This

analysis examines how variations in parameters, such as column size, base plate dimension and thickness, anchor rods' diameter, level of axial loading and material properties, impact the performance of the column base connections.

4.4.2.1 Mode of failure

Three factors were examined to identify the failure mode of the connections: 1) The deformed shape of the connection at the peak of the last cycle; 2) The stresses and plastic deformations throughout the simulations; and 3) The development of a mechanism and loss of moment-carrying capacity. The deformed shapes of the connections at the first peak of the last cycle of loading are shown in Figure 4.15. The connections were categorized into three groups as illustrated in Table 4.7. Group one includes connections that experienced a drop in their moment-carrying capacity and have rigid base plates. These connections are characterized by their base plates completely losing contact with the grout layer in the tensile region of the base plate. Group one connections exhibited early yielding in the anchor rods, followed by the yielding of the flanges, then the yielding of their base plates and finally the yielding of the web of the columns. This sequence is justified by the presence of thick base plates. Group two includes connections comprising flexible base plates. Connections in group two did not exhibit a loss in moment-carrying capacity, and their base plates did not lose contact with the grout layer. The anchor rods in group two exhibited delayed yielding compared to the anchor rods in group one connections, and no cross-section necking was observed. It should be noted that stresses experienced by the connections' components in group two were well below the stresses experienced by connections in group one. Group three connections, however, exhibited a transitional mode of failure, where the base plates showed flexible deformability, and the anchor rods underwent stresses near their tensile strength. Except

for S8 and S10, connections in group three experienced delayed anchor rod yielding similar to that of group two connections. Nevertheless, there was no delay between the yielding of the base plate and flanges of the connections in group three. Connections S8 and S10 exhibited early yielding in anchor rods, similar to group one connections, and hence showed some cross-section necking. However, their base plates exhibited the deformability experienced by group two connections.

Varying the anchor rods' diameter had a significant impact on the failure mode, as evidenced by comparing the following connection pairs: (S1-S2), (S6-S7) and (S9-S10). Increasing the diameter of the anchor rods resulted in an increase in the flexible deformability of the base plates. In contrast, increasing the column size in (S3-S4) and (S7-S8), or the thickness of the base plates in (S4-S5) and (S8-S9), increased the rigidity of the base plates. The increase in rigidity due to thicker base plates is clearly justified. However, the enhanced rigidity resulting from an increase in column size can be attributed to the confinement provided by the larger columns to the base plates. Finally, a change in the base plate dimension did not affect the failure mode, as observed in (S2-S3) and (S5-S6). Other parameters, such as $\%P_y$, base plate material and the transverse spacing between the anchor rods did not alter the failure mode of the connections. However, the transverse spacing of the anchor rods did impact the deformability of the base plates. Isometric views of connections S19 and S21 are presented in Figure 4.16.a and Figure 4.16.b, respectively. It was observed that increasing the transverse spacing between anchor rods enhanced the flexibility of the base plate, particularly in the middle section of its width. These parameters will be discussed in detail in the following sections.

4.4.2.2 Moment - rotation relationship

The moment-rotation relationships of the simulated column base connections are plotted in Figure 4.17 to Figure 4.38. All connections exhibited the flag-shape hysteresis that was reported in the literature for the exposed column base connections (eg., Gomez, 2010, Lim et al., 2017a, and Kavoura et al., 2017). This flag-shape hysteresis was also observed in the response of the tested column base connection specimens in Chapter 3. The moment-rotation relationships of the simulated connections, and the exposed column base connections in general, can be characterized by the following stages:

- 1- Initially, as the loading is small, the response remains elastic. This continues until the initiation of yielding in one of the connection's components, typically the anchor rods in our case, which results in a noticeable change in stiffness.
- 2- As loading progresses and plastic deformation increases, another change in stiffness occurs, indicating the yielding of another component of the connection. Depending on the type of base plate (e.g., flexible or rigid), one of the following scenarios takes place:
 - Rigid base plate connections tend to concentrate plastic deformations in the anchor rods. With the aid of yielding in other components, a yield plateau is developed. After the formation of the mechanism, a loss in moment-carrying capacity occurs. If loading continues, a descending (negative) stiffness characterizes the moment-rotation relationship until loading is stopped. This behaviour was observed in connections in group one.
 - Flexible base plate connections, on the other hand, distribute plastic deformation along the width of their base plates, which delays the formation of the mechanism. As a result,

no loss in moment-carrying capacity occurs until loading stops. This can be seen in the response of connections in group two.

- 3- The next stage occurs when unloading begins. The washers start losing contact with the nuts, resulting in a decrease in stress on the anchor rods and base plate. This stage is characterized by an approximately constant backward stiffness.
- 4- The following stage begins when the washers completely lose contact with the nuts, and the anchor rods no longer contribute in resisting the loading. The type of base plate influences the response, leading to two distinct behaviours:
 - In connections with rigid base plates, the base plate moves freely downwards. A pinching behaviour develops, and the connection exhibits an approximately constant loading plateau, corresponding to the moment capacity of the base plate only due to the compression region. The base plate starts closing the gap with the grout, developed due to plastic deformation, from the compression region towards the tensile region.
 - Flexible base plates do not completely lose contact with the grout. When they relax after the washers have completely lost contact with the nuts, they start closing the gap from the tensile region towards the compression region. Closing the gap in the tensile region results in another drop in moment-carrying capacity, unlike the loading plateau experienced by rigid base plates.
- 5- The final stage in the half-cycle of loading begins when the gap between the base plate and the grout is closed. The loading stiffness rapidly increases in the negative direction because the connection is now intact, and the anchor rods, which were previously in the compression region, will now act in tension, similarly the compression and tensile regions on the base plate switch.

The five stages explained above are repeated while completing the second half of the cycle. It is worth mentioning that after completing a full cycle, the subsequent cycles of loading will incorporate strength and stiffness deterioration due to the history of plastic deformations as well as any damages to the grout/RC footing, which result in a change the bearing area below the base plate.

The moment-rotation relationships of the simulated connections were investigated, and a summary of the yielding moment, rotation and stiffness, as well as the moment and rotation at the ultimate points, is shown in Table 4.8. The same procedure outlined in Chapter 3 was used to identify the yielding points of the connections. The results showed that the positive and negative yielding moments, rotations and stiffnesses for each connection are approximately the same. The influence of the investigated parameters on the moment-relationship response is summarized in Table 4.9

Increasing the diameter of the anchor rods in connection pairs (S1-S2), (S6-S7), (S9-S10) and (S11-S12) led to an increase in the yielding moments. This is because the anchor rods are the first components to yield in the connections, as discussed in the mode of failure section. It also increased the base rotation at the onset of yielding and decreased the initial stiffness. On average, the increase in the anchor rods' diameter resulted in approximately a 24% increase in the ultimate moments. Additionally, connections with rigid base plates achieved a 27% increase in the base rotation angle at the ultimate moments, while the effect on the flexible base plate connections was less pronounced. These changes can be attributed to the flexible deformability achieved by the base plates with the increase in the anchor rods.

The effects of varying the base plate dimensions are more noticeable in the rigid base plate connections compared to the flexible ones, as can be seen in connections (S2-S3) and (S5-S6), respectively. The change in the yielding and ultimate response is almost negligible in (S2-S3), whereas the (S5-S6) connection pair showed approximately a 5% increase in the moment values, a 25% increase in the base rotation angle at the onset of yielding and a 10% increase in the base rotation angle at the ultimate moment.

Increasing the column size (e.g., W250, W310, or W360) had a significant impact on the yielding moment-rotation relationship. For example, changing the column sections from W250 to W310 and from W310 to W360 in (S3-S4) and (S7-S8), respectively, resulted in an approximate 45% increase in the yielding moments and a 32% decrease in the rotations at yielding. Additionally, the initial stiffnesses were doubled. Similarly, the ultimate moments experienced an average increase of 45%. However, in connection S8, the base rotation did not change significantly.

Similarly, increasing the thickness of the base plate in connection pairs (S4-S5), (S8-S9), (S13-S14) and (S15-S16) resulted in a decrease in the base rotation at yielding by 23%, 25%, 16% and 31%, respectively. It also increased the stiffness by 40%, 35%, 27% and 57%, respectively. However, there was a slight maximum increase of 8% in the yielding moments observed with the increase in the thickness of the base plate. Furthermore, increasing the thickness of the base plate decreased the base rotation angles by an average of 32%, due to the added rigidity provided by the thicker base plates. It is worth noting that the mentioned connection pairs comprised anchor rods aligned with the edges of the flanges. However, it was found that connections with anchor rods not aligned with the edges of the flanges reacted differently. For instance, in connections S19 and

S20, where the transverse spacing of anchor rods was decreased by 25 mm, and in connections S21 and S22, where the spacing was increased by 25 mm, increasing the base plate thickness led to a decrease in the yielding moments, ultimate moments, rotations at the ultimate point and initial stiffnesses.

Varying the level of axial loading had a significant impact on the moment-rotation response. Increasing the level of axial loading by 10% P_y led to, on average, 18% increase in the yielding and ultimate moments, 32% decrease in the base rotations at yielding and 52% increase in the initial stiffnesses of connections S11 to S16 compared to their counterparts, as outlined in Table 4.9. The level of the axial load, however, insignificantly affected the rotation angles at ultimate moments.

Using higher-grade steel for the base plate in connections S17 and S18 had almost no effect on the yielding and ultimate moments. However, the response to the use of higher-grade base plate steel depended on the type of base plate. In connection S17, which has a flexible base plate, there was a decrease in the rotation angles at yielding and ultimate. However, it maintained an 18% increase in the initial stiffness. On the other hand, connection S18, which comprises an intermediate base plate as classified previously, showed a 10% increase in the rotation angle at yielding. There was no change in the base rotation at ultimate, but a 7% decrease in initial stiffness was observed.

The impact of the transverse spacing between the anchor rods was more pronounced in connections comprising rigid base plates (S20 and S22) compared to intermediate base plates (S19 and S21). It is important to note that increasing or decreasing the spacing between the anchor rods had approximately the same effects on the base rotation at yielding and initial stiffness. Decreasing

the transverse spacing by 25 mm in connections S19 and S20 or increasing it by 25 mm in connections S21 and S22 increased the rotation angle at yielding and reduced the stiffness. It also resulted in a decrease in the yielding moments for the rigid base plate connections S20 and S22, while it had an insignificant effect on the yielding moments of the flexible base plate connections S19 and S21. At the ultimate moment, changing the spacing between the anchor rods had little effect on the moment and rotation of connections comprising intermediate base plates. However, connections with rigid base plates exhibited an 18% decrease in their ultimate moment values. Decreasing the transverse spacing in the rigid base plate connection pair (S5-S20) decreased the rotation angle at ultimate by 16%, while increasing the transverse spacing in the rigid base plate connection pair (S5-S22) increased the rotation angle at ultimate by 19%.

4.4.2.3 Ductility and energy dissipation capacity

Ductility is defined as the ability of a connection to undergo plastic deformations before failure. It plays a crucial role in ensuring structural safety and reducing the risk of brittle failures. Engineers can estimate the ductility using the ductility factor (DF), which is calculated as the ratio of the base rotation angle at failure (θ_u) to the base rotation angle at the onset of yielding (θ_y). The failure point is defined as the instant of maximum moment throughout the simulation if the connection experiences a loss of moment-carrying capacity, such as in rigid base plate connections. On the other hand, the failure point is defined by the peaks of the last cycle of loading in connections that do not experience a loss of moment-carrying capacity.

All connections demonstrated significant ductility, indicating their ability to undergo inelastic deformations before failure. The DF of the simulated connections and their failure mode for convenience, are shown in Table 4.10. The minimum DF value of three was observed in connection

S20, which had a rigid base plate and a 25 mm reduced transverse spacing between the anchor rods. On the other hand, connections S13 and S14, subjected to 30% P_y , exhibited the maximum DF value of eight. On average, the connections comprising flexible base plates had an average DF of four, while connections with rigid and intermediate base plates had average DF values of five and six, respectively. This can be attributed to the early yielding of connections with intermediate base plates, while not experiencing a loss of moment-carrying capacity until the end of the simulation.

The ductility of the simulated connections was influenced by the investigated parameters. Increasing the column size or the level of axial loading resulted in higher DFs. Conversely, increasing the diameter of the anchor rods, base plate thickness or dimensions had a negative impact on the DFs of the connections. Furthermore, connections that had anchor rods not aligned with the edges of the flanges exhibited a reduction in their DFs, with the reduction being more significant in connections with rigid base plates. The use of higher-grade steel for the base plate had a slight effect on the DFs. For example, it slightly increased the DF for the flexible base plate connection in the (S2-S17) pair, while it reduced the DF in the intermediate base plate connection as concluded from (S4-S18).

The evaluation of energy dissipation in steel column base connections is essential for ensuring seismic performance and reducing residual displacements. The energy dissipation capacity was determined by calculating the area enclosed within the first cycle per targeted rotation angle on the moment-rotation curve. The cumulative energy dissipation capacity, obtained by summing the energy dissipation capacity from zero up to the desired rotation angle, is plotted in Figure 4.39 for

connections S1 to S5, Figure 4.40 for connections S6 to S10, Figure 4.41 for connections S11 to S16 and Figure 4.42 for connections S17 to S22.

Investigating the energy dissipation response of the simulated connections reveals the following conclusions: the more flexible the base plate, the greater the energy the connection can dissipate. This is evident from the increase in cumulative dissipated energy with an increase in the anchor rods' diameter, a decrease in the base plate thickness and a lower level of axial loading. Moreover, increasing the column size in connection pairs (S3-S4) and (S7-S8) resulted in an 84% and 37% increase in cumulative dissipated energy, respectively. On the other hand, varying the base plate dimensions, using higher-grade steel for the base plate material, or changing the transverse spacing between the anchor rods had an insignificant impact (less than 10%) on the energy dissipation response. Additionally, the impact of these parameters depended on the type of base plate in the connection. For instance, increasing the base plate dimensions in connection S3 (flexible base plate) resulted in a 7% decrease in cumulative dissipated energy, while in connection S6 (rigid base plate), it led to a 10% increase. Similarly, using higher-grade steel in the flexible base plate connection S17 decreased the energy by 8%, while the intermediate base plate connection S18 gained an additional 5% cumulative energy dissipation capacity at the end of the simulation. Moreover, intermediate base plate connections (S19 and S21) benefited from a 9% increase in the cumulative energy dissipation capacity by decreasing the transverse spacing between the anchor rods by 25 mm. Conversely, the rigid base plate connection S20 experienced a 9% decrease in the cumulative energy dissipation capacity when the transverse spacing was decreased.

4.5 Summary and conclusions

Finite element models were developed using the ABAQUS CAE2020 (Dassault Systèmes, 2020) platform to simulate the cyclic response of exposed column base connections. The modeling approach, including assumptions and recommendations, was presented. The robustness of the modeling approach was ensured by including two connections from different research programs found in the literature, resulting in a total of four connections used for model validation purposes. A simulation matrix was then developed and executed to investigate the following factors' influence on the cyclic response of steel column base connections: anchor rods' diameter and transverse spacing, base plate thickness and dimensions, column section size, level of axial loading and the grade of steel used in the base plate. The results led to the following conclusions:

- 1- The developed models successfully replicated the cyclic response of the tested column base connections, accurately capturing moment capacity, strength deterioration and pinching behaviour.
- 2- The simulations demonstrated a high level of agreement with the tested four anchor rod connections. While the simulation of two anchor rod connections also showed good agreement, further improvement is expected with additional data to accurately model the grout material.
- 3- The models assumed elastic perfectly plastic behaviour for nuts and washers. However, the testing program revealed damage and plastic deformations, suggesting that defining the actual mechanical properties of nuts and washers would enhance the simulation's accuracy in capturing strength deterioration.

- 4- The simulated connections were categorized into three groups (rigid, flexible and intermediate base plate connections) based on their mode of failure and deformed shapes. The type of base plate significantly influenced moment-rotation relationships, ductility and energy dissipation capacity of the connections under varied parameters.
- 5- The simulated connections exhibited a flag-shaped hysteresis passing through five stages, which are crucial for modeling purposes in the structure-level simulation. (i.e., NRHA).
- 6- Increasing the anchor rods' diameter resulted in higher yielding and ultimate moments and increased energy dissipation capacity, but it reduced ductility.
- 7- Rigid base plate connections showed higher sensitivity to changes in base plate dimensions regarding moment-rotation relationships. Increasing base plate dimensions decreased the ductility factor but enhanced energy dissipation for rigid base plate connections.
- 8- Increasing the column section size improved moment-rotation relationships and increased both ductility and energy dissipation capacity.
- 9- Increasing base plate thickness increased the rigidity of the connections, enhancing initial stiffness but decreasing ductility and energy dissipation response.
- 10- Higher levels of axial loading were associated with a noticeable increase in moment capacity, initial stiffness and ductility. However, connections tended to dissipate less energy with increased axial loading.
- 11- The use of higher-grade steel for the base plate had insignificant effects on moment capacity, ductility and energy dissipation capacity. However, it increased initial stiffness by 18% for flexible base plate connections and decreased it by 7% for intermediate base plate connections.

12- Varying the transverse spacing between anchor rods had a more pronounced impact on rigid base plate connections. Misalignment of anchor rods with flange edges reduced ductility, and decreasing transverse spacing reduced energy dissipation capacity in rigid base plate connections but increased it in intermediate base plate connections.

Table 4.1: Mesh details

Part	Global mesh size (mm)	Elements minimum edge length (mm)	Location of the smallest edge length
Column	25	4.44	Web
Base Plate	12.5	1.00	Anchor rods' holes
Grout	12.5	4.44	Near the web location
RC Foundation	50	11.00	Region below the grout
Anchor rods	6.25	1.35	The embedded part in the RC
Nut	5.5	2.25	Along the diameter
Washer	5.5	2.00	Along the thickness

Table 4.2: Elastic-plastic steel material definition and properties

Part	E (GPa)	F_y (MPa)	Plastic strain At F_y	F_u (MPa)	Plastic strain at F_u
Steel rebars	200	400	0	401	0.2
Nut	200	400	0	401	0.2
Washer	200	400	0	401	0.2

Table 4.3: Combined hardening steel material definition and properties

Part	E (GPa)	F_{yo} (MPa)	C_l (MPa)	γ_l	Q_∞ (MPa)	b
Web	239	350.58	2082.99	11.09	101.13	4.44
Flange	206	322.41	2510.33	12.89	104.83	5.16
Base plate	187	410.13	2658.59	15.84	90.39	6.33
Anchor rods	198	286.04	3452.09	15	123.95	6

Table 4.4: CDP flow parameters

Parameter	Value
ψ	36°
e	0.1
f_{bol}/f_{co}	1.16
K	0.6667
μ	0.0

Table 4.5: Parametric simulation matrix

No	Connections	Column size	BPL dimension	AR D	BPL t	Axial loading % P_y	BPL F_y MPa	Variable
S1	W250-19x350x500-19	W250	350x500	19	19	20	250	AR D
S2	W250-19x350x500-25	W250	350x500	25	19	20	250	
S3	W250-19x400x550-25	W250	400x550	25	19	20	250	Co. Size
S4	W310-19x400x550-25	W310	400x550	25	19	20	250	
S5	W310-25x400x550-25	W310	400x550	25	25	20	250	BPL DIM
S6	W310-25x450x600-25	W310	450x600	25	25	20	250	
S7	W310-25x450x600-32	W310	450x600	32	25	20	250	Co. Size
S8	W360-25x450x600-32	W360	450x600	32	25	20	250	
S9	W360-32x450x600-32	W360	450x600	32	32	20	250	AR D
S10	W360-32x450x600-38	W360	450x600	38	32	20	250	
S11 (1)	W250-19x350x500-19	W250	350x500	19	19	30	250	Increasing % P_y with changed AR D
S12 (2)	W250-19x350x500-25	W250	350x500	25	19	30	250	
S13 (4)	W310-19x400x550-25	W310	400x550	25	19	30	250	Increasing % P_y with changed BPL t
S14 (5)	W310-25x400x550-25	W310	400x550	25	25	30	250	
S15 (4)	W310-19x400x550-25	W310	400x550	25	19	10	250	Decreasing % P_y with changed BPL t
S16 (5)	W310-25x400x550-25	W310	400x550	25	25	10	250	
S17 (2)	W250-19x350x500-25	W250	350x500	25	19	20	300	Using BPL Gr. 300
S18 (4)	W310-19x400x550-25	W310	400x550	25	19	20	300	
S19 (4)	W310-19x400x550-25	W310	400x550	25	19	20	250	Decreasing the spacing between AR 25 mm
S20 (5)	W310-25x400x550-25	W310	400x550	25	25	20	250	
S21 (4)	W310-19x400x550-25	W310	400x550	25	19	20	250	Increasing the spacing between AR 25 mm
S22 (5)	W310-25x400x550-25	W310	400x550	25	25	20	250	

- Connection notation is “Column size” – “base plate thickness x width x length” – “Anchor rods’ diameter”
- Numbers in brackets in the first column of the table refer to the corresponding connection from the first set.

Table 4.6: Simulation matrix materials

Material	E (GPa)	F_{yo} (MPa)	C_I (MPa)	γ_I	Q_∞ (MPa)	b
G40.12 - Web	200	350	1500	8.5	101.13	4.44
G40.12 - Flange	200	290	2300	11	104.83	5.16
A36 - Base plate	200	250	6895	25	172	2
A36 - Anchor rods	200	250	1883.5	12	123.95	6

Table 4.7: Summary of connections' mode of failure

No	Connection	Group			Mode of failure
		One	Two	Three	
S1	W250-19x350x500-19	×			Rigid base plate
S2	W250-19x350x500-25		×		Flexible base plate
S3	W250-19x400x550-25		×		Flexible base plate
S4	W310-19x400x550-25			×	Intermediate base plate
S5	W310-25x400x550-25	×			Rigid base plate
S6	W310-25x450x600-25	×			Rigid base plate
S7	W310-25x450x600-32			×	Intermediate base plate
S8	W360-25x450x600-32			×	Intermediate base plate
S9	W360-32x450x600-32	×			Rigid base plate
S10	W360-32x450x600-38			×	Intermediate base plate
S11 (1)	W250-19x350x500-19	×			Rigid base plate
S12 (2)	W250-19x350x500-25		×		Flexible base plate
S13 (4)	W310-19x400x550-25			×	Intermediate base plate
S14 (5)	W310-25x400x550-25	×			Rigid base plate
S15 (4)	W310-19x400x550-25			×	Intermediate base plate
S16 (5)	W310-25x400x550-25	×			Rigid base plate
S17 (2)	W250-19x350x500-25		×		Flexible base plate
S18 (4)	W310-19x400x550-25			×	Intermediate base plate
S19 (4)	W310-19x400x550-25			×	Intermediate base plate
S20 (5)	W310-25x400x550-25	×			Rigid base plate
S21 (4)	W310-19x400x550-25			×	Intermediate base plate
S22 (5)	W310-25x400x550-25	×			Rigid base plate

Table 4.8: Summary of connections' moment-rotation relationships

No	Connection	$M_y(+)$ (kN.m)	$\Theta_y(+)$ (% rad)	$k_y(+)$ (kN.m/rad)	$M_y(-)$ (kN.m)	$\Theta_y(-)$ (% rad)	$k_y(-)$ (kN.m/rad)	$M_u(+)$ (kN.m)	$\Theta_u(+)$ (% rad)	$M_u(-)$ (kN.m)	$\Theta_u(-)$ (% rad)
S1	W250-19x350x500-19	85.0	0.64	13231	-85.5	-0.65	13138	106.7	3.26	-106.2	-3.34
S2	W250-19x350x500-25	106.2	0.90	11814	-106.7	-0.90	11808	135.2	3.77	-134.2	-3.75
S3	W250-19x400x550-25	105.9	0.93	11374	-107.4	-0.98	10981	134.9	3.77	-133.9	-3.75
S4	W310-19x400x550-25	157.5	0.64	24723	-158.2	-0.63	25025	204.0	4.26	-202.2	-4.27
S5	W310-25x400x550-25	168.7	0.49	34619	-169.9	-0.49	34882	215.1	2.75	-214.3	-2.89
S6	W310-25x450x600-25	175.3	0.58	30351	-178.1	-0.62	28738	224.6	3.05	-224.4	-3.13
S7	W310-25x450x600-32	220.2	0.92	23805	-221.6	-0.91	24413	282.2	3.93	-280.6	-3.91
S8	W360-25x450x600-32	307.9	0.64	48276	-306.7	-0.63	48669	391.2	3.87	-390.4	-4.00
S9	W360-32x450x600-32	310.5	0.47	65915	-315.6	-0.48	65094	396.2	2.74	-395.1	-2.89
S10	W360-32x450x600-38	394.4	0.73	54318	-395.3	-0.74	53361	497.1	3.52	-496.8	-3.63
S11 (1)	W250-19x350x500-19	102.5	0.51	20098	-102.1	-0.51	19978	126.0	3.40	-126.0	-3.30
S12 (2)	W250-19x350x500-25	118.3	0.65	18315	-118.1	-0.63	18743	151.2	3.38	-152.0	-3.56
S13 (4)	W310-19x400x550-25	188.3	0.43	43630	-189.7	-0.49	38926	241.7	3.99	-243.4	-4.13
S14 (5)	W310-25x400x550-25	200.7	0.39	51893	-200.1	-0.38	52264	255.8	2.94	-255.3	-2.89
S15 (4)	W310-19x400x550-25	127.2	0.98	13038	-127.9	-0.98	13086	161.0	4.45	-161.3	-4.44
S16 (5)	W310-25x400x550-25	138.5	0.68	20320	-138.2	-0.67	20668	176.9	3.23	-175.6	-2.42
S17 (2)	W250-19x350x500-25	107.4	0.77	13927	-108.0	-0.77	13988	135.9	3.29	-136.7	-3.31
S18 (4)	W310-19x400x550-25	160.1	0.67	23865	-163.5	-0.73	22521	204.1	4.26	-206.0	-4.27
S19 (4)	W310-19x400x550-25	163.6	0.71	23183	-166.6	-0.74	22482	209.9	4.24	-212.0	-4.23
S20 (5)	W310-25x400x550-25	140.2	0.70	20097	-139.2	-0.67	20782	175.2	2.38	-173.0	-2.38
S21 (4)	W310-19x400x550-25	156.9	0.73	21544	-158.7	-0.74	21433	199.4	4.27	-200.4	-4.27
S22 (5)	W310-25x400x550-25	142.2	0.83	17115	-141.3	-0.80	17723	179.2	3.35	-176.6	-3.37

Table 4.9: Comparison of connections' moment-rotation relationships results

Pair	Investigated parameter	M_y (%)	Θ_y (%)	k_y (%)	M_u (%)	Θ_u (%)
(S1-S2)	Increasing anchor rods' diameter	25	39	-10	27	14
(S6-S7)	Increasing anchor rods' diameter	25	53	-18	25	27
(S9-S10)	Increasing anchor rods' diameter	26	53	-18	26	27
(S11-S12)	Increasing anchor rods' diameter	16	25	-8	20	4
(S2-S3)	Increasing base plate dimensions	0	6	-5	0	0
(S5-S6)	Increasing base plate dimensions	4	23	-15	5	10
(S3-S4)	Increasing column size	48	-33	123	51	13
(S7-S8)	Increasing column size	39	-31	101	39	0
(S4-S5)	Increasing base plate thickness	7	-23	40	6	-34
(S8-S9)	Increasing base plate thickness	2	-25	35	1	-28
(S13-S14)	Increasing base plate thickness	6	-16	27	5	-28
(S15-S16)	Increasing base plate thickness	8	-31	57	9	-37
(S19-S20)	Increasing base plate thickness	-15	-5	-10	-17	-44
(S21-S22)	Increasing base plate thickness	-10	11	-19	-11	-21
(S1-S11)	Increasing axial load by 10% P_y	20	-21	52	18	2
(S2-S12)	Increasing axial load by 10% P_y	11	-29	57	13	-8
(S4-S13)	Increasing axial load by 10% P_y	20	-28	66	19	-5
(S5-S14)	Increasing axial load by 10% P_y	18	-21	50	19	3
(S4-S15)	Decreasing axial load by 10% P_y	-19	54	-47	-21	4
(S5-S16)	Decreasing axial load by 10% P_y	-18	39	-41	-18	0
(S2-S17)	Using base plate Gr. 300	1	-14	18	1	-12
(S4-S18)	Using base plate Gr. 300	3	10	-7	1	0
(S4-S19)	Decreasing anchor rods' spacing by 25 mm	5	14	-8	4	-1
(S5-S20)	Decreasing anchor rods' spacing by 25 mm	-17	40	-41	-19	-16
(S4-S21)	Increasing anchor rods' spacing by 25 mm	0	16	-14	-2	0
(S5-S22)	Increasing anchor rods' spacing by 25 mm	-16	67	-30	-17	19

Table 4.10: Ductility of the simulated connections along with their failure modes

No	Connection	Mode of failure	DF
S1	W250-19x350x500-19	Rigid base plate	5
S2	W250-19x350x500-25	Flexible base plate	4
S3	W250-19x400x550-25	Flexible base plate	4
S4	W310-19x400x550-25	Intermediate base plate	7
S5	W310-25x400x550-25	Rigid base plate	6
S6	W310-25x450x600-25	Rigid base plate	5
S7	W310-25x450x600-32	Intermediate base plate	4
S8	W360-25x450x600-32	Intermediate base plate	6
S9	W360-32x450x600-32	Rigid base plate	6
S10	W360-32x450x600-38	Intermediate base plate	5
S11 (1)	W250-19x350x500-19	Rigid base plate	6
S12 (2)	W250-19x350x500-25	Flexible base plate	5
S13 (4)	W310-19x400x550-25	Intermediate base plate	8
S14 (5)	W310-25x400x550-25	Rigid base plate	8
S15 (4)	W310-19x400x550-25	Intermediate base plate	5
S16 (5)	W310-25x400x550-25	Rigid base plate	4
S17 (2)	W250-19x350x500-25	Flexible base plate	4
S18 (4)	W310-19x400x550-25	Intermediate base plate	6
S19 (4)	W310-19x400x550-25	Intermediate base plate	6
S20 (5)	W310-25x400x550-25	Rigid base plate	3
S21 (4)	W310-19x400x550-25	Intermediate base plate	6
S22 (5)	W310-25x400x550-25	Rigid base plate	4

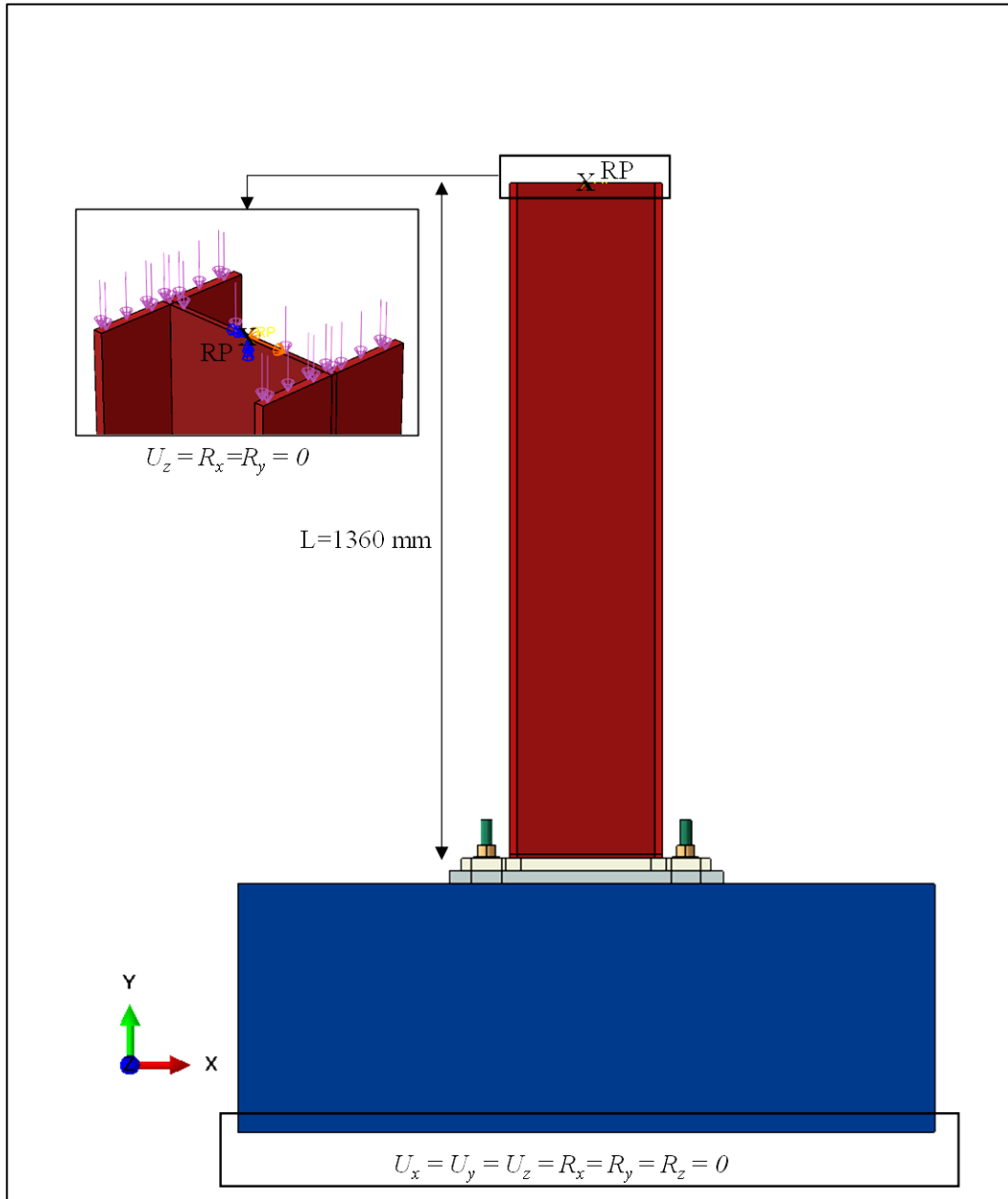


Figure 4.2: Boundary conditions

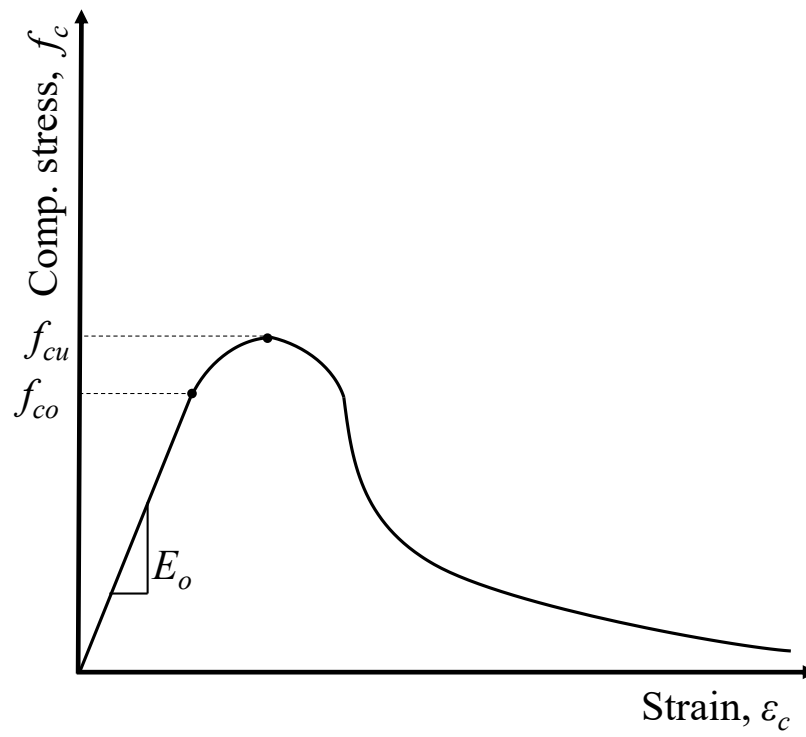


Figure 4.3: CDP model compressive relationship

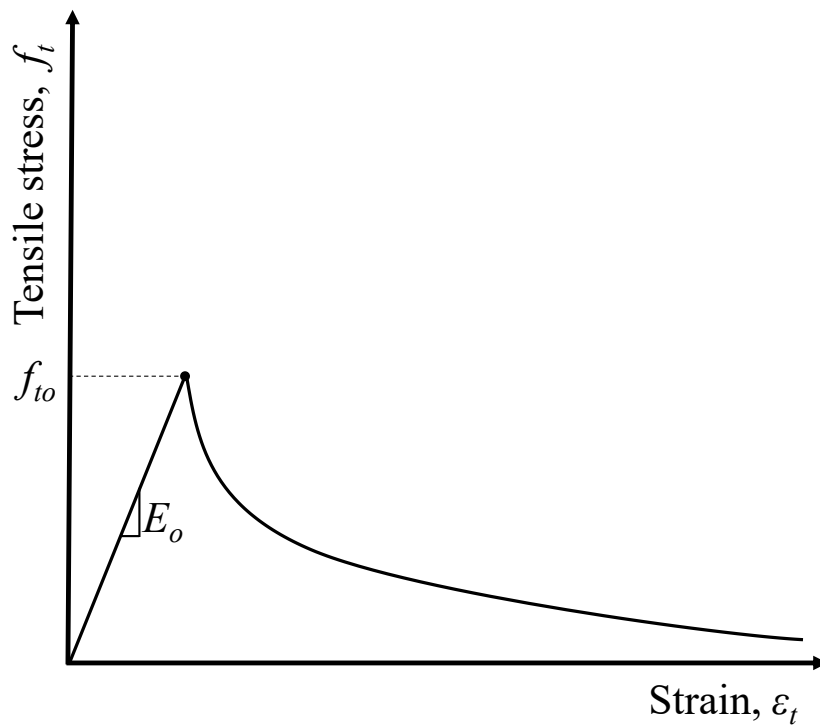


Figure 4.4: CDP model tensile relationship

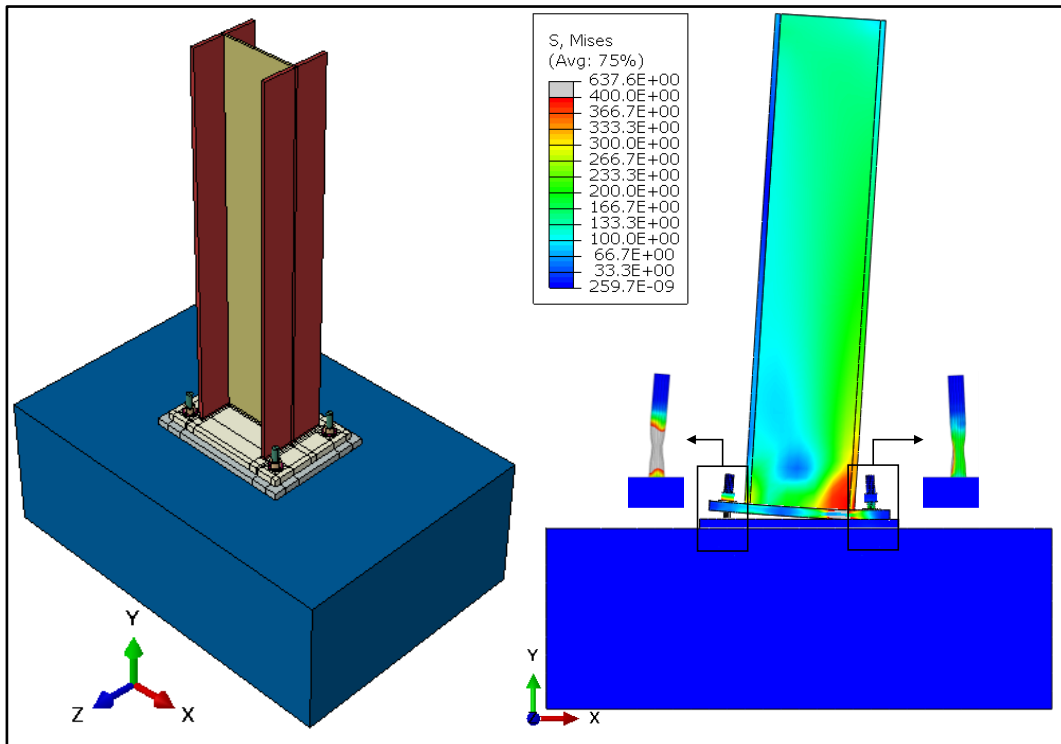


Figure 4.5: Specimen 4-AR-U and its deformed shape



(a)



(b)

Figure 4.6: 4-AR-U base connection deformation, (a) Test and (b) FE model

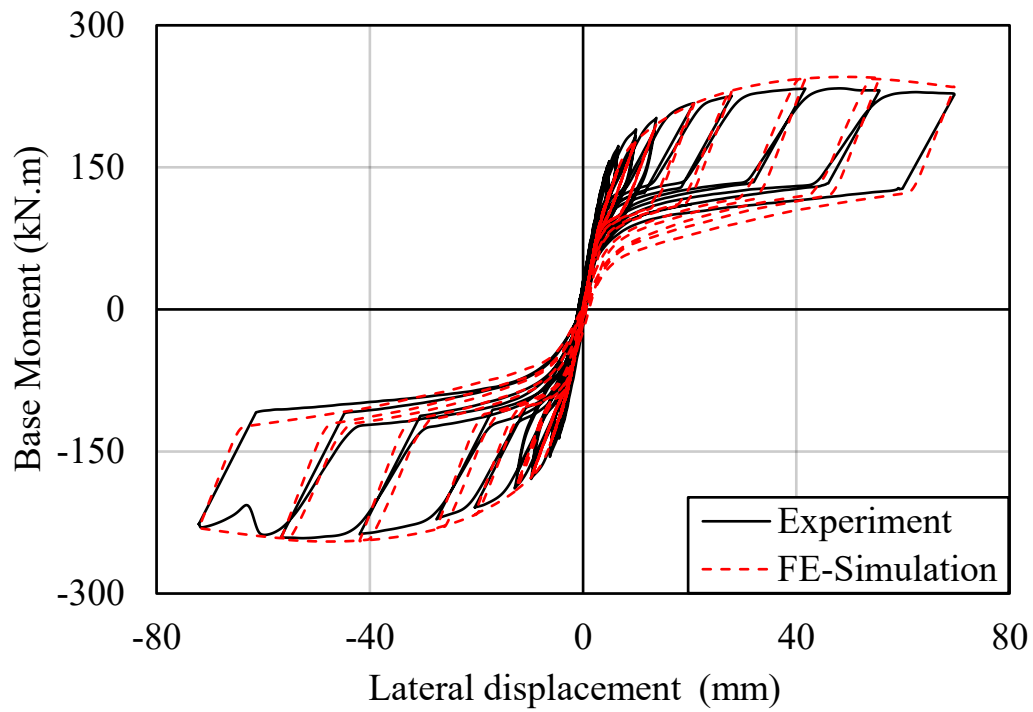


Figure 4.7: Moment-displacement relation for FE-model validation, 4-AR-U specimen

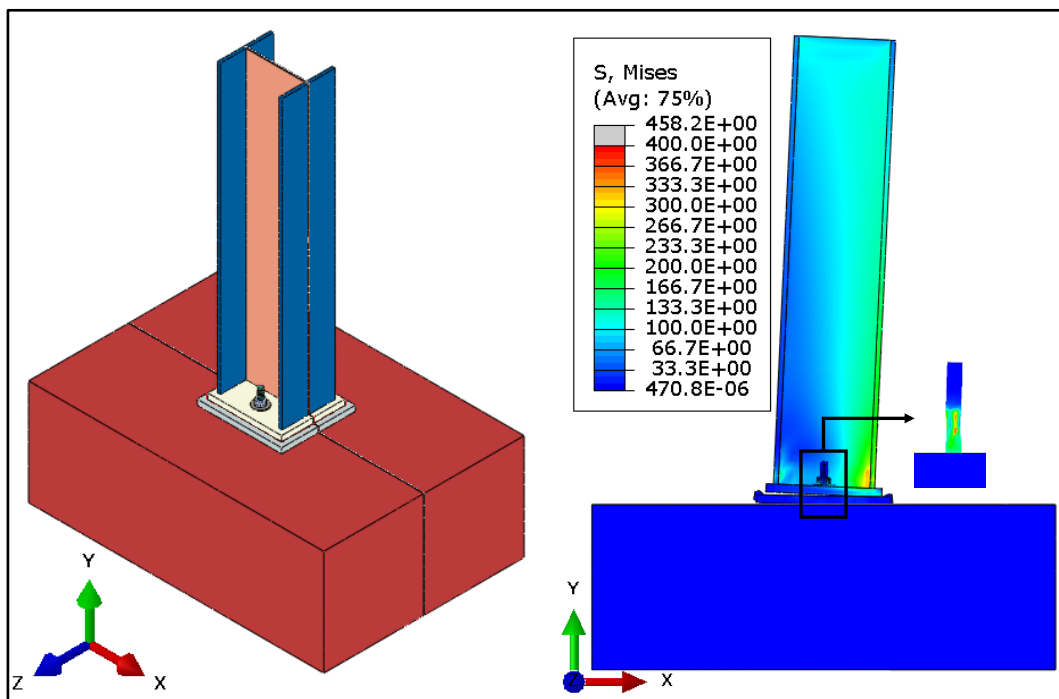
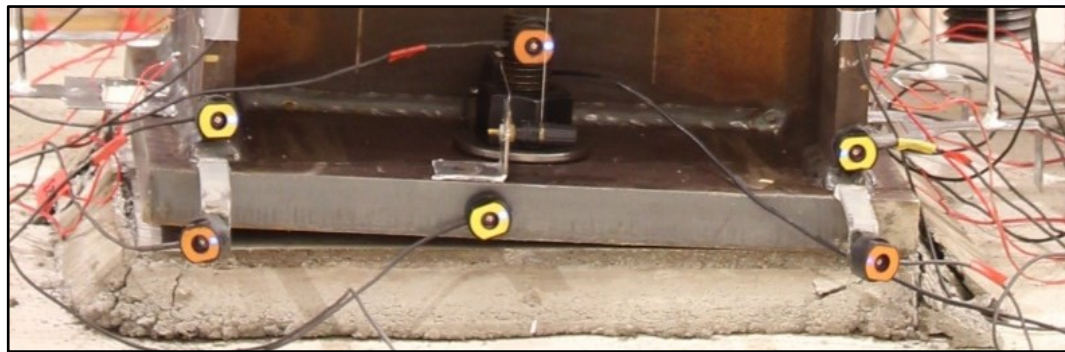
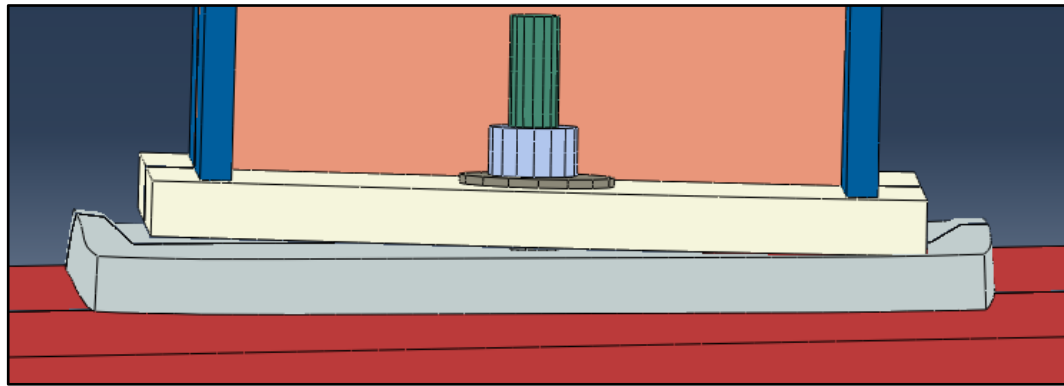


Figure 4.8: Specimen 2-AR-C and its deformed shape



(a)



(b)

Figure 4.9: 2-AR-C base connection deformation, (a) Test and (b) FE model

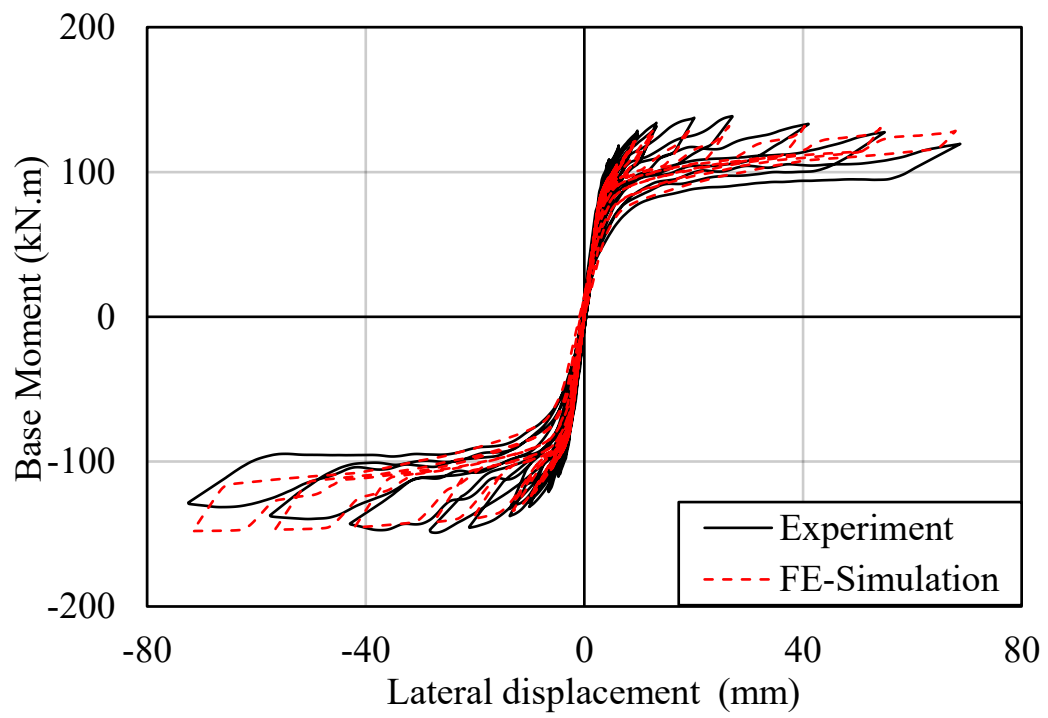


Figure 4.10: Moment-displacement relation for FE-model validation, 2-AR-C specimen

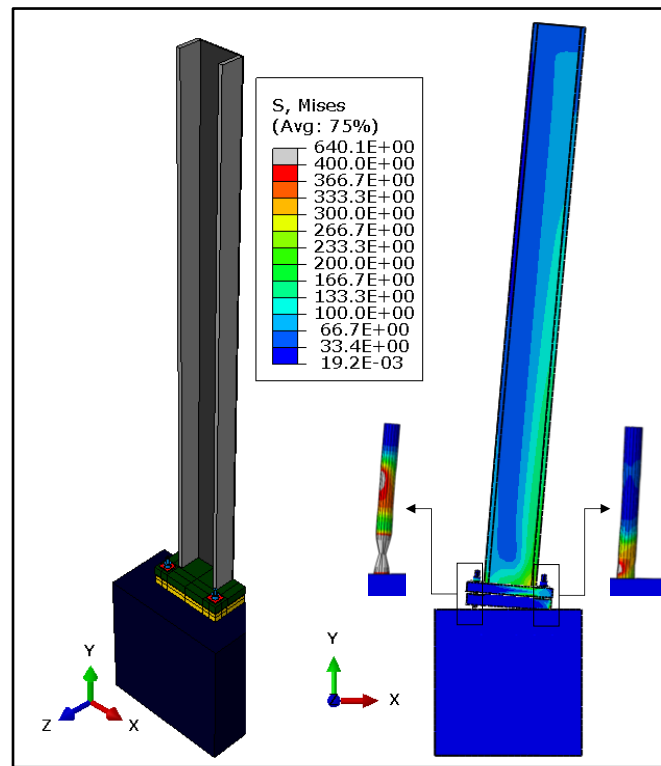


Figure 4.11: Specimen No.4 FE model (Gomez, 2010) and its deformed shape

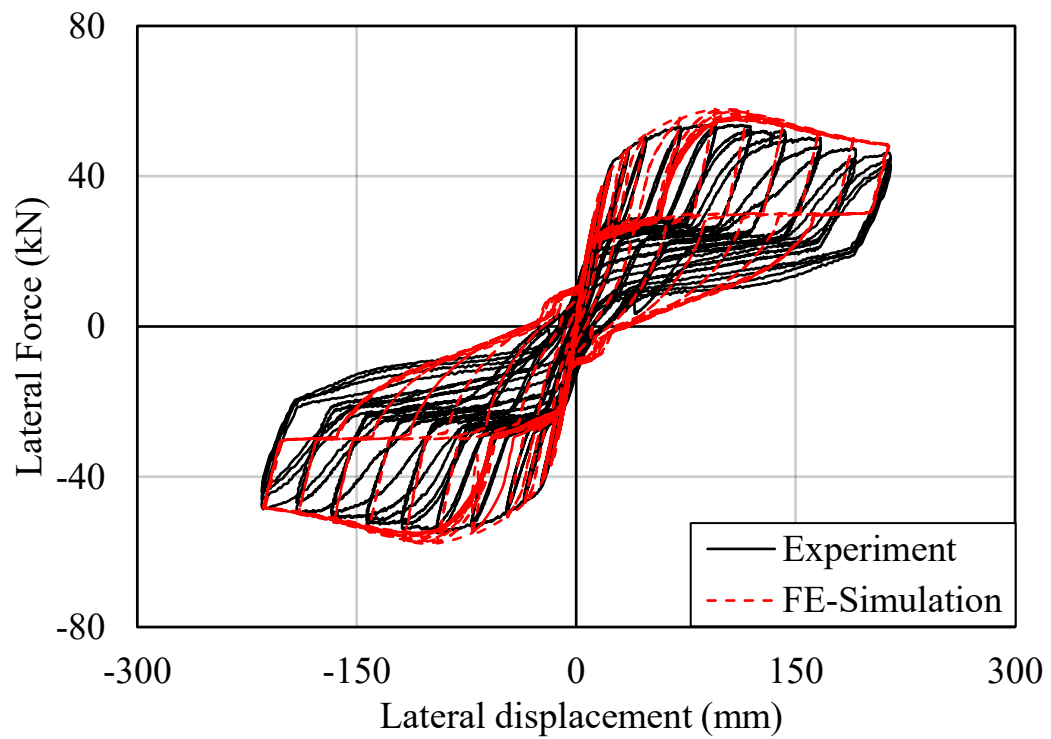


Figure 4.12: Moment-rotation relation for FE-model validation, specimen No.4 (Gomez, 2010)

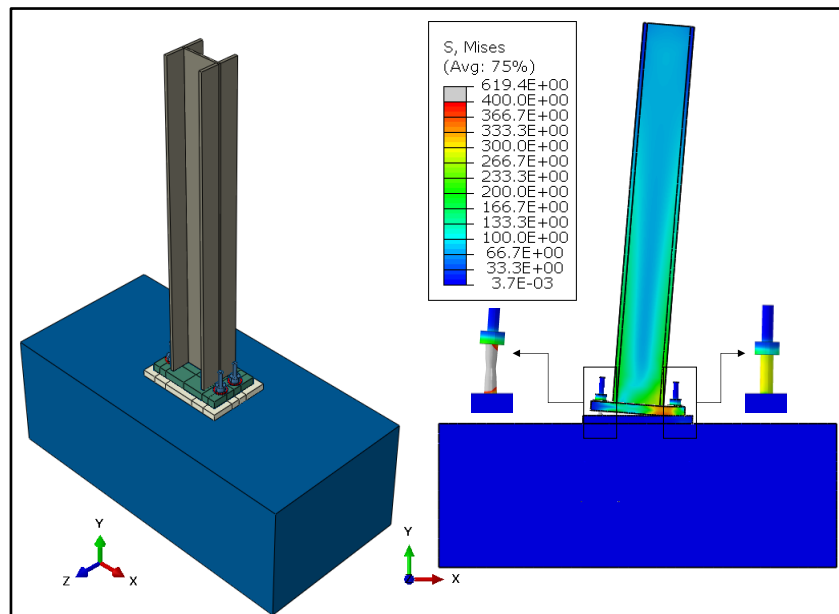


Figure 4.13: Specimen 8F FE model (Picard and Beaulieu, 1985) and its deformed shape

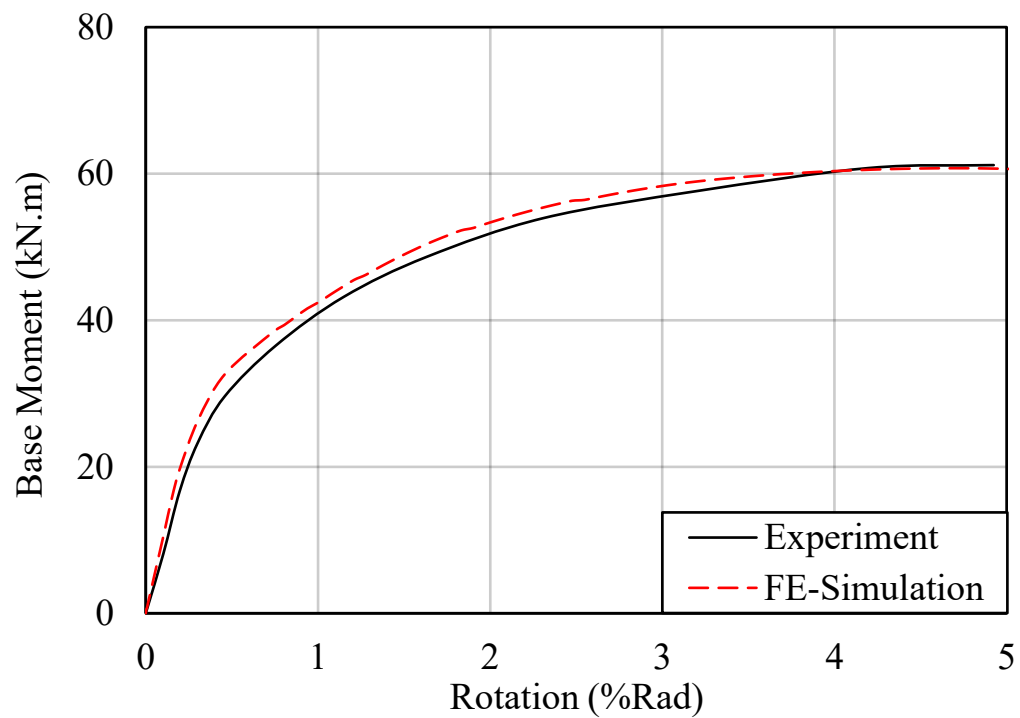
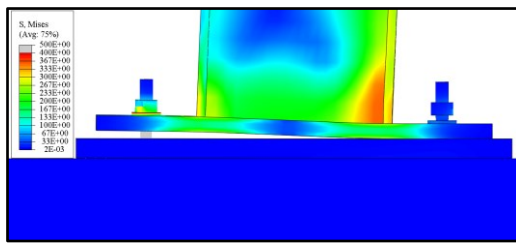
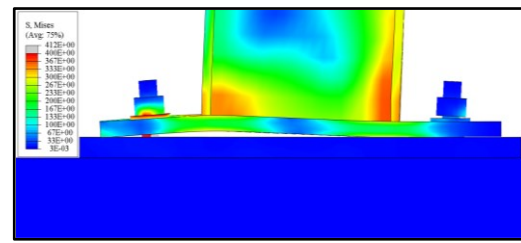


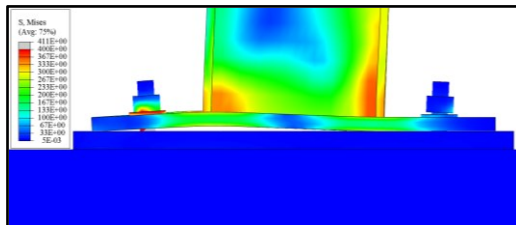
Figure 4.14: Moment-rotation relation for FE-model validation, specimen 8F (Picard and Beaulieu, 1985)



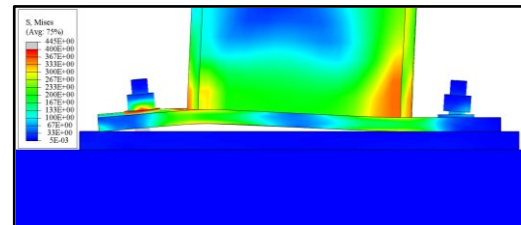
S1-W250-19x350x500-19



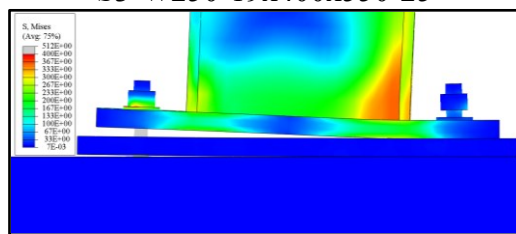
S2-W250-19x350x500-25



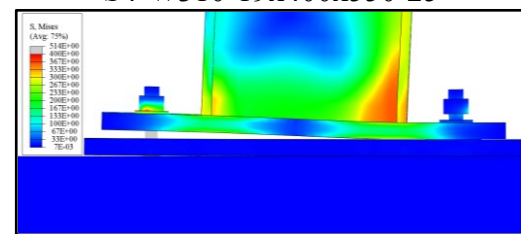
S3-W250-19x400x550-25



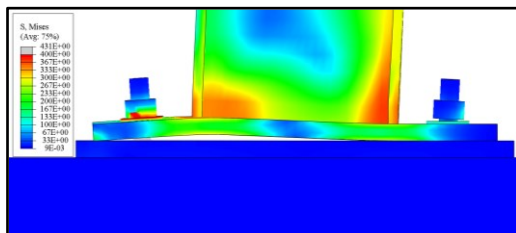
S4-W310-19x400x550-25



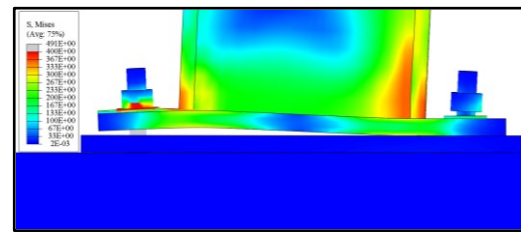
S5-W310-25x400x550-25



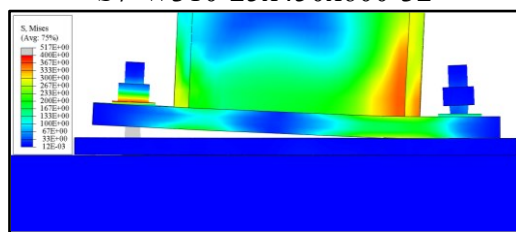
S6-W310-25x450x600-25



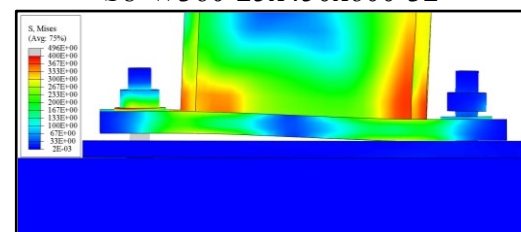
S7-W310-25x450x600-32



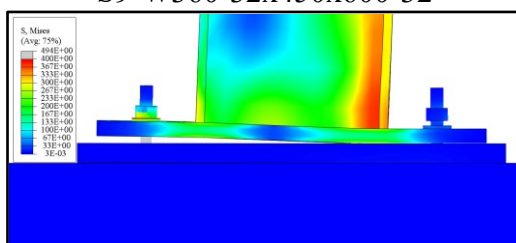
S8-W360-25x450x600-32



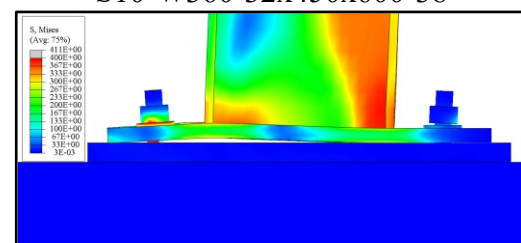
S9-W360-32x450x600-32



S10-W360-32x450x600-38



S11-S1-W250-19x350x500-19-30%



S12-S2-W250-19x350x500-25-30%

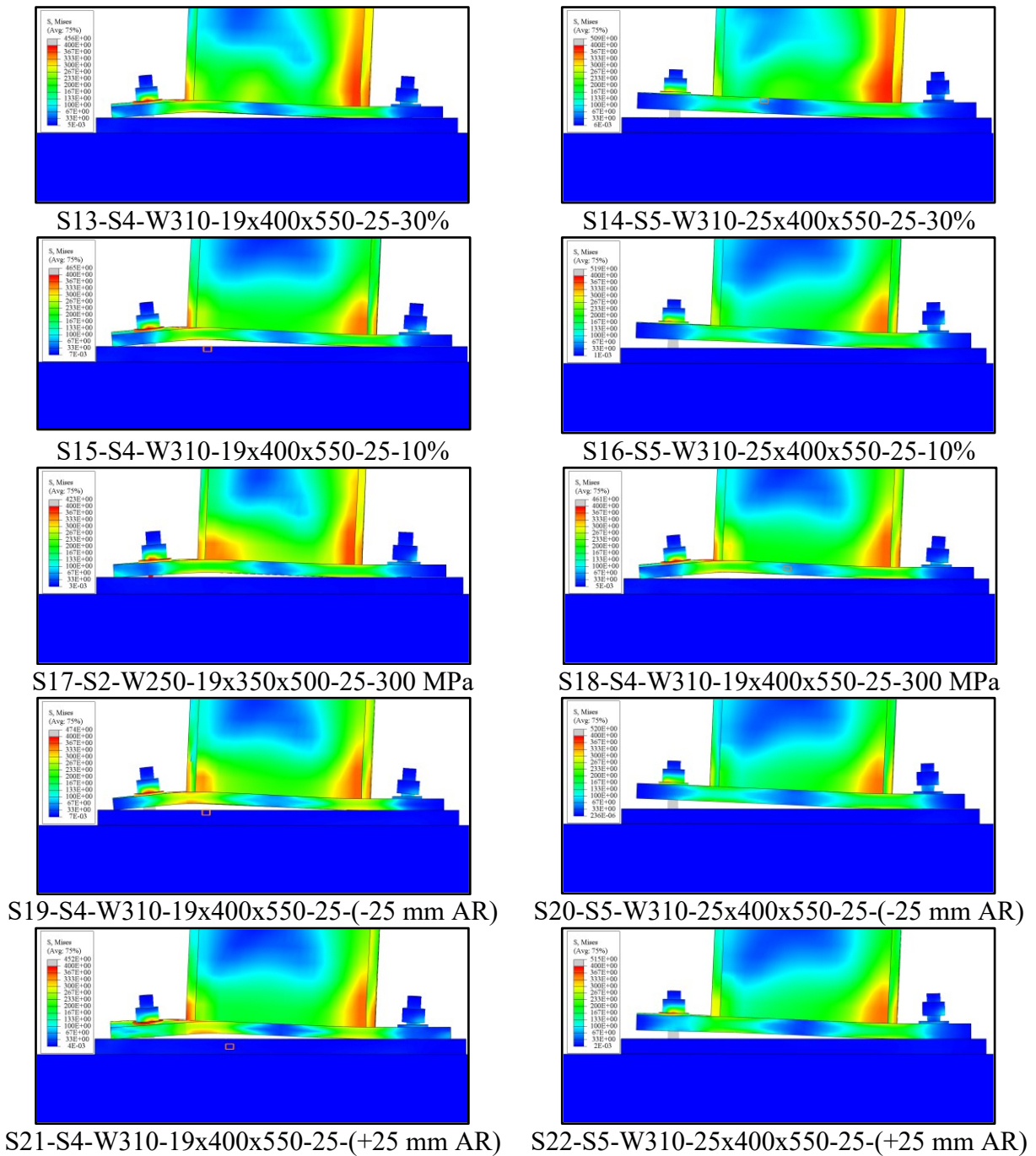
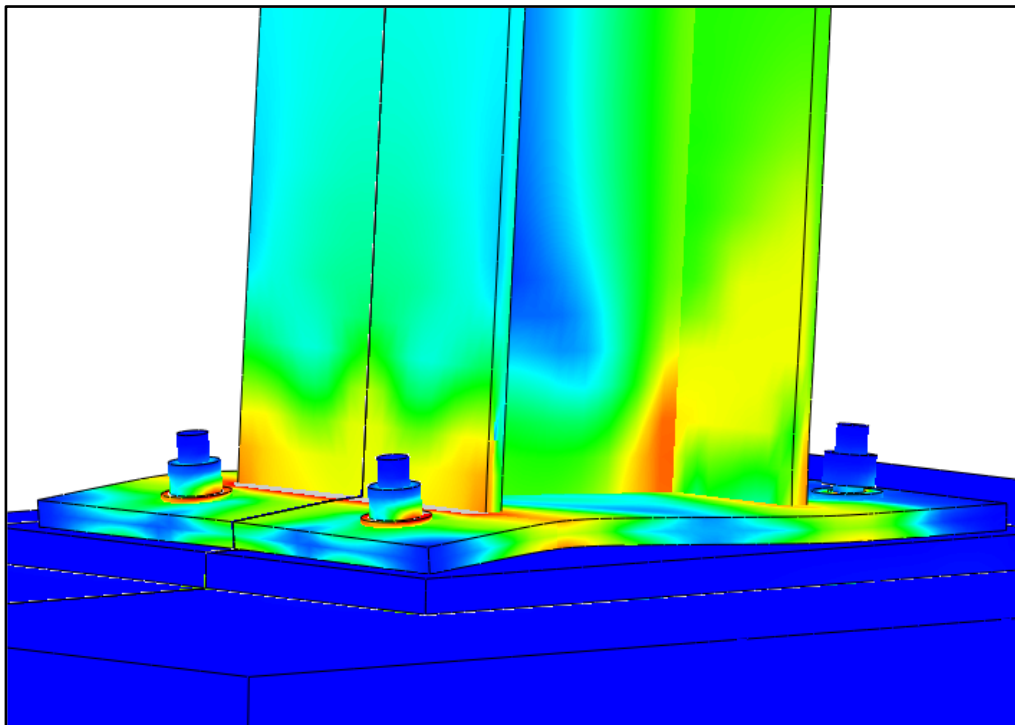
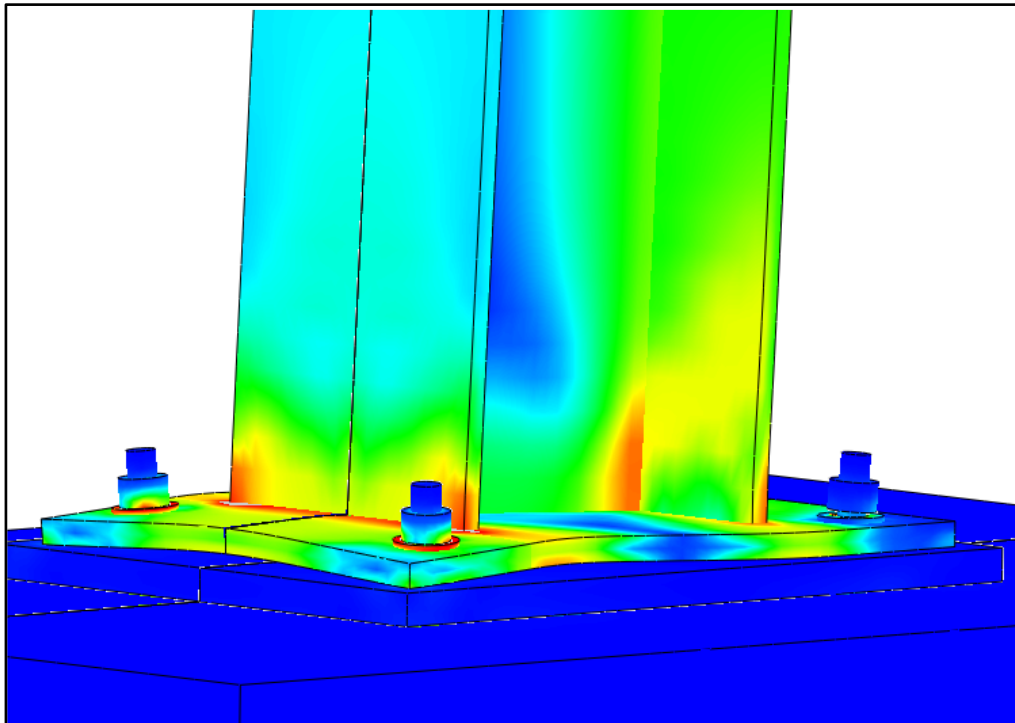


Figure 4.15: Deformed shape of the connections at the first peak of the last cycle of simulation

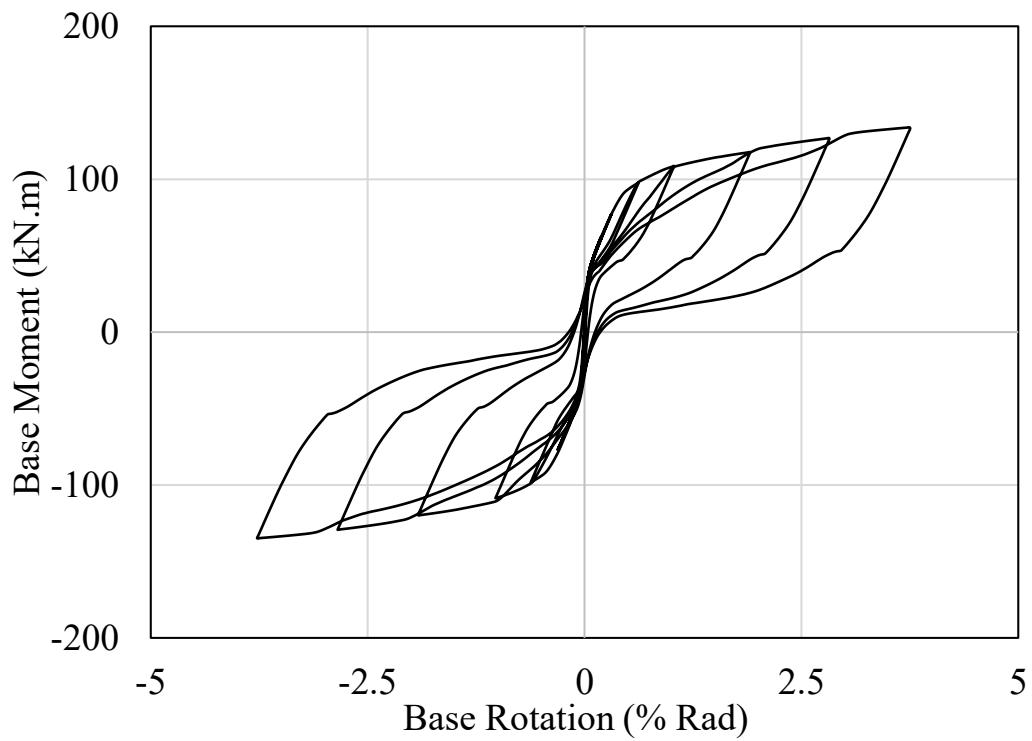
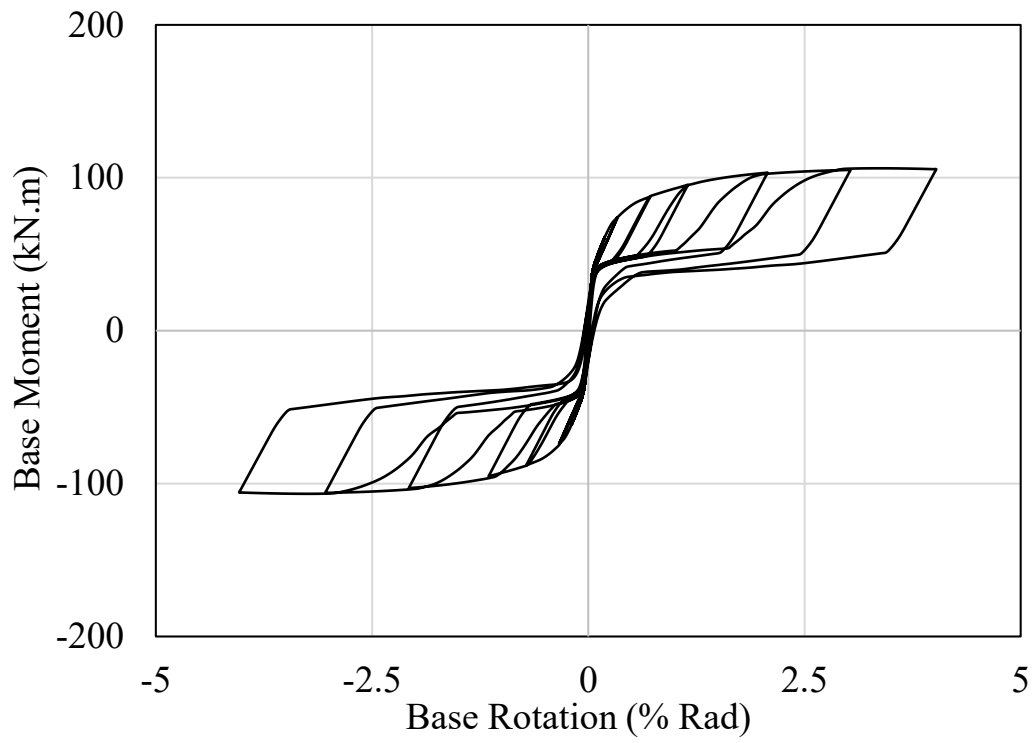


(a)



(b)

Figure 4.16: Effect of transverse spacing on the deformability of the base plate, (a) S19 and (b) S21



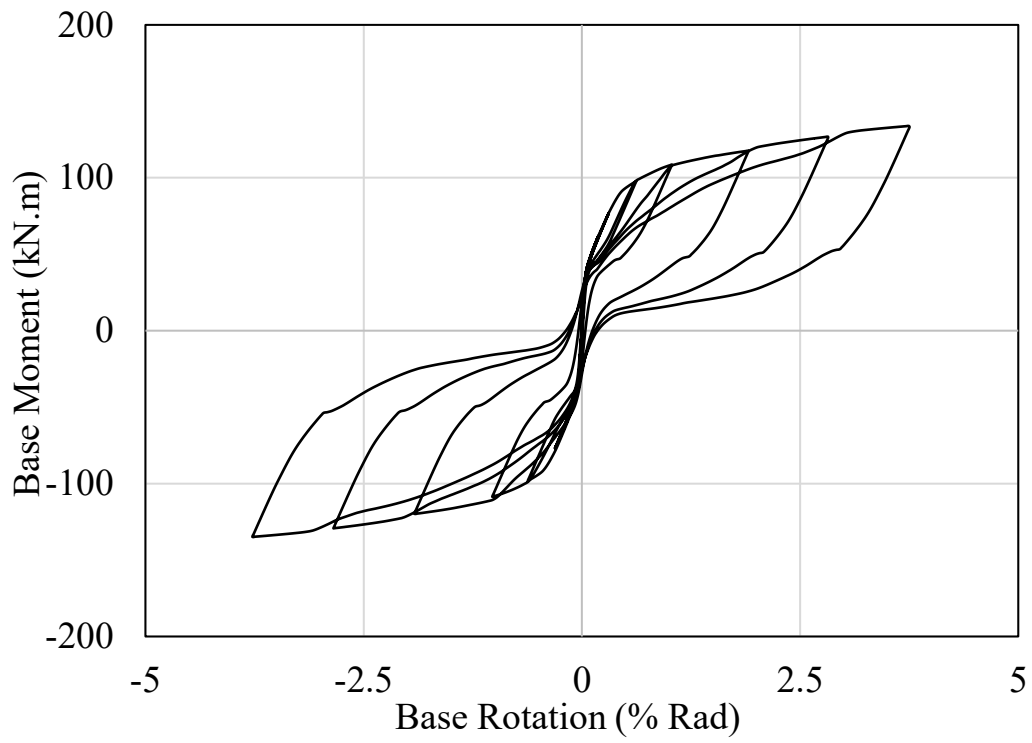


Figure 4.19: Moment-rotation relationship S3-W250-19x400x550-25

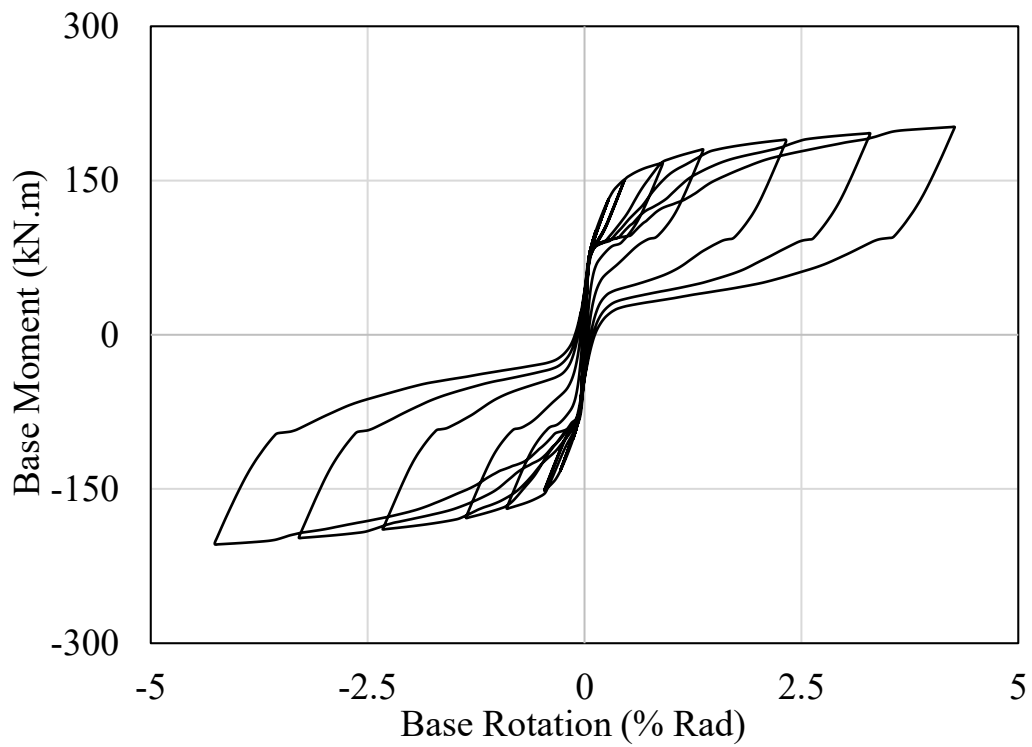


Figure 4.20: Moment-rotation relationship S4-W310-19x400x550-25

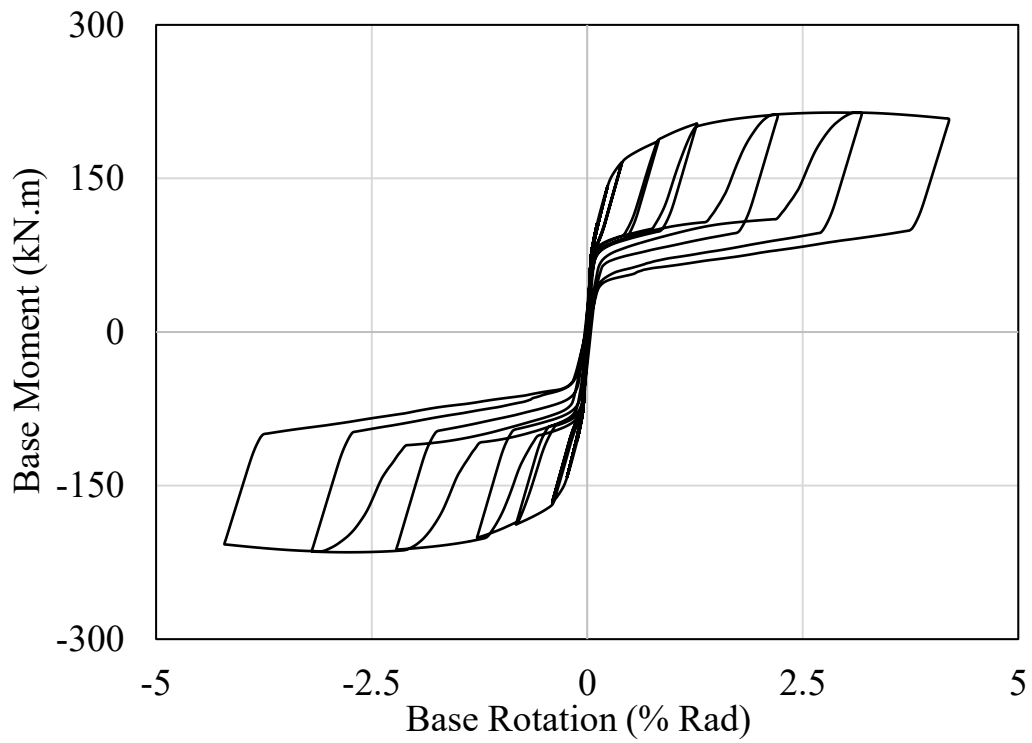


Figure 4.21: Moment-rotation relationship S5-W310-25x400x550-25

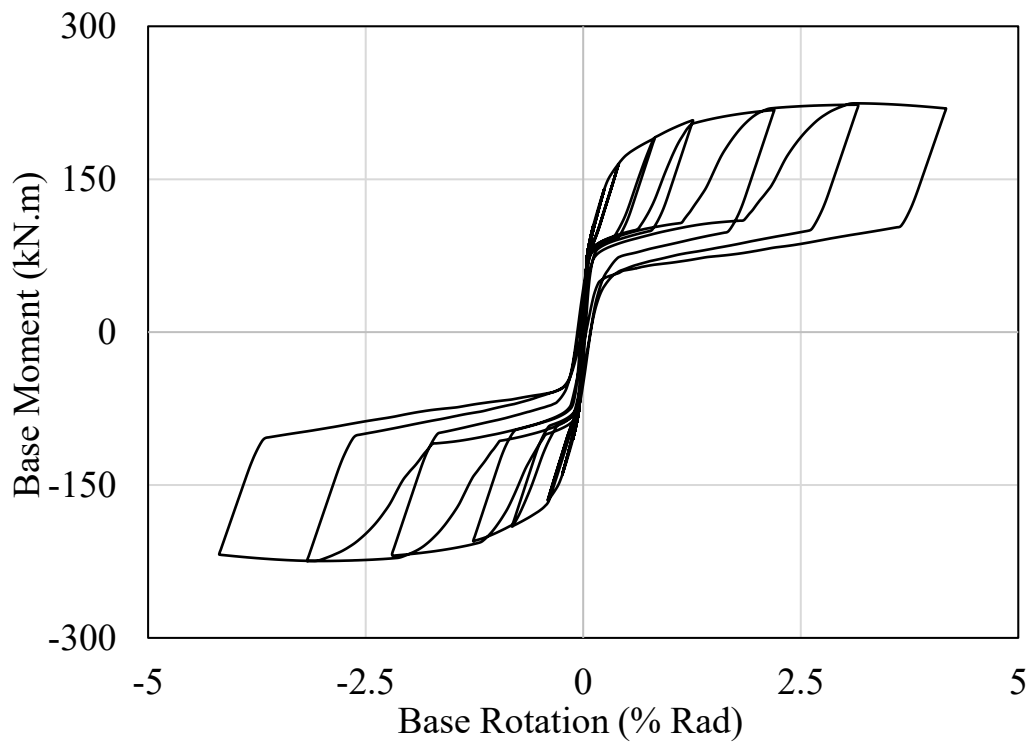


Figure 4.22: Moment-rotation relationship S6-W310-25x450x600-25

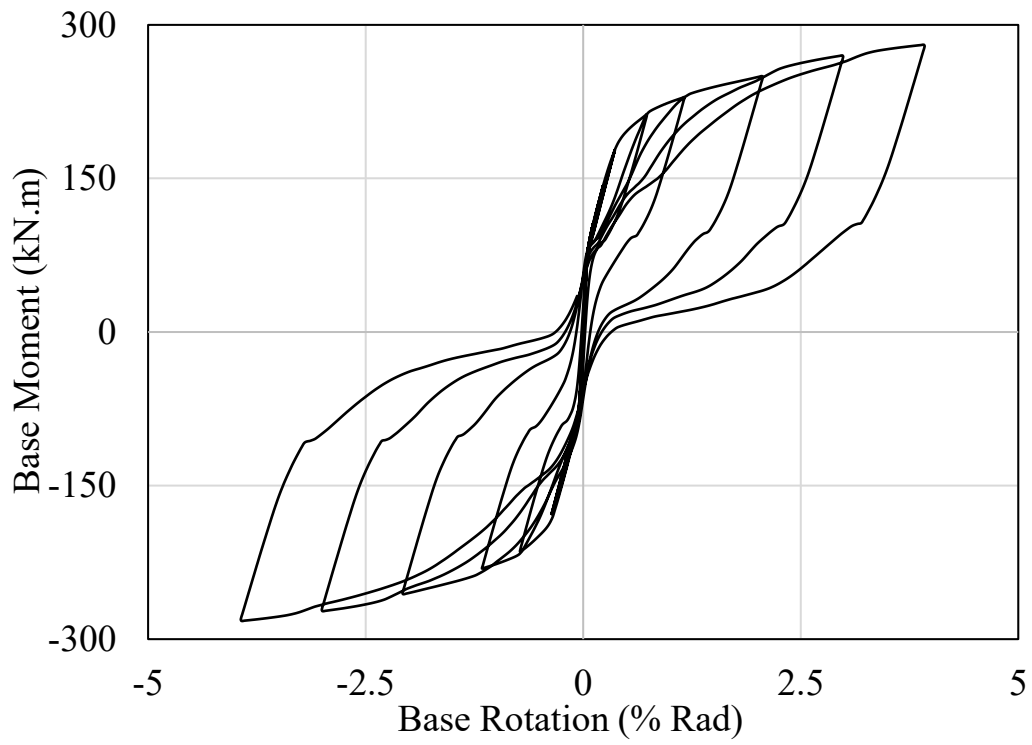


Figure 4.23: Moment-rotation relationship S7-W310-25x450x600-32

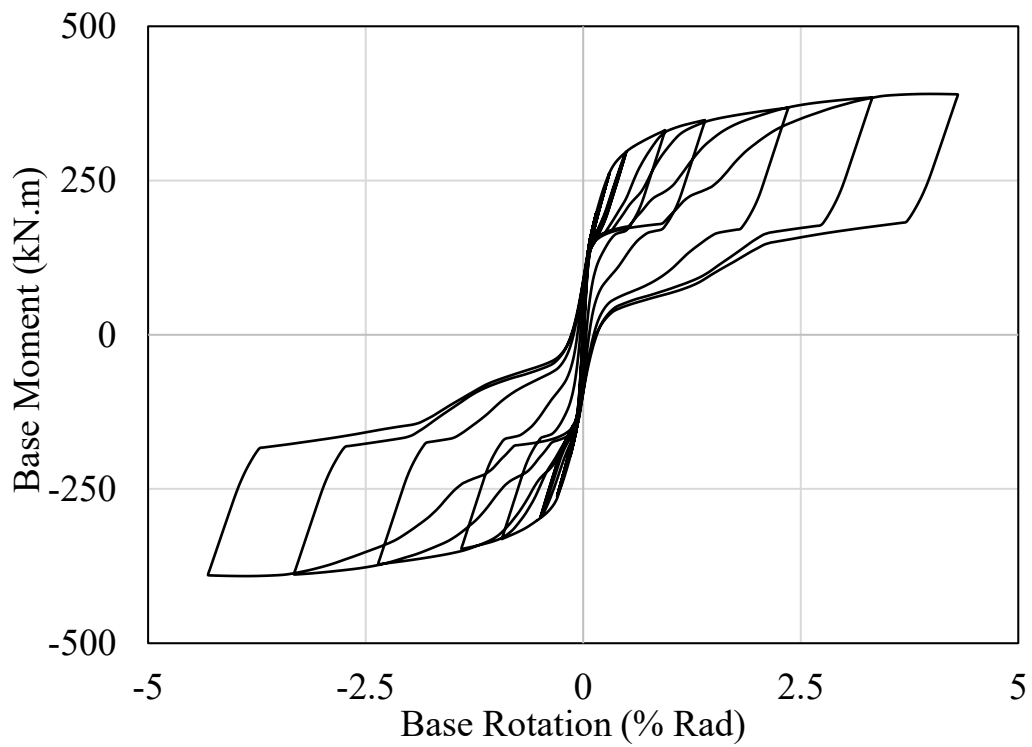


Figure 4.24: Moment-rotation relationship S8-W360-25x450x600-32

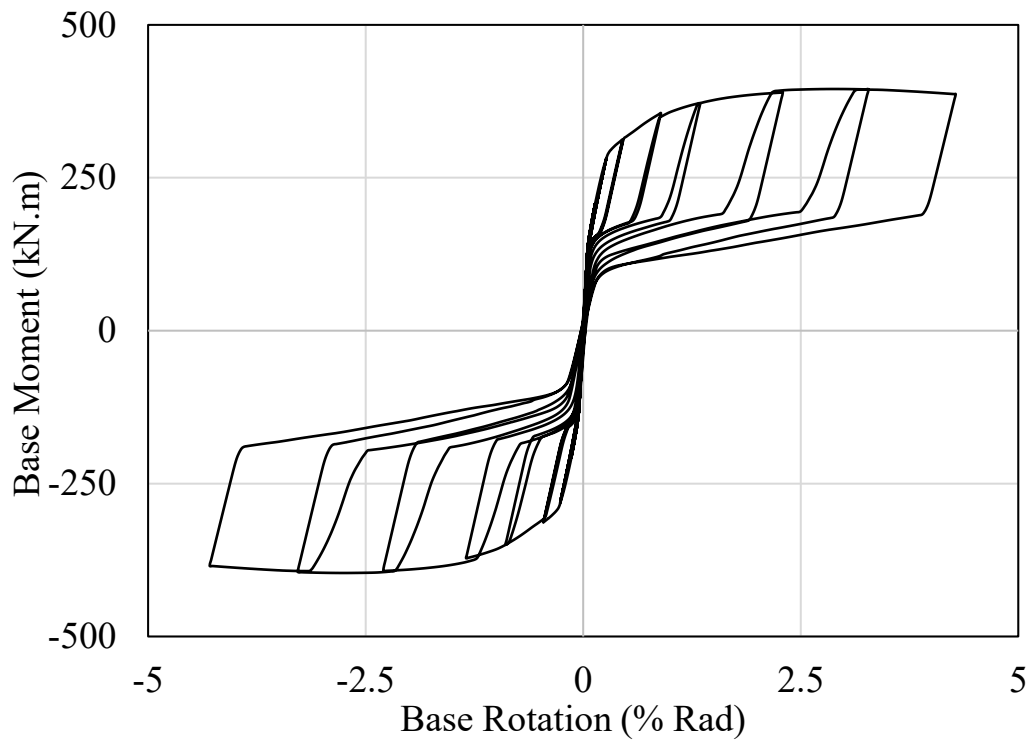


Figure 4.25: Moment-rotation relationship S9-W360-32x450x600-32

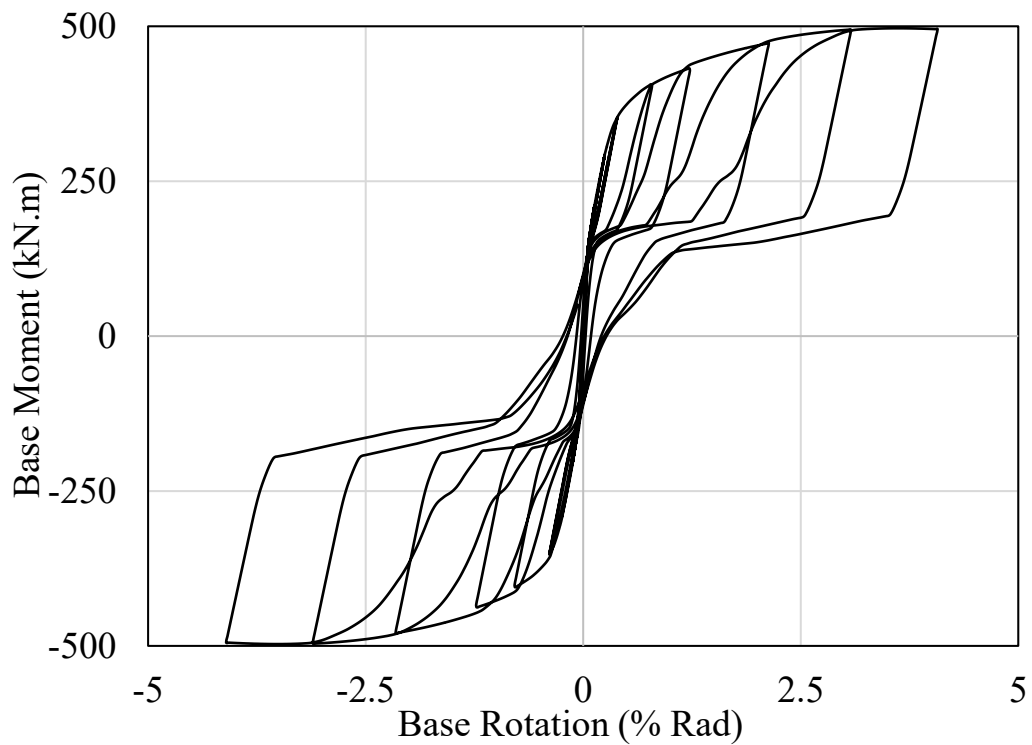


Figure 4.26: Moment-rotation relationship S10-W360-32x450x600-38

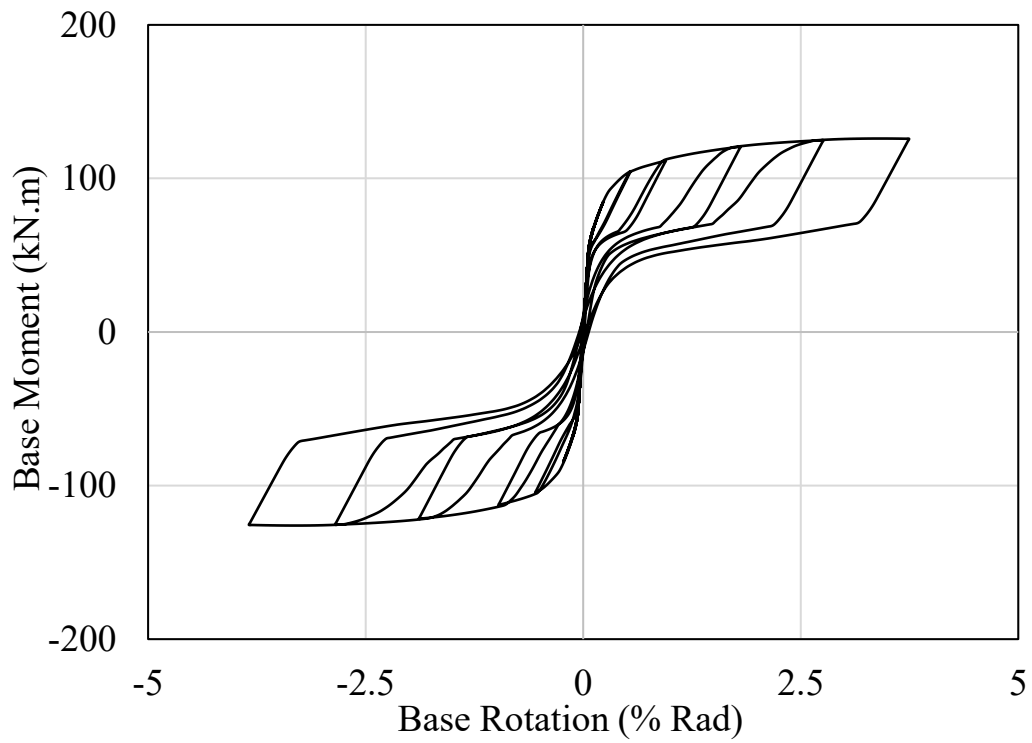


Figure 4.27: Moment-rotation relationship S11-S1-W250-19x350x500-19-30%

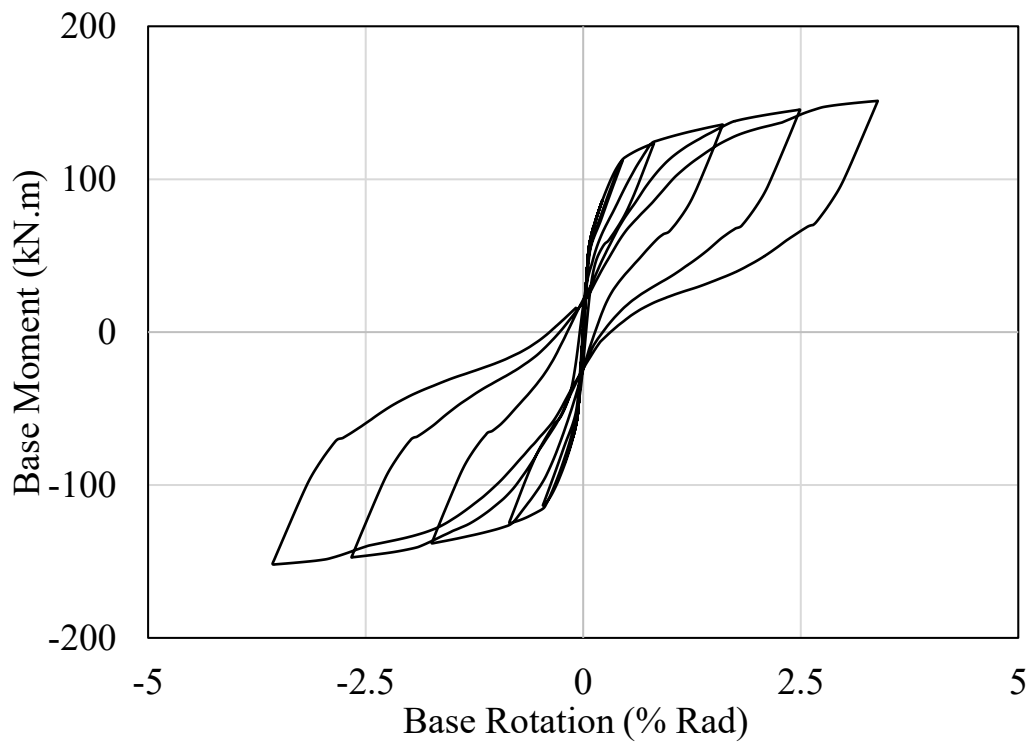


Figure 4.28: Moment-rotation relationship S12-S2-W250-19x350x500-25-30%

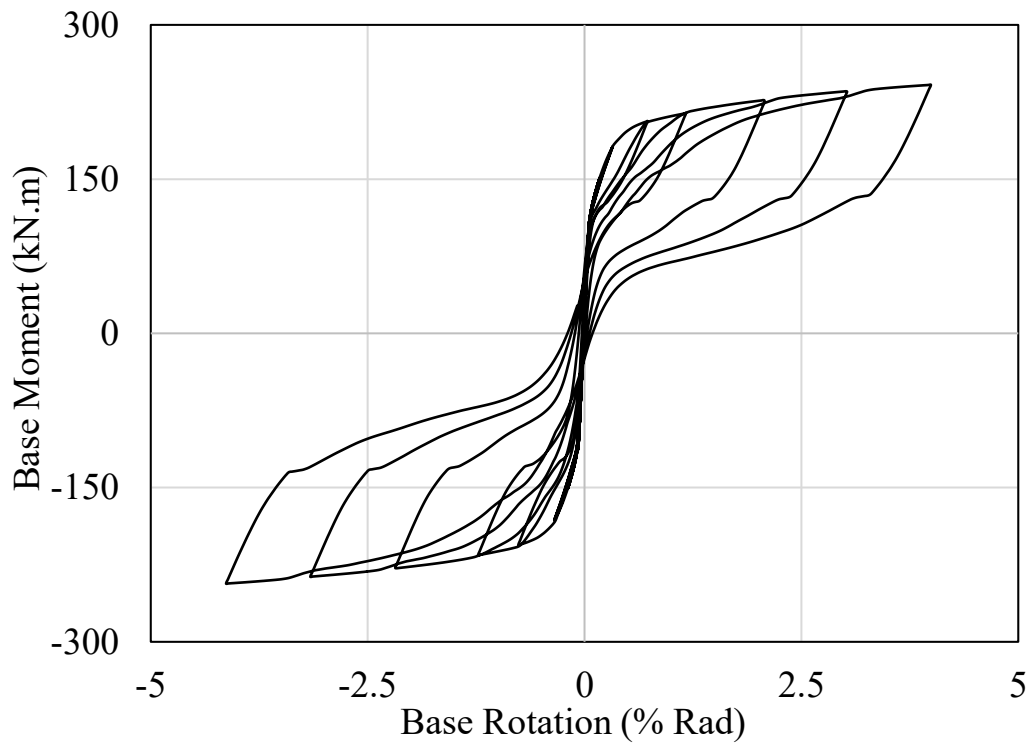


Figure 4.29: Moment-rotation relationship S13-S4-W310-19x400x550-25-30%

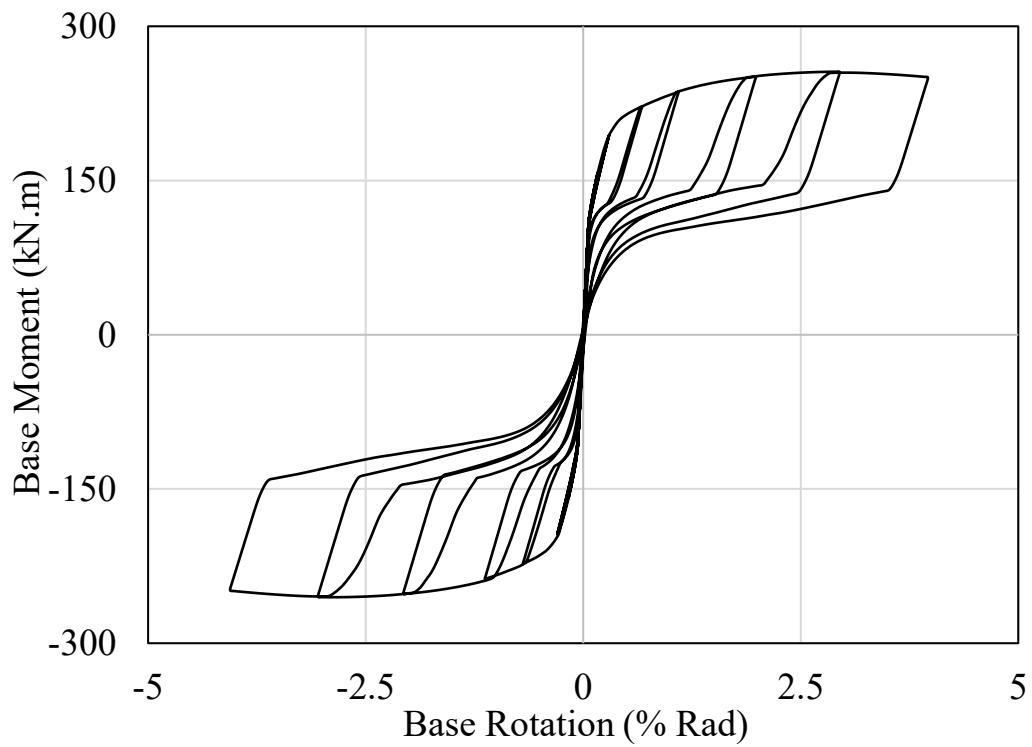


Figure 4.30: Moment-rotation relationship S14-S5-W310-25x400x550-25-30%

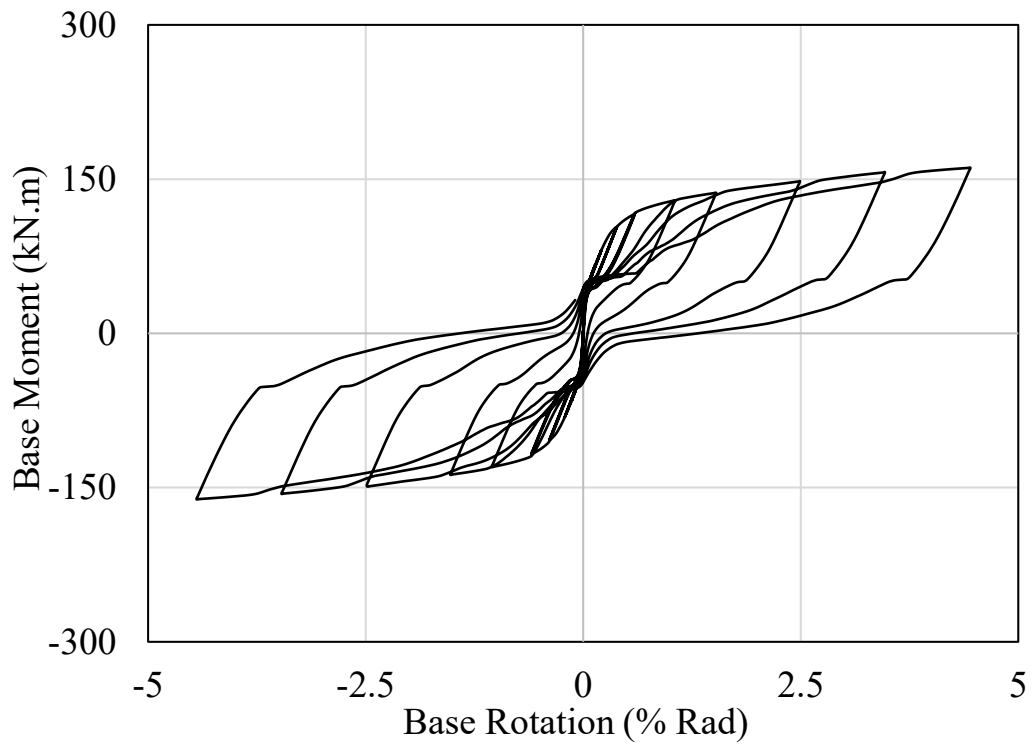


Figure 4.31: Moment-rotation relationship S15-S4-W310-19x400x550-25-10%

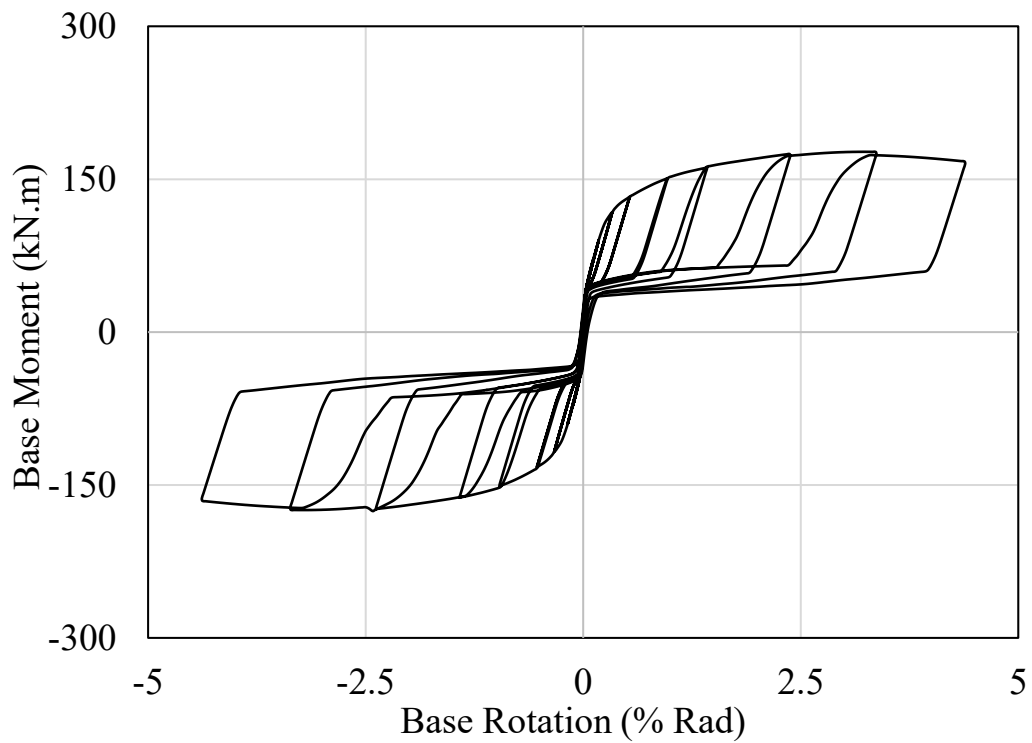


Figure 4.32: Moment-rotation relationship S16-S5-W310-25x400x550-25-10%

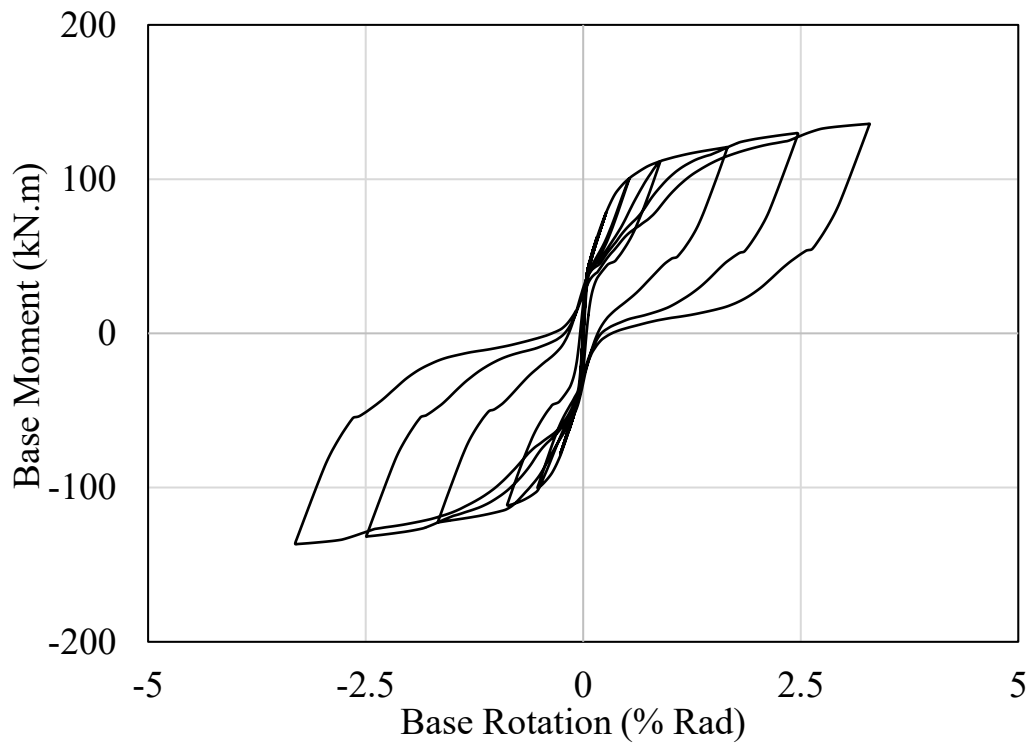


Figure 4.33: Moment-rotation relationship S17-S2-W250-19x350x500-25-300 MPa

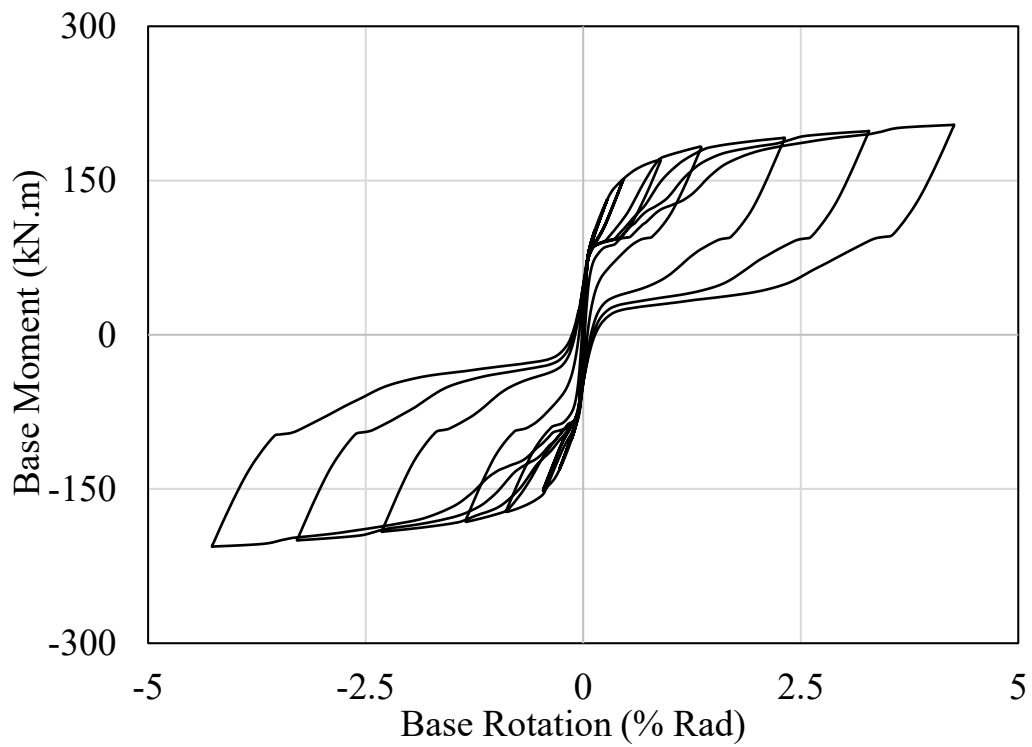


Figure 4.34: Moment-rotation relationship S18-S4-W310-19x400x550-25-300 MPa

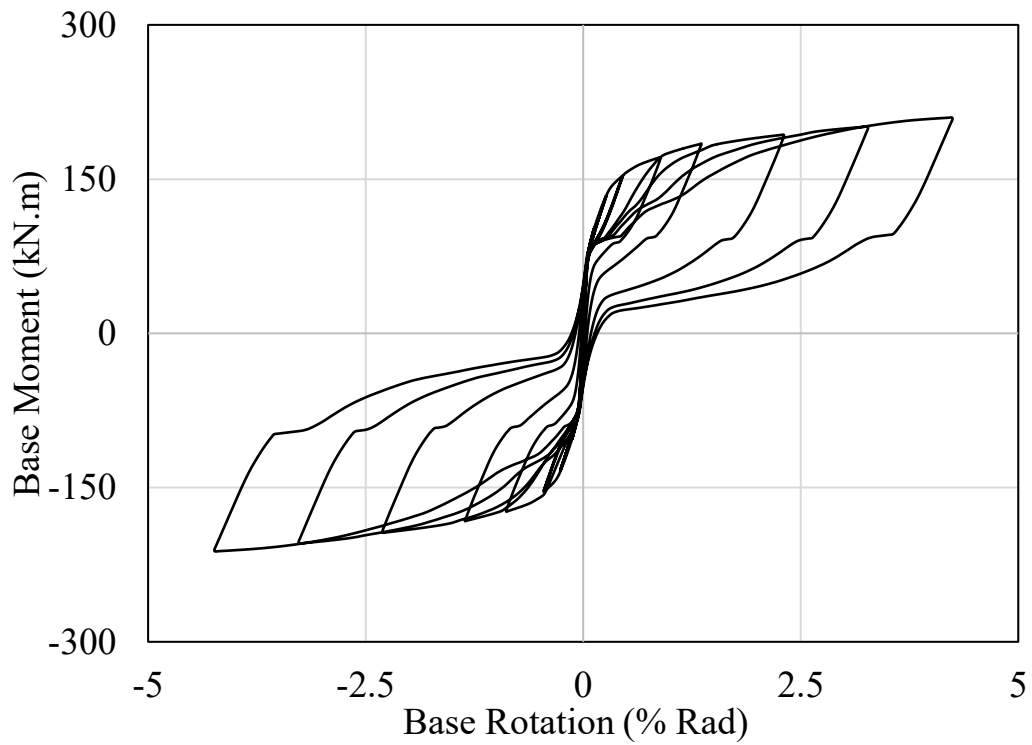


Figure 4.35: Moment-rotation relationship S19-S4-W310-19x400x550-25-(-25 mm AR)

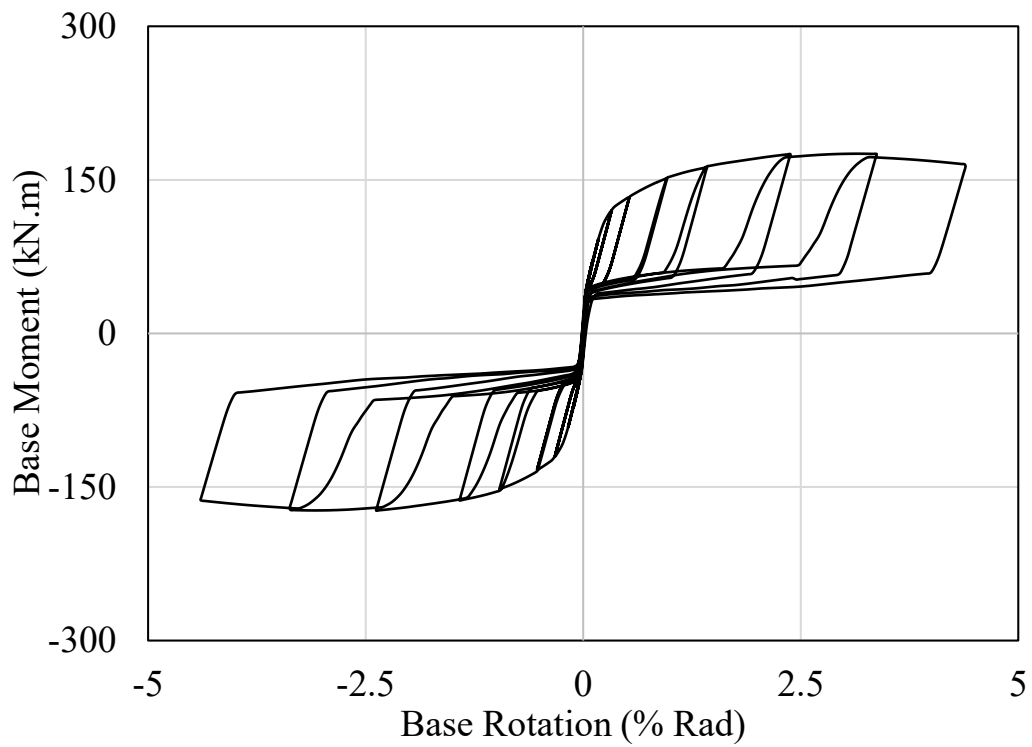


Figure 4.36: Moment-rotation relationship S20-S5-W310-25x400x550-25-(-25 mm AR)

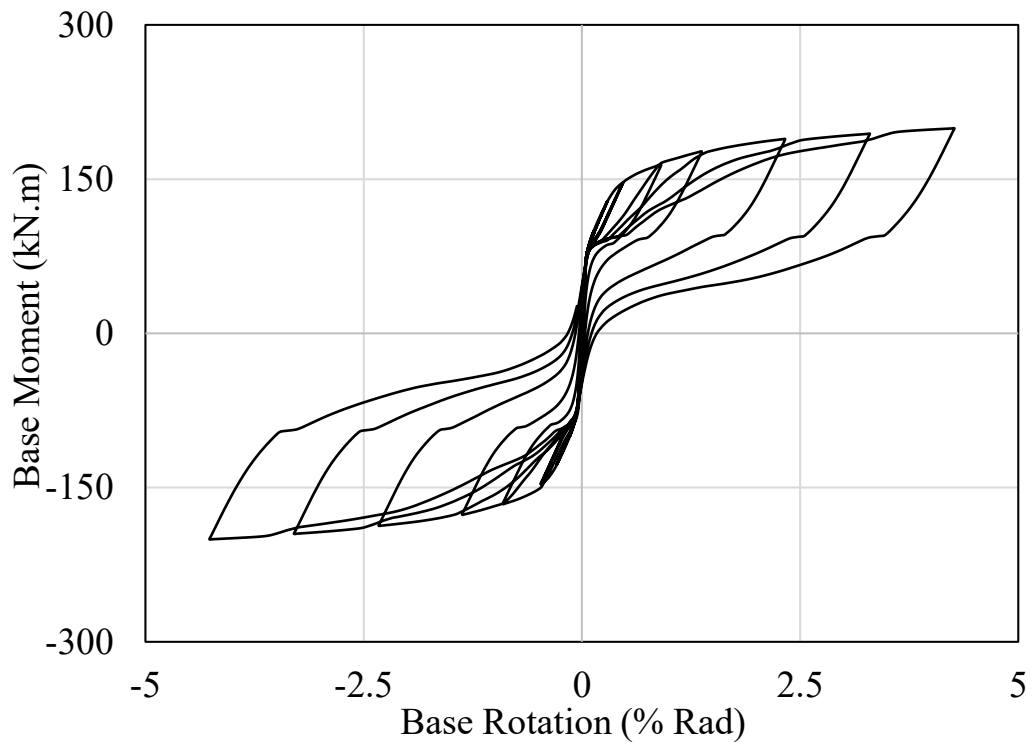


Figure 4.37: Moment-rotation relationship S21-S4-W310-19x400x550-25-(+25 mm AR)

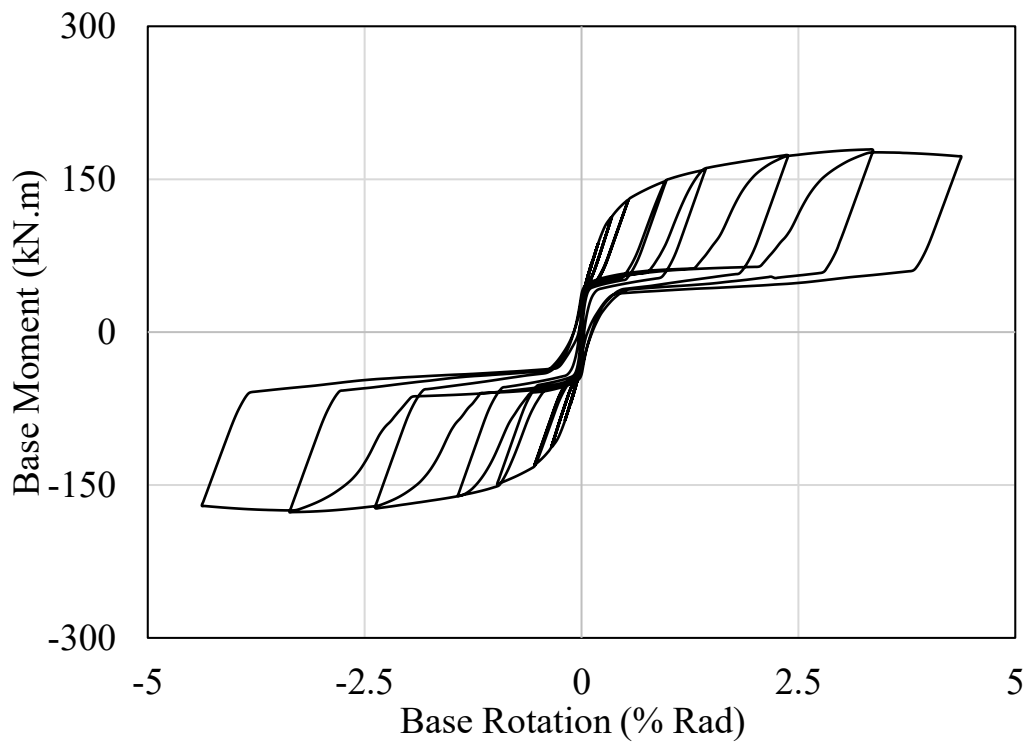


Figure 4.38: Moment-rotation relationship S22-S5-W310-25x400x550-25-(+25 mm AR)

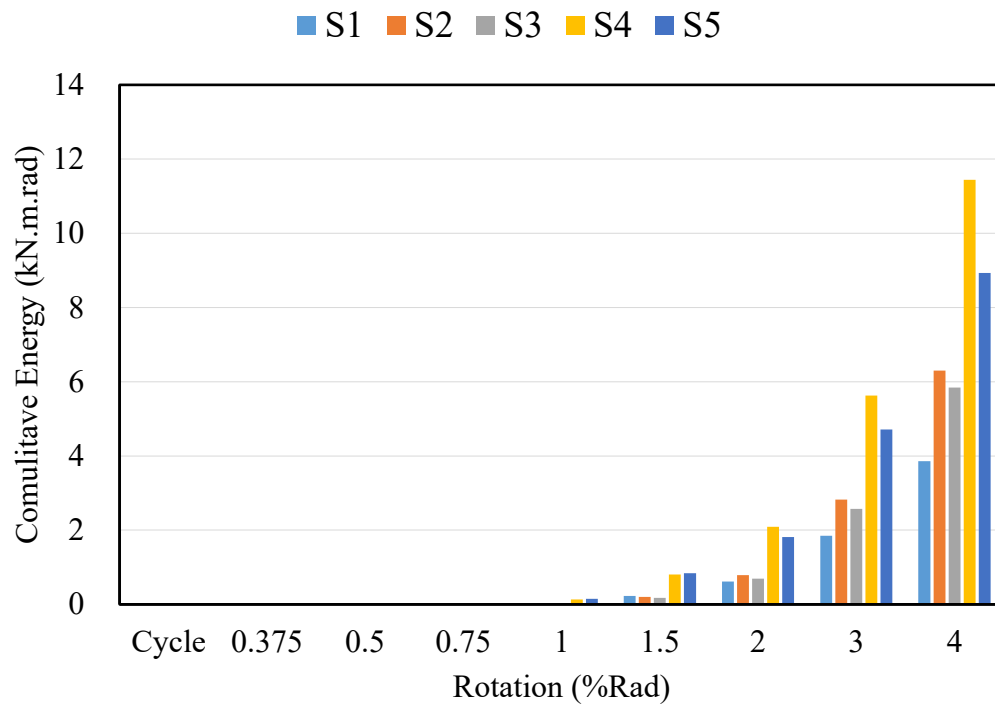


Figure 4.39: Cumulative energy dissipation capacity of connections S1 to S5

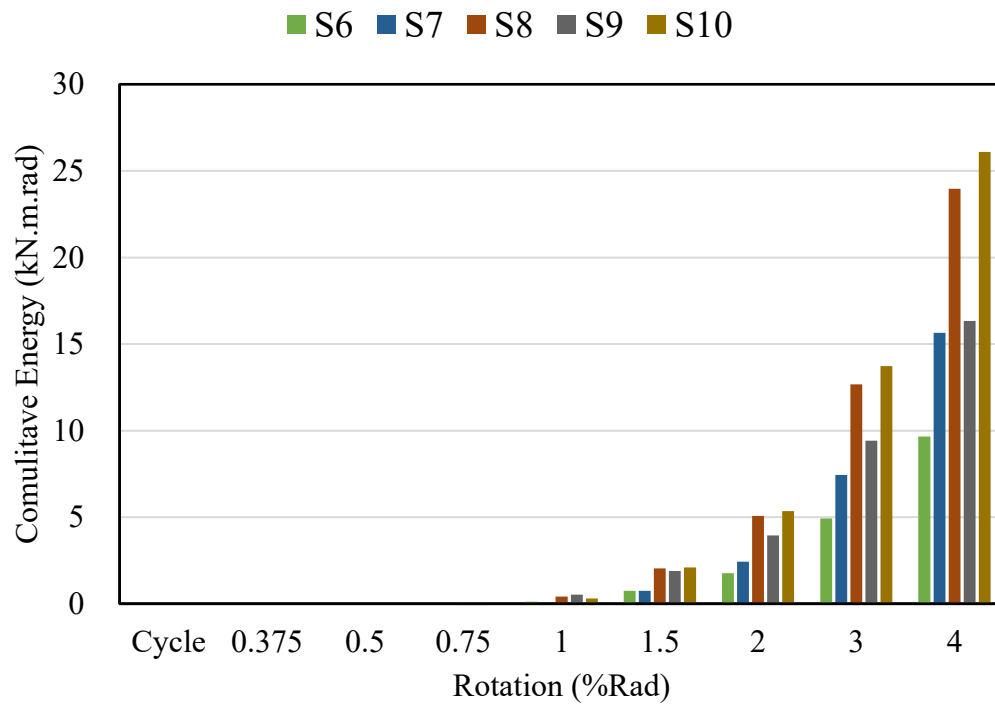


Figure 4.40: Cumulative energy dissipation capacity of connections S6 to S10

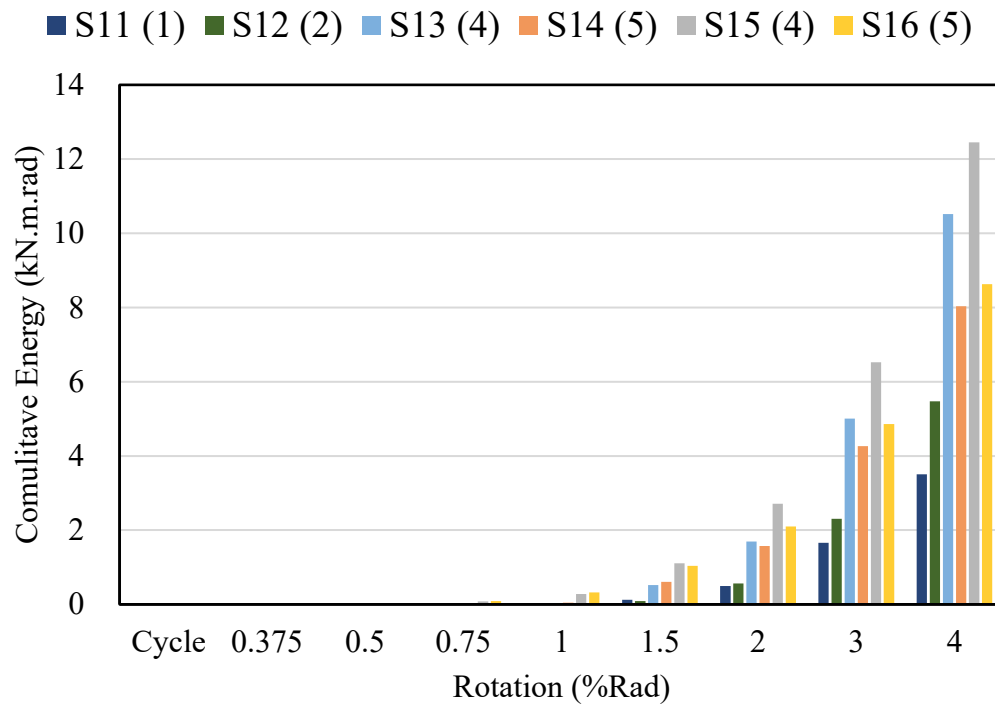


Figure 4.41: Cumulative energy dissipation capacity of connections S11 to S16

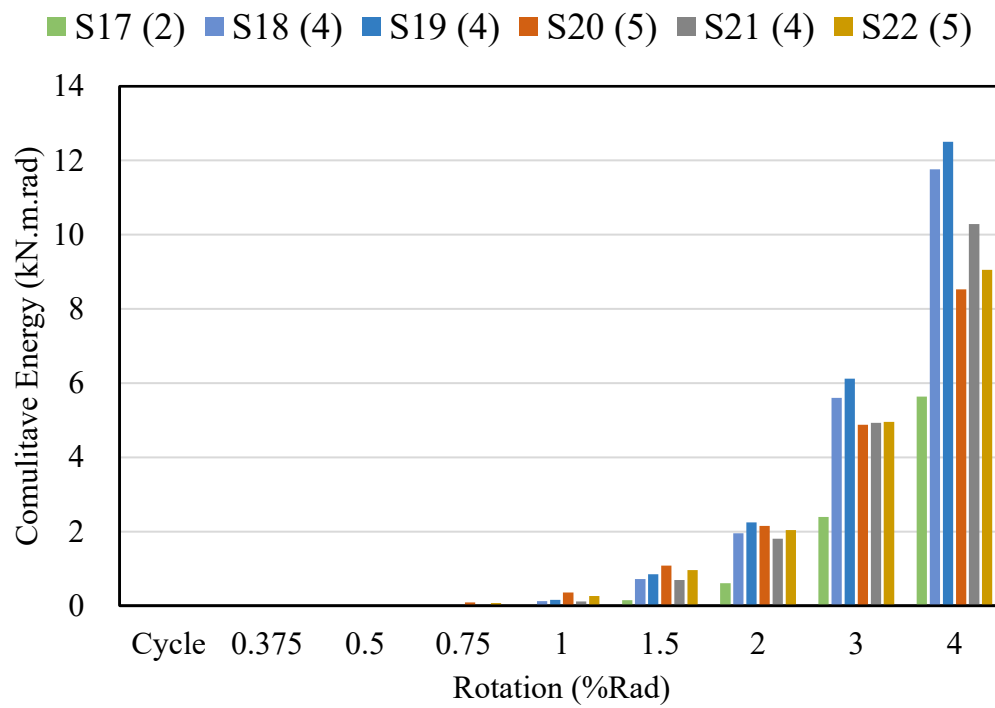


Figure 4.42: Cumulative energy dissipation capacity of connections S17 to S22

Chapter 5: Seismic Evaluation of 1960s Steel Moment Resisting Frame Structure

5.1 Introduction

The seismic assessment of existing steel Moment-Resisting Frame (MRF) structures has become a central focus in the research community. As highlighted in the comprehensive literature review in Chapter 2 of this thesis, there is a critical need to inspect these structures due to their widespread prevalence and vulnerability to seismic hazards, especially in light of evolving standards. The exploration proceeds through a case study, wherein a steel MRF structure was designed according to the 1965 National Building Code of Canada (NBC) (NRC, 1967) and S16-1969 (CSA, 1970) standards. The selected structure is a four-storey building assumed to be a hospital located in Montreal, Quebec, Canada. Drawing on insights from recent studies with a similar research focus, a comparative analysis is conducted. Addressing certain aspects of the existing research gap, the case study concludes with informed recommendations, contributing to the ongoing discourse in this field.

5.2 Design of a four-storey steel structure

Due to the limited number of studies on the topic, a building was designed based on the 1965 standards. The objective is to offer researchers interested in further exploring this subject additional options upon which to base their investigations. Recent studies on the topic have primarily adopted the type-2 design and construction approach, as observed in the works by Kyriakopoulos and Christopoulos (2013) and Gómez et al. (2015). According to these studies, the dominant design approach of the targeted era involves proportioning the beams of the steel MRF

as simply supported, with the columns designed to bear lateral loads, while assuming rigid beam-to-column joints. They argue that wind loading typically governs the lateral loading design of steel structures designed according to the 1960s standards, prioritizing it over code-specified seismic loading of the time. However, the case study presented herein demonstrated that earthquake loadings can control lateral load-resisting system design. This is particularly pertinent for low-rise structures expected to bear high gravity loads, leading to larger seismic weights, consequently larger seismic design loads.

5.2.1 Prototype building

A representative steel MRF was designed in compliance with the 1965 NBC (NRC, 1967) in Montreal City, with reference to the 2nd edition – 1st printing of the Handbook of Steel Construction (CISC, 1970) that included S16-1969 (CSA, 1970) standard. The plan view comprises an approximately square layout of four bays by five bays, each spanning 6.0 m in the east – west (EW) direction and 5.0 m in the north – south (NS) direction, respectively. The structure is symmetric in both directions, as illustrated in Figure 3.1. The lateral load-resisting system in the EW direction perimeter consists of steel MRFs, while the NS direction perimeter consists of braced frames. In the elevation view, the building consists of a ground floor with a height of 4.5 m and a typical height for the remaining floors of 3.6 m, resulting in a total height of 15.3 m, as shown in Figure 5.2. The building is assumed to be a hospital, and therefore, gravity loading data were extracted from the 1965 benchmark hospital building studied by Kyriakopoulos (2012). Table 5.1 provides details on gravity loading.

Climatic information for building design in Canada was available in Supplement No. 1 (NRC, 1967) to the NBC for various cities in Canada. Wind, snow and earthquake design parameters for the city of Montreal are:

- Ground snow load (S_g) = 54 psf (2.6 kPa)
- Wind pressure (q) = 15 psf (0.72 kPa)
- Earthquake intensity factor (R) = 4, for zone 3

The snow load on any surface (S) is the product of the ground snow load (S_g) and the snow load coefficient (C_s), C_s is typically 0.8 (Gómez et al., 2015). According to the 1965 NBC (NRC, 1967) In roofs, which are flat and have no parapet or obstacles preventing the drifting of snow, C_s can be reduced to 0.6. Therefore, the total snow load on the roof of the building (e.g., 24×25 m) is 936 kN. According to the 1965 NBC articles 4.1.3.11 to 4.1.3.12 (NRC, 1967), the total wind force, F_w , on a surface is given by $q \times C_h \times C_p \times A$, where q is the specified wind design pressure, C_h is the height factor, C_p is the total effect of external and internal pressure coefficients C_{pe} and C_{pi} , respectively, and A is the area of the surface considered. A summary of the wind load calculation is presented in Table 5.2, and the evaluated wind forces are illustrated for one frame in Figure 5.3. The design base shear, V , for earthquake loading was evaluated in accordance with article 4.1.3.15 of the 1965 NBC (NRC, 1967), where V is $K \times W$, K equals $R \times C \times I \times F \times S$ and W is “the total of the design load due to materials of construction incorporated in the building, the design load resulting from the use of the building for storage and the design load due to the weight of service equipment and machinery” as defined by the 1965 NBC (NRC, 1967). The minimum design parameter K and seismic weight W calculations are summarized in Table 5.3 and Table 5.4, respectively, whereas the resulting design earthquake loading is depicted in Figure 5.4 for one

MRF. It is worth mentioning that the base shear force is distributed among the structure levels according to the contribution of the storey to the seismic weight, w_i , and the height, h_i , according to the following equation:

$$F_{eqi} = \frac{V w_i h_i}{\sum w h} \quad \text{Eq. 5-1}$$

5.2.2 Steel design

The design process commenced with an assessment of gravity loading on the beams. The beam selection was based on simply supported conditions, following the type-2 construction process and utilizing CSA G40.12 steel Gr.40 (275 MPa) (CSA, 1970), a steel popular in the reviewed structure plans for beams and columns. Columns were preliminarily selected by assessing axial loading due to gravity only by tributary area. The structure was then analyzed including the lateral loading, where the load combinations following the guidelines in Table 1 from S16-1969 (CSA, 1970) were applied. Specifically, the load combinations featured factors of one when analyzing gravity loads alone or when combining dead load with one of the lateral loads (i.e., wind or earthquake). Probability factors of 0.75 were applied when combining all gravity loads with one of the lateral loads. It is noteworthy that the design was based on the Allowable Stress Design (ASD) Method, as the permitted criterion to assess capacity against demand for design validation (CISC, 1970).

The design loads are shown in Table 5.5. The assumed uniformly distributed (UD) loads were calculated by considering a one-way distribution. The UD load W_D incorporates dead loads from floors and walls, while W_L and W_S represent live and snow loads, respectively. Additionally, reactions from gravity loads on exterior beams in the transverse direction were added to the

columns of the MRF to account for any exterior wall loads. Beam sections were chosen using the beam selection table for CSA G40.12 Gr.40 (CSA, 1970) found in Part 5 of the 2nd edition – 1st printing of the Handbook of Steel Construction (CISC, 1970). Specifically, W16×40 (i.e., W410×60) was selected for roof beams, and W21×62 (i.e., W530×92) for other storeys. Preliminary estimates for column loading were calculated using tributary area, considering only gravity loading. Details of preliminary column sections are listed in Table 5.6. The analysis was then conducted incorporating all design loads (i.e., dead, live, snow, wind and earthquake). Notably, earthquake loading took precedence in governing the lateral load for design, leading to the exclusion of wind loading. Considering the possibility of earthquake forces from a reverse direction, columns in tension in one direction were evaluated under compression loading in the opposite direction. This focused solely on compression, as it's expected to be a more critical scenario, given that gravity loading consistently induces compression forces. Finally, the validation of the design considered only two scenarios: 1) including dead, live and snow with a probability factor of one, and 2) dead, live, snow and earthquake with a probability factor of 0.75.

The analysis results for the columns are presented in Table 5.7, in imperial units for convenience when using old Steel Handbook. It is worth noting that the columns in storey three were extensions from storey two; therefore, only the results for storey two are included. The final column sections are shown in Table 5.8. Additionally, effective length factors for the major axis, K_x , are shown in Table 5.8. They were determined using the equations employed to develop the nomographs in Figure C1 from Part 4 of the Handbook of Steel Construction (CISC, 1970). These calculations considered a sidesway permitted case, assuming a rigidity factor, G , of 10 for the base of the columns, as specified in part 4 – C6. from the 2nd edition – 1st printing of the Handbook of

Steel Construction (CISC, 1970). Meanwhile, the effective length factors for the minor axis, K_y , were uniformly set to 1.0.

For allowable combined stresses, clause 17.1.1 from S16-1969 (CSA, 1970) specifies the interaction formulas for the strength and stability check as shown by equations 5-2 and 5-3, respectively.

$$\frac{f_a}{0.6F_y} + \frac{f_b}{F_b} \leq 1.0 \quad \text{Eq. 5-2}$$

$$\frac{f_a}{F_a} + \frac{C_m f_b \alpha}{F_b} \leq 1.0 \quad \text{Eq. 5-3}$$

Where:

- f_a is the axial stress,
- f_b is the bending stress,
- F_y is yield strength,
- F_a is the allowable axial stress assuming no bending stress,
- F_b is the allowable bending stress assuming no axial stress,
- C_m is the coefficient determining the equivalent uniform bending stress (set to 0.85 for members bent in double curvature with no transverse loading between supports),
- α is the amplification factor, calculated as $1/(1 - f_a / F'_e)$, where $F'_e = 149000/(kl/r)^2$ and kl/r represents the slenderness ratio in the plan of bending.

Two column base connections were designed with: one for exterior columns and another for interior columns. Steel A36, with a yield strength of 36 ksi (250 MPa) and conforming to the ASTM A36-66 Structural Steel Standard (ASTM, 1966), was utilized for both the base plate material and the anchor rods. The 1970 Handbook of Steel Construction (CISC, 1970) provides

guidance for designing base plates subjected solely to axial loads, leaving it to engineers to perform proper designs when base plates are subjected to combined bending, axial and shear forces. Considering a concrete compressive strength of 28 MPa and the base plate being supported by the entire concrete area, the allowable bearing stress, F_p , was calculated as 25% of the specified compressive strength, resulting in $F_p = 7$ MPa. Determination of base plate size accounted for stress from axial column loads and moments at the column base. The base plates' sizes were established at 450×600 mm and 500×700 in for exterior and interior columns, respectively, with the larger length aligned with the major axis of the column. Base plate thickness was estimated based on a cantilever beyond 0.95 of the column depth and 0.8 of the column width. Considering an allowable bending stress, F_b , of $0.75 F_y$, which equals 186 MPa for A36 steel, the base plates' thicknesses were set at 57 mm ($2 \frac{1}{4}$ in) and 63.5 mm ($2 \frac{1}{2}$ in) for exterior and interior columns, respectively. For A36 steel, allowable tensile, F_t , and shear, F_v , stresses are determined as $0.45 F_y$ (112 MPa) and $0.4 F_y$ (99 MPa), respectively, as concluded from article 16.2 of the S16-1969 (CSA, 1970). Consequently, four 75 mm (3.0 in) and four 82.5 mm ($3 \frac{1}{4}$ in) anchor rods were used in the column base connections for exterior and interior columns, respectively. It's important to note that an interaction formula must be met to verify the selection of anchor rods. This formula requires the sum of the ratios of tensile stress to allowable tensile stress and shear stress to allowable shear stress to be less than or equal to 1.0.

5.3 Nonlinear building model

A two-dimensional (2D) steel MRF was modeled using the Open System for Earthquake Engineering Simulation (OpenSees) platform (McKenna, 1997). The steel beams within the frame were modeled using a concentrated (lumped) plasticity approach, as they were not anticipated to

yield during the simulation owing to their large sections. The modeling approach is outlined in the Guidelines for Nonlinear Structural Analysis for Design of Buildings (NIST, 2017) report, developed by the Applied Technology Council (ATC) for the National Institute of Standards and Technology (NIST). This approach incorporates the nonlinear deterioration component model by Lignos and Krawinkler (2011), with consideration given to the proposed updates by Lignos et al. (2019). The 2D model incorporated panel zone shear deformation based on the modeling approach by Skiadopoulos et al. (2021). The steel columns were modeled with single-force-based distributed plasticity beam-column elements comprising five integration points along their length, utilizing the updated Voce-Chaboche (UVC) uniaxial stress states material model built in OpenSees by Hartloper et al. (2021). Additionally, a realistic depiction of the column base connections was modeled based on a 2D mechanics-based numerical model developed by Inamasu et al. (2021). The influence of the unreinforced masonry infill walls on the nonlinear dynamic performance of the steel MRF was examined using the macro-modeling approach discussed by Furtado et al. (2015). Specifically, the unreinforced infill walls were modeled using four diagonal elastic elements connected to a central nonlinear element representing the nonlinearity exerted by the walls. To account for the gravity columns, which were not explicitly presented in the 2D OpenSees model, a single-bay fictitious gravity frame as proposed by Gupta and Krawinkler (1999) and discussed in Elkady and Lignos (2015) was included. This frame represents the gravity P-Delta loads of the building. Four OpenSees models were analyzed: a bare steel frame, a steel frame including the base plate, a steel frame including the infill walls and a complete model incorporating the steel frame, column base connections and infill walls. Figure 5.5 illustrates a representation of the developed 2D OpenSees models. Further details on the modeling approaches for the various components of the model are summarized in the subsequent sections.

5.3.1 Modeling of steel beams

The beams of the steel MRF frame were modeled with elastic beam-column elements. Nonlinear rotational springs were used at the ends of these elements following the modified Ibarra-Medina-Krawinkler (IMK) phenomenological deterioration model (Ibarra et al., 2005; Lignos and Krawinkler, 2011). The authors developed a set of equations to characterize the moment-rotation relationship of reduced beam section (RBS) members and non-RBS beams. Figure 5.6 shows the idealized moment-rotation relationship of the rotation springs that were utilized at the beams' ends. The elastic flexural stiffness of the end springs, K_{spring} , is computed as follows:

$$K_{spring} = n \frac{6EI_{b,mod}}{L_b} \quad \text{Eq. 5-4}$$

$$I_{b,mod} = \frac{n+1}{n} I_b \quad \text{Eq. 5-5}$$

In this equation, n represents a factor used to adjust the initial stiffness of the backbone curve. Ideally, this factor should be infinite, but for practical reasons, it is often taken as 10 to prevent convergence problems during analysis (Ibarra et al., 2005). The modulus of elasticity of the steel material, E , is assumed to be 200 GPa. To account for the additional elastic flexibility of the rotational spring elements, the strong-axis moment of inertia of the beams, I_b , is modified, where $I_{b,mod}$ represents the modified moment of inertia of the elastic beam element (Ibarra et al., 2005), and L_b is the clear beam length. It's important to note that different equations were developed to address various types of steel beam end conditions such as the reduced beam section (RBS) and non-RBS beams. Hartloper (2016), through regression analysis of available pre-Northridge connections' tests, derived the following equations, which are intended to characterize the moment-rotation relationships of the beam-to-column connections in the existing steel MRF

structures built before 1990s. The effective yield moment M_y , the capping moment M_u and the residual moment M_r of the steel beam are estimated as follows:

$$M_y = R_y S_b F_y \quad \text{Eq. 5-6}$$

$$M_u = 1.1 R_y Z_b F_y \quad \text{Eq. 5-7}$$

$$M_r = 0.2 M_y \quad \text{Eq. 5-8}$$

in which, S_b is the elastic section modulus of the steel beam with respect to its strong axis, R_y is the expected overstrength factor of the steel and Z_b is plastic section modulus of the steel beam. The pre-peak plastic rotation, θ_p , the post-peak plastic rotation, θ_{pc} and the ultimate rotation capacity, θ_{ult} , of the pre-Northridge beams connections where depth of the beam, d_b , is < 610 mm (24") are evaluated as follows:

$$\theta_p = 0.046 - 0.0013d_b \quad \text{Eq. 5-9}$$

$$\theta_{pc} = -0.003 + 0.0007d_b \quad \text{Eq. 5-10}$$

$$\theta_{ult} = 0.05 \quad \text{Eq. 5-11}$$

5.3.2 Modeling of steel columns

The steel wide flange columns were modeled using single force-based distributed plasticity beam-column elements, each comprising five integration points along their length. The column cross sections were discretized with eight fibers along the flange width and web depth and three fibers along the flange and web thicknesses. The UVC material for uniaxial stress states (Hartloper et al., 2021) was assigned to each fiber element to capture material yielding and cyclic hardening. This material is an advanced version of the classic nonlinear isotropic/kinematic hardening material model, based on the Voce isotropic hardening law (Voce, 1948) and the Chaboche

kinematic hardening law (Chaboche et al., 1979). The UVC material incorporates an updated isotropic hardening law with parameter constraints, enabling simulation of the permanent decrease in yield stress associated with initial plastic loading, a phenomenon observed in mild steels. The material properties of CSA G40.12 Gr.40 (CSA, 1970) steel from Table 4.6 were used for the column elements.

5.3.3 Modeling of panel zone

A parallelogram model consisting of eight rigid elements connected to a nonlinear spring, as illustrated in Figure 5.7, was employed to explicitly incorporate the force-shear distortion behaviour of the panel zone in the OpenSees model. The *Hysteretic uniaxialMaterial*, available in OpenSees, was utilized to define the nonlinear material of the panel zone spring, as discussed in Skiadopoulos et al. (2021). Particularly, the yield shear strength ($V_{y,pz}$), elastic modulus (K_e), yield distortion angle (γ_y), plastic shear strength at $4\gamma_y$ ($V_{p,pz}$) and ultimate shear strength at $6\gamma_y$ ($V_{u,pz}$) of the panel zone were evaluated as follows:

$$V_{y,pz} = \frac{F_y}{\sqrt{3}} a_y (d_c - t_{cf}) t_{pz} \quad \text{Eq. 5-12}$$

$$K_s = t_{pz} (d_c - t_{cf}) G \quad \text{Eq. 5-13}$$

$$K_b = \frac{12 E I}{d_b^3} d_b \quad \text{Eq. 5-14}$$

$$K_e = (K_s K_b) / (K_s + K_b) \quad \text{Eq. 5-15}$$

$$\gamma_y = V_{y,pz} / K_e \quad \text{Eq. 5-16}$$

$$K_f = (K_{sf} K_{bf}) / (K_{sf} + K_{bf}) \quad \text{Eq. 5-17}$$

$$K_{sf} = 2 (t_{cf} b_{cf} G) \quad \text{Eq. 5-18}$$

$$K_{bf} = \frac{12 E (t_{cf} b_{cf}^3 / 12)}{d_b^3} d_b \quad \text{Eq. 5-19}$$

$$V_{p,pz} = \frac{F_y}{\sqrt{3}} [a_{w,eff,p} (d_c - t_{cf}) t_{pz} + a_{f,eff,p} (b_{cf} - t_{pz}) 2 t_{cf}] \quad \text{Eq. 5-20}$$

$$V_{u,pz} = \frac{F_y}{\sqrt{3}} [a_{w,eff,u} (d_c - t_{cf}) t_{pz} + a_{f,eff,u} (b_{cf} - t_{pz}) 2 t_{cf}] \quad \text{Eq. 5-21}$$

Where F_y is the yield strength of the steel material, a_y equals 0.9 and 1.0 for slender and stocky (flanges thicker than 30–40 mm) panel zones, respectively, d_c is column depth, t_{cf} is the thickness of the column flange, t_{pz} is the thickness of the panel zone and equals thickness of the column web including the doubler plate, if any, K_s is the shear contribution to the elastic stiffness of the panel zone, K_b is the bending contribution to the elastic stiffness of the panel zone, G is the shear modulus, E is the elastic modulus, I is the moment of inertia of the column including the doubler plate, if any, b_{cf} is the width of the column flange, d_b is beam depth, $a_{w,eff,p}$ and $a_{w,eff,u}$ are the web normalized average shear stress and equal 1.1 and 1.15 for $4\gamma_y$ and $6\gamma_y$, respectively. $a_{f,eff,p}$ and $a_{f,eff,u}$ are the flange normalized average shear stress and equal $0.93 (K_f / K_e) + 0.015$ and $1.05 (K_f / K_e) + 0.02$ for $4\gamma_y$ and $6\gamma_y$, respectively. Finally, the three points required to construct the trilinear backbone curve of the rotational spring in the panel zone are $(\gamma_y, M_{y,pz})$, $(4\gamma_y, M_{p,pz})$ and $(6\gamma_y, M_{u,pz})$ where the moment values are equal to the specified shear strengths (e.g., $V_{y,pz}$, $V_{p,pz}$ and $V_{u,pz}$) multiplied by the beam depth.

5.3.4 Modeling of column base connections

Inamasu et al. (2021) developed a modeling approach to incorporate nonlinearity in exposed column base connections. The model is based on the mechanics of the various connection components and encompasses different force transfer scenarios between these components. Anchor rods are represented using circular fiber sections assigned to force-based elements. Depending on the threading length or the presence of leveling nuts, multiple segments may be

utilized along the anchor rod's length to define different material properties. The base plate is modeled with a displacement-based element incorporating a fiber section that extends beyond the column flanges, along with an elastic beam-column element containing rigid material between the column flanges. Winkler springs simulate the behaviour of grout or concrete. Specifically, an elastic no-tension material is assigned to equally spaced truss elements along the base plate length, allowing for column base uplifting. The modeling approach was evaluated against various connections from Chapter 4 of this Thesis. Particularly, column base connections S1, S4 and S9, representing different failure modes, were modeled in OpenSees incorporating the proposed approach. Figure 5.8 depicts a comparison between the connections' responses in ABAQUS and OpenSees. The results confirm the ability of the 2D OpenSees modeling approach to simulate the behaviour of the column base connection under cyclic loading. The column base connections of the prototype building were included in the OpenSees model using the approach by Inamasu et al. (2021); The material properties from Table 4.6 were utilized to define the UVC uniaxial material for the anchor rods and base plate, while other modeling assumptions are shown in Table 5.9. Two connections were modeled: internal and external column base connections, as discussed in the steel design section of the prototype building.

5.3.5 Modeling of the masonry infill

Various modeling techniques for simulating the behaviour of infill walls are documented in the literature. Some researchers have focused on rigorous micro-level modeling, such as Dhanasekar and Page (1986), Shing and Lofti (1991), Mehrabi and Shing (1997) and Stavridis and Shing (2010). They aimed to gain a comprehensive understanding of how the geometry and material of infill walls influence the dynamic performance of structures. On the other hand, others

have adopted a more simplified macro-level approach, such as Dolsek and Fajfar (2002), El-Dakhakhni et al. (2003), Crisafulli and Carr (2007) and Furtado et al. (2015). These methods have shown excellent ability to simulate the global response of the interaction between frames and infill walls. The primary objective of this research is to characterize the seismic response of existing steel MRF structures. Therefore, it was deemed sufficient to use macro-level modeling of the infill to avoid increasing the complexity of the simulation and deviating from the primary objective. Consequently, the macro-level modeling approach proposed by Furtado et al. (2015) was adopted to incorporate the influence of unreinforced masonry infill walls on the dynamic response of the prototype building. Specifically, the unreinforced infill walls were modeled using four diagonal elastic elements connected to a central nonlinear element representing the nonlinearity exerted by the walls. The nonlinear central element was assigned *Pinching4 uniaxialMaterial*, which exhibits pinched load-deformation response and degrades under cyclic loading. Cyclic degradation of strength and stiffness occurs in three ways: unloading stiffness degradation, reloading stiffness degradation and strength degradation. Four points (yielding, $f_{i,y}$, cracking, $f_{i,c}$, maximum, $f_{i,max}$, and residual, $f_{i,r}$) were defined to model the stress-strain behaviour of the central element of the infill wall representation. These points can be obtained by calibrating previous testing programs. The review conducted by Furtado et al. (2015) concluded that the ratio $f_{i,c} / f_{i,max}$ can be taken as 0.55, while the cracking strain lies between 0.075% and 0.12%. $f_{i,y}$ is in the range of 65% to 75% of $f_{i,max}$, whereas the yielding strain ranges between 0.15% and 0.35%. Residual strength can be set to 20% $f_{i,max}$ and is estimated to occur at 5 times the strain at yielding. The maximum strength of the wall is expected between strain values of 0.25% and 0.5%, and it can be calculated using the following formula:

$$f_{i,max} = 0.818 \frac{f_{tb}}{C_I} (1 + \sqrt{C_I^2 + 1}) \quad \text{Eq. 5-22}$$

$$C_I = 1.925 \frac{L_i}{H_i} \quad \text{Eq. 5-23}$$

where f_{tb} is the cracking strength, t , L_i and H_i are the thickness, length and height of the infill wall, respectively. Additionally, the *Pinching4 material* necessitates the definition of parameters governing loading and unloading degradation of stiffness and strength, as well as the type of damage model, whether cyclic or energy-based. Readers are encouraged to refer to the OpenSees manual and relevant literature for a deeper understanding of these parameters. Nevertheless, overlooking differences in column and beam sizes between storeys, and accounting for the variation in height of the first storey from other typical storeys, resulted in defining two nonlinear materials, as outlined in Table 5.10: one for simulating the infill wall in the first storey and the other for the remaining storeys. Furtado et al. (2020) investigated the mechanical properties of various types of masonry infill walls, including existing ones. They determined that the cracking strength of an existing infill wall is 0.38 MPa, which is adopted for the current study.

5.4 Seismic performance assessment

The seismic performance assessment of the building was conducted using the OpenSees platform (McKenna, 1997). Initially, gravity loading simulation was performed, followed by eigenvalue analysis. Four modal shapes, along with their corresponding natural periods, were identified for four modeling cases: Bare steel frame (BSF), frame with column base connections (SFX), frame with masonry infill walls (SFM) and the most realistic representation of the building, which includes steel frame, column base connections and infill walls (SFR). Subsequently, the four models underwent monotonic nonlinear static (pushover) analysis based on the first modal

shape of each frame, as determined from the eigenvalue analysis. This analysis provided preliminary insights into the building's performance under lateral loading. Additionally, ground motion records were selected and scaled using Method A from Part 4 of Division B in the Structural Commentaries provided by NBC (NBC, 2015). Nonlinear response history analysis was then carried out for 22 ground motion records. Finally, the seismic performance of the steel building was assessed and summarized.

5.4.1 Gravity and eigenvalue analysis

Gravity loading was applied to the nodes at the centerline of the columns' top ends, while seismic masses were applied to nodes at the centerlines of the beams' ends. Eigenvalue analysis was conducted after applying the gravity load, and the fundamental periods are presented in Table 5.11. Accounting for the column base connections and infill walls in the simulation altered the fundamental periods of the structure. Although the increase in the periods of the structure due to the inclusion of column base connections is relatively small in the SFX model and almost negligible in the SFR model, the added flexibility at the columns' ends compared to the fixed end support condition in the BSF modified the dynamic properties of the structure and allowed for extended rotations at the bases. On the other hand, the inclusion of infill walls dramatically reduced the natural period of the structure. For instance, the fundamental period of the BSF model was 1.569 sec, whereas it decreased to 1.296 sec when only the infill walls were added to the bare steel frame in the SFM model. This decrease in the fundamental period of the structure not only affects the dynamic properties of the structure but, most importantly, triggers shear forces associated with smaller natural periods that were often ignored in the design phase.

5.4.2 Nonlinear static (pushover) analysis

The Pushover analysis was conducted based on the first mode pattern to gain insight into the building's behaviour under lateral loading. The normalized base shear forces, by seismic weight, for four scenarios (BSF, SFX, SFM and SFR) are plotted against the roof drift-to-building height ratio in Figure 5.9. All models exhibited adequately large roof drift capacity, ranging from 7.05% to 8.26%, before completely losing lateral load-carrying capacity. The SFX model showed the least maximum roof drift ratio, while the BSF model exhibited the maximum roof drift ratio. The maximum peak base shear attained by the BSF model is 7.78% of W . The inclusion of column base connections in the SFX model resulted in an approximately 30% decrease in peak base shear compared to the BSF. However, this inclusion showed an insignificant influence on the structure's performance when combined with masonry infill, as seen in the SFR model compared to the SFM model. In contrast, the inclusion of masonry infill in the SFM model increased the peak base shear by 15% compared to the BSF. This increase is justified by the additional stiffness provided by the infill walls. Moreover, the inclusion of infill walls dominated the structure's response to lateral loading, as evidenced by the negligible effects of column base connections on the SFR compared to the SFM model. Furthermore, although the SFX model experienced the least peak base shear, it's worth noting that the SFX model attained the peak base shear at a 3.33% roof drift ratio, whereas the BSF attained its peak base shear at a 2.28% roof drift ratio. The models comprising masonry infill walls attained their base shear capacities as early as a 1.6% roof drift ratio. It should be mentioned that the pushover analysis, while providing valuable insights into the building's response to lateral loading, does not reflect the performance of the structure when subjected to seismic excitations since the pushover represents a predefined shape of lateral deformations (e.g.,

T_1 modal shape). Hence, more insights into the structure's performance during ground shaking events are presented by means of nonlinear response history analysis in the following section.

5.4.3 Nonlinear response history analysis

Nonlinear Response History Analysis (NRHA) stands as a sophisticated computational method employed to comprehensively assess the seismic performance of structures. NRHA particularly captures the nonlinear behaviour inherent in materials and structural components, including yielding, energy dissipation, stiffness and strength degradation. NRHA was carried out with the developed 2D building models utilizing selected and scaled ground motion records using the 2020 NBC standard (NRC, 2022). Adaptive time-step as well as different solution algorithms were employed to overcome numerical convergence issues. Various engineering demand parameters are presented and discussed.

5.4.3.1 Ground motion selection and scaling

The ground motion selection process followed Method A outlined in Part 4 of Division B in the Structural Commentaries provided by 2015 NBC (NRC, 2015). Initially, the design spectrum was developed using the 2020 NBC online Seismic Hazard Tool (NRC, 2022) with site class C for the City Hall of Montreal (latitude: 45.509° and longitude: -73.554°), representing the 5% damped 2%-in-50-year Uniform Hazard Spectrum (UHS). UHS ordinates at periods of 0.2, 0.5, 1.0, 2.0, 5.0 and 10 sec are summarized in Table 5.12. It's noteworthy that the online Seismic Hazard Tool generates the final modified design spectrum, unlike the 2015 NBC (NRC, 2015) Seismic Hazard Tool, where site class factors are needed.

The next step involved specifying the period range for selecting and scaling ground motions. The upper-bound period needed to be greater than or equal to twice the first-mode period but not less than 1.5 sec. Whereas, the lower bound period should encompass the periods necessary to achieve 90% mass participation, yet not exceed 0.15 times the first-mode period. Since the first two modes of vibration achieved 90% mass participation, the lower-bound period was determined as the minimum of 0.15 times T_1 (1.297 sec) and T_2 (0.554 sec) of the SFR model, for it has the smallest T_1 , resulting in 0.194 sec for the lower bound period. The upper bound was determined by the SFX model, yielding a required period range, TR , from 0.194 sec to 3.208 sec.

Hariri (2023), developed a tool to select and scale ground motions for both Eastern and Western Canada following Method A. This tool facilitated the selection and scaling of 22 ground motions, covering a TR from 0.15 sec to 4.0 sec. Two suites of ground motion records were selected to address appropriate segments of the period range, considering the dominant earthquake magnitude-distance ($M-R$) combinations revealed by the site-specific seismic hazard disaggregation as discussed by Halchuk et al. (2007). Suite-I encompassed (magnitude 6) $M6$ events occurring at fault distances between 10 and 30 km, covering the period range, TR_{s1} , from 0.05 to 0.8 sec. Suite-II included $M7$ events occurring at greater distances between 20 and 70 km, addressing the period range, TR_{s2} , from 0.5 to 4.0 sec. The target spectrum along with period ranges are shown in Figure 5.10. Simulated ground motions from the Engineering Seismology Toolbox website by Atkinson (2009) were utilized as alternatives to historical records due to the absence of recorded ground motions from earthquake events in Montreal. Each ground motion was individually scaled to ensure its 5% damped response spectrum matches the design spectrum within the specified scaling-range assigned by the $M-R$ scenario for each suite. Furthermore, the scaling process involved verifying that the Suites' mean spectra do not fall lower than 10% of the

design spectrum within their corresponding scaling range. The selected and scaled records are plotted against their respective mean and target spectra for suite-I and suite-II in Figure 5.11 and Figure 5.12, respectively.

5.4.3.2 NRHA global results

NRHA was conducted on four models: BSF, SFX, SFM and SFR using selected and scaled ground motions. The peak absolute storey drift ratio (SDR) was evaluated for each ground motion record for the four models, as depicted in Figure 5.13. Additionally, Figure 5.13 provides the mean, 16th and 84th percentiles of the peak absolute SDR. All models exhibited a peak SDR of less than 2.5%, except for the SFX model, which has column base connections added to the bare steel frame. In the SFX model, a few ground motion records showed responses exceeding the 2.5% SDR in the first storey. Furthermore, all models demonstrated higher SDR in the top storey. This can be attributed to the weaker members selected for the top storey during the design stage, owing to smaller demands at the roof level. However, the SFX model experienced a larger SDR at the first storey compared to the top storey. The rotational flexibility provided by modeling the column base connections allowed for greater inter-storey drift at the first storey. This observation is critical as it raises concerns about how such a structure would perform in a higher intensity earthquake, and whether a soft first storey would lead to instability and collapse. On the other hand, models that accounted for masonry infill walls (e.g., SFM and SFR) exhibited more uniform inter-storey SDRs. The interaction of the composite system, combined with the added stiffness, took precedence over the other models in reducing overall drifts.

Similarly, the peak absolute storey shear is plotted in Figure 5.14, which includes the mean, 16th and 84th percentiles. It should be noted that these storey shear values are normalized by the seismic weight of the structure. Recalling that the structure was designed for 7.5% of its total weight, as discussed in Section 5.2.1, the models developed more than the design base shear. The mean base shear for models accounting for the infill walls (i.e., SFM and SFR) is approximately 9% of W . It is noteworthy that there were few records exhibiting base shear larger than 11% of W without collapse. Similarly, the bare steel frame model, BSF, exhibited base shear values of approximately 8.5% W for the mean with single records hitting 10.5% of W . In contrast, the SFX model demonstrated base shear smaller than the upper storeys. This can be attributed to the large SDR, which led to larger P-delta effects, consequently resulting in the loss of shear capacity at the first storey in the SFX model and the development of the soft storey mechanism.

The residual SDR of the four models, at the end of the free vibration set beyond the ground motion records, is plotted in Figure 5.15. Typically, the largest residual SDR is exhibited by the top storey, except for the SFX model, where the largest residual SDR is at the first storey. Overall, the top storey of the bare steel model (i.e., BSF) experienced the largest residual SDR compared to all other models. This can be ascribed to 1) the presence of the infill walls, which took precedence in controlling the dynamic behaviour over the other elements of the models; hence, modeling the infill walls, in SFM and SFR models, increased the stiffness of the weak top storey and reduced the differential difference in stiffness between the consecutive storeys, resulting in a more uniform residual SDR in the top storeys of the SFM and SFR models. Meanwhile, the developed soft first storey in the SFX model allowed for more drifts to concentrate at the base storey of the structure, resulting in lowering the residual drifts in the middle storeys.

5.4.3.3 NRHA local results

The local performance of the frame's beams, panel zones and columns is plotted in Figures 5.16 to 5.19. The results were analyzed to identify the elements experiencing yielding throughout the simulation of the 22 ground motion records. Then the number of successful yielding events was divided by 22 to evaluate the probability of yielding at each location/element of the frame. The beams remained elastic throughout the simulations in all models. The adopted design method allowed designing the beams for the gravity loads only, assuming simply supported beams; this resulted in overly designed sections for the beams, leading to the beams remaining elastic throughout the simulations. It is noteworthy that this unfavourable weak column – strong beam design is not permitted anymore in the current design standards such as the 2020 NBC (NRC, 2022). The columns' ends in the top storey and the base of interior columns in the first storey were the only yielding in the columns for the BSF, SFM and SFR models. The yielding of the columns in the top storey is justified by the small sections used in the design; consequently, the concentration of the inelastic deformations due to the development of a weak storey, compared to the adjacent storey. As for the interior column at the base storey, the demand – to – strength ratio of these columns was very close to one; hence it can be concluded that the demand produced by the dynamic nonlinear analysis exceeded the design values set by the static procedure in the 1960s NBC standard (NRC, 1967). Similarly, the beams of the SFX model remained elastic, as seen in the other models. The columns in the SFX model, however, did not experience the yielding exhibited by the top storey and the interior base storey columns of the other models. This can be ascribed to two reasons. Firstly, the formation of the soft first storey reduced the demand on the top storey. Secondly, the modeling of the column base connections allowed for energy dissipation through the different components of the column base connections (e.g., base plate and anchor rods)

and resulted in lowering the demand on the interior columns in the base storey. The panel zones exhibited a higher frequency of yielding compared to other elements, such as columns. Particularly, in the BSF, SFM and SFR models, panel zones in the top two floors exhibited over 90% probability of yielding. Generally, interior panel zones experienced a higher frequency of yielding, compared to exterior columns' panel zones, across all models, including the SFX model.

5.5 Summary and conclusions

A four-storey steel MRF structure, representative of low- to mid-rise buildings in moderate seismic regions in North America, was designed in accordance with the 1965 NBC (NRC, 1967) in Montreal City, Eastern Canada. CSA G40.12 steel Gr.40 (275 MPa) (CSA, 1970) was utilized for the beams and columns of the structure, while ASTM A36-66 (250 MPa) (ASTM, 1966) material was used for the design of the base plates and anchor rods. Four 2D nonlinear building models were developed to characterize the seismic performance of the structure, including a bare steel frame (BSF), a steel frame with realistic modeling of the column base connections (SFX), a steel frame model accounting for unreinforced masonry infill walls (SFM) and finally a steel frame model combining all aforementioned components (SFR). Gravity and modal analyses were conducted, followed by pushover analysis based on the first modal shapes of the structure. Nonlinear response history analysis was carried out utilizing 22 ground motions selected and scaled based on Method A from the 2015 NBC (NRC, 2015). A thorough discussion of global and local seismic performance was presented, with the main findings summarized as follows:

- 1- Previous studies conducted on steel MRF structures from the 1960s concluded that wind loading typically governs the lateral loading design of steel structures designed according to the 1960s standards, prioritizing it over code-specified seismic loading of the time.

However, the case study presented herein demonstrated that earthquake loadings can control the lateral load-resisting system design.

- 2- Steel structures built in the 1960s lack proper guidance on designing column base connections. The 1970 Handbook of Steel Construction (CISC, 1970) provides guidance for designing base plates subjected solely to axial loads, leaving it to engineers' judgment to design column base connections subjected to combined bending, axial and shear forces.
- 3- Accounting for the column base connections and the unreinforced masonry infill walls altered the dynamic properties of the studied structure, consequently affecting its natural frequency and period, which are fundamental factors in the design according to current standards such as the 2020 NBC, NRC (2022).
- 4- The pushover analysis concluded that all models exhibited adequately large roof drift capacity, ranging from 7.05% to 8.26%, before completely losing lateral load-carrying capacity.
- 5- Accounting for the column base connections in the pushover analysis resulted in a 30% decrease in peak base shear, whereas the inclusion of the infill walls resulted in a 15% increase in the peak base shear when compared with the bare steel frame model.
- 6- The NRHA concluded that the added rotational flexibility by accounting for the column base connections, in the SFX model, resulted in a soft first storey mechanism. Consequently, increased SDR and residual inter-storey drifts were observed in the first storey, in addition to the loss in storey shear resistance.
- 7- Most of the damage in the BSF, SFM and SFR models was in the top storey. While the bare steel framed exhibited the largest SDR at the top storey compared to the other models.

This can be attributed to the weaker members selected for the top storey during the design stage, owing to smaller demands at the roof level.

- 8- The infill walls dominated the dynamic properties when included in any model. For instance, although most of the damage in the SFM and SFR models was in the top storey, the SDR and residual drifts were much more uniform and smaller when compared to BSF and SFX models, respectively.
- 9- No beam yielding was recorded by the NRHA. The columns, however, in the top storey of the BSF, SFM and SFR models experienced yielding, in addition to the base of the interior columns in the first storey. On the other hand, no beams nor column yielding was recorded in the SFX model, which can be ascribed to the allowed energy dissipation through the different components of the column base connections (e.g., base plate and anchor rods).

Table 5.1: Gravity loading details

Load	Value (kPa)	Details
Dead		
Roof	3.1	Total
	0.3	Membrane + Insulation
	1.9	2.5+1.5 inch thick slab
	0.1	Steel deck
	0.3	Steel structure
	0.5	Mechanical
Typical floor	4.8	Total
	0.65	Partitions
	1.2	2 inch terrazzo
	1.85	2.5+1.5 inch thick slab
	0.1	Steel deck
	0.4	Steel structure
	0.3	Mechanical
	0.3	Ceiling
Exterior wall	1.95	
Live		
Roof	1	
Typical floor	4.8	

Table 5.2: Wind load calculation

Quantity	Value	Details
q	0.72 kPa	Supplement No. 1 – city of Montreal
C_h	Varies	1965 NBC – Section 4.1 – Table 4.1.3.D
C_P	1.4	Supplement No. 3 – case A – C_{pe} (0.9) and C_{pj} (0.5)
A	Varies	Half of wall for the storey above and below the level of consideration

Table 5.3: Minimum earthquake design load parameter, K , estimation

Quantity	Value	Details
R	4	Intensity factor – Supplement No. 1 – zone 3 – city of Montreal
C	0.75	Type of construction factor – 1965 NBC – steel MRF type
I	1.3	Importance of the building factor – 1965 NBC – hospital
F	1	Foundation condition factor – 1965 NBC – non highly compressible soil
S	0.0192	Number of storeys (N) factor – 1965 NBC – $0.25/(9 + N)$
K	0.075	$R \times C \times I \times F \times S$

Table 5.4: Seismic weight, W , evaluation

Level	h_x (m)	D. L. Floor ^a (kN)	D. L. walls (kN)	$w_x h_x$ (kN.m)	F_{eqx} (kN)	V_x^b (kN)
roof	15.3	1860	344	639803	91	91
3	11.7	2880	688	1981325	283	374
2	8.1	2880	688	1981325	283	657
1	4.5	2880	774	2228990	318	975
Total		10500	2494	6831443	975	

^a. D. L. stands for Dead load

^b. Storey shear

Table 5.5: Beams design loads and preliminary moments

Storey	W_D (kN/m)	W_L (kN/m)	W_S (kN/m)	L (m)	M_u (kN.m)	L (ft)	M_u (K-ft)
4	7.75	2.50	3.90	6	63.7	19.7	47.0
3	19.02	12.00	-	6	139.6	19.7	103.0
2	19.02	12.00	-	6	139.6	19.7	103.0
1	19.02	12.00	-	6	139.6	19.7	103.0

Table 5.6: Preliminary column sections

Storey	Location	Section
4	Exterior	W8×18
	Interior	W8×18
3	Exterior	W8×18
	Interior	W8×24
2	Exterior	W8×24
	Interior	W8×24
1	Exterior	W8×24
	Interior	W8×40

Table 5.7: Column analysis results

Storey	Column	Load	Axial (kip)	Shear (kip)		Moment (kip-in)		
Four	Exterior	Dead	-4.6	-0.6	-0.6	-44	-0.6	43
		Live	-1.6	-0.34	-0.34	-26	0	22
		Snow	-2.2	-0.12	-0.12	-6	2.5	10.8
		EQ	0.7	1.8	1.8	123	-2.8	-129
	Interior	Dead	-10	0	0	0	0	0
		Live	-3	0	0	0	0	0
		Snow	-5	0	0	0	0	0
		EQ	0	2.2	2.2	159	-2	163
Two and three	Exterior	Dead	-30.8	-0.7	-0.7	-47	1.9	50.8
		Live	-15.6	-0.45	-0.45	-31	1	33
		Snow	-2.3	0	0	-0.6	0.2	1.1
		EQ	14.8	14.1	14.1	993	-7	-1007
	Interior	Dead	-64	0	0	0	0	0
		Live	-37	0	0	0	0	0
		Snow	-5	0	0	0	0	0
		EQ	-2.9	15	15	1071	-7.5	-1087
one	Exterior	Dead	-43.4	-0.2	-0.2	-11.8	6	24
		Live	-22.4	-0.134	-0.134	-8	4	16
		Snow	-2.3	0	0	0	0	0
		EQ	92.1	14.9	14.9	1345	22.6	-1300.2
	Interior	Dead	-90	0	0	0	0	0
		Live	-55	0	0	0	0	0
		Snow	-5	0	0	0	0	0
		EQ	-5.9	26.7	26.7	2384.7	21	-2342.5

1 kip = 4.44822 kN

1 kip-in = 0.113 kN-m

Table 5.8: Final column sections

Storey	Location	Section	K_x
4	Exterior	W8×18	1.10
	Interior	W8×21	1.07
3	Exterior	W12×35	1.25
	Interior	W12×50	1.17
2	Exterior	W12×35	1.25
	Interior	W12×50	1.17
1	Exterior	W14×53	1.86
	Interior	W18×60	1.84

Table 5.9: Column base connection assumptions in OpenSees model

Variable	Exterior (W14X53)	Interior (W18X60)
Column depth (mm)	354	464
Column flange width (mm)	205	192
Column web thickness (mm)	9.4	10.6
Column flange thickness (mm)	16.7	17.7
Column radius of fillet at web and flange (mm)	15.0	10.3
Base plate length (mm)	610	711
Base plate width (mm)	457	508
Base plate thickness (mm)	57.15	63.5
Number segments to define type of anchor rods material	1	1
Anchor rods diameter (mm)	76	83
Location of anchor rods from edge of the base plate (mm)	64	64
Anchor rods length (mm)	940	940
Number of anchor rods per row	2	2
Number of Winkler elements	7	8
Length of Winkler elements (mm)	508	508
Stiffness factor of Winkler elements	1	1
Young's modulus for concrete/grout (GPa)	25	25
Damping factor for anchor rods elements	0.000005	0.000005
Damping factor for Winkler elements	0.00000001	0.00000001

Table 5.10: Details of infill walls' material and assumptions in OpenSees model

Variable	1 st storey	Typical storeys	Unit	Assumptions
f_{ib}	0.38	0.38	MPa	Furtado et al. (2020)
L_i	5540	5690	mm	Bay length – W18 depth
H_i	3970	3070	mm	Storey height – W21 depth
C_I	2.69	3.57	–	Using Furtado et al. (2015) equation
t	100	100	mm	
$f_{i,max}$	0.447	0.410	MPa	Using Furtado et al. (2015) equation
$f_{i,c}$	0.246	0.225	MPa	55% $f_{i,max}$
$f_{i,y}$	0.313	0.287	MPa	70% $f_{i,max}$
$f_{i,r}$	0.089	0.082	MPa	20% $f_{i,max}$
$\delta_{i,max}$	0.45	0.45	%	Range 0.250 – 0.50
$\delta_{i,c}$	0.1	0.1	%	Range 0.075 – 0.12
$\delta_{i,y}$	0.25	0.25	%	Range 0.150 – 0.35
$\delta_{i,r}$	1.25	1.25	%	5 $\delta_{i,y}$

Table 5.11: Eigenvalue analysis results, periods in sec

Mode	BSF	SFX	SFM	SFR
T_1	1.569	1.604	1.296	1.297
T_2	0.662	0.672	0.554	0.554
T_3	0.356	0.363	0.317	0.318
T_4	0.212	0.215	0.203	0.203

Table 5.12: 2% per 50 years acceleration using NBC 2020 Seismic Hazard Tool

$S(0.05)$	$S(0.1)$	$S(0.2)$	$S(0.3)$	$S(0.5)$	$S(1.0)$	$S(2.0)$	$S(5.0)$	$S(10.0)$	PGA	PGV
1.27	1.18	0.84	0.66	0.49	0.26	0.12	0.03	0.01	0.459	0.336

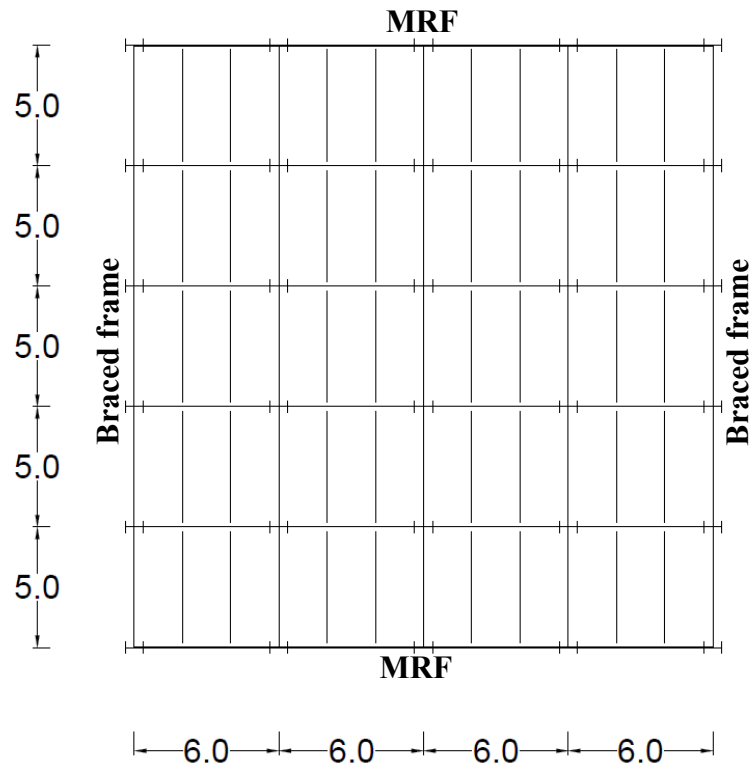


Figure 5.1: Building layout, dimensions in m

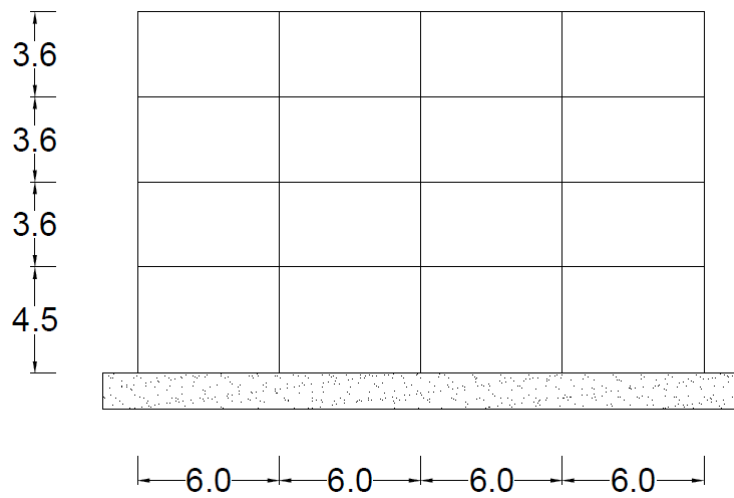


Figure 5.2: Building elevation, dimensions in m

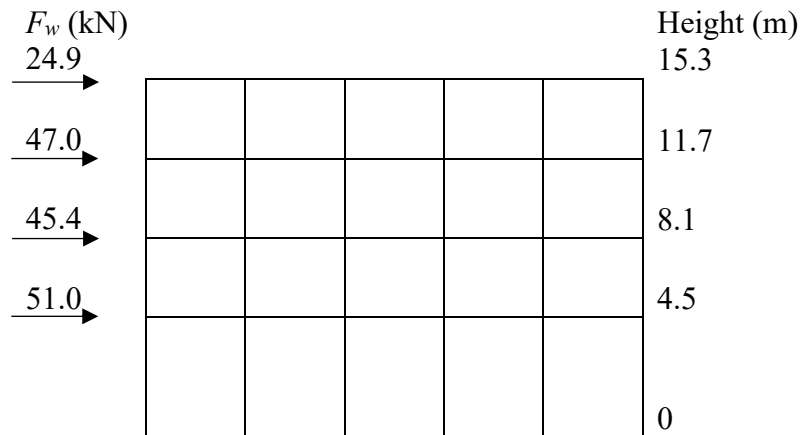


Figure 5.3: MRF wind loads.

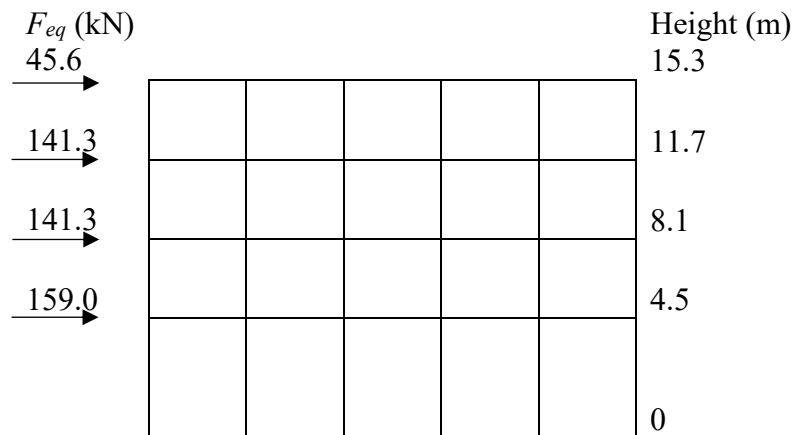


Figure 5.4: MRF earthquake loads.

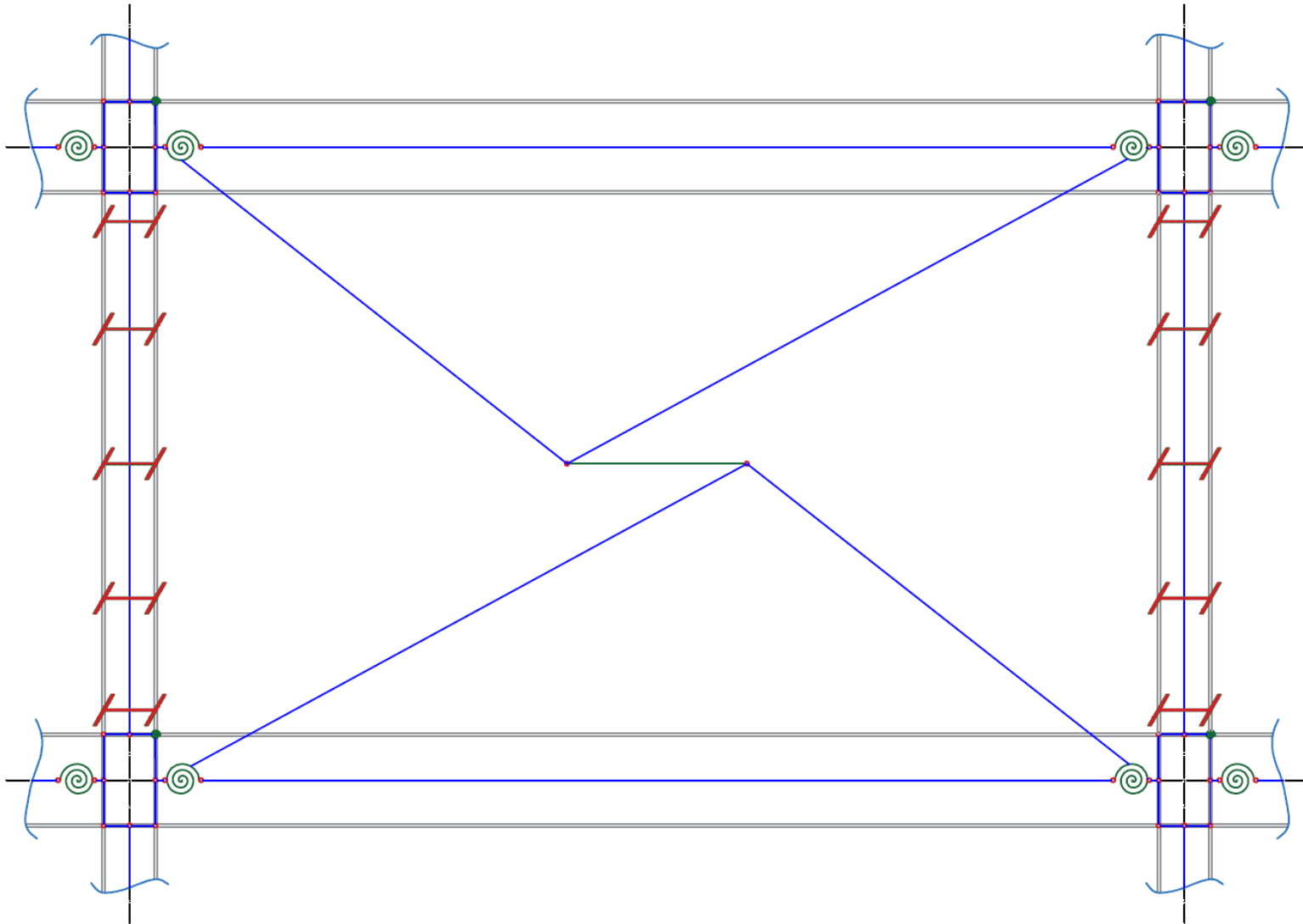


Figure 5.5: Representation of OpenSees model

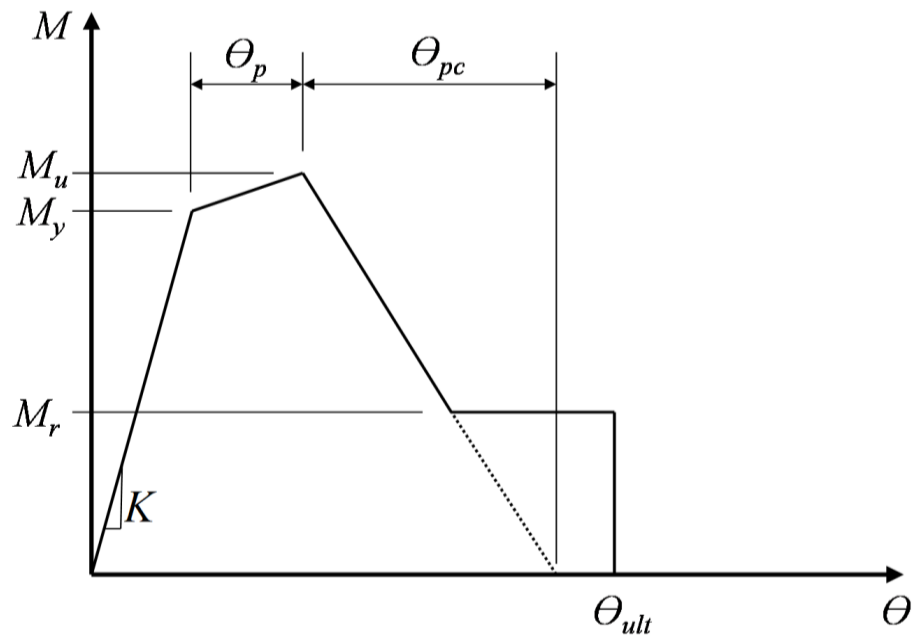


Figure 5.6: Idealized moment-rotation relation's backbone curve

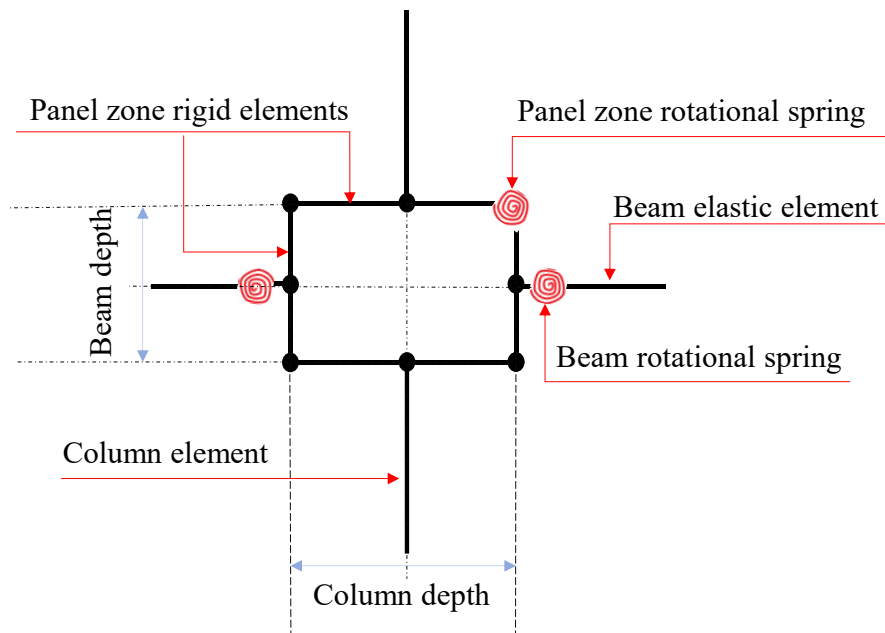


Figure 5.7: Schematic of the panel zone parallelogram model

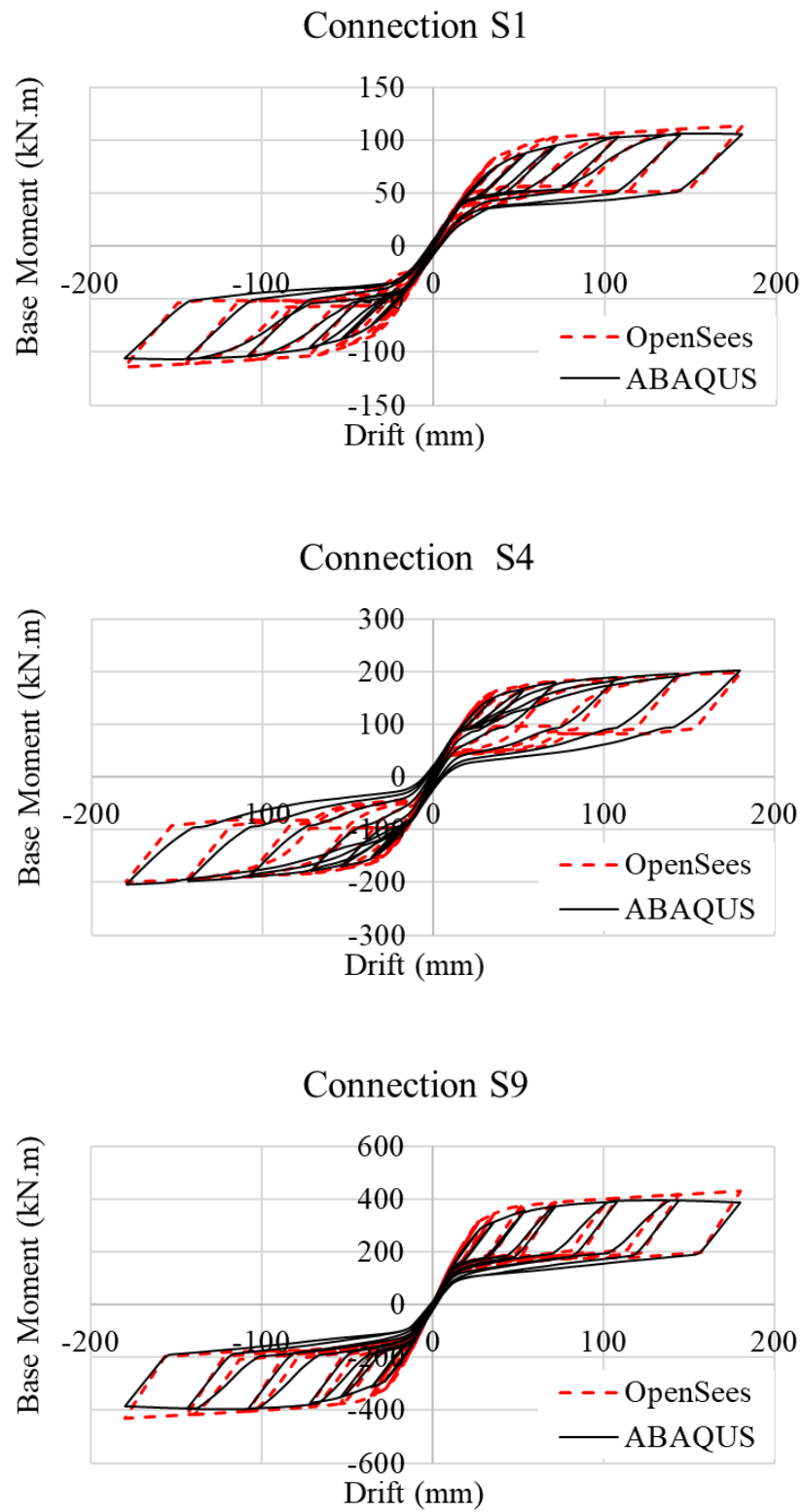


Figure 5.8: Column base connections' response in ABAQUS vs OpenSees

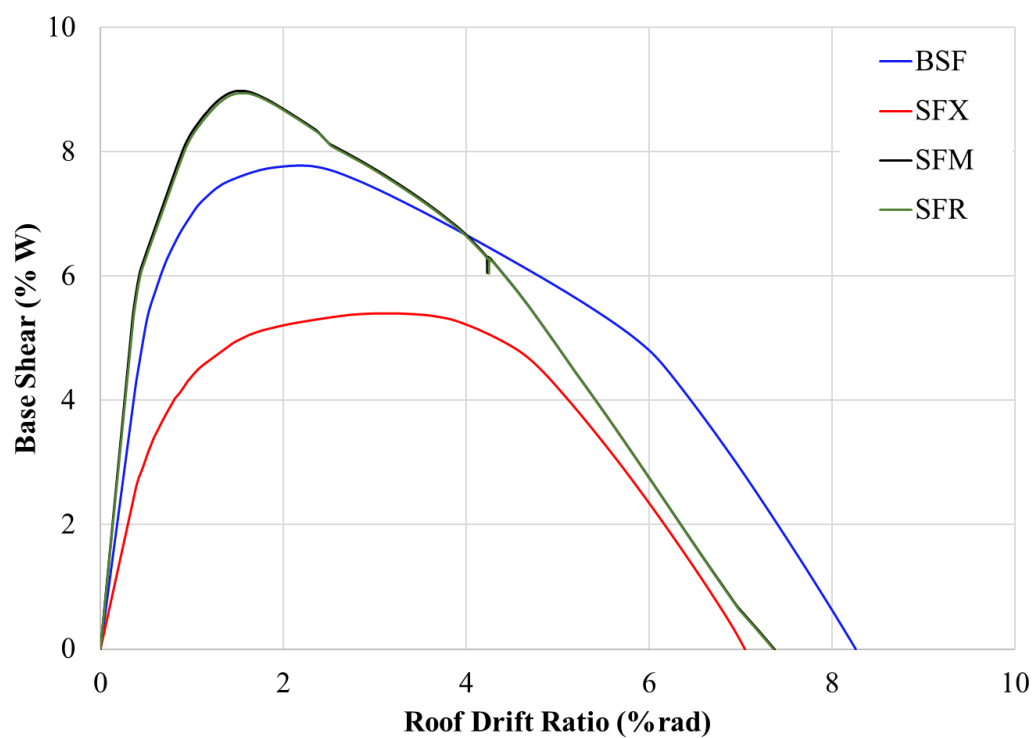


Figure 5.9: Pushover base shear vs roof drift ratios

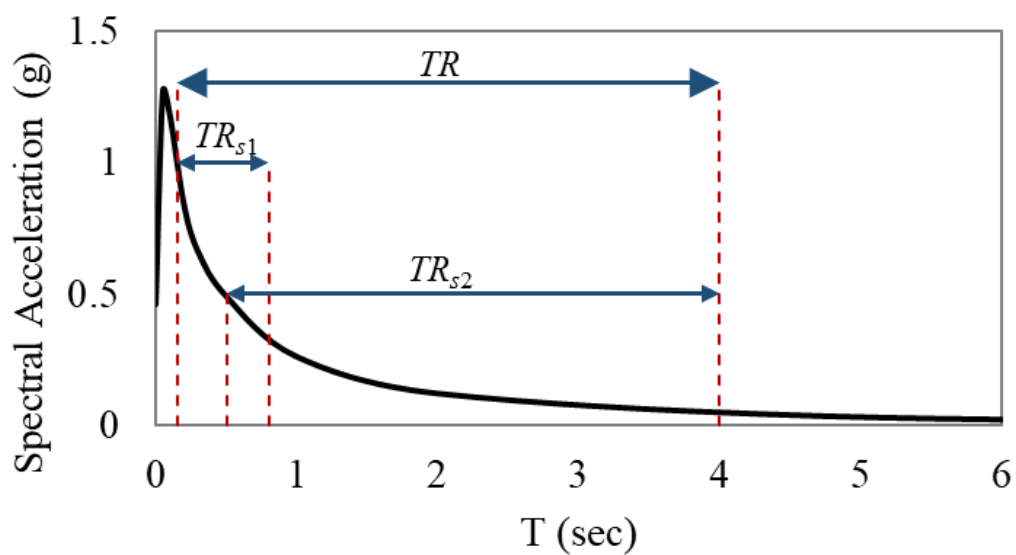


Figure 5.10: Target spectrum and period ranges

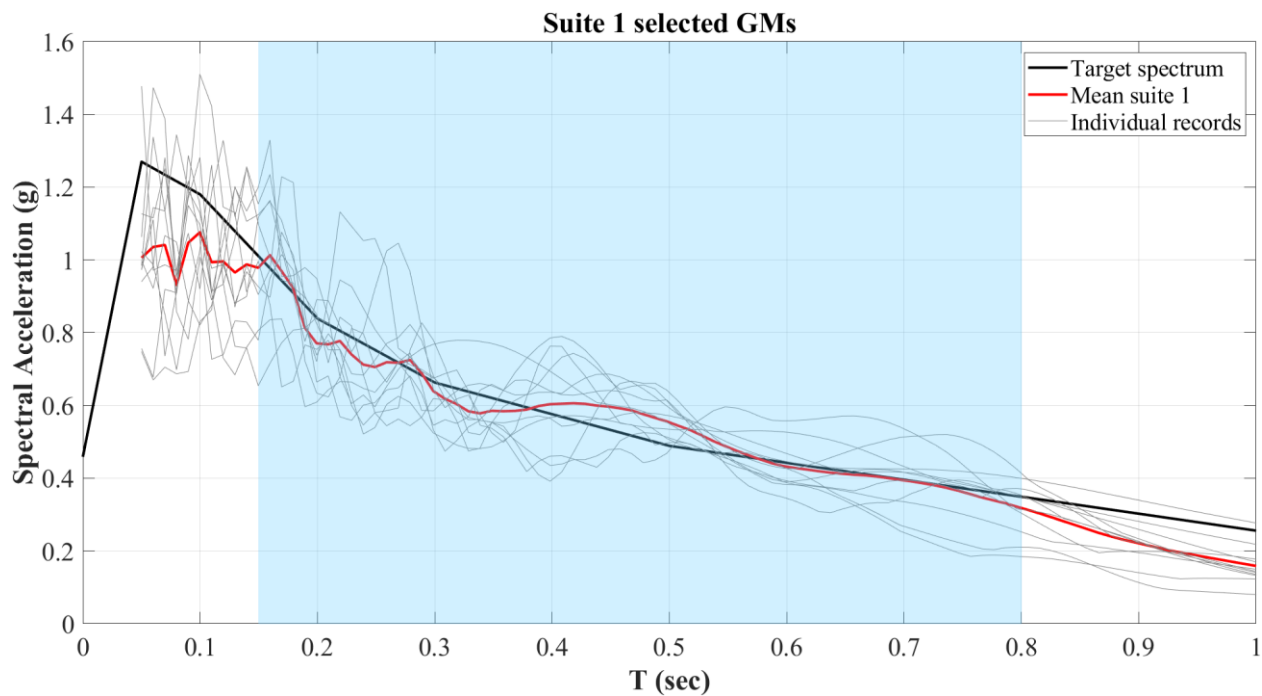


Figure 5.11: Target spectrum and suite 1 individual records

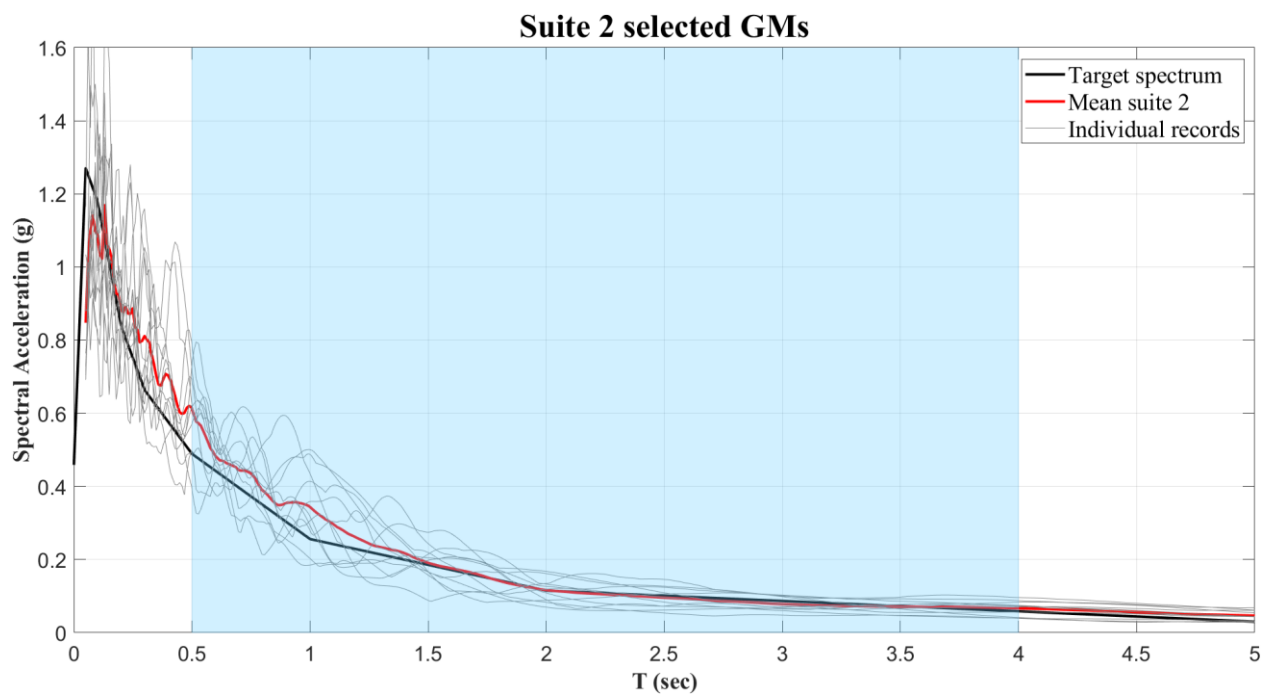


Figure 5.12: Target spectrum and suite 2 individual records

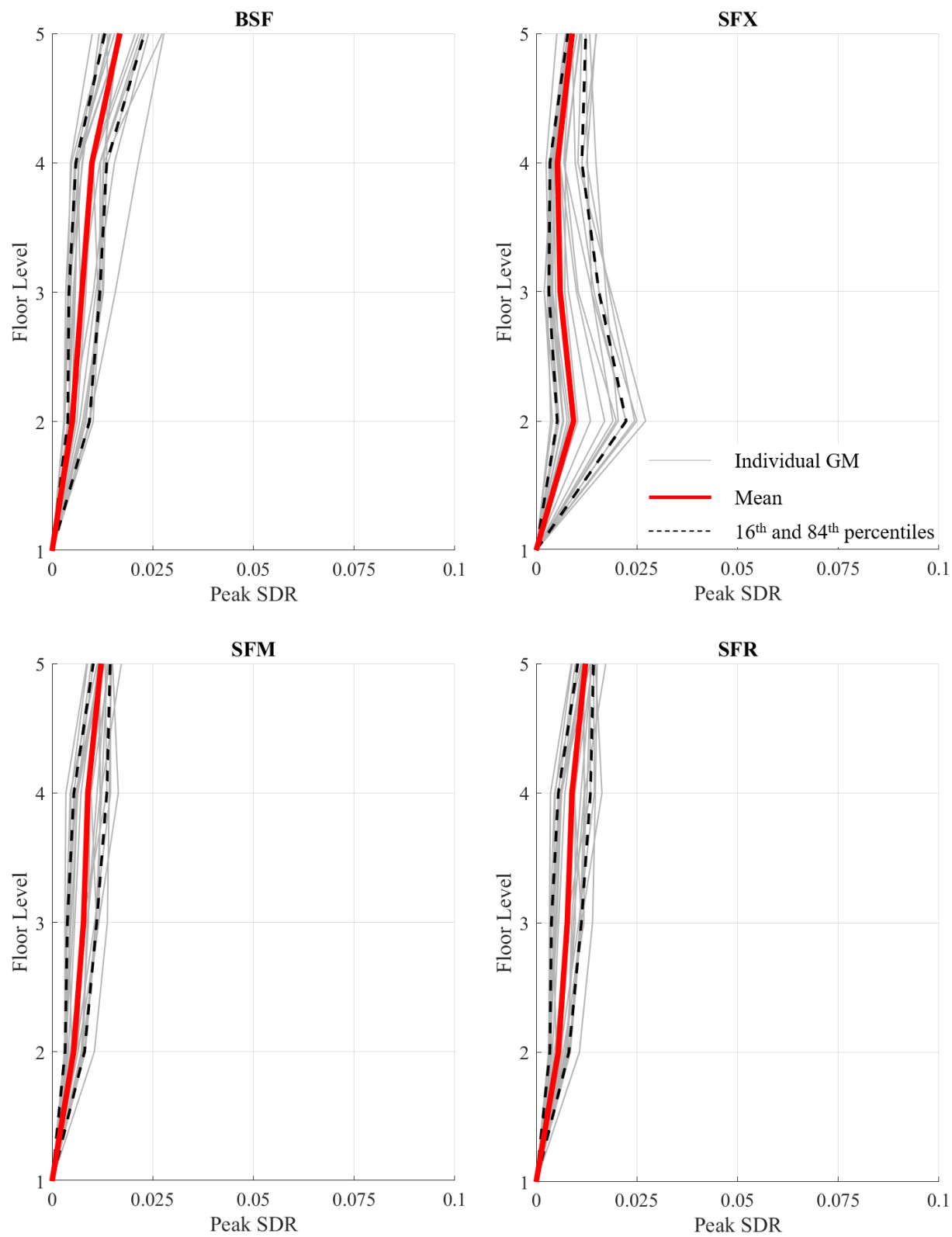


Figure 5.13: NRHA peak SDR

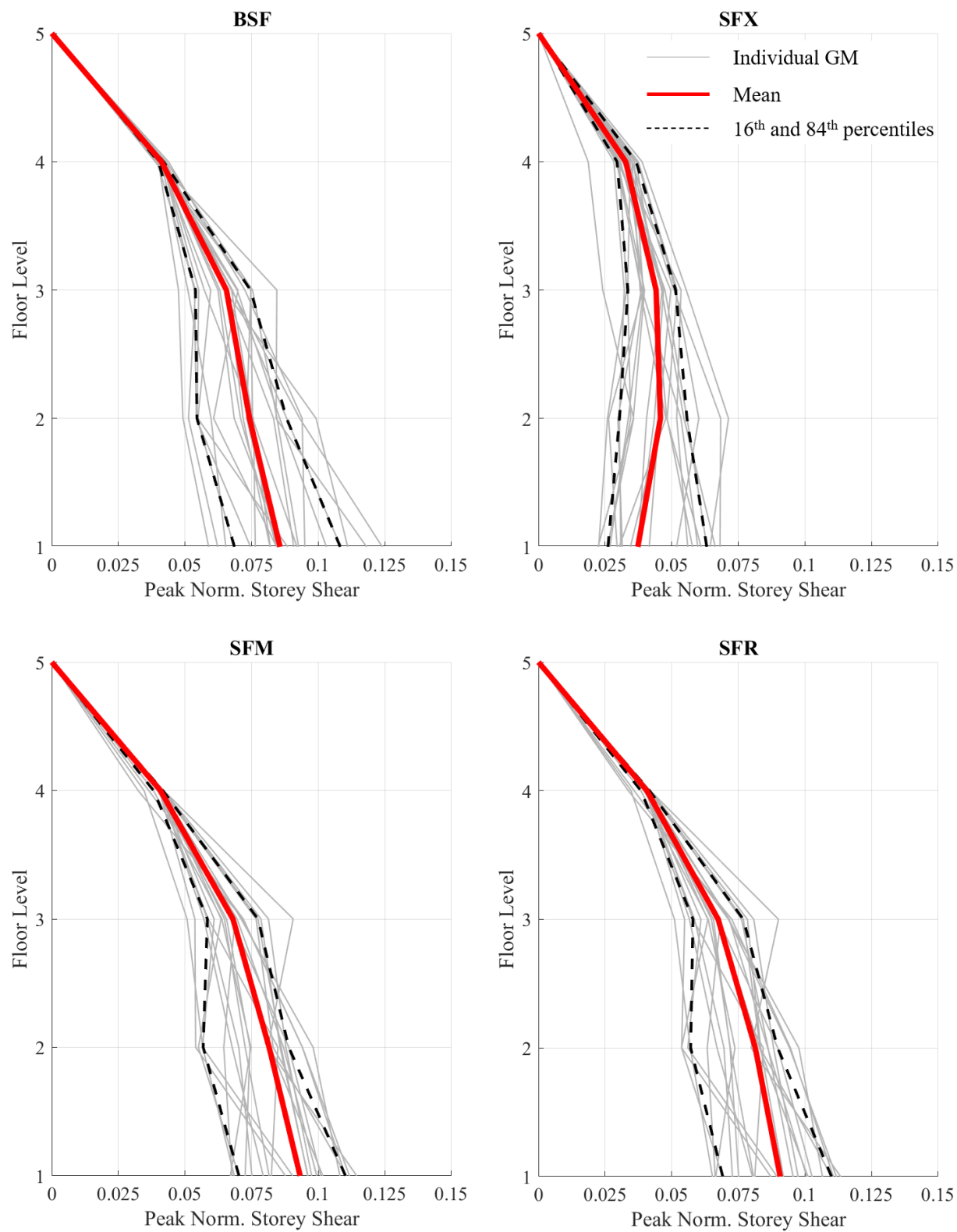


Figure 5.14: NRHA peak normalized storey shear

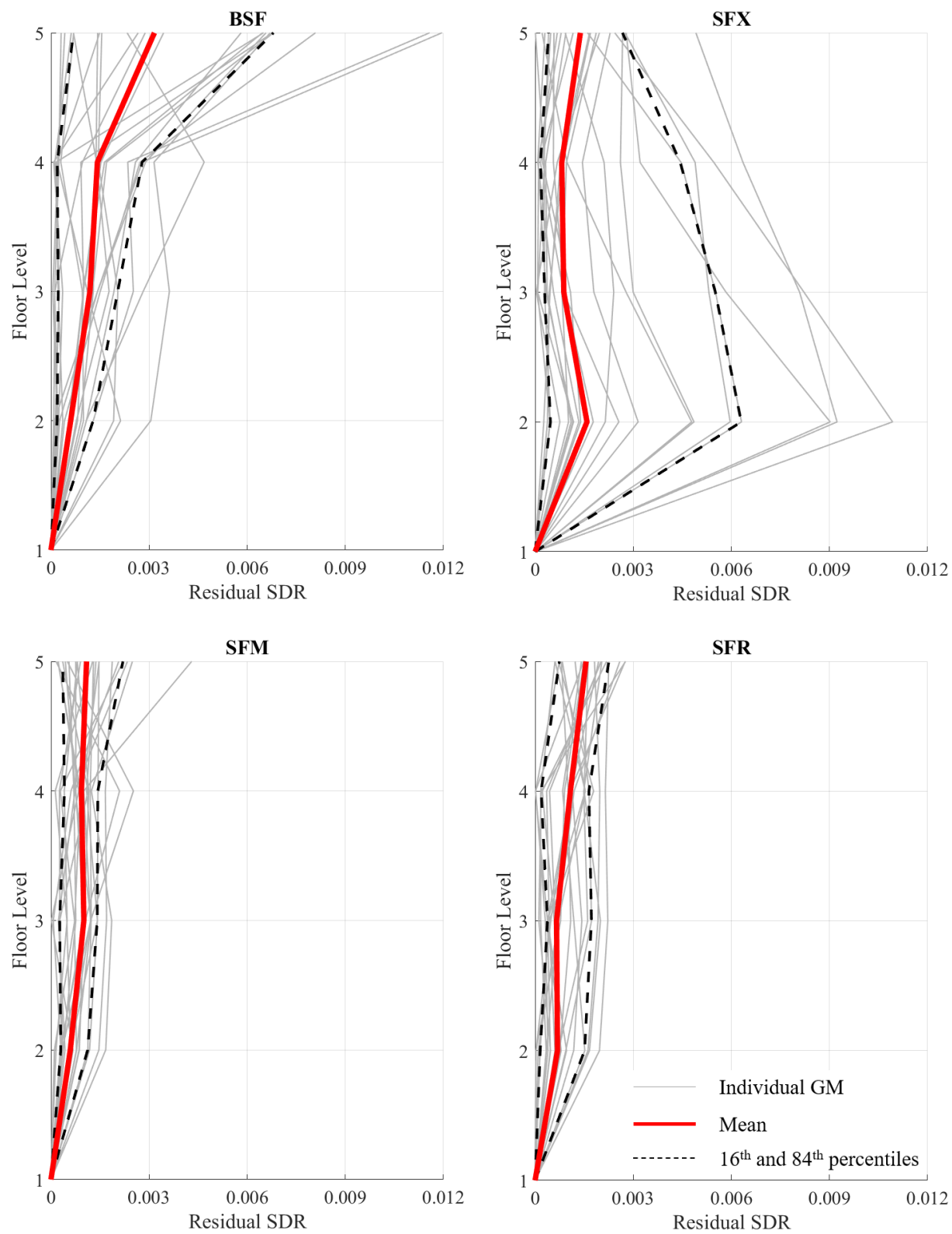


Figure 5.15: NRHA residual SDR

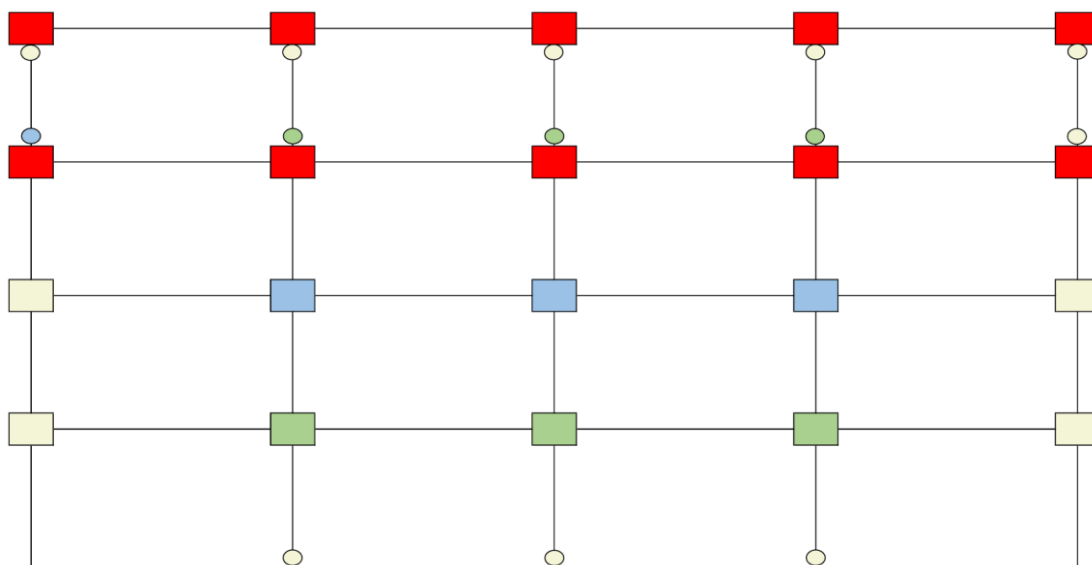


Figure 5.16: Elements probability of yielding across the 22 ground motions – BSF model

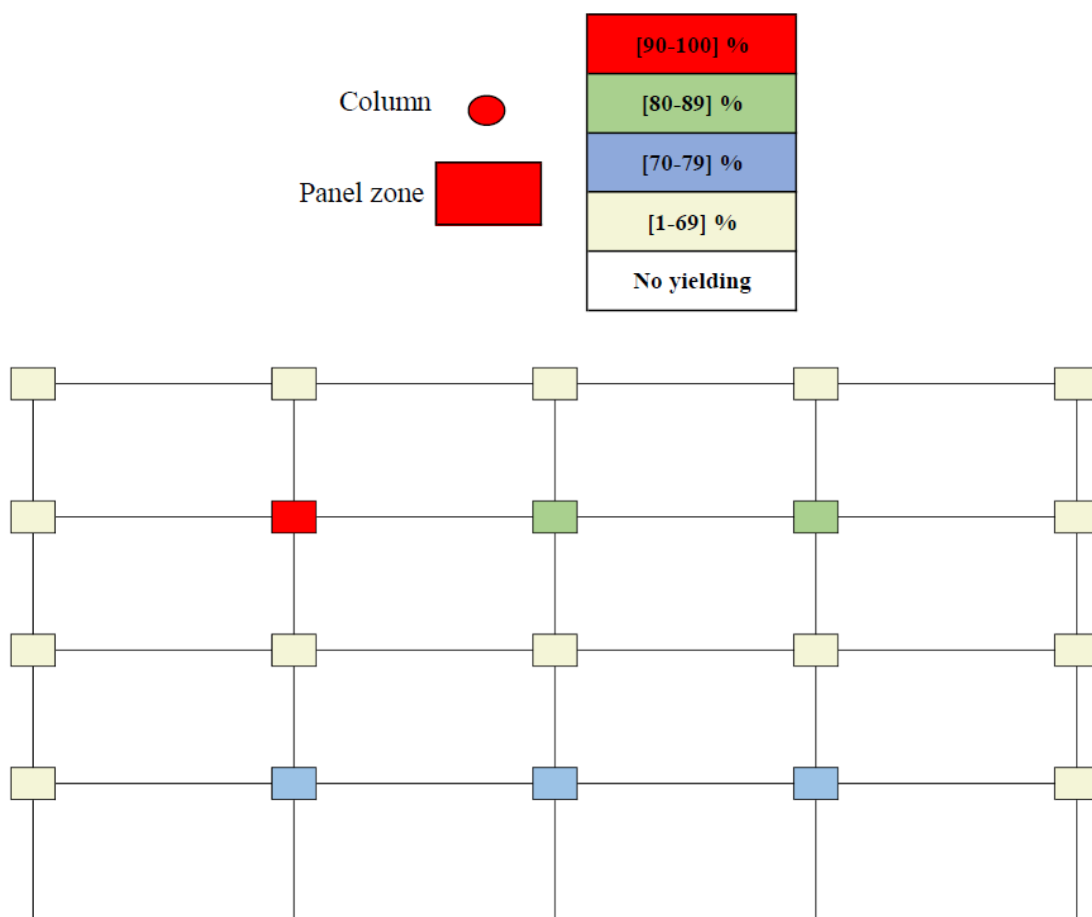


Figure 5.17: Elements probability of yielding across the 22 ground motions – SFX model

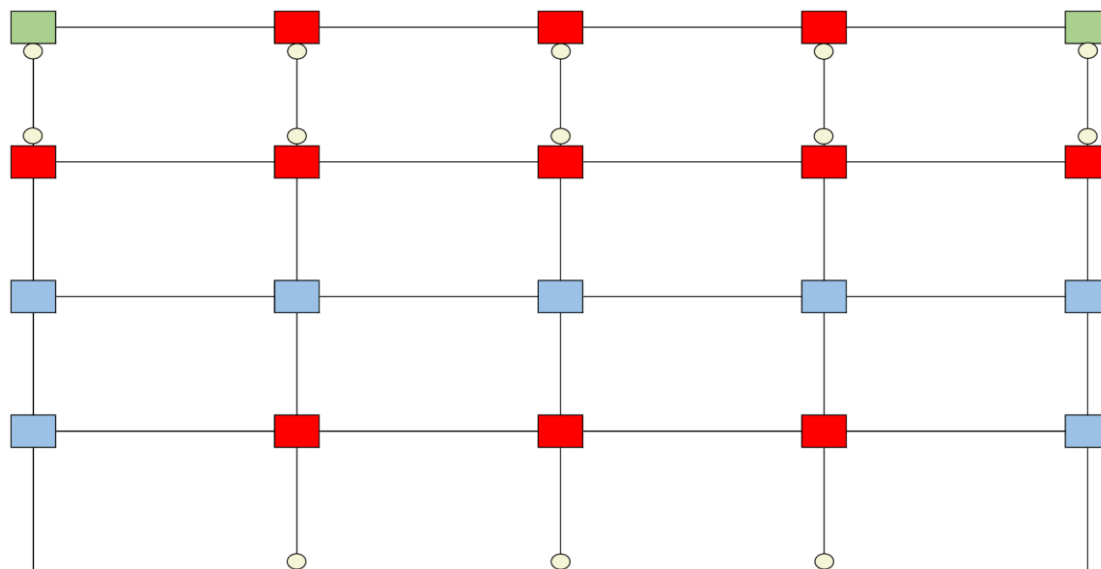


Figure 5.18: Elements probability of yielding across the 22 ground motions – SFM model

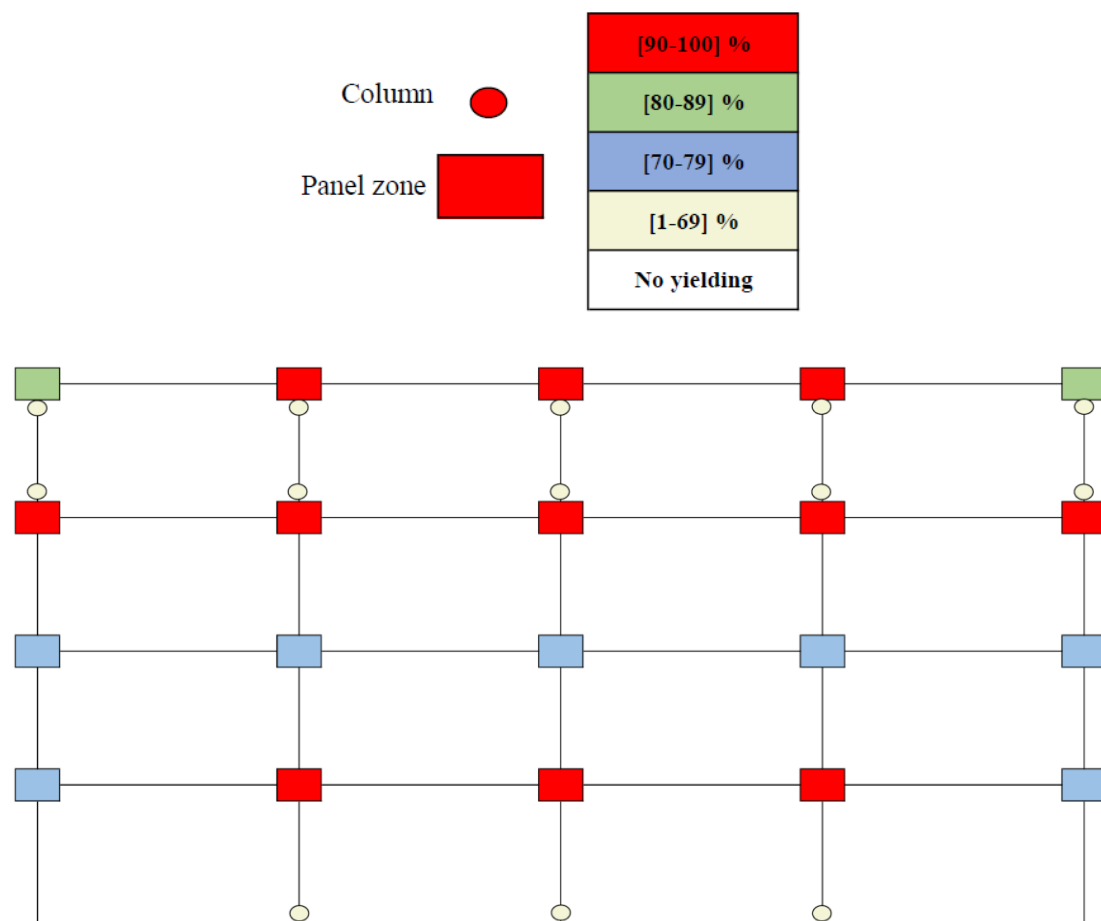


Figure 5.19: Elements probability of yielding across the 22 ground motions – SFR model

Chapter 6: Research Summary and Conclusions

6.1 Summary

The main objective of this research is to evaluate the seismic performance of existing steel MRF structures built before the 1990s in regions of moderate seismic activity in North America. The motivation behind selecting this topic stems from several factors: significant uncertainties exist in assessing the ability of old steel MRF structures to withstand seismic events under the latest standards, contradictory conclusions arise regarding the performance of old construction and design practices of beam-to-column connections, there is a limited number of studies in the literature focusing on column base connections, and the importance of incorporating unreinforced masonry infill walls in the assessment of steel MRF structures, which has received limited attention in the literature.

The objective was achieved through conducting a comprehensive literature review of the related research, identifying research gaps, conducting experimental testing on column base connections, developing FE models to evaluate the cyclic response of column base connections, conducting a parametric study aimed at assessing the influence of various factors on column base connections, designing a prototype hospital building according to 1960s standards, and developing numerical models for subsequent execution of nonlinear static and response history analyses to evaluate the seismic performance of existing steel MRF structures while incorporating column base connections and unreinforced masonry infill walls.

6.2 Conclusions

6.2.1 Experimental testing on column base connections

The full-scale reversed cyclic tests conducted on column base connections, comprising either two or four L-shaped anchor rods and incorporating the influence of anchor rod corrosion, yielded the following conclusions:

- All specimens exhibited plastic deformations in the anchor rods and demonstrated pinch and slip hysteresis. While the four-AR specimens showed a symmetric moment-deformation hysteresis, the behaviour of the two-AR specimens' hysteresis was asymmetric and influenced by the initial loading direction.
- The number and configuration of anchor rods significantly influenced the strength of the connections. Specifically, the four-AR specimens exhibited approximately 58% and 56% larger peak and yielding moments, respectively, compared to the two-AR specimens.
- Specimens with anchor rods considering corrosion effects (i.e., 2-AR-C and 4-AR-C) demonstrated smaller base rotation angles at yielding, resulting in higher ductility factors compared to their counterpart specimens.
- All specimens demonstrated the ability to dissipate energy through inelastic deformations. The corrosion effect on the energy dissipation capacity of anchor rods was more pronounced in the two-AR specimens, while the four-AR specimens exhibited nearly identical cumulative energy dissipation capacity at the conclusion of testing.

6.2.2 Development of FE models and parametric study

The parametric study conducted on the column base connections, following the FE modeling and validation, investigated the influence of the anchor rods' diameter and transverse spacing, the base plate thickness and dimensions, the column section size, the level of axial loading and the grade of steel used in the base plate on the cyclic performance of the column base connections.

The findings from this study are summarized as follows:

- The simulated connections were classified into three groups: rigid, flexible and intermediate base plate connections, based on their mode of failure and deformed shapes. The type of base plate played a significant role in affecting moment-rotation relationships, ductility and energy dissipation capacity of the connections across different parameters.
- Increasing the anchor rods' diameter resulted in larger yielding and ultimate moments, along with increased energy dissipation capacity, albeit at the expense of reduced ductility.
- Rigid base plate connections showed higher sensitivity to changes in the base plate dimensions, with increased dimensions decreasing ductility but enhancing energy dissipation.
- Larger column section sizes improved moment-rotation relationships while increasing both ductility and energy dissipation capacity.
- Larger base plate thickness increased connection rigidity, enhancing initial stiffness but decreasing both ductility and energy dissipation.
- Higher levels of axial loading were associated with increased moment capacity, initial stiffness and ductility, albeit with decreased energy dissipation.

- The use of higher-grade steel for the base plate had minimal effects on moment capacity, ductility and energy dissipation but increased initial stiffness for flexible base plate connections and decreased it for intermediate base plate connections.
- Varying transverse spacing between anchor rods had a pronounced impact on rigid base plate connections, with misalignment reducing ductility. Decreasing transverse spacing reduced energy dissipation in rigid connections but increased it in intermediate ones.

6.2.3 Design of a prototype building and seismic assessment

The assessment of existing steel MRF structures involved the design of a hospital steel MRF building in Montreal City, Eastern Canada, adhering to the 1965 NBC (NRC, 1967) standard. Four 2D nonlinear building models were developed: a bare steel frame (BSF), a steel frame with realistic modeling of column base connections (SFX), a steel frame model considering unreinforced masonry infill walls (SFM) and a comprehensive steel frame model integrating all aforementioned components (SFR). These models underwent nonlinear static and response history analyses, with the main findings summarized as follows:

- The case study revealed that earthquake loadings, contrary to recent studies, can control the lateral load-resisting system design. Moreover, designing beams as simply supported elements under gravity loading, following the Type Two design approach in the 1965 NBC NRC (1967), resulted in a strong beam – weak column design, now prohibited by contemporary standards, particularly critical given the mandate of capacity design provisions.
- Accounting for column base connections and unreinforced masonry infill walls proved crucial, as it altered the dynamic properties of the structure, impacting its natural frequency

and period, vital factors in contemporary design standards such as the 2020 NBC, NRC (2022). Moreover, In the pushover analysis, considering column base connections led to a 30% decrease in peak base shear, while incorporating infill walls resulted in a 15% increase compared to the bare steel frame model.

- The NRHA highlighted that accounting for column base connections, as in the SFX model, introduced a soft first-storey mechanism, resulting in increased SDR and residual inter-storey drifts, along with reduced storey shear resistance, emphasising the significance of considering these connections in the evaluation existing steel MRF structures.
- Damage predominantly occurred in the top storey of the BSF, SFM, and SFR models, with the bare steel frame exhibiting the largest SDR due to weaker members selected for the top storey during design.
- Infill walls significantly influenced dynamic properties, with the SFM and SFR models showing more uniform and smaller SDR and residual drifts compared to BSF and SFX models.
- No beam yielding occurred, but columns in the top storey of BSF, SFM, and SFR models experienced yielding, along with the base of interior columns in the first storey. The SFX model, however, experienced no beam or column yielding, attributed to the energy dissipation through column base connections.

6.3 Limitations and recommendations for future studies

Given the broad spectrum and significance of the topic, the following recommendations are proposed based on the limitations encountered and to further the understanding of the topic:

- Considering the research scope and time constraints, the testing program was limited to two nominal connections (one with two anchor rods and one with four anchor rods). Therefore, it's recommended that further experimental studies be conducted to deepen our understanding of exposed column base connections in existing steel MRF structures. These studies could investigate additional configurations, such as employing four anchor rods within column flanges, partial welding and the utilization of leveling nuts. Additionally, conducting cyclic testing on steel components to evaluate hardening parameters and further testing on the mechanical properties of the grout material should significantly enhance the modeling of these connections.
- The methodology used to account for anchor rods' corrosion, although it provided insightful conclusions regarding its impact on the performance of column base connections, involved milling and pitting predefined locations on the anchor rods. A more realistic representation, and therefore a better understanding, could be achieved by constructing these connections and subjecting them to accelerated corrosion, which would affect the entire body of the anchor rods.
- Site surveys of existing steel MRF structures are essential due to the limited documentation available on their construction and any potential damage they may have incurred over time. These surveys are crucial for designing testing programs and will greatly enhance the modeling of beam-to-column connections, column base connections and connections between infill walls and the frame.
- The nonlinear assessment of existing steel MRF structures conducted in this research was limited to 2D modeling of a four-storey building, utilizing macro in-plane modeling of unreinforced masonry infill walls and based on design spectrum.

Expanding the analysis to include 3D modeling covering a broader range of storeys, multi-directional shaking, and collapse risk evaluation would significantly enhance our understanding of the seismic vulnerability of existing steel MRF structures.

Bibliography

Anderson, J. C., & Gupta, R. P. (1972). Earthquake resistant design of unbraced frames. *Journal of the Structural Division*, 98(11), 2523-2539.

Andrade, C., Alonso, C., & Molina, F. J. (1993). Cover cracking as a function of bar corrosion: Part I-Experimental test. *Materials and structures*, 26, 453-464.

Arnold, P., Adams, P. F., & Lu, L. W. (1968). Strength and behavior of an inelastic hybrid frame. *Journal of the Structural Division*, 94(1), 243-266.

Asgarian, A., & McClure, G. (2014). Impact of seismic rehabilitation and presence of unreinforced masonry (URM) infill walls on the dynamic characteristics of a hospital building in Montreal. *Canadian Journal of Civil Engineering*, 41(8), 748-760.

ASTM A36. (1966). Standard Specification for Structural Steel 1966, A36-66. American Society for Testing and Materials. West Conshohocken, PA, United States.

Atkinson, G. M. (2009). Earthquake time histories compatible with the 2005 National building code of Canada uniform hazard spectrum. *Canadian Journal of Civil Engineering*, 36(6), 991-1000.

Benenson, W., Harris, J. W., & Stocker, H. (2002). *Handbook of physics* (p. 430). H. Lutz (Ed.). New York: Springer.

Bertero, V., & Brokken, S. (1983). Infills in seismic resistant building. *Journal of Structural Engineering*, 109(6), 1337-1361.

Biddah, A., & Heidebrecht, A. C. (1998). Seismic performance of moment-resisting steel frame structures designed for different levels of seismic hazard. *Earthquake spectra*, 14(4), 597-627.

Carpenter, L. D., & Lu, L. W. (1973). Reversed and repeated lost tests of full-scale steel frames.

Castro e Sousa, A. D., Hartloper, A. R., & Lignos, D. G. (2021). Cyclic metal plasticity model parameters with limited information: Constrained optimization approach. *Journal of Engineering Mechanics*, 147(7), 04021035.

Celarec, D., Vamvatsikos, D., & Dolšek, M. (2011). Simplified estimation of seismic risk for

reinforced concrete buildings with consideration of corrosion over time. *Bulletin of Earthquake Engineering*, 9, 1137-1155.

Chaboche, J. L., Van, K. D., & Cordier, G. (1979). Modelization of the strain memory effect on the cyclic hardening of 316 stainless steel.

CISC (1970). Handbook of Steel Construction, CAN/CSA S16-1969. Canadian Institute of Steel Construction, Willowdale, ON, Canada.

Clark, P., Frank, K., Krawinkler, H., & Shaw, R. (1997). Protocol for Fabrication, Inspection, Testing, and Documentation of Beam-Column Connection Tests and Other Experimental Specimens. Report No. SAC/BD-97. SAC Joint Venture.

Clough, R. W., & Benuska, K. L. (1967). Nonlinear earthquake behavior of tall buildings. *Journal of the Engineering Mechanics Division*, 93(3), 129-146.

Crisafulli, F. J., & Carr, A. J. (2007). Proposed macro-model for the analysis of infilled frame structures. *Bulletin of the New Zealand society for earthquake engineering*, 40(2), 69-77.

CSA. (2014a). Compressive Strength of Cylindrical Concrete Specimens, CSA A23.2-9C-14. Canadian Standards Association, Rexdale, Canada.

CSA (1970). Design of Steel Structures, CAN/CSA S16-1969, Canadian Standards Association, Mississauga, ON, Canada.

CSA. (2014b). Splitting Tensile Strength of Cylindrical Concrete Specimens, CSA A23.2-13C-14. Canadian Standards Association, Rexdale, Canada.

CSA. (2014c). Flexural Strength of Concrete (Using a Simple Beam with Third Point Loading), CSA A23.2-8C-14. Canadian Standards Association, Rexdale, Canada.

CSA. (2004). Design of masonry structures, CSA S304. Canadian Standards Association, Mississauga, Canada.

Dassault Systèmes. (2020). *ABAQUS CAE*. Dassault Systèmes Simulia Corp., Providence, RI, USA.

Dhanasekhar, M. P. A. W., & Page, A. W. (1986). The influence of brick masonry infill properties on the behaviour of infilled frames. *Proceedings of the Institution of Civil Engineers*, 81(4), 593-605.

- Di Sarno, L., Freddi, F., D'Aniello, M., Kwon, O. S., Wu, J. R., Gutiérrez-Urzúa, F., ... & Strepelias, E. (2021). Assessment of existing steel frames: Numerical study, pseudo-dynamic testing and influence of masonry infills. *Journal of Constructional Steel Research*, *185*, 106873.
- Di Sarno, L., & Wu, J. R. (2021). Fragility assessment of existing low-rise steel moment-resisting frames with masonry infills under mainshock-aftershock earthquake sequences. *Bulletin of Earthquake Engineering*, *19*(6), 2483-2504.
- Dolšek, M., & Fajfar, P. (2002). Mathematical modelling of an infilled RC frame structure based on the results of pseudo-dynamic tests. *Earthquake engineering & structural dynamics*, *31*(6), 1215-1230.
- Engelhardt, M. D., & Husain, A. S. (1993). Cyclic-loading performance of welded flange-bolted web connections. *Journal of Structural Engineering*, *119*(12), 3537-3550.
- El-Dakhakhni, W. W., Elgaaly, M., & Hamid, A. A. (2003). Three-strut model for concrete masonry-infilled steel frames. *Journal of Structural Engineering*, *129*(2), 177-185.
- El-Dakhakhni, W. W., Hamid, A. A., & Elgaaly, M. (2004). Seismic retrofit of concrete-masonry-infilled steel frames with glass fiber-reinforced polymer laminates. *Journal of Structural Engineering*, *130*(9), 1343-1352.
- Elkady, A., and Lignos, D. G. (2015). "Effect of gravity framing on the overstrength and collapse capacity of steel frame buildings with perimeter special moment frames." *Earthquake Engineering & Structural Dynamics*, *44*(8), 1289–1307, DOI: 10.1002/eqe.2519.
- Fahmy, M. (2000). Seismic behavior of moment-resisting steel column bases. Doctoral Thesis, University of Michigan.
- Farazman, S., Izzuddin, B. A., & Cormie, D. (2013). Influence of unreinforced masonry infill panels on the robustness of multistory buildings. *Journal of Performance of Constructed Facilities*, *27*(6), 673-682.
- Fiorato, A. E. (1971). An investigation of the interaction of reinforced concrete frames with masonry filler walls. University of Illinois at Urbana-Champaign.
- Furtado, A., Rodrigues, H., & Arêde, A. (2015). Modelling of masonry infill walls participation in the seismic behaviour of RC buildings using OpenSees. *International Journal of Advanced Structural Engineering (IJASE)*, *7*, 117-127.

Furtado, A., Rodrigues, H., Arêde, A., & Varum, H. (2020). Mechanical properties characterization of different types of masonry infill walls. *Frontiers of Structural and Civil Engineering, 14*, 411-434.

Gomez, I. R. (2010). Behavior and design of column base connections. Doctoral Thesis, University of California.

Gomez, L. V. D., Kwon, O. S., & Dabirvaziri, M. R. (2015). Seismic fragility of steel moment-resisting frames in Vancouver and Montreal designed in the 1960s, 1980s, and 2010. *Canadian Journal of Civil Engineering, 42*(11), 919-929.

Grauvilardell, J. E., Lee, D., Hajjar, J. F., & Dexter, R. J. (2005). Synthesis of design, testing and analysis research on steel column base plate connections in high-seismic zones. Structural engineering report no. ST-04-02. Minneapolis (MN): Department of Civil Engineering, University of Minnesota.

Gupta, A. (1999). Seismic demands for performance evaluation of steel moment resisting frame structures. Doctoral Thesis at Stanford University.

Gupta, A., and Krawinkler, H. (1999). "Seismic demands for the performance evaluation of steel moment resisting frame structures." *Report No. 132*, The John A. Blume Earthquake Engineering Center, Stanford University, CA.

Halchuk, S., Adams, J., & Anglin, F. (2007, June). Revised deaggregation of seismic hazard for selected Canadian cities. In *9th Canadian conference on earthquake engineering* (pp. 420-432).

Hariri, B. (2023). *Innovative steel bracing systems for tall building application in high seismic regions*. Doctoral Thesis at Polytechnique Montréal.

Hartloper, A. R. (2016). *Updates to the Asce-41-13 Nonlinear modelling provisions for performance-based seismic assessment of new existing steel moment resisting frames*. Master's Thesis at McGill University.

Hartloper, A. R., de Castro e Sousa, A., & Lignos, D. G. (2021). Constitutive modeling of structural steels: nonlinear isotropic/kinematic hardening material model and its calibration. *Journal of Structural Engineering, 147*(4), 04021031.

Hassan, A. S., Song, B., Galasso, C., & Kanvinde, A. (2022). Seismic performance of exposed column–base plate connections with ductile anchor rods. *Journal of Structural Engineering, 148*(5), 04022028.

Hassan, A. S., Torres-Rodas, P., Giulietti, L., & Kanvinde, A. (2021). Strength characterization of exposed column base plates subjected to axial force and biaxial bending. *Engineering Structures*, 237, 112165.

Humar, J. (2015). Background to some of the seismic design provisions of the 2015 National Building Code of Canada. *Canadian Journal of Civil Engineering*, 42(11), 940-952.

Ibarra, L. F., Medina, R. A., & Krawinkler, H. (2005). Hysteretic models that incorporate strength and stiffness deterioration. *Earthquake engineering & structural dynamics*, 34(12), 1489-1511.

Inamasu, H., de Castro e Sousa, A., Güell, G., & Lignos, D. G. (2021). Anchor-yield exposed column bases for minimizing residual deformations in seismic-resistant steel moment frames. *Earthquake Engineering & Structural Dynamics*, 50(4), 1083-1100.

Kabir, M. A. B. (2021). Behavior of exposed column base plate connection subjected to combined axial load and biaxial bending. Master's Thesis, Lakehead University.

Kanvinde, A. M., Grilli, D. A., & Zareian, F. (2012). Rotational stiffness of exposed column base connections: Experiments and analytical models. *Journal of Structural Engineering*, 138(5), 549-560.

Kavoura, F., Gencturk, B., & Dawood, M. (2017). Reversed cyclic behavior of column-to-foundation connections in low-rise metal buildings. *Journal of Structural Engineering*, 143(9), 04017095.

Kavoura, F., Gencturk, B., & Dawood, M. (2018). Evaluation of existing provisions for design of "pinned" column base-plate connections. *Journal of Constructional Steel Research*, 148, 233-250.

Klingner, R. E., & Bertero, V. (1977). Infilled frames in earthquake-resistant construction (Doctoral dissertation, University of California, Berkeley).

Krawinkler, H., & Mohasseb, S. (1987). Effects of panel zone deformations on seismic response. *Journal of Constructional Steel Research*, 8, 233-250.

Kyriakopoulos, N. (2012). Upgrade of seismically deficient steel frame structures built in Canada between the 1960s and 1980s using passive supplemental damping. Master's Thesis, University of Toronto.

Kyriakopoulos, N., & Christopoulos, C. (2013). Seismic assessment and upgrade of Type 2

construction steel moment-resisting frames built in Canada between the 1960s and 1980s using passive supplemental damping. *Canadian Journal of Civil Engineering*, 40(7), 644-654.

Leon, R., & Kim, D.H. (2004). Seismic performance of older PR frames in areas of infrequent seismicity. *13th World Conference on Earthquake Engineering*, Vancouver, B.C.

Lignos, D. G., Hartloper, A. R., Elkady, A., Deierlein, G. G., & Hamburger, R. (2019). Proposed updates to the ASCE 41 nonlinear modeling parameters for wide-flange steel columns in support of performance-based seismic engineering. *Journal of Structural Engineering*, 145(9), 04019083.

Lignos, D. G., & Krawinkler, H. (2011). Deterioration modeling of steel components in support of collapse prediction of steel moment frames under earthquake loading. *Journal of Structural Engineering*, 137(11), 1291-1302.

Lim, W. Y., Lee, D., & You, Y. C. (2017a). Exposed column-base plate strong-axis connections for small-size steel construction. *Journal of Constructional Steel Research*, 137, 286-296.

Lim, W. Y., Lee, D., & You, Y. C. (2017b). Cyclic loading tests on exposed column-base plate weak-axis connections of small-size steel structures. *Engineering Structures*, 153, 653-664.

Liu, Y., & Manesh, P. (2013). Concrete masonry infilled steel frames subjected to combined in-plane lateral and axial loading—An experimental study. *Engineering Structures*, 52, 331-339.

McKenna, F., Fenves, G. L., & Scott, M. H. (2000). Open system for earthquake engineering simulation (OpenSees). University of California, Berkeley, CA.

Mehrabi, A. B., & Shing, P. B. (1997). Finite element modeling of masonry-infilled RC frames. *Journal of structural engineering*, 123(5), 604-613.

Mehrabi, A. B., Shing, P. B., Schuller, M. P., & Noland, J. L. (1996). Experimental evaluation of masonry-infilled RC frames. *Journal of Structural Engineering*, 122(3), 228-237.

Memari, A. M., Aghakouchak, A. A., Ashtiany, M. G., & Tiv, M. (1999). Full-scale dynamic testing of a steel frame building during construction. *Engineering Structures*, 21(12), 1115-1127.

Mitchell, D., Paultre, P., Tinawi, R., Saatcioglu, M., Tremblay, R., Elwood, K., ... & DeVall, R. (2010). Evolution of seismic design provisions in the National Building Code of Canada.

Canadian Journal of Civil Engineering, 37(9), 1157-1170.

Nader, M. N., & Astaneh-Asl, A. (1989). Experimental studies of a single story steel structure with fixed, semi-rigid and flexible connections (Vol. 89, No. 15). Earthquake Engineering Research Center, University of California.

NIST (2017). Guidelines for Nonlinear Structural Analysis for Design of Buildings. Applied Technology Council. NIST GCR 17-917-46v1.

NRC. (1967). National Building Code of Canada, NBC 1965. National Research Council of Canada, Ottawa, ON.

NRC. (1971). National Building Code of Canada, NBC 1970. National Research Council of Canada, Ottawa, ON.

NRC. (1981). National Building Code of Canada, NBC 1980. National Research Council of Canada, Ottawa, ON.

NRC. (1986). National Building Code of Canada, NBC 1985. National Research Council of Canada, Ottawa, ON.

NRC. (1992). National Building Code of Canada, NBC 1990. National Research Council of Canada, Ottawa, ON.

NRC. (2003). National Building Code of Canada, NBC 1995. National Research Council of Canada, Ottawa, ON.

NRC. (2008). National Building Code of Canada, NBC 2005. National Research Council of Canada, Ottawa, ON.

NRC. (2010). National Building Code of Canada, NBC 2010. National Research Council of Canada, Ottawa, ON.

NRC. (2015). National Building Code of Canada, NBC 2015. National Research Council of Canada, Ottawa, ON.

NRC. (2022). National Building Code of Canada, NBC 2020. National Research Council of Canada, Ottawa, ON.

Picard, A., & Beaulieu, D. (1985). Behaviour of a simple column base connection. *Canadian Journal of Civil Engineering*, 12(1), 126-136.

- Picard, A., Beaulieu, D., & Perusse, B. (1987). Rotational restraint of a simple column base connection. *Canadian Journal of Civil Engineering*, 14(1), 49-57.
- Popov, E. P., & Bertero, V. V. (1973). Cyclic loading of steel beams and connections. *Journal of the Structural Division*, 99(6), 1189-1204.
- Popov, E. P., & Pinkney, B. R. (1969). Cyclic yield reversal in steel building connections. *Journal of the Structural Division*, 95(3), 327-353.
- Popov, E. P., Yang, T. S., & Chang, S. P. (1998). Design of steel MRF connections before and after 1994 Northridge earthquake. *Engineering Structures*, 20(12), 1030-1038.
- Rabbat, B. G., & Russell, H. G. (1985). Friction coefficient of steel on concrete or grout. *Journal of Structural Engineering*, 111(3), 505-515.
- Redwood, R. G., Lefki, L., & Amar, G. (1990). Earthquake resistant design of steel moment resisting frames. *Canadian Journal of Civil Engineering*, 17(4), 659-667.
- Rodas, P. T., Zareian, F., & Kanvinde, A. (2016). Hysteretic model for exposed column–base connections. *Journal of Structural Engineering*, 142(12), 04016137.
- Roeder, C. W., & Foutch, D. A. (1996). Experimental results for seismic resistant steel moment frame connections. *Journal of Structural Engineering*, 122(6), 581-588.
- Schmidt, T. (1989). Experiments on the nonlinear behaviour of masonry infilled reinforced concrete frames. *Darmstadt Concrete, Annual Journal on Concrete and Concrete Structures*, 4, 185–194.
- Shing, P. B., Lofti, H. R., Barzegarmehrabi, A., & Bunner, J. (1992, July). Finite element analysis of shear resistance of masonry wall panels with and without confining frames. In *Proc., 10th World Conf. on Earthquake Engrg* (pp. 2581-2586).
- SikaGrout® - 212. (2018). *Sika Canada INC. Product Data Sheet*: Pointe-Claire, QC.
- Singh, G., & Woods, J. (2022). 2D and 3D numerical modelling of exposed steel base plate connections under cyclic loading. *Canadian Journal of Civil Engineering*, 49(8), 1402-1414.
- Skiadopoulos, A., Elkady, A., & Lignos, D. G. (2021). Proposed panel zone model for seismic design of steel moment-resisting frames. *Journal of Structural Engineering*, 147(4), 04021006.

Stavridis, A., & Shing, P. B. (2010). Finite-element modeling of nonlinear behavior of masonry-infilled RC frames. *Journal of structural engineering*, 136(3), 285-296.

Stenecker, P., Wiebe, L., & Filiatrault, A. (2018). A Comparison of Recently Developed Analytical Models for Steel Moment-Resisting Frame Connections. In *CSCE Conference Proceedings*, Fredericton, NB.

Suzuki, Y. (2019). Earthquake-induced collapse of steel moment resisting frames with conventional and high performance steel columns. Doctoral Thesis, McGill University.

Tremblay, R., Timler, P., Bruneau, M., & Filiatrault, A. (1995). Performance of steel structures during the 1994 Northridge earthquake. *Canadian Journal of Civil Engineering*, 22(2), 338-360.

Tsai, K. C., & Popov, E. P. (1990). Cyclic behavior of end-plate moment connections. *Journal of Structural Engineering*, 116(11), 2917-2930.

Voce, E. (1948). The relationship between stress and strain for homogeneous deformation. *Journal of the Institute of Metals*, 74, 537-562.

Wu, J. R., Di Sarno, L., Freddi, F., & D'Aniello, M. (2022). Modelling of masonry infills in existing steel moment-resisting frames: Nonlinear force-displacement relationship. *Engineering Structures*, 267, 114699.

Yousuf, M., & Bagchi, A. (2009). Seismic design and performance evaluation of steel-frame buildings designed using the 2005 National building code of Canada. *Canadian Journal of Civil Engineering*, 36(2), 280-294.

Zarnic, R., & Tomazevic, M. (1985). Study of the behaviour of masonry infilled reinforced concrete frames subjected to seismic loading. *Proceedings of the 7th International Conference on Brick Masonry*, 1315–1325. Australia.

Appendix

Table A.1: Summary of reviewed structural plans

Year	Building name	No. of rods	Edge distance	Anchor spacing	Grout thickness
52	Jewish Hospital.	2		6"	
65	Jewish Hospital.				1"
64	ST-FOY CINEMA.	2		5"	
-	-	4	2"	10"	
65	WoolWorth	2		5.5	1 1/2
66	School_Lachute	4	1.5"	8"	
69	Albé-Viau	4	1.5"	6"	
-	-	2		5"	
70	Riverdale	2		5"	1"
71	Pascal Hardware	2		5"	
	-	6	2.5"	5"	
74	Domaine Center	4	2"	8"	
	-	4	2"	6"	
	-	4	1.5"	5"	1"
	-	2		5"	

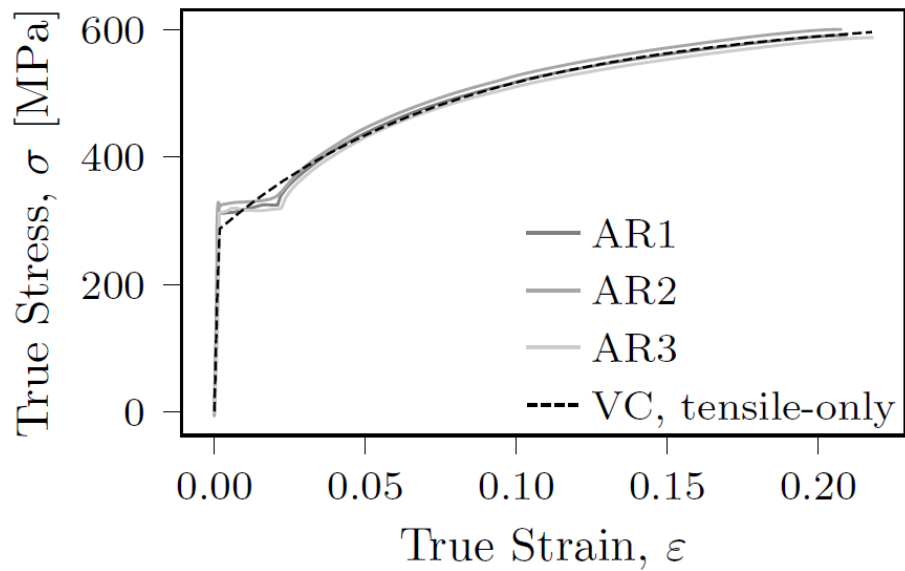


Figure A.1: Comparison of anchor rod coupons and VC model stress-strain curves.

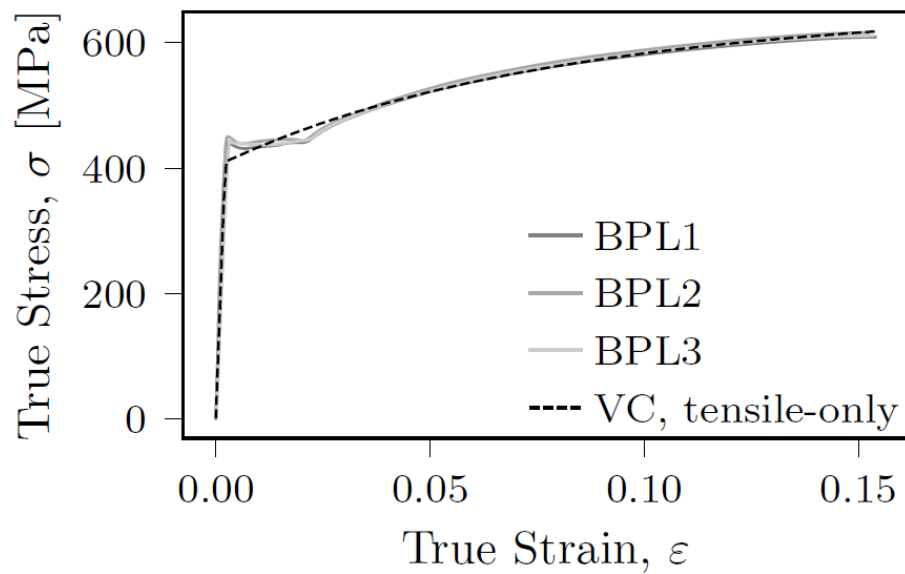


Figure A.2: Comparison of base plate coupons and VC model stress-strain curves.

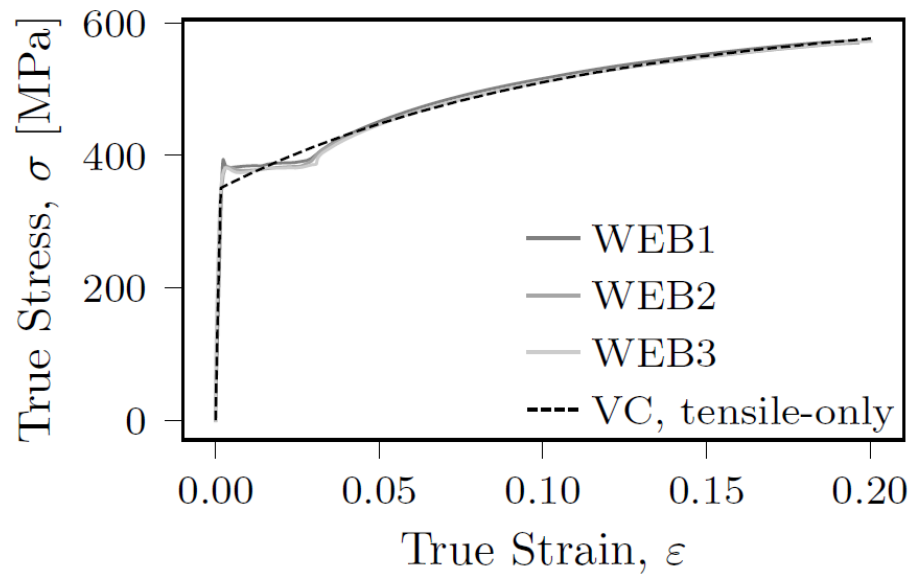


Figure A.3: Comparison of web coupons and VC model stress-strain curves.

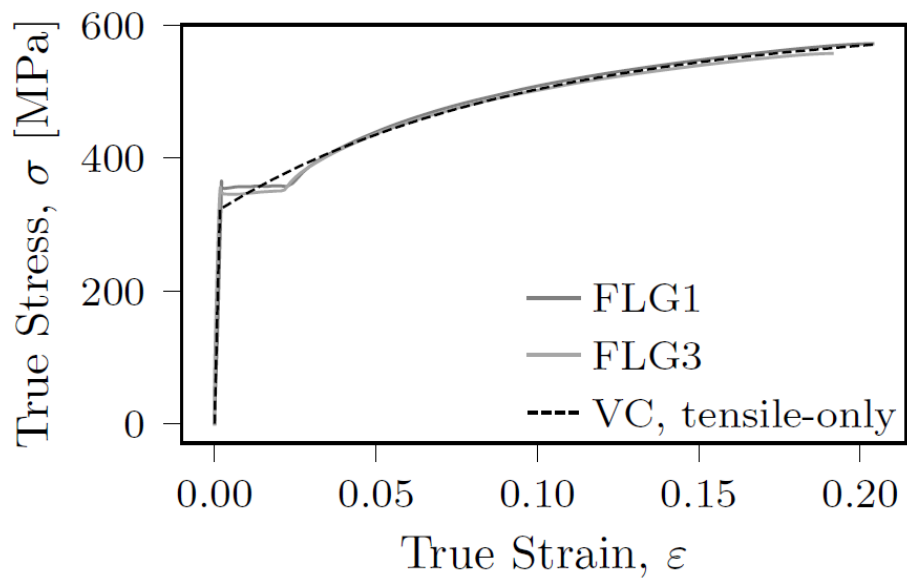


Figure A.4: Comparison of flange coupons and VC model stress-strain curves.

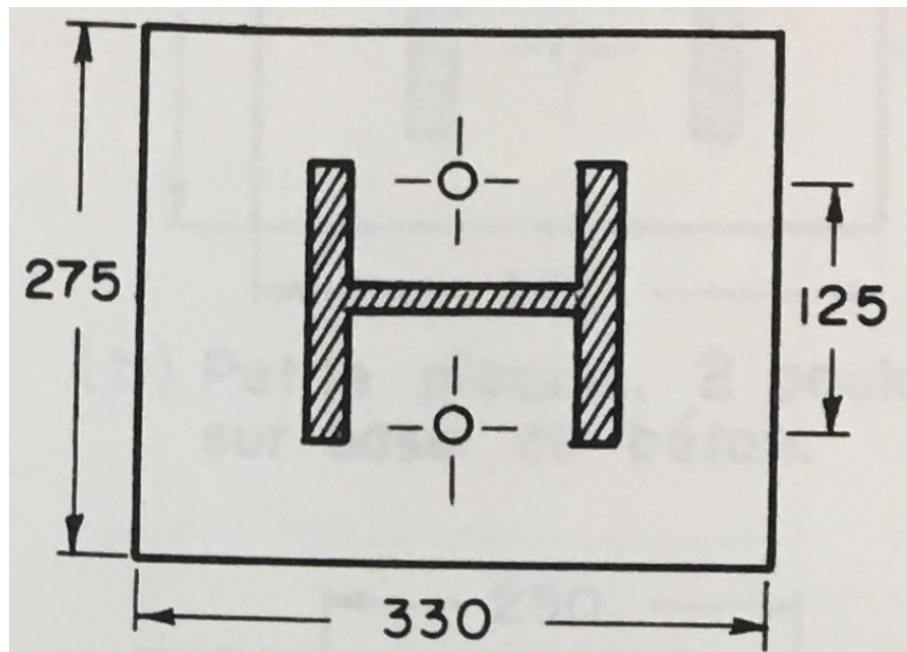


Figure A.5: Standard 2 anchor rods column base connection found in Étude expérimentale de la rigidité d'un assemblage poteau-fondation de type standard (1985)

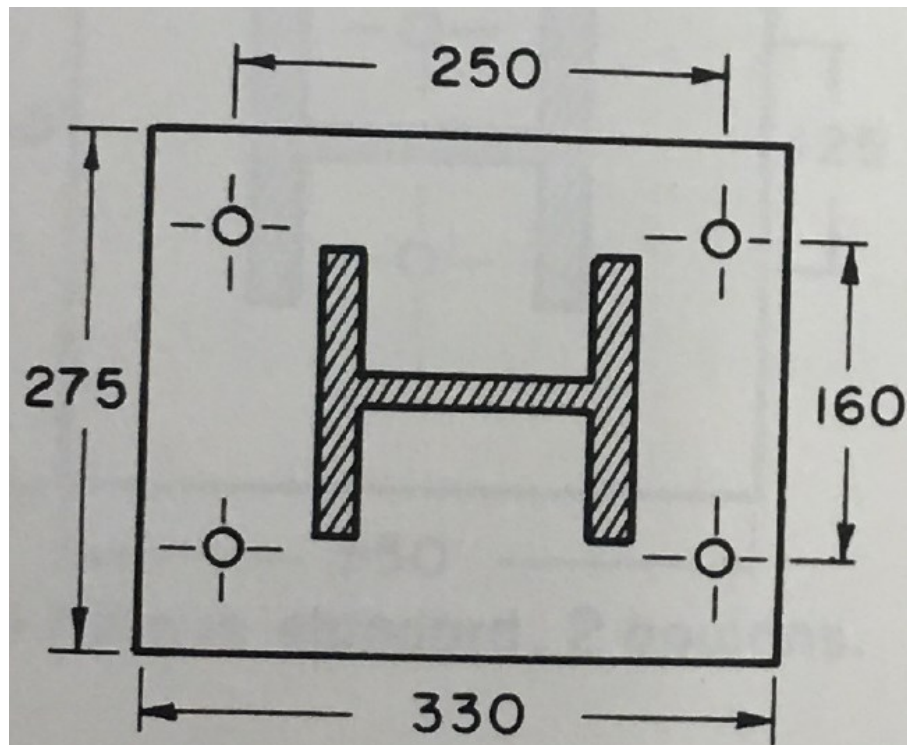


Figure A.6: Standard 4 anchor rods column base connection found in Étude expérimentale de la rigidité d'un assemblage poteau-fondation de type standard (1985)

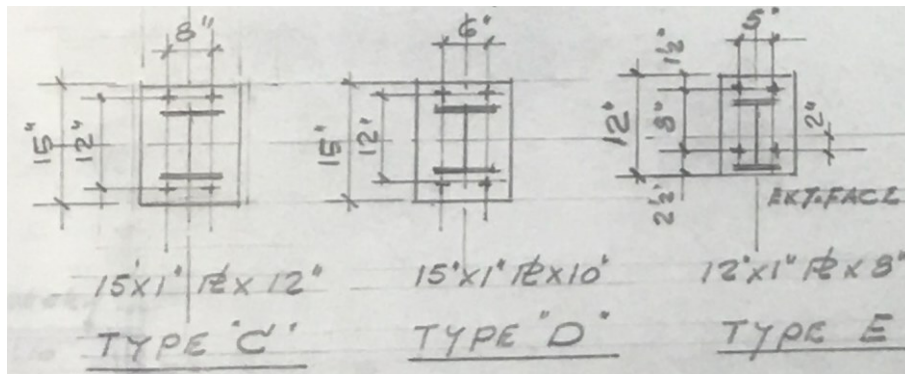


Figure A.7: 4 anchor rods column base connections found in structural plans of Domaine shopping center (1973)

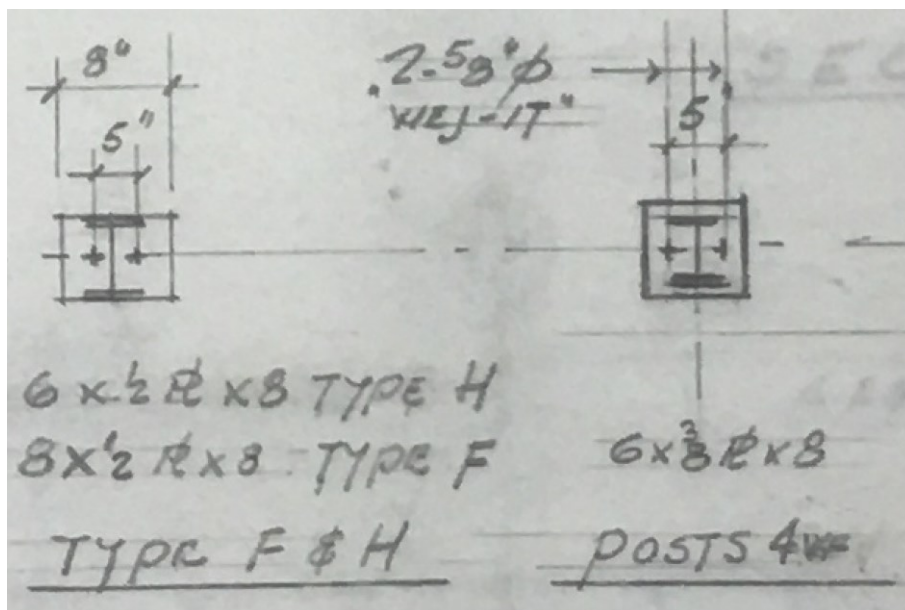


Figure A.8: 2 anchor rods column base connections found in structural plans of Domaine shopping center (1973)

- ① FOUNDATIONS DESIGNED FOR 8000 $\frac{kg}{m^2}$ SOIL LOAD AND ROCK FOUNDATION 20,000 $\frac{kg}{m^2}$
- ② USE 4000 # CONCRETE FOR ALL FOOTINGS.
- ③ CLEARANCE OF REINFORCING IN FOOTINGS 3".
CLEARANCE OF REINFORCING IN CONCRETE COLUMNS 2".
- ④ BETWEEN FOOTINGS AND CONCRETE COLUMNS ABOVE, PLACE 2x20 DIAMETER LONG POWELS OF SAME SIZE AND NUMBER AS COLUMN REINFORCING.
- ⑤ ALL REINFORCING STEEL TO BE INTERMEDIATE GRADE DEFORMED BARS OF 40 $\frac{kg}{cm^2}$ YIELD STRESS, WORKING STRESS 16 $\frac{kg}{cm^2}$.
- ⑥ GROUT 1" THICKNESS BETWEEN TOP OF CONCRETE AND UNDERSIDE OF BASE PLATE.
- ⑦ STRUCTURAL STEEL, FOR ALL COLUMNS AND BASE PLATES TO BE G.40.12 OF 44 $\frac{kg}{cm^2}$ YIELD STRESS.
WORKING STRESS OF ALL STRUCTURAL SHAPES 26.5 $\frac{kg}{cm^2}$
BASE PLATES UP TO 1 1/2" THICKNESS 33 $\frac{kg}{cm^2}$
" " " " " 1 1/2" TO 2 1/2" " 30 $\frac{kg}{cm^2}$
" " " " " OVER 2 1/2" " 27 $\frac{kg}{cm^2}$
- ⑧ WHERE FUTURE EXTENSION IS INTENDED, COLUMNS TO EXTEND SPLICE LENGTH ABOVE PRESENT ROOF LEVEL.

Figure A.9: Specification from structural plans for extension to Jewish Hospital (1965)

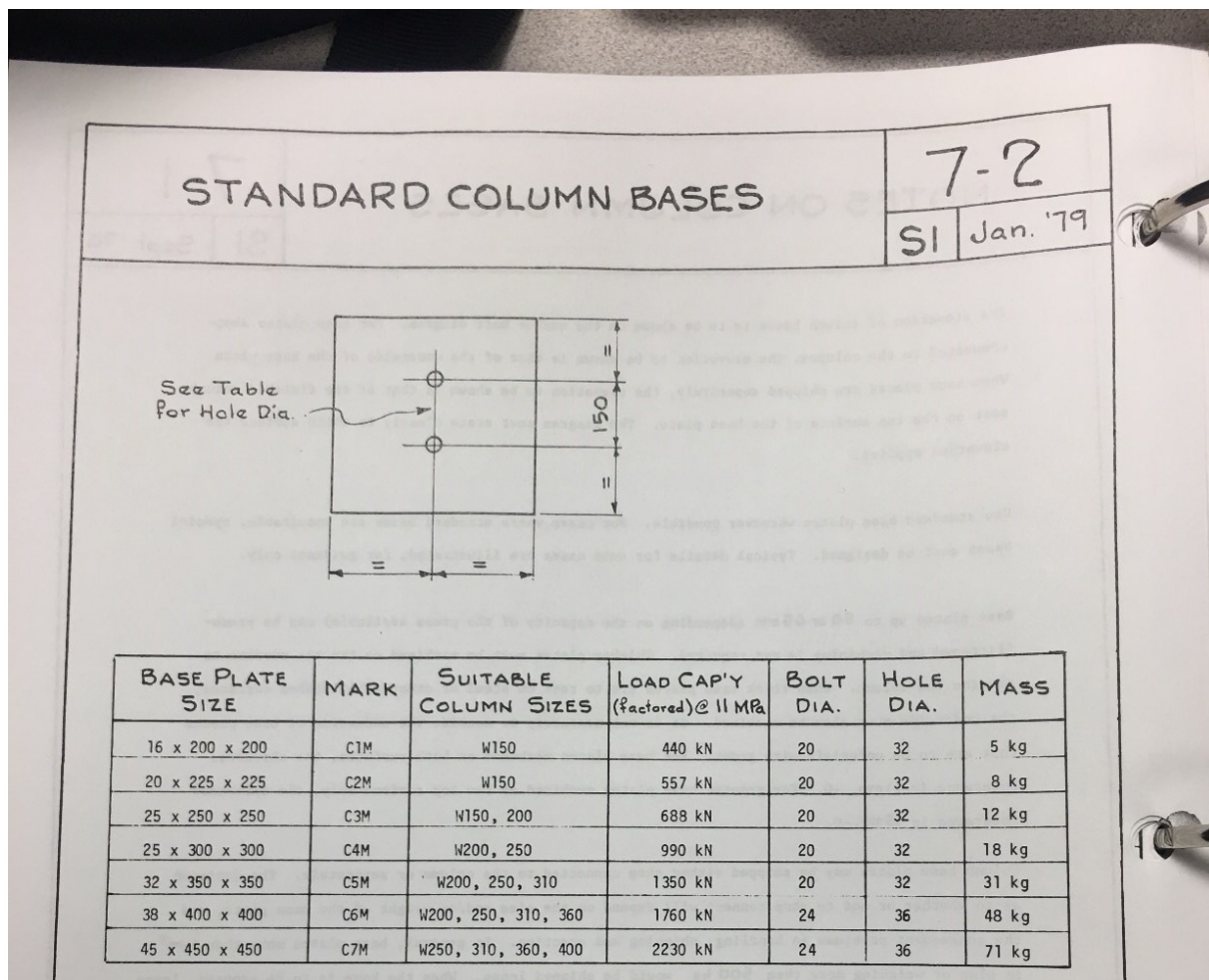


Figure A.10: Standard column base connections from Dominion Bridge-Sulzer INC. Structural Standard

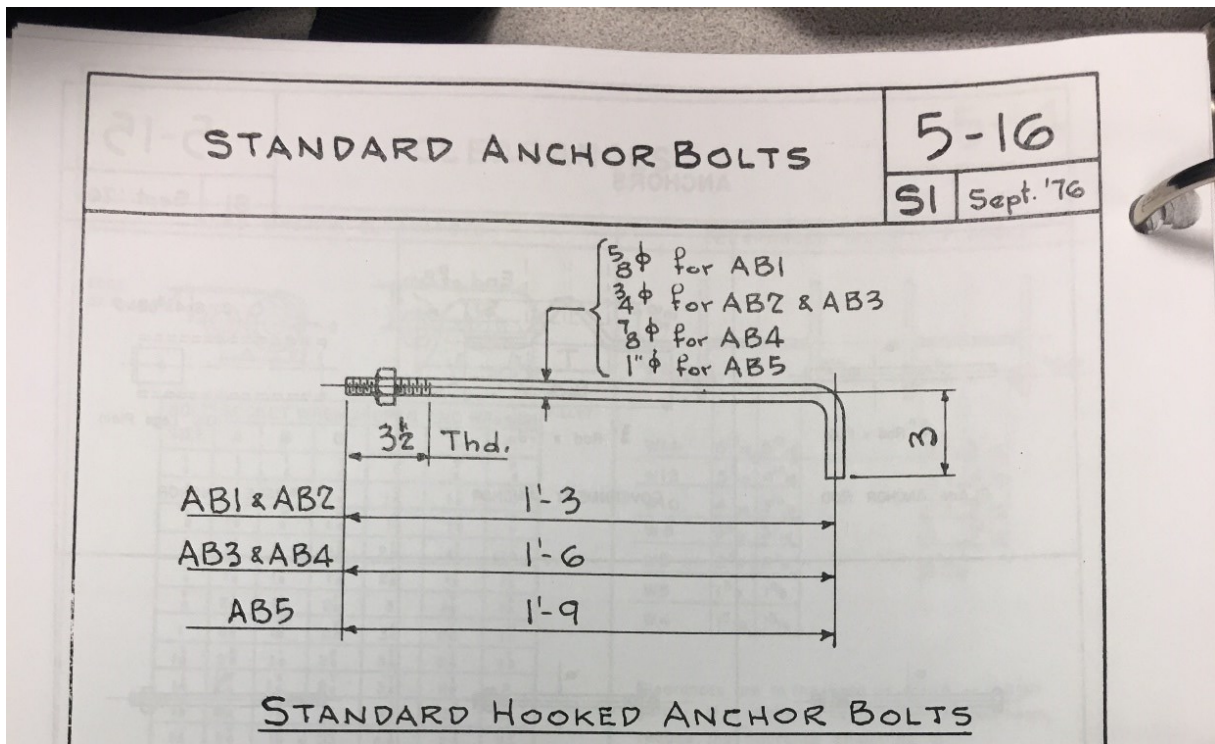


Figure A.11: Standard anchor bolts from Dominion Bridge-Sulzer INC. Structural Standard